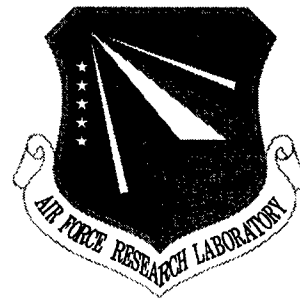


AFRL-SN-RS-TR-1999-191

Final Technical Report

September 1999



COHERENT OPTICAL RECEIVER ENGINEERING (CORE)

TRW, Inc.

**Sponsored by
Defense Advanced Research Projects Agency
DARPA Order No. D065**

APPROVED FOR PUBLIC RELEASE; DISTRIBUTION UNLIMITED.

The views and conclusions contained in this document are those of the authors and should not be interpreted as necessarily representing the official policies, either expressed or implied, of the Defense Advanced Research Projects Agency or the U.S. Government.

**AIR FORCE RESEARCH LABORATORY
SENSORS DIRECTORATE
ROME RESEARCH SITE
ROME, NEW YORK**

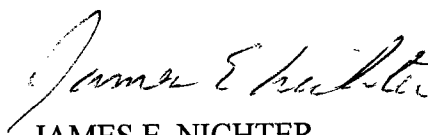
DTIC QUALITY INSPECTED 4

19991208 024

This report has been reviewed by the Air Force Research Laboratory, Information Directorate, Public Affairs Office (IFOIPA) and is releasable to the National Technical Information Service (NTIS). At NTIS it will be releasable to the general public, including foreign nations.

AFRL-SN-RS-TR-1999-191 has been reviewed and is approved for publication.

APPROVED:



JAMES E. NICTER
Project Engineer

FOR THE DIRECTOR:



ROBERT G. POLCE, Acting Chief
Rome Operations Office
Sensors Directorate

If your address has changed or if you wish to be removed from the Air Force Research Laboratory Rome Research Site mailing list, or if the addressee is no longer employed by your organization, please notify AFRL/, Rome, NY 13441-4515. This will assist us in maintaining a current mailing list.

Do not return copies of this report unless contractual obligations or notices on a specific document require that it be returned.

COHERENT OPTICAL RECEIVER ENGINEERING (CORE)

R. Davis
R. Lodenkamper
T. Jung
M. Wickham
L. Lembo
W. Wang
M. Wu

Contractor: TRW, Inc
Contract Number: F30602-96-C-0273
Effective Date of Contract: 27 September 1996
Contract Expiration Date: 30 September 1998
Short Title of Work: Coherent Optical Receiver Engineering
(CORE)
Period of Work Covered: Sep 96 – Sep 98
Principal Investigator: Richard L. Davis
Phone: (310) 813-7540
AFRL Project Engineer: James E. Nichter
Phone: (315) 330-7423

Approved for public release; distribution unlimited.

This research was supported by the Defense Advanced Research
Projects Agency of the Department of Defense and was monitored
by James E. Nichter, AFRL/SNDP, 25 Electronic Pky, Rome, NY.

REPORT DOCUMENTATION PAGE			Form Approved OMB No. 0704-0188	
<small>Public reporting burden for this collection of information is estimated to average 1 hour per response, including the time for reviewing instructions, searching existing data sources, gathering and maintaining the data needed, and completing and reviewing the collection of information. Send comments regarding this burden estimate or any other aspect of this collection of information, including suggestions for reducing this burden, to Washington Headquarters Services, Directorate for Information Operations and Reports, 1215 Jefferson Davis Highway, Suite 1204, Arlington, VA 22202-4302, and to the Office of Management and Budget, Paperwork Reduction Project (0704-0188), Washington, DC 20503.</small>				
1. AGENCY USE ONLY (Leave blank)		2. REPORT DATE September 1999		3. REPORT TYPE AND DATES COVERED Final Sep 96 - Sep 98
4. TITLE AND SUBTITLE COHERENT OPTICAL RECEIVER ENGINEERING (CORE)			5. FUNDING NUMBERS C - F30602-96-C-0273 PE - 62712E PR - D965 TA - 00 WU - 01	
6. AUTHOR(S) R. Davis, R. Lodenkamper, T. Jung, M. Wickham, L. Lembo, W. Wang, and M. Wu				
7. PERFORMING ORGANIZATION NAME(S) AND ADDRESS(ES) TRW, Inc. Space and Technology Division One Space Park Redondo Beach			8. PERFORMING ORGANIZATION REPORT NUMBER N/A	
9. SPONSORING/MONITORING AGENCY NAME(S) AND ADDRESS(ES) Defense Advanced Research Projects Agency AFRL/SNDR 3701 North Fairfax Drive 25 Electronic Pky Arlington, VA 22203-1714 Rome NY 13441-4514			10. SPONSORING/MONITORING AGENCY REPORT NUMBER AFRL-SN-RS-TR-1999-191	
11. SUPPLEMENTARY NOTES AFRL Project Engineer: James E. Nichter/SNDR/(315) 330-7423				
12a. DISTRIBUTION AVAILABILITY STATEMENT Approved for public release; distribution unlimited.			12b. DISTRIBUTION CODE	
13. ABSTRACT (Maximum 200 words) The Coherent Optical Receiver Engineering (CORE) program studied the development of an all optical RF receiver system and produced a prototype receiver. The bench-top demonstration unit instantaneously channelizes 100 GHz of RF bandwidth with 1 GHz resolution and simultaneously translates the center frequency of all the channels to a common intermediate frequency band. The CORE channelizer preserves the signal's complex spectra and can be produced to a compact package that occupies less than 15 in ³ . The coherent optical processor architectures identified in this study could satisfy a wide range of mission requirements and would be of value in a variety of military RF systems. The demonstrated dynamic range of 45 dB into a 1 GHz bandwidth is superior to the performance of existing electronic and acousto-optic approaches to signal channelization. The CORE architectures identified in this report utilize CW injection locking of a mode-locked external cavity semiconductor laser to provide the local oscillator source for the heterodyne process.				
14. SUBJECT TERMS Photonics, Receiver, Optical Frequency Comb, Coherent Optical Heterodyne Link, Mode Locked Laser			15. NUMBER OF PAGES 300	
			16. PRICE CODE	
17. SECURITY CLASSIFICATION OF REPORT UNCLASSIFIED	18. SECURITY CLASSIFICATION OF THIS PAGE UNCLASSIFIED	19. SECURITY CLASSIFICATION OF ABSTRACT UNCLASSIFIED	20. LIMITATION OF ABSTRACT UL	

PREFACE

This final report describes efforts performed during the Coherent Optical Receiver Engineering program. This program was funded by the Defense Advanced Research Projects Agency and monitored by the Air Force Research Laboratory, Rome Operating Center under contract number F30602-96-C-0026.

Most of the work was performed by TRW Space and Electronics Group, Space and Technology Division, Redondo Beach, California. The effort described in Section 5 was performed under subcontract by UCLA, Los Angeles, California. The program manager during the early phase of the program was Dr. Lawrence Lembo. Mr. Richard Davis was the program manager for the program's remainder. Project administration functioned smoothly through the efforts of Mr. Tizoc Loza and Mr. Brian Trimpe, Contracts, and Mr. Gary McKay, Ms. Barbara South, Mr. Richard Huang, and Ms. Angeles Martinez, Project Control, and Ms. Linda Raney, Subcontracts.

The work described in this volume that was performed at TRW was conducted under the technical direction of Dr. Lawrence Lembo and Mr. Richard Davis. Professor Ming Wu directed the subcontract effort at UCLA.

Mr. Richard Hilton was responsible for the application study, and Dr. Robert Lodenkamper performed the analyses of the receiver performance and optical carrier tracking. Additionally he guided the CW laser injection locking experiments. Mr. Thomas Jung, Dr. Ji-Lin Shen, Mr. Sanjeev Murthy, Dr. Dennis Tong, and Dr. Xuejen Meng performed the optical frequency comb generator work at UCLA. Dr. Wenshen Wang and Mr. Thomas Jung were responsible for the channelizer testbed experiments. Other personnel making important contributions to the technical effort were Dr. Paul Nachman who provided critical expertise in the assembly of the channelizer testbed, Ms. Suzanne Casement who developed optical layouts for the channelizer, and Mr. Martin Flannery and Mr. John Yun who designed and evaluated the channelizer optics.

In addition to those named above, we would be remiss if we didn't acknowledge the vision and technical guidance provided by Dr. John Brock throughout the performance of this program, and particularly during its formative stages. We also recognize the

invaluable contributions of Dr. Michael Wickham who furnished much of the conceptual insight that provided a sound footing for this successful program.

The contract was monitored by B. Hendrickson and D. Gammon of the Defense Advanced Research Projects Agency. The COTR for this program was J. Nichter of the Air Force Research Laboratory, Rome Operating Center. Their support and assistance contributed greatly to the success of this program.

TABLE OF CONTENTS

1	INTRODUCTION	1
1.1	OVERVIEW	1
1.2	BACKGROUND	2
1.3	STATEMENT OF OBJECTIVES	4
1.4	ORGANIZATION OF REPORT	5
2	ARCHITECTURE STUDY	7
2.1	APPLICATIONS STUDY	7
2.2	CONCEPTUAL ARCHITECTURE DEVELOPMENT	10
2.2.1	Single-channel receiver with optical heterodyne frequency translation	11
2.2.2	Wavelength-division-multiplex-based multiple receiver system	15
2.2.3	Coherent optical channelized receiver	17
3	RECEIVER PERFORMANCE ANALYSIS	21
3.1	HETERODYNE LINK ANALYSIS: SPUR-FREE DYNAMIC RANGE AND NOISE FIGURE	21
3.1.1	Mach Zehnder modulator nonlinearities and the two tone spurious signals	21
3.1.2	Spur-free dynamic range (SFDR)	24
3.1.3	Noise figure	30
3.2	CHANNEL RESPONSE: LOSS, RIPPLE, AND CROSSTALK	31
3.2.1	Fabry-Perot filter channelizer	32
3.2.2	Free-space, diffraction grating channelizer	35
3.2.3	Additional issues for free-space, diffraction grating channelizer	39
4	OPTICAL CARRIER TRACKING	49
4.1	GENERAL NOISE BACKGROUND	49
4.1.1	Definitions and notation	49
4.1.2	Linear filtering of noise	52
4.1.3	Passband to baseband transformation [5]	52
4.1.4	Phase noise spectra and units	54
4.1.5	Phase modulation of a carrier by noise	55
4.1.6	Special cases for phase modulation of a carrier by noise	56
4.2	OPTICAL SIGNALS AND NOISES	57
4.2.1	Photocurrent	57
4.2.2	Thermal noise	58
4.2.3	Shot noise	58
4.2.4	Laser RIN	59
4.2.5	Optical amplifier noise	59
4.2.6	Laser phase noise	60
4.3	PHASE LOCKED LOOP - THEORY	61
4.3.1	PLL transfer functions	61
4.3.2	Stability	63
4.3.3	Noise filtering	64
4.3.4	External time delay	66

4.4	PHASE LOCKED LOOP – EXPERIMENT	70
4.4.1	Phase-Locked Loop (PLL) Testbed	70
4.4.2	Experimental Results.....	71
4.5	INJECTION LOCKING (CW LASERS) - THEORY	73
4.5.1	Summary	74
4.5.2	Semiconductor laser rate equations.....	75
4.5.3	Low level injection locking.....	78
4.5.4	Transfer functions for $\phi_0 = 0$ injection locking	83
4.5.5	Noise.....	84
4.6	INJECTION LOCKING (CW LASERS) - EXPERIMENT	86
4.6.1	Injection locking testbed	86
4.6.2	Injection locking characteristics	87
4.6.3	RF performance of injection locked lasers.....	91
4.6.4	RF modulation of injection locked semiconductor lasers	94
5	OPTICAL FREQUENCY COMB GENERATION	96
5.1	METHODS FOR OPTICAL FREQUENCY COMB GENERATION.....	97
5.2	MODE-LOCKED LASER EXPERIMENTAL SETUP	98
5.3	MODE-LOCKED LASER EXPERIMENTAL RESULTS	102
5.3.1	Linewidth of an external cavity hybrid mode-locked laser.....	106
5.3.2	Noise of a Mode-Locked Laser	111
5.3.3	Residual phase noise of an actively mode-locked laser	114
5.3.4	Locking Bandwidth of a Mode-Locked Laser	115
5.4	CARRIER TRACKING	117
5.4.1	Injection locking of a hybrid mode-locked semiconductor laser	117
5.4.2	Pulse Characteristics of an Injection Locked Mode-Locked Laser.....	120
5.4.3	Physics of injection locking of a mode-locked laser	123
5.5	CONCLUSIONS	130
6	OPTICAL CHANNELIZER TESTBED	132
6.1	CHANNELIZER DESIGN.....	133
6.1.1	Grating selection.....	135
6.1.2	Channelizer angular dispersion and optical beam diameter.....	142
6.1.3	Channelizer focal plane layout.....	145
6.1.4	Channelizer testbed lens.....	147
6.2	CHANNELIZER TESTBED ASSEMBLY	163
6.3	CHANNELIZER TESTBED EXPERIMENTAL RESULTS.....	168
6.3.1	Optical System Characterization	168
6.3.2	RF Measurements.....	173
7	TOP LEVEL DESIGN PLAN.....	182
8	CONCLUSIONS.....	185
9	REFERENCES	188
10	APPENDICES	194

LIST OF FIGURES

Figure 1-1. Miniature optical channelizer	1
Figure 1-2. The modern signal environment is increasingly populating the higher frequency bands	2
Figure 1-3. The wideband requirements of future military systems motivates the development of optically-based signal processing.....	3
Figure 1-4. The CORE program extends optical analog functionality into the back-end of RF receivers	4
Figure 1-5. CORE program logic	5
Figure 2-1. New activity reported in Janes 1997 radars and ELINT systems.....	7
Figure 2-2. The detection / measurement problem.....	8
Figure 2-3. State-of-the-art phase-noise requirements	10
Figure 2-4. The single-channel coherent optical receiver	12
Figure 2-5. The receiver IF must be sufficiently large to avoid image frequencies.....	13
Figure 2-6. Wide instantaneous bandwidths place challenging requirements on electronic IF frequencies.....	14
Figure 2-7. Optical frequency comb eliminates the need for a widely tunable RF reference oscillator.....	15
Figure 2-8. Wavelength division multiplexing techniques enable increased optical bandwidth utilization	16
Figure 2-9. Wideband RF signals can be partitioned and routed to separate receivers ...	17
Figure 2-10. The coherent optical channelizer receiver uses a dispersion grating to map the optically carried RF signal and LO spectra onto a photodetector array.....	18
Figure 2-11. The CORE Channelizer will be a precursor to further signal processing.....	20
Figure 3-1. The nonlinear response of the modulator determines the dynamic range	24
Figure 3-2. A comprehensive model is the basis for calculation of spur free dynamic range.....	25
Figure 3-3. It is desirable to operate the optical channelized receiver in the ASE noise limited regime in order to maximize the dynamic range.	29
Figure 3-4. Schematic frequency response of several adjacent channel filters. The effect of nonideal channel filters is described by three parameters: loss, ripple and crosstalk, as shown.....	31
Figure 3-5. Ripple-crosstalk trade for direct detection (dotted line) and heterodyne (solid line) Fabry-Perot optical channelizer.....	35
Figure 3-6. Schematic diagrams of output focal plane for a heterodyne DG channelizer. The spot due to the (monochromatic) optical input is shown with a heavy line, the LO comb spots are shown with lighter lines, and the vertical lines indicate the boundaries of the detector array elements. There is a frequency shift between the signal and LO spots, such that if a signal spot coincides with an LO spot, the resulting photocurrent oscillates at the IF frequency.	36
Figure 3-7. Ripple (a) and loss (b) trades vs. crosstalk for direct detection (dotted line) and heterodyne (solid line) free space diffraction grating optical channelizer.	38
Figure 3-8. w parameter (Gaussian radius/array element spacing) for direct detection (dotted line) and heterodyne (solid line) DG optical channelizers	39

Figure 3-9. Output intensity ($I = h^2$) distribution due to finite grating length ($b = 3$) for $w = 0.46$. Dotted line is intensity distribution from an infinitely long grating, for comparison. The units of position are channel spacings, so this plot shows the intensity distribution for a spot centered on detector 0 where the detector edges are at 0.5, 1.5, 2.5 etc.	40
Figure 3-10. Crosstalk vs. grating aperture for -70 dB crosstalk example. b is the ratio of grating length to Gaussian spot radius at the grating.	41
Figure 3-11. s_2 (a) and s_3 (b) vs. b (the grating aperture) for a heterodyne DG channelizer with -70 dB of crosstalk.	43
Figure 3-12. Spot size vs fill factor for heterodyne DG channelizer with -70 dB crosstalk	45
Figure 3-13. Ripple (a) and loss (b) vs. detector array fill factor for heterodyne DG channelizer with -70 dB crosstalk.	46
Figure 3-14. LO (a) and carrier (b) w parameters vs. ripple for a heterodyne DG channelizer with -70 dB crosstalk.....	47
Figure 3-15. Loss (a) and q (b) vs. ripple for heterodyne DG channelizer with -70 dB crosstalk	48
Figure 4-1. Block diagram of an optical phase lock loop	61
Figure 4-2. Additive phase noise in PLL with $r = 0.7$ A/W, $P_1 = P_2$ and $RIN_1 = RIN_2$. The curves are labeled with the laser RIN [dB/Hz].....	65
Figure 4-3. Additive phase noise in PLL with $r = 0.7$ A/W, $P_1 = 0.01 \cdot P_2$ and $RIN_1 = RIN_2$. The curves are labeled with the laser RIN [dB/Hz].....	66
Figure 4-4. Schematic block diagram for external heterodyne of PLL-locked lasers.....	68
Figure 4-5. PLL testbed block diagram.....	71
Figure 4-6. Preliminary phase noise measurement from PLL testbed	72
Figure 4-7. Phase noise measurement from PLL testbed.....	73
Figure 4-8. Optical injection locking phasor diagram.....	74
Figure 4-9. Stable regions in the phase/injection plane. Injection level p is on the horizontal axis, and the relative phase ϕ_0 is on the vertical axis. The various curves correspond to $\alpha = 0.5, 1, 2$, and 6 , where as α increases, the curves generally move to the left and closer to $\phi_0 = 0$. For each α there are two lines which give the stability region (patterns correspond on plot), and a point is stable if it is below the upper line and to the left of the lower line. Points below the lowest point of the lower curve are not stable.	81
Figure 4-10. Stable regions in the detuning/injection plane. Injection level is on the horizontal axis, and the normalized detuning is on the vertical axis. Regions below (or to the left of) the lines and between $y = 1$ and $y = -1$ are stable. The various curves correspond to $\alpha = 0.5, 1, 2$, and 6 , where as α increases, the curves move down and to the left.....	82
Figure 4-11. Experimental setup for optical injection locking of CW lasers.....	86
Figure 4-12. Optical spectrum of DFB slave laser.....	87
Figure 4-13. Linewidth of SDL external cavity laser measured with 250 nsec delay	88
Figure 4-14. Linewidth of free-running DFB laser measured with 250 nsec delay	89
Figure 4-15. Linewidth of injection locked DFB slave laser measured with 100 nsec delay	90
Figure 4-16. Total locking range at various bias currents.....	91

Figure 4-17. Heterodyne tone of injection locked semiconductor laser.....	92
Figure 4-18. Injection locked phase noise, -15 dB injection ratio	93
Figure 4-19. Phase noise at various injection levels	93
Figure 4-20. Increased modulation bandwidth of slave laser under injection locking.....	94
Figure 4-21. Second harmonic distortion suppression under injection locking at various modulation frequencies	95
Figure 5-1. Coherent optical channelizer concept.....	96
Figure 5-2. Side mode suppression of a harmonic mode-locked fiber laser	98
Figure 5-3. External cavity mode-locked laser configuration	99
Figure 5-4. EMBH multi-quantum well three section laser	99
Figure 5-5. Frequency response of monolithic external cavity without external feedback	100
Figure 5-6. Frequency response of a 1 GHz external cavity	101
Figure 5-7. Frequency response of a double pass external cavity.....	101
Figure 5-8. Incomplete mode-locking and coherence spikes	102
Figure 5-9. Autocorrelation trace of external cavity hybrid mode-locked laser	103
Figure 5-10. Optical spectrum of hybrid mode-locked laser.....	103
Figure 5-11. Pulseswidth at various center wavelengths	104
Figure 5-12. Resolved modes of the hybrid mode-locked laser.....	105
Figure 5-13. Coupled cavity effect due to imperfect AR coating	105
Figure 5-14. Linewidth of hybrid mode-locked, external cavity laser	106
Figure 5-15. Anti-resonant fabry perot saturable absorber (AFP-SA).....	107
Figure 5-16. Saturable Bragg reflector (SBR).....	108
Figure 5-17. External cavity mode-locked semiconductor laser using SBR.....	109
Figure 5-18. Optical spectrum of passively mode-locked external cavity laser using a SBR	109
Figure 5-19. Compressed pulseswidths at various stages of pulse compression using single mode fiber.....	110
Figure 5-20. 570 fs compressed pulseswidth using 40 meters of single mode fiber	110
Figure 5-21. Detected RF spectrum of hybrid mode-locked laser	112
Figure 5-22. Fundamental tone of external cavity hybrid mode-locked laser.....	113
Figure 5-23. Phase noise hybrid mode-locked laser fundamental tone.....	115
Figure 5-24. Phase noise with increased RF drive power	115
Figure 5-25. Pulse shaping process for detuning a mode-locked laser	116
Figure 5-26. Phase noise measured at various mode-locked frequencies	116
Figure 5-27. Phase noise floor measured at frequencies 10 kHz offest across the detuning range.....	117
Figure 5-28. Experimental setup for injection locking of a mode-locked semiconductor laser	118
Figure 5-29. Heterodyne detection of injection locked mode-locked laser	119
Figure 5-30. Heterodyne tones of injection locked mode-locked laser.....	119
Figure 5-31. Autocorrelation of mode-locked laser with no injection.....	121
Figure 5-32. Autocorrelation trace of mode-locked laser with -12.5 dBm injection	121
Figure 5-33. Autocorrelation trace of mode-locked laser with -9.5 dBm injection	122
Figure 5-34. Pulseswidth at various injection levels	122
Figure 5-35. Sideband generation in a mode-locked laser	123

Figure 5-36. Generation of sidebands from injected mode	124
Figure 5-37. Generation of sidebands for various injection locking schemes	125
Figure 5-38. Locking range at various optical injection ratio	126
Figure 5-39. Pulling of mode-locked laser modes	127
Figure 5-40. Experimental setup to filter the output of the mode-locked laser.....	128
Figure 5-41. Filtered modes of the external cavity mode-locked laser	128
Figure 5-42. Heterodyne detection of filtered mode-locked laser modes and master laser	129
Figure 5-43. Heterodyne detection of filtered mode-locked laser modes and master laser under low injection.....	130
Figure 6-1. The channelizer testbed is a powerful tool for characterizing coherent optical receiver performance.....	133
Figure 6-2. The channelizer design is based on a suitable off-the-shelf diffraction grating and the RF performance requirements.....	134
Figure 6-3. k-vector diagram for Bragg diffraction from a grating. We have illustrated the case of diffraction order $m = 2$	136
Figure 6-4. Channelizer layout using gratings with 316 grooves per mm	137
Figure 6-5. Channelizer layout using gratings with 452 grooves per mm	138
Figure 6-6. Channelizer optical layout that uses a single diffraction grating.....	139
Figure 6-7. Diffraction efficiency as a function of incident angle for grating "A".....	140
Figure 6-8. Diffraction efficiency as a function of incident angle for grating "B"......	140
Figure 6-9. Diffraction grating tooth profile	141
Figure 6-10. Diffraction efficiency for grating "B" various tooth profiles	142
Figure 6-11. Angular dispersion in a multi-pass geometry	143
Figure 6-12. Channelizer testbed focal plane layout.....	146
Figure 6-13. Reducing the size of the fiber mode spot requires a high-speed lens.....	148
Figure 6-14. Far-field pattern for Fujikura single-mode fiber.....	149
Figure 6-15. CodeV traces rays through the optical system to evaluate lens performance and optimize the lens design	151
Figure 6-16. Computer-optimized channelizer testbed lens comprises three elements manufactured from two glasses.....	151
Figure 6-17. A beamsplitter was incorporated in the first lens element.....	152
Figure 6-18. Physical optics calculation showing the output of a single-mode fiber and its mode profile.	153
Figure 6-19. Physical optics calculation shows the image of the single-mode fiber in the output focal plane of the lens after propagating through the optical system. The position of the input is on the optic axis.	154
Figure 6-20. Output image of a +50GHz offset beam after propagating through the optical system. The location of the input is on the optic axis.....	154
Figure 6-21. Output image of a -50GHz offset beam after propagating through the optical system. The location of the input is on the optic axis.....	155
Figure 6-22. Output image of the single-mode fiber after propagating through the optical system. The input is 0.5mm off the optic axis.	156
Figure 6-23. Output image of -50GHz offset beam after propagating through the optical system. The input is 0.5mm off the optic axis.	156

Figure 6-24. Output image of -50GHz offset beam after propagating through the optical system. The input is 1.0mm off the optic axis.	157
Figure 6-25. Refocusing can compensate for an error in the curvature r_{21} :	158
Figure 6-26. Refocusing can compensate for an error in the curvature r_{22} :	158
Figure 6-27. Refocusing can compensate for an error in the spacing d_{12} :	158
Figure 6-28. Setup for measuring the imaging properties of the channelizer's lens.....	160
Figure 6-29. A scanning knife-edge technique was used to determine the intensity profiles of the imaged spots.	160
Figure 6-30. Measured intensity profile for spot on the optic axis	161
Figure 6-31. Measured intensity profile for spot above the optic axis.....	162
Figure 6-32. Measured intensity profile for spot diagonal to the optic axis	162
Figure 6-33. The channelizer lens point spread function was evaluated at three positions in the focal plane.....	163
Figure 6-34. Grating mounting fixture.....	164
Figure 6-35. Custom roof mirror assembly.....	165
Figure 6-36. Channelizer lens mounting assembly	166
Figure 6-37. I/O optical layout for channelizer testbed.....	167
Figure 6-38. Scale drawing of the channelizer testbed layout on the optical bench	167
Figure 6-39. Photograph of the CORE channelizer testbed	168
Figure 6-40. CORE RF channelizer optical layout	169
Figure 6-41. Channelizer testbed output spot intensity profile	170
Figure 6-42. Measured mode profile for the single-mode fiber used in the channelizer	171
Figure 6-43. Channelizer testbed lens beamsplitter	172
Figure 6-44. Fiber-to-fiber throughput was measured for both optical paths in the channelizer	173
Figure 6-45. Block diagram of the basic RF characterization setup	174
Figure 6-46. The measured 5 GHz microwave signal at the spectrum analyzer.....	175
Figure 6-47. Ripple for the case of equal L.O. and signal spot sizes	177
Figure 6-48. Setup for creating elliptical beam waist	178
Figure 6-49. Ripple for the case of unequal L.O. and signal spot sizes	178
Figure 6-50. Channelizer individual channel passband response (unequal spot size case)	179
Figure 6-51. Channelizer crosstalk measurement	180
Figure 7-1. Miniaturized coherent optical channelizer	183
Figure 7-2. Vertical beam compression is accomplished with cylindrical surfaces on the beam turning prism (shown here with optical path unfolded)	183

LIST OF TABLES

Table 2-1. Systems that require broadband ESM.....	9
Table 2-2. Nominal receiver requirements.....	9
Table 6-1. Nominal channelizer RF performance requirements	133
Table 6-2. Grating sizes for two channelizer layouts	138
Table 6-3. Lens design specifications	150
Table 6-4. Performance of the channelizer lens's beamsplitter	172
Table 6-5. Channelizer optical throughput summary	173
Table 6-6. Channelizer spur-free dynamic range	181
Table 7-1. Exploratory development model parts list	184

1 INTRODUCTION

1.1 OVERVIEW

The Coherent Optical Receiver Engineering (CORE) program has produced a sound technical foundation for future coherent optical receivers and set the stage for the development of a prototype channelized optical receiver. During an initial program task we studied the feasibility of coherent optical processing and identified coherent optical processor architectures that could satisfy a wide range of mission requirements and would be of value in a variety of military RF systems. We then constructed and demonstrated a coherent optical processor that can instantaneously channelize 100GHz of RF bandwidth with 1 GHz resolution and simultaneously translate the center frequency of all the channels to a common intermediate frequency band. The CORE channelizer preserves the signals' complex spectra and we have shown that this processor is capable of providing state-of-the-art RF performance. This performance can be delivered in a very compact package. In Figure 1 we show a layout for an optical system that is equivalent to our benchtop processor and occupies less than 15 in³.

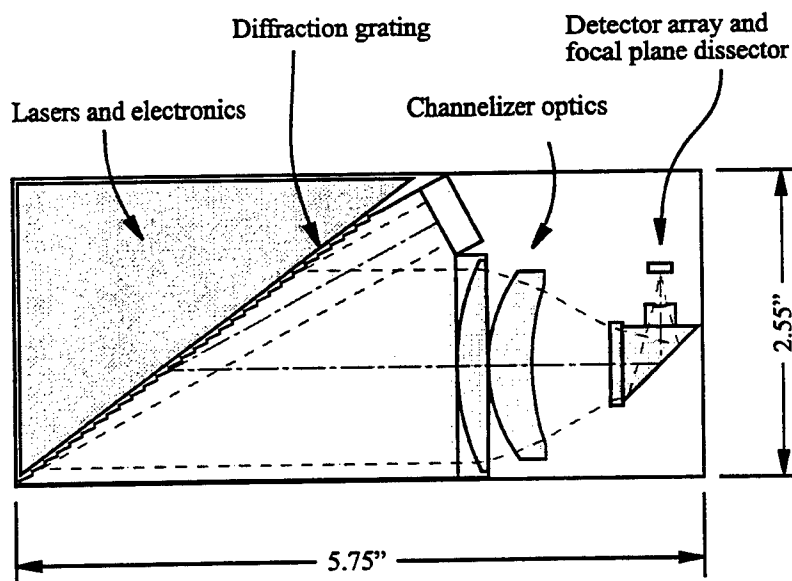


Figure 1-1. Miniature optical channelizer

The path to this miniaturized free-space version of the channelizer is a straightforward engineering exercise based on the results of our efforts on Phase 1 of this program.

CORE has produced the groundwork for a high-performance, photonics-based receiver. What remains is to tailor the technology in terms of form, fit and function to a specific wideband processing requirement, and develop a prototype receiver.

1.2 BACKGROUND

Future military RF systems are increasingly being driven towards higher frequencies and larger bandwidths by user requirements. This situation is depicted in Figure 1-2, where we show a few of the types of emitters that increasingly are populating the higher frequency bands. For example, available communications bandwidth is disappearing as the number of users and the bandwidth per user escalate. This is forcing communications links to ever-higher carrier frequencies. Other requirements such as the need for low probability of intercept links are extending the frequencies of planned communications systems out to 60 GHz and beyond. Likewise modern missile seekers and imaging radars are also moving to frequencies approaching 100 GHz to achieve antenna directivity and higher resolution from small aperture systems. Recent advances in solid-state electronics

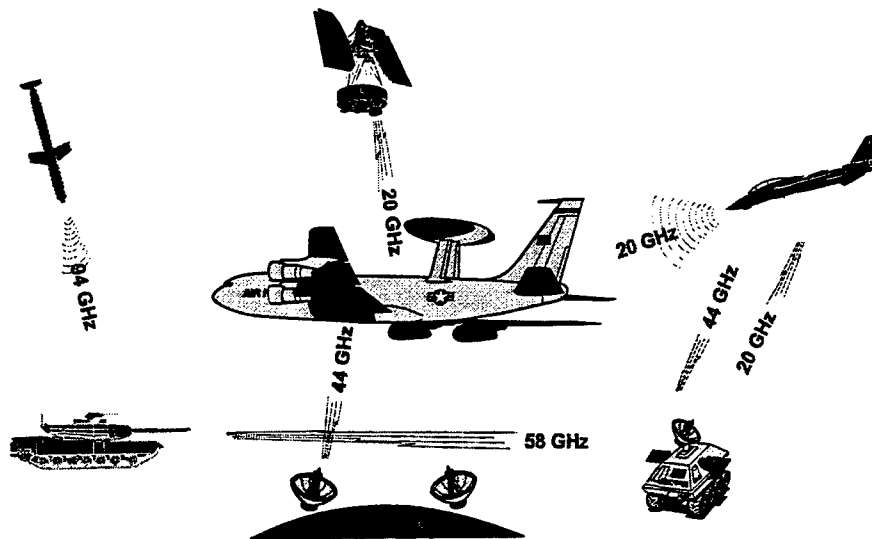


Figure 1-2. The modern signal environment is increasingly populating the higher frequency bands

are enabling the RF designer to develop such high-frequency systems. However it is very difficult to process large data bandwidths, either tunable or instantaneous, using

conventional electronics. As the frequencies and bandwidths escalate we enter a realm where photonics technologies can play an important role in signal transmission and processing. Figure 1-3 illustrates the scenario presented by the wideband requirements of future military systems. Developments in antennas are advanced to the state where coverage of 100GHz bandwidths may require as few as two apertures. We anticipate that many next generation RF systems will elect to employ optical carrier transmission of the RF signal transmission, which will circumvent the very high transmission losses and the sheer bulk attendant with conventional RF cabling and waveguides. Already RF photonic signal transmission is relatively well developed. Recently developed optical modulators and detectors are nearing 100 GHz bandwidths with the requisite low noise and distortion. Thus conventional receiver electronics becomes the bandwidth bottleneck and development is timely for optical processing of wideband signals.

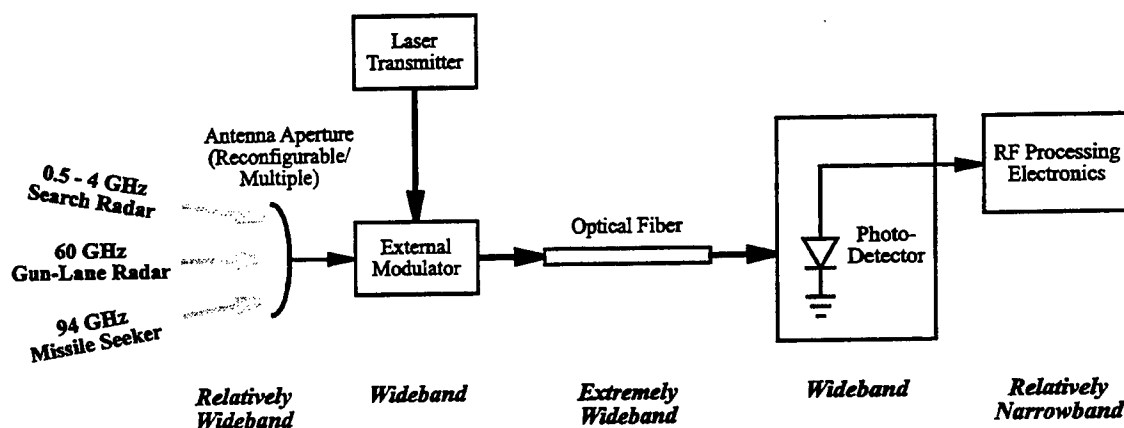


Figure 1-3. The wideband requirements of future military systems motivates the development of optically-based signal processing

In spite of the rapid maturation of optical transmission technologies, the extension of photonic processing further back into the receiver where optical signal processing techniques can be used to advantage has, until recently, received little attention. Certainly since the signal is impressed on an optical carrier, it makes sense to exploit the analog functionality offered by optics to ease the processing load on the electronics. Figure 1-4 presents a conceptual receiver architecture wherein analog processing is applied to the signal prior to digitization. The delineation between optical and RF analog

processing is not clear cut, and depends on factors that include the relative maturity and cost of RF and photonic components, mission functional requirements, and system bandwidth requirements (both instantaneous and tunable). This is the problem addressed by the Coherent Optical Receiver Engineering (CORE) program. Furthermore, since most modern and projected RF systems use both amplitude and phase data, this program specifically targeted wideband coherent optical receivers.

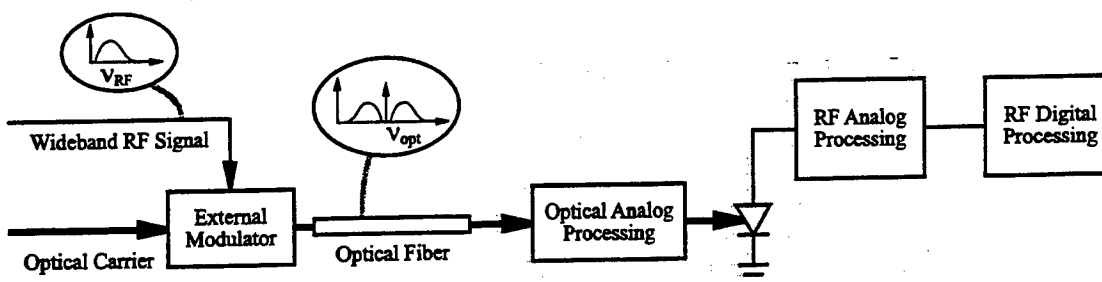


Figure 1-4. The CORE program extends optical analog functionality into the back-end of RF receivers

The CORE program comprises two phases. Phase I, which is complete and the subject of this report, focused on 1) establishing a range of mission requirements and identifying the set of receiver architectures needed to address them, 2) identifying the modular functions and their performance requirements necessary to implement the architectures, 3) identifying the technical options available for implementing the functions, and 4) building and testing flexible testbeds to validate our approaches, resolve open issues and help select the preferred approaches. The optional Phase II will use the results of Phase I as a foundation for the design, fabrication, and testing of a prototype photonic receiver that demonstrates the most promising architecture identified during Phase I.

1.3 STATEMENT OF OBJECTIVES

The overall objective of the CORE program is to design, fabricate, and test an engineering development model for a coherent optical receiver architecture that will enable the capability for sorting, identifying, and tracking emitter signals in the very dense signal environments anticipated in the near future. The projected signal densities

and bandwidths constitute a severe data processing load that greatly exceeds the capability of present and near-term receiver systems.

The approach to meet this objective was to employ the logical progression shown in Figure 1-5. It was most practical to partition the program into two phases. During the completed first phase research was performed to make a technical assessment of photonics architectures. The results of the assessment will then guide the engineering development of a prototype receiver.

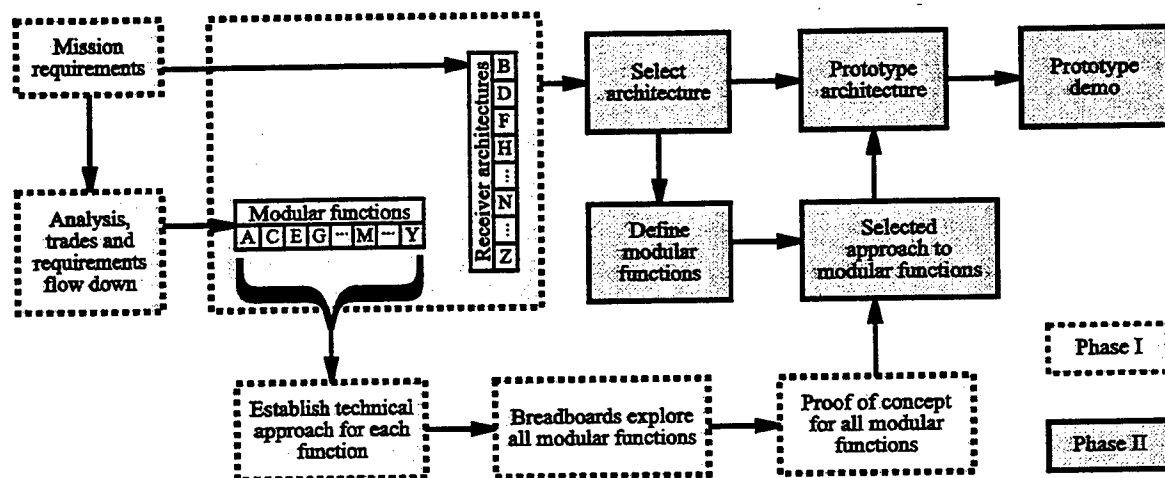


Figure 1-5. CORE program logic

1.4 ORGANIZATION OF REPORT

During the remainder of this report we will discuss the various tasks that were performed during the performance of this project. Section 2 presents a discussion the applications study, which produced the set of mission requirements that guided the determination of potentially useful receiver architectures. During this study we also performed analyses and trades that led to the definition of a set of modular functions that would be required to implement the architectures. In section 3 we present our analysis of the coherent optical receiver's RF performance capabilities. This is a very comprehensive section, which includes theoretical background for many of the calculations in order that the reader may better appreciate the results and conclusions. The results of this analysis show a clear path for optical technology to produce RF performance consistent with the requirements presented by the future receiver systems. Section 4 addresses techniques

for performing optical carrier tracking and presents results of experiments to evaluate the phase-noise performance delivered by two different approaches. One significant result was an improvement by several orders of magnitude in the phase noise power spectral density for injection-locked, semiconductor lasers. Section 5 summarizes the work done to develop an optical frequency comb generator. This task was performed by UCLA under subcontract to TRW as part of the CORE program. Their main focus was on an external-cavity, semiconductor hybrid mode-locked laser approach that produced near transform-limited pulses. Their flexible testbed construction allowed the incorporation of such novel features as an intra-cavity filter to reduce the spectral content of the laser output (thereby concentrating more of the pulse energy in the modes required for our receiver application) and provide tunability for the laser's center frequency. Section 6 covers the design, construction, and testing of an optical channelized receiver testbed. The channelizer is based on a high-resolution grating spectrometer with provisions in the optical input/output for demonstrating the essential receiver functions such as channelization and frequency translation. With the testbed we demonstrated actual RF performance capability that is required by future EW receivers. In Section 7 we present a top-level design plan and cost estimate to fabricate an exploratory development model (EDM) of a coherent optical channelized receiver.

2 ARCHITECTURE STUDY

2.1 APPLICATIONS STUDY

An assessment of useful mission applications determines the types of signal processing functions required of coherent receivers. TRW performed a study to identify mission-driven architectures for coherent optical receivers and performed system-level analyses to tier mission performance specifications to the receiver.

The basic mission of the broadband ESM system is to detect emitters throughout frequency band of interest that are incident on the platform anywhere from within a 360° field-of-view. The initial factor driving the development of wideband receivers is the fact that the bandwidths of emerging threats are escalating into the 100 GHz regime, and the density of threats in the higher frequencies is increasing rapidly. This is depicted graphically in Figure 2-1, where we show data presented in the 1997 edition of Janes Radars and ELINT systems. In the figure, the number at the top of each bar is the total number of systems reported that are operating in the frequency band spanned by that particular bar. The height of each bar measures the percentage of the total number of systems that are “new”, that is they are being reported in Janes for the first time. It can be seen that while there continues to be substantial development in the traditional search

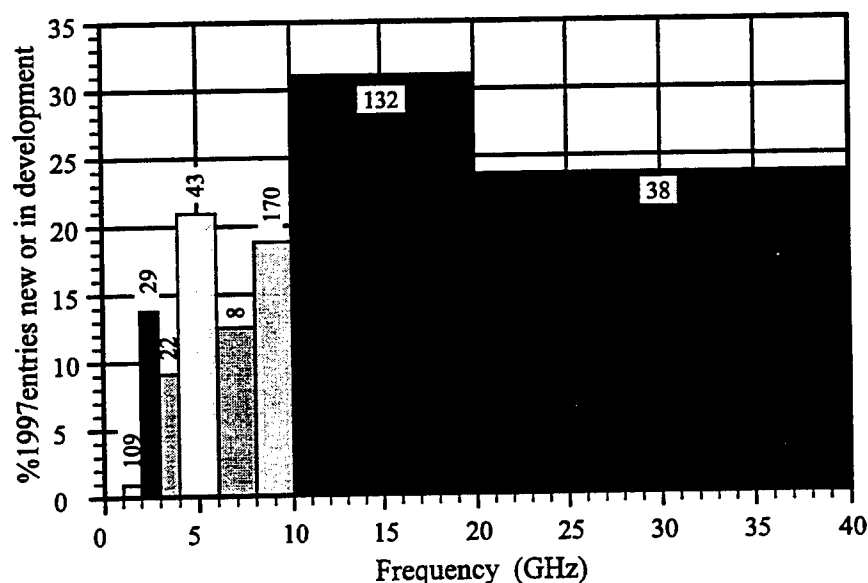


Figure 2-1. New activity reported in Janes 1997 radars and ELINT systems

radar bands, more and more activity is appearing in the higher frequency bands. Although Janes only lists systems up to 40 GHz, this is a continuing trend through frequencies approaching 100 GHz.

In order to assess the demands placed on a receiver system by these signal environments we consider the 3-d representation of the signal environment shown in Figure 2-2. The graphic at the left of the figure is a qualitative depiction of the relative pulse density as a function of frequency. Realistic considerations of conventional hardware size and power consumption preclude real-time, high-resolution monitoring of the entire spectrum, thus the problem is broken down into signal acquisition followed by a precision measurement of AOA and pulse parameters.

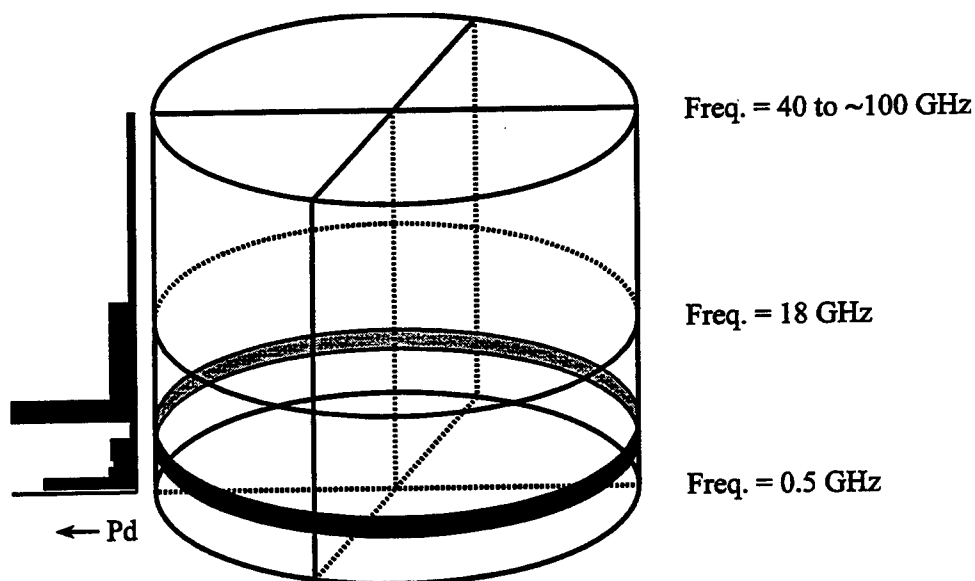


Figure 2-2. The detection / measurement problem

The need to perform a timely search of the entire band with a high probability of capturing signals of interest poses a requirement for wide instantaneous bandwidth for the acquisition receiver, typically 500 MHz to 1 GHz. The shaded band in Figure 2-2 illustrates this requirement. A narrow channel bandwidth, ~ 50 MHz, at the output of the acquisition receiver is required to handle the pulse density and achieve the sensitivity required by most applications. These requirements are made explicit if we survey military systems that need a broadband ESM capability. Table 2-1 lists various platforms

with planned wideband ESM systems and some of the key performance requirements for each application.

Table 2-1. Systems that require broadband ESM

Channelized Receiver Insertion/ Number of Systems	Required Receiver Characteristics				
	Input Frequency (GHz)	Instantaneous Bandwidth (MHz)	Channel Bandwidth (MHz)	SFDR (dB)	Sensitivity (dBm)
Joint Strike Fighter (ISS) >3000 AC	IF 2.5	500	50	60	-60
HARM >2000 MSI	IF	----- Sufficient to Counter Modern Threats -----			
JASA High Band >20 AC	IF	----- Classified -----			
SLQ-32/MILSATCOM >300 Ships	2 - 18	500	50	55	-60
SEAD Targeting >100 AC	2 - 18	500	50	60	-80

The functional requirements for the coherent optical receiver should support the performance goals presented in the table above as well as provide further performance enhancement through more efficient coverage of bandwidths extending to 100 GHz. On consideration of the RF requirements for a high-performance ESM receiver we have compiled a set of performance requirements for a coherent optical receiver. These are shown in Table 2-2.

Table 2-2. Nominal receiver requirements

Parameter	Performance Specification
Frequency Coverage	0.1 to 100 GHz
Instantaneous Band Coverage	500 MHz to 1 GHz
Spur-Free Dynamic Range	50 to 60 dB
Noise Figure	< 15 dB
IF Output Frequency	160 MHz to 5 GHz
Filter Skirts	< -70 dB
Phase Noise	< -130 dBc/Hz @ 1MHz Offset

The phase noise specification states the requirement for large offsets, although in reality the requirement exists on the phase noise power spectral density over a wide range of offsets. In Figure 2-3 we show an example of state-of-the-art phase noise PSD that we adopted as a specification for our receiver development.

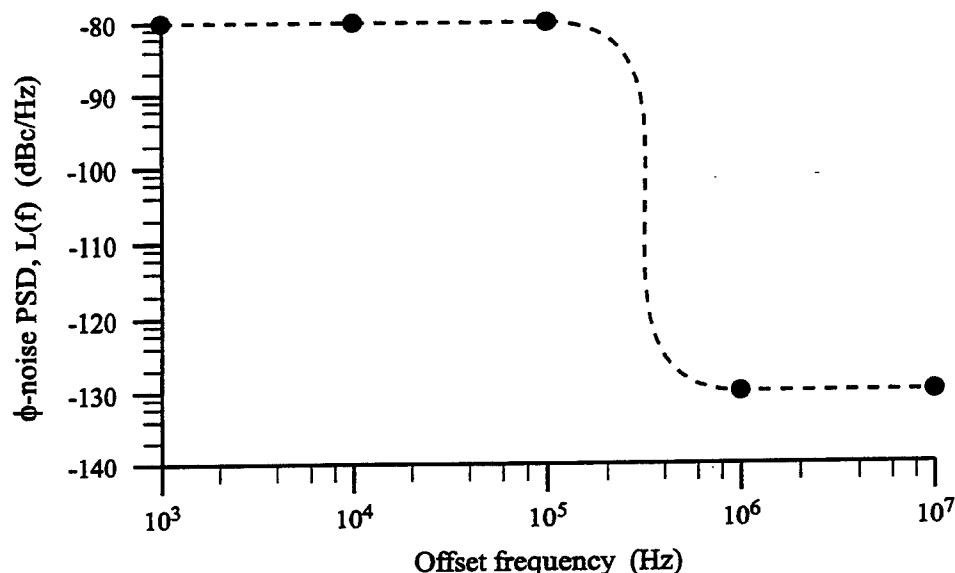


Figure 2-3. State-of-the-art phase-noise requirements

For the remainder of the program the requirements presented in Table 2-2 and Figure 2-3 served as design goals to help us identify useful optical receiver types and make preliminary assessments of where optical approaches may give the highest payoff.

2.2 CONCEPTUAL ARCHITECTURE DEVELOPMENT

While coherent optical receivers have been considered as detectors for optical-RF links for some time, little consideration has been directed at the broader system level issues, and their associated technical challenges, discussed in the previous section. For example in practical applications, coherent optical receivers may be required to lock a local oscillator to a modulated optical carrier transmitted from a remote site. Carrier tracking in RF systems is a mature field that is well understood; the same cannot be said for optical coherent communications systems. Emphasis to the present time has been placed on phase-locking of two unmodulated sources and it is unclear whether the general optical carrier tracking problem is a tenable one. As a second example, careful consideration of the distribution and density of signals within the 100 GHz frequency

range of modern military signals is needed to ensure that image-frequencies are rejected. Image frequency rejection in wideband systems may require coherent optical receivers with high-frequency photodetectors and high-frequency RF reference sources. Meeting this challenge will require careful analysis of mission requirements as well as innovative optical approaches to microwave frequency generation. A final example relates specifically to the channelization of an optical carrier modulated with wideband RF signals. Whereas the very small fractional bandwidth of RF modulation relative to an optical carrier frequency offers many advantages such as gain flatness and dispersionless transmission and switching, it makes more difficult the task of spectrally dispersing the optically carried signal.

Through our assessment of useful mission applications and our consideration of the technical challenges that are presented by the required signal processing functions we identified three mission-driven architectural classes for coherent optical receivers. In the succeeding sections we present a conceptual design of each of the architectures and we make an assessment of where an optical approach may give the highest payoff. Our assessment takes into consideration the fact that there exists an overlap of the modular functionality required of the three receiver approaches. We also wished to develop the architecture that will provide the most utility for future military systems. In that sense, the CORE architectural concept development may be viewed as a judgment of which RF functions should be moved into the optical regime.

2.2.1 Single-channel receiver with optical heterodyne frequency translation

The simplest function to bring into the optical regime is heterodyne frequency translation. This provides the foundation for the most basic coherent receiver type, the single-channel receiver. Figure 2-4 shows the operation of this type of receiver. An optical modulator impresses RF information onto an optical carrier, which will most probably be supplied at a remote user site, but may be co-located with the rest of the receiver. A local-oscillator (LO) laser with the appropriate optical frequency offset is then mixed with the signal laser on a high-speed photodetector. The optical heterodyne process translates the original RF signal band, which is now elevated to a range of optical frequencies, to a convenient postdetection intermediate frequency (IF) band (centered on f_0 in the figure).

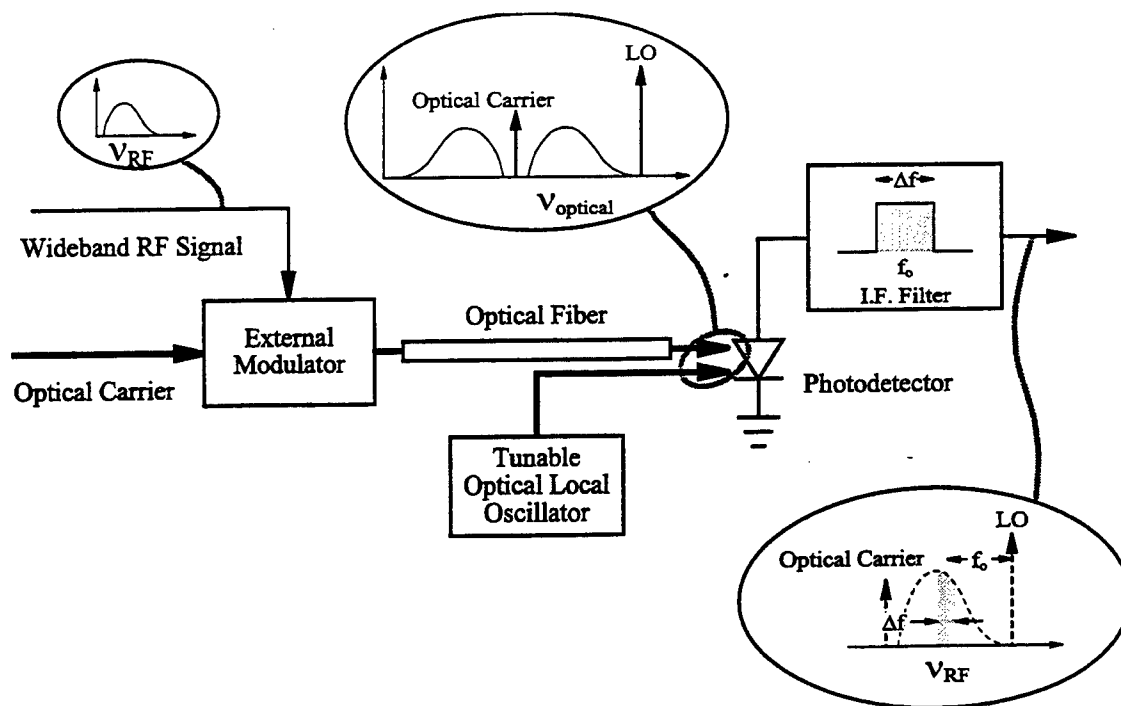


Figure 2-4. The single-channel coherent optical receiver

Although the photonic components of the receiver can be designed to serve an RF spectrum as wide as 0-100 GHz, the modulated optical carrier may never contain this much information at one time. One advantage to providing this bandwidth capability in the optical receiver maybe summarized as mission flexibility. By optical tuning and frequency translation, the same optimized receiver electronics can be used for a wide set of common carrier bands. To illustrate, the front-end RF signal source may be limited to one specific RF band, for example, X-band. After modulation onto the optical carrier, the optical local oscillator could then be tuned to downconvert the X-band signal to an IF frequency that is easily processed by the receiver electronics. The system requirements may either call for receiver processing of the entire X-band signal or for examination of a more limited, tunable subband. In the latter case, tuning of the optical LO shifts the desired subband into a postdetection IF that has been optimized to process the more limited bandwidth. With wideband photonic components in place, the same receiver electronics could be used equally well for L-, X-, K-, V-, and W-band reception simply by appropriate tuning of the local-oscillator laser. This would allow use of common IF

postdetection electronics and avoid the use of RF mixers that must operate at demanding high frequencies. The optical coherent receiver could thus serve as a universal all-band module in a wide variety of systems. Alternatively, the receiver may also find use in multifunction missions that require servicing different frequency bands from time to time.

The advantages presented by this architecture are that the tunable LO shifts the RF band to a fixed IF band and the RF LO is replaced with a more widely tunable optical counterpart. Yet there exist two primary issues that must be considered. The first of these is the requirement for an intermediate frequency of greater than 50 GHz, which results from the necessity to avoid image frequency problems within the 100 GHz spectrum. This can be understood by viewing the situation presented in Figure 2-5.

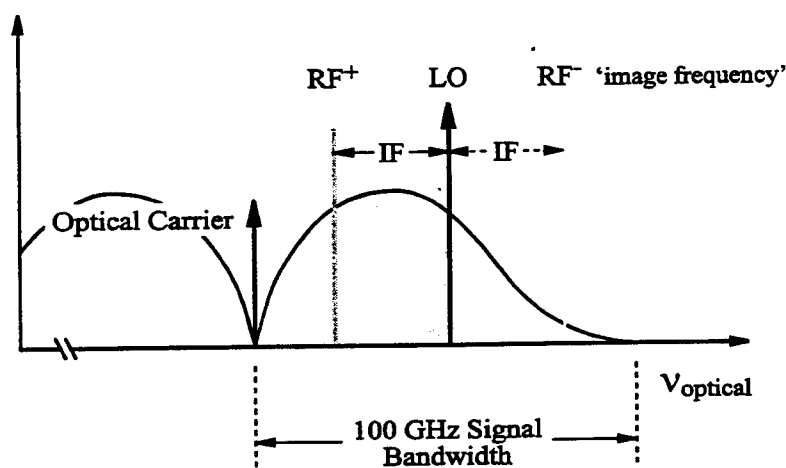


Figure 2-5. The receiver IF must be sufficiently large to avoid image frequencies

When a single frequency LO laser is combined with the signal sideband-bearing carrier laser in a photodetector, every frequency component in the signal spectrum will appear in the detector's output at a frequency equal to the difference between that component's optical frequency and the LO laser's frequency. We can view the frequency as being positive if the signal component lies to the left of the LO and negative if the signal lies to the right of the LO. A bandpass filter at the output of the detector determines the intermediate frequency and the bandwidth of the receiver. By changing the frequency of the LO we can cause any portion of the signal spectrum to fall within the IF band. Image

frequencies arise when the LO is immersed in the signal band and the IF is small enough such that both positive and negative signal components fall within the IF band. Thus to preclude that occurrence and be able to examine unambiguously the entire spectrum the IF must be greater than half the signal bandwidth. This results in a 50 GHz IF, which is incompatible with any conceivable downstream electronic processor, therefore an additional frequency translation of the IF band with a conventional electronic mixer would be required. The second issue relates to the technique used to generate the optical LO. The most widely used method to generate an optical frequency offset is to reference two lasers through an RF source. For the high bandwidth presented by our intended application this technique places a highly burdensome requirement on the RF reference generator, as shown in Figure 2-6. In general for an instantaneous bandwidth of Δf , the IF must be greater than $\Delta f/2$, and the RF reference must be able to tune from $\Delta f/2$ to $3\Delta f/2$. This latter problem can be overcome by using a mod-locked laser to provide an

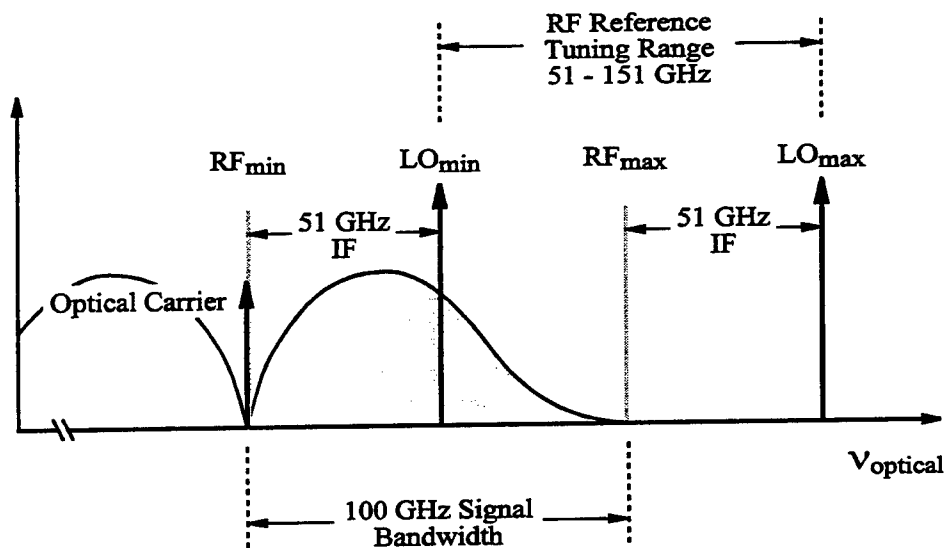


Figure 2-6. Wide instantaneous bandwidths place challenging requirements on electronic IF frequencies

optical frequency comb as shown in Figure 2-7. In the straightforward approach, a single tine of the frequency comb can be picked off with an optical filter and used as the source for the signal carrier. Then other frequency components of the mode-locked laser's spectrum can be selected in a similar fashion to act as the local oscillator. This works

particularly well since the various spectral lines comprising the mode-locked laser's output are phase coherent, thereby reducing the problem of optical carrier tracking to one of optical path length matching. The accuracy of the path-length match depends on the linewidths of the laser. This will be discussed in greater detail in a following section of this report. A variant on this approach is based on a technique for synthesizing RF/microwave frequencies developed by Ron Logan and coworkers at Uniphase Telecommunications Products.¹ In their approach the optical filters are implemented by using CW semiconductor lasers as slaves that are injection-locked to the desired frequency comb lines of the mode-locked laser. The system is configured so that the locking range for the injection-locking process is less than the comb's line spacing. By varying the CW laser's drive current, its lasing frequency can be tuned to be near one of the comb lines. Thus even though the entire frequency comb is injected into the slave's cavity, the slave will lock itself only to the single component within the locking range. Highly phase-coherent optical sources are realized this way with the result that much greater optical powers are available than if passive filters were used.

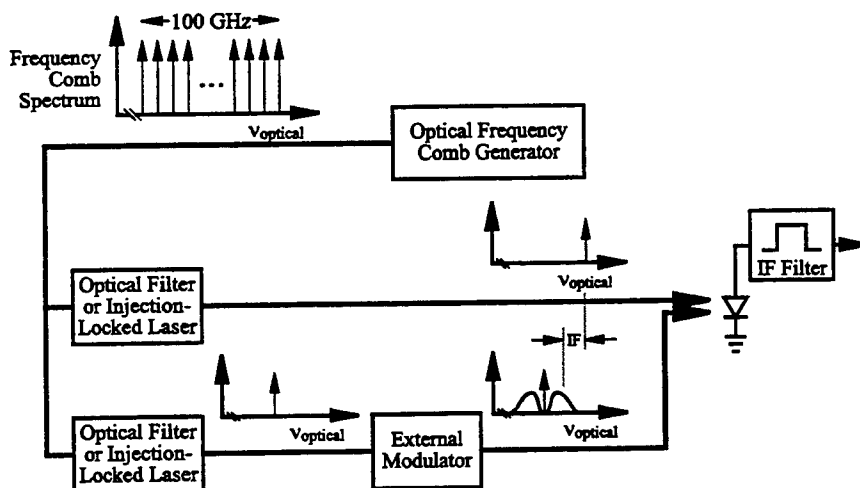


Figure 2-7. Optical frequency comb eliminates the need for a widely tunable RF reference oscillator

2.2.2 Wavelength-division-multiplex-based multiple receiver system

Figure 2-8 depicts a conceptually straightforward modification of the single coherent receiver, where the optically-carried signal is distributed to a number of (possibly

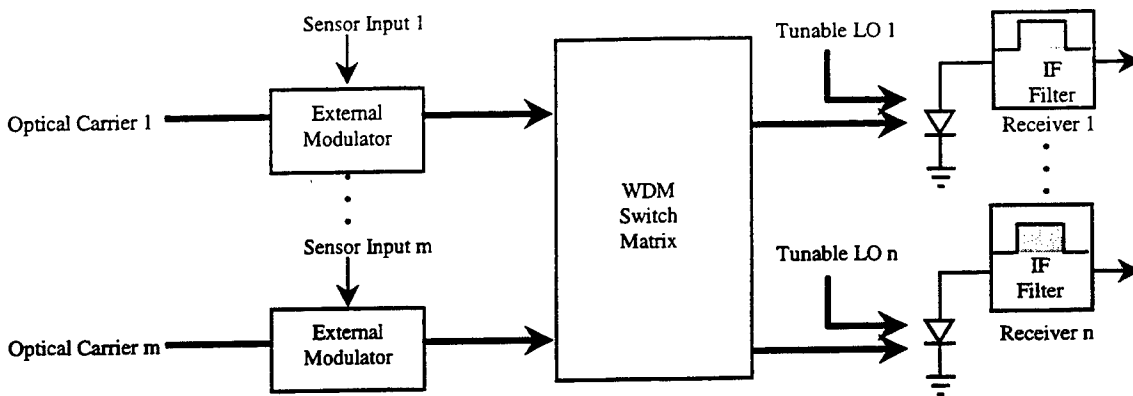


Figure 2-8. Wavelength division multiplexing techniques enable increased optical bandwidth utilization

identical) parallel receivers. Each of the receivers consists of its own tunable local oscillator laser, a front-end photodetector, and postdetection demodulator. Thus each of the receivers has the ability to independently examine any frequency band or subband. Signal distribution to the receivers is accomplished by employing several distinct optical carriers, each on a different optical wavelength. Such a multi-receiver network would enjoy great utility in wideband systems with many distinct signal sources (such as a suite of antenna apertures). By employing a wavelength-division-multiplex (WDM) switch matrix, individual receive sensors can be assigned their own carrier wavelength and signals can be routed to receivers that are available. Since it is unlikely that all sensors (or reception bands) will be occupied simultaneously, a set of m sensors can be serviced by a set of n ($< m$) receivers. Also with this configuration, the signal bandwidth associated with each of the carriers is only a fraction of the total bandwidth, thereby through judicious choice of IF, mitigating the image-frequency problem that is present in the single receiver architecture. Figure 2-9 shows an alternative arrangement that uses the same basic architecture to route various subbands of a wideband signal to the set of multiple receivers. For example, the original wideband signal input can be RF demuxed and routed to receivers according to signal types that are expected in the various subbands.

The optical carriers and local oscillators can be separate laser sources that are referenced through conventional means by using RF oscillators. This task becomes much less challenging due to the reduced signal bandwidth. It would also be possible to use a mode-locked laser to provide a source of multiple carriers and local oscillators through

either of the schemes outlined in the previous section. If this approach were employed it would place some challenging requirements on the WDM switch regarding the channel spacing and inter-channel isolation.

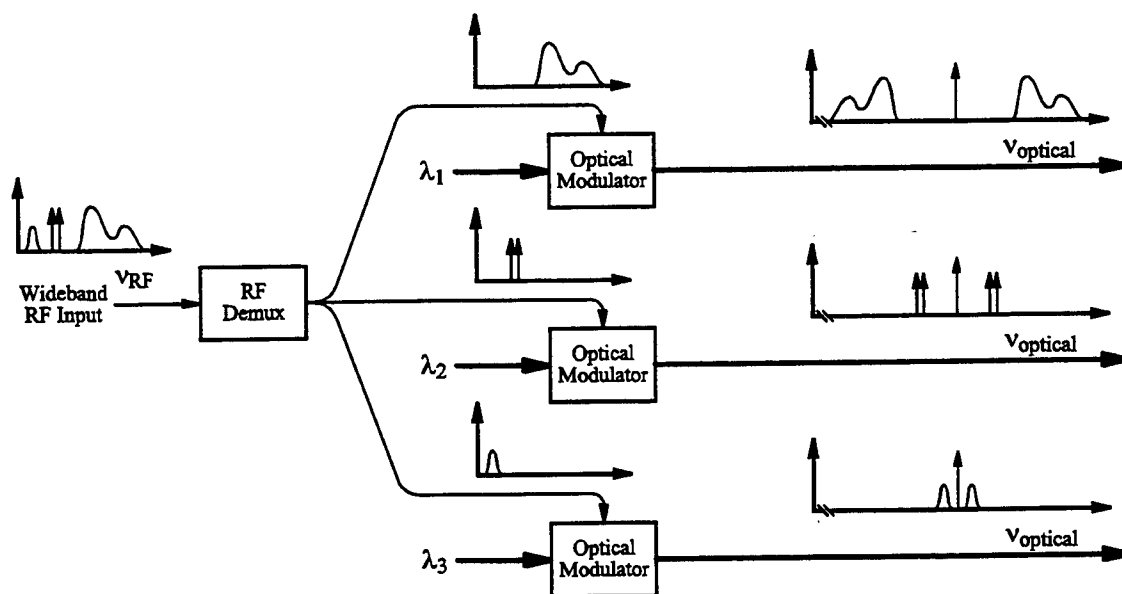


Figure 2-9. Wideband RF signals can be partitioned and routed to separate receivers

2.2.3 Coherent optical channelized receiver

Optical channelizers are a particular type of receiver designed to perform spectral analysis. Optical channelizers can process wider bandwidths than their RF counterparts for real-time identification of complex signal signatures. Channelizers that have been developed previously use acousto-optic techniques, and are limited to RF bandwidths of approximately 1 GHz. Spectral identification of modern military signals therefore requires the development of channelizers that are based on different photonic technologies.

We pursued an approach that is substantially different from previous embodiments of optical-based spectrum analyzers and channelizers. A wide variety of optical processor architectures have been proposed and built.¹⁻³ The most common approach is to spatially impress the unknown signal onto a light beam and Fourier transform the result with a lens, then sample the transform with an array of photodetectors in the lens's transform plane. Systems have been built that are either incoherent, producing a power spectrum of the input signal, or coherent, in which the output preserves both the amplitude and phase

of the input signal. The limiting factor, in terms of bandwidth, in these systems is the spatial light modulator used to transduce the electrical signal into the optical realm. In general acousto-optic Bragg cells are used, and these are limited to RF bandwidths of at most a few GHz.⁴

An alternative approach is based on a system wherein the RF signal is temporally impressed onto the optical carrier and the optical spectrum is analyzed directly. The advantage here is that modulators are available with bandwidths exceeding 50 GHz with near-term projections reaching 100 GHz. Also the very small fractional bandwidth of RF modulation relative to an optical carrier frequency offers other advantages such as gain flatness and dispersionless transmission and switching. The difficulty presented is that the same small fractional bandwidth of RF makes the task of spectrally dispersing the optically carried signal very challenging. The channelizer is shown in Figure 2-10. In this arrangement the RF signal spectrum is spatially mapped onto positions across the photodetector array by using an optically dispersive element such as a diffraction grating. A mode-locked laser provides a comb of optical local oscillators whose frequencies are

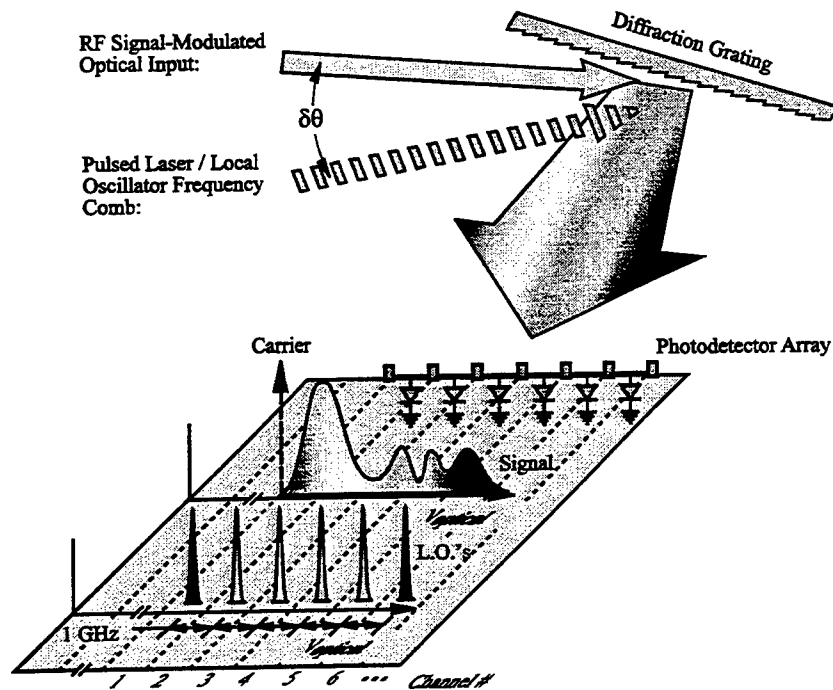


Figure 2-10. The coherent optical channelizer receiver uses a dispersion grating to map the optically carried RF signal and LO spectra onto a photodetector array

separated by the desired channel spacing. The local oscillator comb is dispersed with the same grating used to disperse the signal spectrum. In this way, each photodetector generates the same optical beat frequency, so that each detector channel may use the same postdetection electronics. The IF beat frequency is determined by adjusting the offset in incident angles at which the signal and local oscillator lasers illuminate the grating. This arrangement allows the use of relatively slow photodetectors, even for channels corresponding to very high RF signal frequencies. The signal's power spectrum is determined by measuring the RF power of the heterodyne products generated in each photodetector channel. The complex signal spectrum (phase and amplitude) can be extracted by measuring the in-phase and quadrature components of the heterodyne products.

The optical channelizer occupies a unique position among the three foregoing receiver architectures. Future battlefield radar surveillance channelizer receivers with high probability of intercept may require an instantaneous bandwidth from HF through EHF, and thus suggest most strongly the use of optics to process these signal environments in a timely manner. The coherent optical channelizer makes use of the two most commonly touted advantages offered by optics – the wide instantaneous bandwidth offered by optical transmission media, and the parallel nature of optical processing – to channelize signal bands and translate their frequencies to bandwidths that can be further processed by more conventional electronic systems. Also as a development model, the channelizer is more desirable to pursue because the required channelizer functions subsume the functions required of the simpler single-receiver and WDM-based receivers. It is for these reasons that all subsequent development under this program focused on the analysis, design and fabrication of a coherent channelizer receiver.

Consideration of the RF performance requirements for a coherent optical receiver that were established in section 2.1 and shown in Table 2-2, leads to the conclusion that an extremely wide instantaneous bandwidth channelizer with 1GHz channels can provide a great deal of utility to the overall receiver system. More specifically, a grating-based channelizer approach is scalable to handle the anticipated 100GHz throughput. Such a channelizer will almost certainly be a precursor to further signal processing. This is illustrated in Figure 2-11 where we show a channelizer and a variety of processing

alternatives. Depending on the ultimate application, further processing may be performed in either the electronic regime or the optical regime. For example, an electronic activity detector and/or a finer resolution RF digital or analog processor may follow the channelizer. Another alternative would have finer optical channelization (~40MHz) of a particular 1GHz slice of the original wideband signal spectrum.

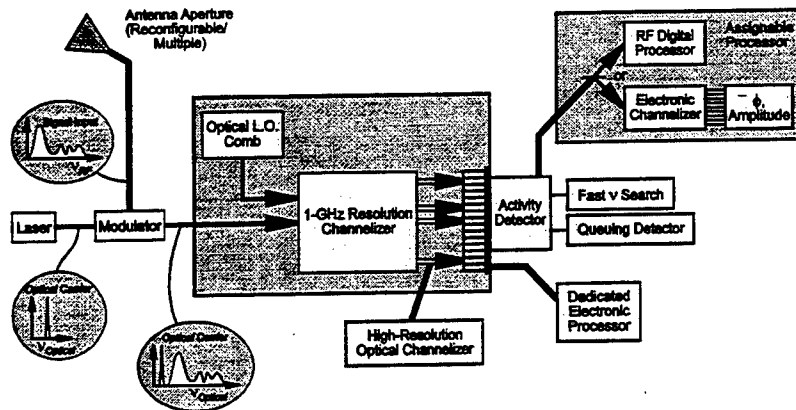


Figure 2-11. The CORE channelizer will be a precursor to further signal processing

3 RECEIVER PERFORMANCE ANALYSIS

To trade the various methods of implementing the coherent receiver functions for specific applications, we determined RF system performance requirements and tiered them to the photonic subsystems. The key RF performance requirements that we calculated included spur-free dynamic range and the channel response characteristics for the optical channelizer. Additionally we performed an in depth investigation of two techniques for optical carrier tracking: optical phase locked loops, and optical injection locking. The results of these analyses proved instrumental in guiding the selection of the approaches used to implement the receiver's functional subsystems. Additionally, many of the design details for the subsystems were specified. Through our modeling and simulations we were able to develop system configurations that enabled us to meet or exceed most of the receiver performance requirements listed in Table 2-2.

3.1 HETERODYNE LINK ANALYSIS: SPUR-FREE DYNAMIC RANGE AND NOISE FIGURE

In this section we calculate the properties of a coherent optical channelized receiver that are related to the optical heterodyne nature of the detection system. These properties are influenced primarily by the characteristics of the optical modulator. In a coherent receiver system we wish to modulate the optical field, not the intensity, in a manner linearly related to the signal's electric field. This suggests that an interferometric modulator would be best suited for impressing the signal onto the optical carrier. Our calculations therefore, are based on the use of a Mach-Zehnder modulator. For the dynamic range calculation we assume that the dominant nonlinearity is due to the form of the modulator's transfer function. The optical receiver's noise figure is influenced by the modulator through the value of the modulator's v_{π} , which is the voltage applied to the modulator that causes its output to swing from 0% transmission to 100% transmission.

3.1.1 Mach Zehnder modulator nonlinearities and the two tone spurious signals

The input RF signal voltage to Mach Zehnder is represented as

$$v(t) = v_b + v_o[(\cos(2\pi f_1 t) + \cos(2\pi f_2 t))] , \quad (3.1-1)$$

where v_b is the DC bias voltage, v_o is the voltage amplitude of the applied modulation signals, f_1 and f_2 are the two modulator frequencies in the two tone test. The Mach-Zehnder optical intensity output is given by

$$P = P_0 \cos^2[\pi v/(2v_\pi)], \quad (3.1-2)$$

and the optical field is

$$E = [E_0 \cos(2\pi v_0 t)] \cos[\pi v/(2v_\pi)], \quad (3.1-3)$$

where v_0 is the optical carrier frequency. Throughout this section we will use the convention relating the optical power to the optical field.

$$P_0 = \langle E_0 \cos(2\pi v_0 t) \rangle^2 = \frac{1}{2} E_0^2, \quad (3.1-4)$$

where $\langle \rangle$ indicates a time average.

The optical signal field that is incident to the grating is then

$$\begin{aligned} E_s &= E_0 \cos\{\theta_b + \phi_s[(\cos(2\pi f_1 t) + \cos(2\pi f_2 t))]\cos(2\pi v_0 t)\} \\ &= \frac{1}{2} E_0 \cos\{2\pi v_0 t + \theta_b + \phi_s[(\cos(2\pi f_1 t) + \cos(2\pi f_2 t))]\} \\ &\quad + \frac{1}{2} E_0 \cos\{2\pi v_0 t - \theta_b + \phi_s[(\cos(2\pi f_1 t) + \cos(2\pi f_2 t))]\} \end{aligned} \quad (3.1-5)$$

where θ_b is $\pi v_b/(2v_\pi)$, and ϕ_s is $\pi v_o/(2v_\pi)$. Note that $\theta_b = \pi/2$ is the condition for low biasing and, as we show below, eliminates the even order harmonics and mixing products.

In order to identify the terms relevant to the two tone signal, we need to expand (3.1-5) to collect the two tone terms of interest, i.e. the $2f_1 - f_2$ and the $2f_2 - f_1$ terms. By using common trigonometric identities the field can be written.

$$\begin{aligned} E_s/E_0 &= \cos(\theta_b) \cos\{\phi_s[\cos(2\pi f_1 t) + \cos(2\pi f_2 t)]\} - \sin(\theta_b) \sin\{\phi_s[\cos(2\pi f_1 t) + \cos(2\pi f_2 t)]\} \\ &= \cos(2\pi v_0 t + \theta_b) \cos\{\phi_s[\cos(2\pi f_1 t) + \cos(2\pi f_2 t)]\} \\ &\quad - \sin(2\pi v_0 t + \theta_b) \sin\{\phi_s[\cos(2\pi f_1 t) + \cos(2\pi f_2 t)]\} \\ &\quad + \cos(2\pi v_0 t - \theta_b) \cos\{\phi_s[\cos(2\pi f_1 t) + \cos(2\pi f_2 t)]\} \\ &\quad + \sin(2\pi v_0 t - \theta_b) \sin\{\phi_s[\cos(2\pi f_1 t) + \cos(2\pi f_2 t)]\}. \end{aligned} \quad (3.1-6)$$

This can now be grouped appropriately by using the Bessel function identities

$$\cos[x \cos(\theta)] = J_0(x) - 2J_2(x) \cos(2\theta) + 2J_4(x) \cos(4\theta) - \dots \quad (3.1-7)$$

and

$$\sin[x \cos(\theta)] = 2J_1(x) \cos(\theta) - 2J_3(x) \cos(3\theta) + \dots \quad (3.1-8)$$

After substitution of (6) and (7) into (5) we find, after performing some algebra and retaining terms to 3rd order, the following expression for the modulated field.

$$E_s/E_o = [J_0(\varphi_s)]^2 \cos(\theta_b) \cos(2\pi\nu_0 t) \quad (3.1-9i)$$

$$- J_0(\varphi_s) J_1(\varphi_s) \sin(\theta_b) \{ \cos[2\pi(\nu_0 + f_1)t] + \cos[2\pi(\nu_0 + f_2)t] \\ + \cos[2\pi(\nu_0 - f_1)t] + \cos[2\pi(\nu_0 - f_2)t] \} \quad (3.1-9ii)$$

$$- J_0(\varphi_s) J_2(\varphi_s) \cos(\theta_b) \{ \cos[2\pi(\nu_0 + 2f_1)t] + \cos[2\pi(\nu_0 + 2f_2)t] \\ + \cos[2\pi(\nu_0 - 2f_1)t] + \cos[2\pi(\nu_0 - 2f_2)t] \} \quad (3.1-9iii)$$

$$- [J_1(\varphi_s)]^2 \cos(\theta_b) \{ \cos[2\pi(\nu_0 + f_1 + f_2)t] + \cos[2\pi(\nu_0 + f_1 - f_2)t] \\ + \cos[2\pi(\nu_0 - f_1 - f_2)t] + \cos[2\pi(\nu_0 - f_1 + f_2)t] \} \quad (3.1-9iv)$$

$$- J_0(\varphi_s) J_3(\varphi_s) \sin(\theta_b) \{ \cos[2\pi(\nu_0 + 3f_1)t] + \cos[2\pi(\nu_0 + 3f_2)t] \\ + \cos[2\pi(\nu_0 - 3f_1)t] + \cos[2\pi(\nu_0 - 3f_2)t] \} \quad (3.1-9v)$$

$$- J_1(\varphi_s) J_2(\varphi_s) \sin(\theta_b) \{ \cos[2\pi(\nu_0 + f_1 + 2f_2)t] + \cos[2\pi(\nu_0 - f_1 + 2f_2)t] \\ + \cos[2\pi(\nu_0 + 2f_1 + f_2)t] + \cos[2\pi(\nu_0 + 2f_1 - f_2)t] \\ + \cos[2\pi(\nu_0 + f_1 - 2f_2)t] + \cos[2\pi(\nu_0 - f_1 - 2f_2)t] \\ + \cos[2\pi(\nu_0 - 2f_1 + f_2)t] + \cos[2\pi(\nu_0 - 2f_1 - f_2)t] \} \quad (3.1-9vi)$$

In the above (i) corresponds to the optical carrier, (ii) corresponds to the fundamentals, (iii) corresponds to the second harmonics of the fundamentals, (iv) corresponds to the second order mixing products, (v) corresponds to the third harmonics, and (vi) corresponds to the third order two-tone intermodulation products. Upon inspection of the above expression we see that the even order terms depend on $\cos(\theta_b)$, which confirms our previous assertion that when the modulator is low-biased the even order terms vanish. Since the odd order terms depend on $\sin(\theta_b)$ the low-bias condition maximizes the desired fundamental term. Using the small argument approximation for the Bessel functions, $J_n \approx x^n / (2^n n!)$ [1], we find that the dominant spurious tone results from the two-tone mixing products given in (3.1-9vi). We can now write for the terms of interest

$$E_{fund}/E_o \approx \frac{1}{2} \varphi_s \quad (3.1-10)$$

and

$$E_{3rd}/E_o \approx \frac{1}{16} \varphi_s^3 \quad (3.1-11)$$

3.1.2 Spur-free dynamic range (SFDR)

As shown in the preceding section, the largest distortion products are the third-order, two-tone intermodulation products. These limit the upper end of the channelizer's dynamic range, because they appear as spurious components of the two-tone spectrum in adjacent channels. The maximum allowable signal level is reached when the heterodyne product of a two-tone signal spur and the L.O. equals the noise floor. The dynamic range is defined as the ratio of the signal power in the maximum allowable signal to the signal power that produces a fundamental response equal to the noise floor. This is illustrated in Figure 3-1.

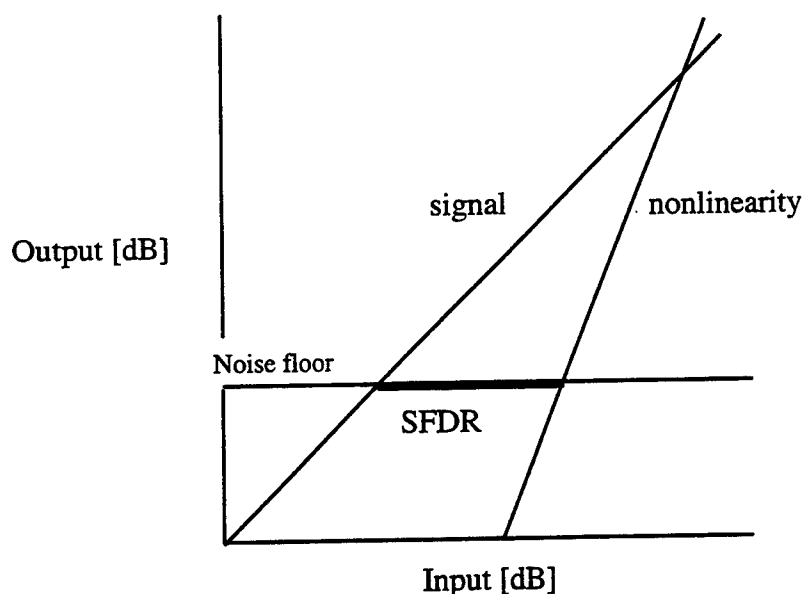


Figure 3-1. The nonlinear response of the modulator determines the dynamic range

For the calculation of dynamic range we will assume that all of the various frequency components in the modulated field will appear in separate channels. At this point the particular mechanism used to perform the channelization is irrelevant. Also as a basis for the calculation, we will employ the model of the channelized receiver shown in Figure 3-2. We include optical amplifiers in order to assess the influence of amplifier gain and noise figure on the receiver's performance. We assume that each of the channels has its own associated photodetector, which is characterized by its responsivity, s , and resistance, R . The detectors are assumed to be responsive to the desired intermediate frequency (I.F.). A post-detection bandpass filter sets the I.F. and the noise bandwidth

relevant to the dynamic range calculation. Although the throughputs for the separate optical paths are attributed to the channelizer in the figure, it is understood that they represent the net throughput from the lasers to the detector.

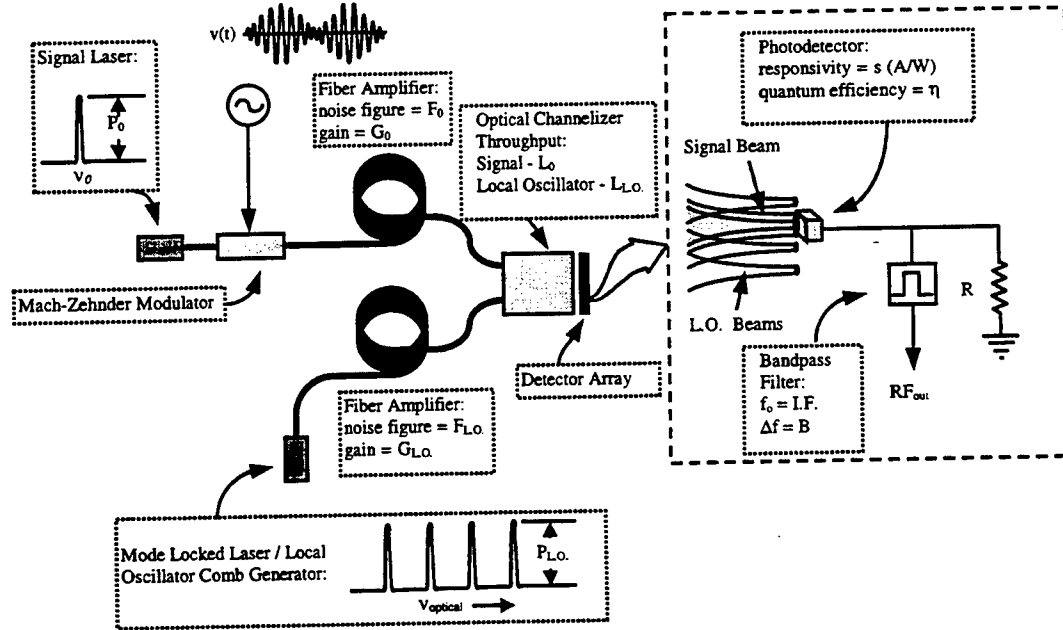


Figure 3-2. A comprehensive model is the basis for calculation of spur free dynamic range.

In optical heterodyne detection the field incident on a detector is the sum of the modulated signal field component and the local oscillator. The detector responds to the optical intensity, and the resulting photocurrent is given by

$$\begin{aligned} i &= s (E_{\text{sig}} + E_{\text{L.O.}})^2 \\ &= s (E_{\text{sig}}^2 + E_{\text{L.O.}}^2 + 2 E_{\text{sig}} E_{\text{L.O.}}), \end{aligned} \quad (3.1-12)$$

where s is the detector responsivity in A/W.

Now consider that the two-tone signal given in (3.1-1) is applied to the low-biased modulator. We have from (3.1-9) and Figure 3-2 for a fundamental tone at f_1

$$E_{\text{sig}} = E_0 J_0(\phi_s) J_1(\phi_s) \cos[2\pi(\nu_0 + f_1)t]. \quad (3.1-13)$$

The local oscillator field is given by

$$E_{\text{L.O.}} = E_{\text{L.O.}} \cos(2\pi\nu_0 t), \quad (3.1-14)$$

where $E_x = E_x(G_x L_x)^{1/2}$. G_x and L_x are defined in Figure 3-2.

Substitution of (3.1-13) and (3.1-14) into (3.1-12), then averaging over optical frequencies, leads to the following expression for the photocurrent.

$$\begin{aligned} i &= s \left[\frac{1}{2} E_0^2 J_0^2(\varphi_s) J_1^2(\varphi_s) + \frac{1}{2} E_{L.O.}^2 + E_0 E_{L.O.} J_0(\varphi_s) J_1(\varphi_s) \cos(2\pi f_1 t) \right] \\ &= s \left[P_0 G_0 L_0 J_0^2(\varphi_s) J_1^2(\varphi_s) + P_{L.O.} G_{L.O.} L_{L.O.} \right. \\ &\quad \left. + 2 \{ P_0 G_0 L_0 P_{L.O.} G_{L.O.} L_{L.O.} \}^{1/2} J_0(\varphi_s) J_1(\varphi_s) \cos(2\pi f_1 t) \right]. \end{aligned} \quad (3.1-15)$$

The first two terms on the right represent D.C. currents due to the illumination of the detector by the signal and L.O. beams. The term of interest is the third term on the right, which is the heterodyne product of the fundamental signal at f_1 . The RF power generated at the detector is $P_{fund} = \langle i_{fund}^2 \rangle R$, where R is the resistance of the photo diode. We have

$$\begin{aligned} P_{fund} &= 2 R s^2 P_0 G_0 L_0 P_{L.O.} G_{L.O.} L_{L.O.} J_0^2(\varphi_s) J_1^2(\varphi_s) \\ &\equiv (R s^2 P_0 G_0 L_0 P_{L.O.} G_{L.O.} L_{L.O.}) (\varphi_s^2) / 2. \end{aligned} \quad (3.1-16)$$

Similarly for the RF power produced by one of the intermodulation products we have

$$\begin{aligned} P_{3rd} &= 2 R s^2 P_0 G_0 L_0 P_{L.O.} G_{L.O.} L_{L.O.} J_1^2(\varphi_s) J_2^2(\varphi_s) \\ &\equiv (R s^2 P_0 G_0 L_0 P_{L.O.} G_{L.O.} L_{L.O.}) (\varphi_s^6) / 128. \end{aligned} \quad (3.1-17)$$

Equating P_{3rd} to the noise power, P_{noise} , we solve (3.1-17) for the value of φ_s that corresponds to the maximum signal.

$$(\varphi_s)_{max} = [128 P_{noise} / (R s^2 P_0 G_0 L_0 P_{L.O.} G_{L.O.} L_{L.O.})]^{1/6} \quad (3.1-18)$$

Substituting this value of $(\varphi_s)_{max}$ into (3.1-16) and forming the ratio of $(P_{fund})_{max}$ to P_{noise} we arrive at the following expression for the spur-free dynamic range.

$$SFDR = [4 (R s^2 P_0 G_0 L_0 P_{L.O.} G_{L.O.} L_{L.O.}) / P_{noise}]^{2/3} \quad (3.1-19)$$

Noise power

The total RF in band noise power, P_{noise} , referred to above can consist of several components, which include thermal, shot, laser relative intensity noise (RIN) and amplified spontaneous emission (ASE) noise related to the optical amplifiers. In the following we will explore the detailed nature of each of these possible noise contributors and generate an expression for P_{noise} and discuss the operating regime that maximizes the dynamic range.

Thermal noise is generated within the photodetector and is given by [2]

$$P_{th} = 4kTB, \quad (3.1-20)$$

where k is Boltzmann's constant, T is the temperature ($^{\circ}$ Kelvin), and B is the measurement bandwidth.

Shot noise is due to the continuous illumination of the photodetector by the local oscillator laser and is given by [2]

$$P_{\text{shot}} = 2 q i B R. \quad (3.1-21)$$

In the above q is the electronic charge (1.602×10^{-19} coulombs) and i is the detector photocurrent induced by the local oscillator. Substituting the appropriate expression for photocurrent into (3.1-21) leads to

$$P_{\text{shot}} = 2 q s P_{\text{L.O.}} G_{\text{L.O.}} L_{\text{L.O.}} B R. \quad (3.1-22)$$

Next we mention RIN because it would appear to be a possible major noise source in the receiver, but we will show that it can in fact be neglected. The contribution of laser RIN to the noise is due to the local oscillator laser and is given by [3]

$$P_{\text{RIN}} = 10^{\text{RIN}/10} (s P_{\text{L.O.}} G_{\text{L.O.}} L_{\text{L.O.}})^2 B R, \quad (3.1-23)$$

where RIN is the specified laser RIN (e.g. -165dB/Hz). We note however, that in the channelizer the L.O. RIN spectrum is dispersed by the grating, which results in the production of noise frequency components in any given channel that are no greater than half the channel bandwidth. For example, if the channelizer is designed for 1GHz channels the RIN noise in a channel will have frequencies of 500MHz or less. For reasons discussed in section 3.2 below the I.F. must be several times the channel bandwidth, therefore the post-detection I.F. filter will eliminate the RIN noise.

Finally, we consider optical amplifier noise, which can manifest itself in several forms. We assume the ASE power spectral density can be written as [4]

$$\text{ASE} = \frac{1}{2} F (G - 1) h \nu_0, \quad (3.1-24)$$

where F and G are respectively the noise figure and gain of the optical amplifier, h is Planck's constant. We have chosen to use the multiplicative representation of the noise figure rather than the exponential one (i.e. noise figure = $10^{F/10}$, and F is given in dB). First there is the shot noise produced by the sum of the ASE output from the signal and L.O. amplifiers, which is given by

$$P_{\text{ASE-shot}} = 2 q s (\text{ASE}_0 L_0 + \text{ASE}_{\text{L.O.}} L_{\text{L.O.}}) \Delta \nu B R. \quad (3.1-25)$$

$\Delta\nu$ is the optical bandwidth, which for an optical channelizer will be equal to the electrical bandwidth, B . Numerical evaluation of (3.1-25) for reasonable values of F and G shows that this term is about five or six orders of magnitude less than the thermal noise thus we can ignore the ASE shot noise.

Second, the heterodyne mixing of the two ASE spectra will produce a noise term given by

$$P_{\text{ASE} \times \text{ASE}} = \frac{1}{4} [s h\nu_0 (\text{ASE}_0 L_0 + \text{ASE}_{\text{L.O.}} L_{\text{L.O.}}) B]^2 R. \quad (3.1-26)$$

This contribution is also negligible compared to the thermal noise and will not be considered further. Finally, there is the noise produced by the beating of the ASE spectra with the local oscillator in each channel. If we first consider the contribution due to the mixing of $\text{L.O.} \times \text{ASE}_{\text{L.O.}}$ we can employ the same reasoning as we did for the laser RIN to see that this process will produce frequency components that are out of the I.F. filter bandwidth, so we can ignore them. On the other hand the contribution due to the mixing of $\text{L.O.} \times \text{ASE}_0$ will produce in-band components that may be at least comparable to the thermal noise. We have for this noise term

$$\begin{aligned} P_{\text{L.O.} \times \text{ASE}} &= 4 s^2 h\nu_0 (\text{ASE}_0 L_0) P_{\text{L.O.}} G_{\text{L.O.}} L_{\text{L.O.}} B R \\ &= 2 s^2 h\nu_0 F_0 G_0 L_0 P_{\text{L.O.}} G_{\text{L.O.}} L_{\text{L.O.}} B R \\ &= \eta P_{\text{shot}} F_0 G_0 L_0, \end{aligned} \quad (3.1-27)$$

where we have assumed that $G_0 \gg 1$ and we have used the detector quantum efficiency, $\eta = s h\nu_0 / q$.

We can now write the following expression for the total noise power relevant to the dynamic range calculation.

$$\begin{aligned} P_{\text{noise}} &= P_{\text{th}} + P_{\text{shot}} + P_{\text{L.O.} \times \text{ASE}} \\ &= 4kTB + 2 q s P_{\text{L.O.}} G_{\text{L.O.}} L_{\text{L.O.}} B R + 2 s^2 h\nu_0 F_0 G_0 L_0 P_{\text{L.O.}} G_{\text{L.O.}} L_{\text{L.O.}} B R \\ &= 4kTB + 2 q s P_{\text{L.O.}} G_{\text{L.O.}} L_{\text{L.O.}} B R (1 + \eta F_0 G_0 L_0) \\ &= 4kTB + 2 s^2 h\nu_0 F_0 G_0 L_0 P_{\text{L.O.}} G_{\text{L.O.}} L_{\text{L.O.}} B R, \end{aligned} \quad (3.1-28)$$

where we have made the assumption that $(\eta F_0 G_0 L_0) \gg 1$, and substituted the expression for quantum efficiency from above. The spur-free dynamic range can now be written as

$$\begin{aligned} \text{SFDR} &= [4(Rs^2 P_0 G_0 L_0 P_{\text{L.O.}} G_{\text{L.O.}} L_{\text{L.O.}}) / \\ &\quad (4kTB + 2 s^2 h\nu_0 F_0 G_0 L_0 P_{\text{L.O.}} G_{\text{L.O.}} L_{\text{L.O.}} B R)]^{2/3} \end{aligned} \quad (3.1-29)$$

Define the relative noise parameter,

$$\Theta \equiv 2 s^2 h\nu_0 F_0 G_0 L_0 P_{L.O.} G_{L.O.} L_{L.O.} R / 4kT, \quad (3.1-30)$$

and the expression for the dynamic range becomes

$$SFDR = \{[2 P_0 / h\nu_0 B F_0] [\Theta / (1 + \Theta)]\}^{2/3}. \quad (3.1-31)$$

The significance of Θ can be interpreted as follows. Small values of Θ indicate that the system noise is dominated by thermal noise, and examination of (3.1-31) reveals that in this regime the dynamic range is proportional to $\Theta^{2/3}$. On the other hand, when Θ is large the system is dominated by the ASE noise from the signal laser's optical amplifier and the dynamic range approaches a maximum value given by

$$SFDR_{\max} = (2 P_0 / h\nu_0 B F_0)^{2/3}. \quad (3.1-32)$$

Thus our analysis shows clearly that it is desirable to have ASE noise dominate over thermal noise. Also for a given channel bandwidth and optical frequency, the dynamic range is solely a function of the output power of the signal laser and the noise figure for the optical amplifier used in the signal laser path.

Figure 3-3 shows the dependence of the spur-free dynamic range on the relative noise parameter, Θ .

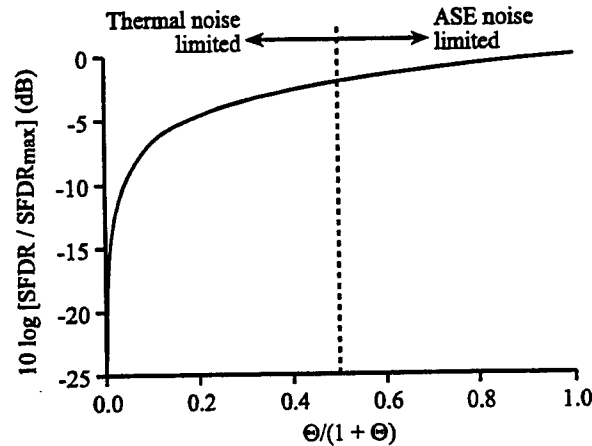


Figure 3-3. It is desirable to operate the optical channelized receiver in the ASE noise limited regime in order to maximize the dynamic range.

As an example, consider the following parameter values:

$$R = 50 \, \Omega,$$

$$s = 0.7 \, \text{A/W},$$

$$B = 10^9 \, \text{Hz},$$

$$h\nu_0 = 1.28 \times 10^{-19} \text{ Joules } (\lambda = 1.55\mu\text{m}),$$

$$4kT = 1.63 \times 10^{-20} \text{ Joules } (T = 295^\circ \text{ K}),$$

$$F_0 = 2.75 \text{ (4.4dB)},$$

$$G_0 = G_{L.O.} = 100,$$

$$L_0 = L_{L.O.} = 0.2,$$

$$P_{L.O.} = 10^{-5} \text{ W, and}$$

$$P_0 = 10^{-1} \text{ W.}$$

In this case we have:

$$\Theta = 4.25,$$

$$\text{SFDR}_{\text{max}} = 6.85 \times 10^5 \text{ (58.4dB), and}$$

$$\text{SFDR} = 5.95 \times 10^5 \text{ (57.8dB).}$$

3.1.3 Noise figure

The conventional definition of noise figure is the ratio of the input signal-to-noise ratio to the output signal-to-noise ratio, with the input noise consisting of thermal noise from a source at room temperature. In the case of our receiver, the input signal is applied to a Mach-Zehnder interferometric modulator that has a characteristic input resistance R_{mod} , typically 50 Ω . The input signal-to-noise ratio is given by

$$\text{SNR}_{\text{in}} = (v_o^2 / 2 R_{\text{mod}}) / 4kTB. \quad (3.1-33)$$

From (3.1-16) and (3.1-28) we find the output signal-to-noise ratio,

$$\begin{aligned} \text{SNR}_{\text{out}} &= [\frac{1}{2} (R s^2 P_0 G_0 L_0 P_{L.O.} G_{L.O.} L_{L.O.}) (\varphi_s^2)] / \\ &\quad [4kTB + 2 s^2 h\nu_0 F_0 G_0 L_0 P_{L.O.} G_{L.O.} L_{L.O.} B R] \\ &= [\pi^2 v_o^2 P_0 \Theta] / [(1 + \Theta) 16 v_\pi^2 h\nu_0 B F_0], \end{aligned} \quad (3.1-34)$$

where we have used (3.1-30) and the definition of φ_s to arrive at the final expression. If we now form the ratio of (3.1-33) to (3.1-34) we arrive at the following expression for the receiver noise figure, F .

$$F = [2 v_\pi^2 F_0 h\nu_0 (1 + \Theta)] / [\Theta \pi^2 R_{\text{mod}} P_0 kT]. \quad (3.1-35)$$

A couple of points are to be made concerning (3.1-35). First, we see that just as it was for the dynamic range, it is desirable to be ASE noise limited (i.e. Θ should be large) and P_0 should be as large as possible. Also we can see that noise figure depends strongly on

the modulator's v_{π} , thus we want v_{π} to be as small as possible. By way of example, if we use the same set of parameters that went into the dynamic range example and calculate noise figure for $v_{\pi} = 5V$, we find the following:

$$F = 107.5 \text{ (20.3dB)}.$$

If we can obtain a modulator with an improved value of $v_{\pi} = 2V$, then the noise figure improves to:

$$F = 17.2 \text{ (12.4dB)}.$$

3.2 CHANNEL RESPONSE: LOSS, RIPPLE, AND CROSSTALK

The basic channelizer front-end architecture we considered is an array of identical RF bandpass filters with equally spaced center frequencies, each of which sees the entire input RF signal. The difference between the center frequencies of two adjacent filters is, by definition, the channel spacing. Figure 3-4 is a schematic sketch of the frequency response of several adjacent channel filters.

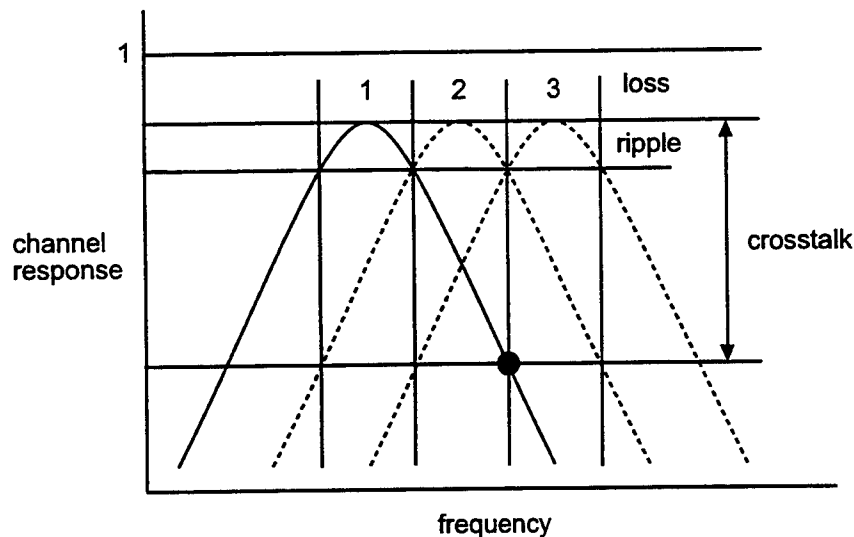


Figure 3-4. Schematic frequency response of several adjacent channel filters. The effect of nonideal channel filters is described by three parameters: loss, ripple and crosstalk, as shown.

Figure 3-4 also gives a picture for the three parameters (loss, ripple, and crosstalk) we employ to quantify the effect of nonideal channel filtering. Ripple is the ratio of center response to edge response for each channel, and is a reasonable measure of the nonuniformity of response within a channel, provided the maximum and minimum

channel responses are at the center and edge of the channel as sketched. This condition will hold for all channelizers considered in this section. Loss is the ratio of “no-channelization” response to channel center response. In simple cases, such as channelization with conventional RF filters, the loss is given by the insertion loss of the filter. Crosstalk is not as straightforward to specify as ripple and loss. The definition we employ here is that crosstalk is the ratio of “far edge of adjacent channel” response to channel center response. For example, consider channel 1 in Figure 3-4 (solid line). A signal at the far edge of channel 2 is “at the far edge of an adjacent channel” relative to channel 1, and the response of channel 1 to a signal of this frequency is shown by the heavy dot. As shown in Figure 3-4, crosstalk is the ratio of this response to the response at channel center. This definition of crosstalk is motivated in part by the difficulty of obtaining low ripple and low worst case adjacent channel crosstalk simultaneously, since the channel response must be continuous. It is possible, in principle, to obtain low ripple and low worst case 2nd nearest neighbor crosstalk simultaneously, and this worst case is precisely what is calculated in the definition of crosstalk we employ. We will consistently give numerical values of loss, ripple, and crosstalk in dB, since they are all defined as ratios. In addition, the definitions have been arranged so that reducing the numerical value of any of these parameters is a performance improvement.

3.2.1 Fabry-Perot filter channelizer

The first optical channelizer approach we consider is probably the most conceptually straightforward approach, and consists of a number of optical Fabry-Perot (FP) filters whose center frequencies are spaced by the desired channel spacing. The optical power transmittance of a Fabry-Perot filter is given by

$$T_{FP}(f) = \frac{1}{1 + \frac{4FSR^2}{\pi^2 \Delta f^2} \sin^2\left(\frac{\pi f}{FSR}\right)}, \quad (3.2-1)$$

where f is the optical frequency [Hz], Δf is the full-width half-maximum linewidth [Hz] of the transmission peaks, and FSR is the free spectral range [Hz], which is the frequency separation between adjacent transmission maxima. We assume that these filters are arranged in an idealized chain, where the signal that does not pass through filter 1 to

detector 1 is reflected toward the rest of the chain, and so on for each successive filter-detector pair, so that each filter (approximately) sees the entire relevant signal. This system performs a channelization function, since if an optical carrier that has been modulated with a wideband RF signal is input into the filter chain, each detector will see a portion of the modulation sideband of the optical carrier whose bandwidth is essentially that of the FP filter, which can be much less than the total RF bandwidth of the modulating signal. Here we are assuming the filters are tuned to the appropriate offset frequencies relative to the optical carrier frequency for channelization of either the upper or lower optical sideband to occur.

An optical channelizer of the kind described above could perform as an activity detector to identify the channels where sources are broadcasting, but any functionality that requires electronic post-detection processing of the channelizer outputs is effectively ruled out by the square-law nonlinearity of the detector. In order for an optical channelizer to be compatible with most forms of electronic post-detection processing, the optical detection must be coherent so that the detector really mixes down the optical signal to an RF "intermediate frequency" in a linear manner. Throughout this work, we will typically assume this intermediate frequency is nonzero (i.e. a heterodyne system as opposed to a homodyne system). In the particular case of the FP channelizer above, it is possible in principle to make a heterodyne channelizer by setting the nominal intermediate frequency (IF) equal to the free spectral range of the FP filters. Accordingly, if an appropriate (i.e. frequency offset from the band to be channelized by the IF) optical local oscillator (LO) comb is superposed with the modulated optical carrier at the input to the filter chain, each detector will mix its portion of the modulated optical spectrum down to an IF band centered on the FSR of the optical filter. Here we assume the total channelization bandwidth is less than the FSR of the FP filters, so that neither the modulated input nor the corresponding LO comb span more than one transmission peak of any given FP filter.

For our purposes, it is convenient to express all frequencies as multiples of the channel spacing, so that the channel spacing is 1 by definition. Thus in (3.2-1), Δf is to be understood as the ratio of linewidth to channel spacing, and FSR is the ratio of the free spectral range to the channel spacing. The loss for either a direct detection or heterodyne

FP channelizer under our assumptions is zero, since (3.2-1) does not include transmission loss. We then have the following expressions for ripple and crosstalk of a direct detection FP channelizer (calculated into channel 0 centered at $f = n$ FSR, n integer):

$$\begin{aligned} r_D &= \left[\frac{rT_{FP}(0)P_s}{rT_{FP}(0.5)P_s} \right]^2 = [T_{FP}(0.5)]^{-2}, \\ x_D &= \left[\frac{rT_{FP}(1.5)P_s}{rT_{FP}(0)P_s} \right]^2 = [T_{FP}(1.5)]^2 \end{aligned} \quad (3.2-2)$$

where r_D is the ripple, x_D is the crosstalk, r is the detector responsivity [A/W] and P_s is the incident optical power. Note the detector responsivity and incident optical power do not affect r_D or x_D , since these quantities divide out of the defining ratios as shown, and the periodicity of T_{FP} is employed to simplify the results. Similarly, for a heterodyne FP channelizer, we have

$$\begin{aligned} r_H &= \left[\frac{(rT_{FP}(FSR+0)P_i)(rT_{FP}(0)P_s)}{(rT_{FP}(FSR+0)P_i)(rT_{FP}(0.5)P_s)} \right] = [T_{FP}(0.5)]^{-1} \\ x_H &= \left[\frac{(rT_{FP}(FSR+1)P_i)(rT_{FP}(1.5)P_s)}{(rT_{FP}(FSR+0)P_i)(rT_{FP}(0)P_s)} \right] = T_{FP}(1.5)T_{FP}(1) \end{aligned} \quad (3.2-3)$$

To obtain the result for x_H , it is necessary to assume that an IF bandpass filter is placed after the detector to reject signals that fall out of the proper IF band (i.e. $f_1 - 0.5 \leq f \leq f_1 + 0.5$). This is why the "crosstalk" term $T_{FP}(1.5)T_{FP}(FSR+0)$, which has larger magnitude than x_H , is neglected.

The crosstalk and ripple for a FP optical channelizer depend on the two parameters (3.2-1), namely the linewidth and the free spectral range, so the ripple-crosstalk trade is, in principle, a family of curves (e.g. ripple vs. crosstalk with linewidth as a parameter, for various free spectral ranges). However, the dependence of these curves on the free spectral range is very weak for large FSR, and a definite limit is approached as the FSR is allowed to go to infinity. In this limit, the ripple crosstalk trade is more favorable than it is for any finite FSR, although the difference is very small if the FSR is greater than roughly 10 channel spacings. Therefore, we can plot the ripple-crosstalk trade with linewidth as a parameter for infinite FSR as a (slightly) optimistic approximation to the real situation where the FSR must be finite, and this plot is given in Figure 3-5.

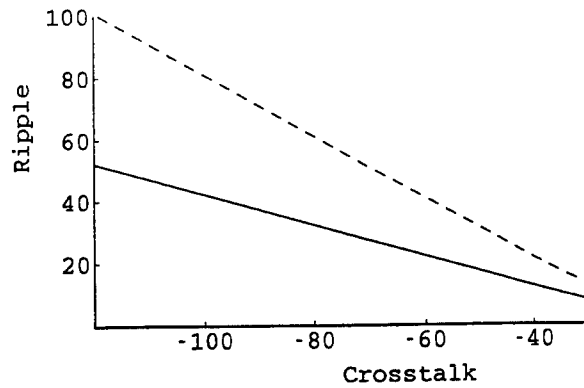


Figure 3-5. Ripple-crosstalk trade for direct detection (dotted line) and heterodyne (solid line) Fabry-Perot optical channelizer

From Figure 3-5, we immediately see that the ripple is extremely large for either type (heterodyne or direct detection) of FP optical channelizer. For example, a typical crosstalk specification is -70 dB, and for this level of crosstalk the ripple is 51 dB for a direct detection FP channelizer and 27 dB for a heterodyne FP channelizer. From the results shown in Figure 3-5, we conclude that Fabry-Perot filters are not a viable optical channelization approach, since even our optimistic model predicts very poor performance.

3.2.2 Free-space, diffraction grating channelizer

In the previous section, we saw that an optical Fabry-Perot filter based channelizer cannot provide any reasonable level of channelization performance because the FP filter lineshape (3.2-1) does not attenuate out-of-band optical signals sufficiently well. Therefore, another channelization approach is necessary, and the approach we will concentrate on is the use of a free space dispersive optical system combined with a detector array in order to perform the channelization. More specifically, we assume that a monochromatic optical input to the system gives a Gaussian spot in the output focal plane, where the detector array is located. Due to the system dispersion, the position of the output spot depends on its frequency, and we assume this relation between position and frequency is linear over the relevant frequency range (i.e. the total bandwidth to be channelized). Since the dispersive element we use in our implementation of this

approach is a free space diffraction grating (DG), we refer to this approach as the DG approach for brevity. Either direct detection or heterodyne channelization can be implemented with the DG approach, since all that is required to implement heterodyne channelization is the introduction of a suitable optical LO comb offset in frequency by the desired IF. For example, if a diffraction grating spectrograph is used, the desired frequency offset is obtained by spatially separating the signal and LO inputs appropriately.

Figure 3-6 gives schematic sketches of the spot pattern in the output focal plane of a heterodyne DG channelizer for two cases of interest. Three elements of the detector array (numbered 1, 2, and 3) are shown, along with the corresponding LO spots (light lines centered on array elements), and a "signal" spot (heavy line). Part a shows the configuration for calculating ripple for channel 2, since the signal is at the edge of channel 2.

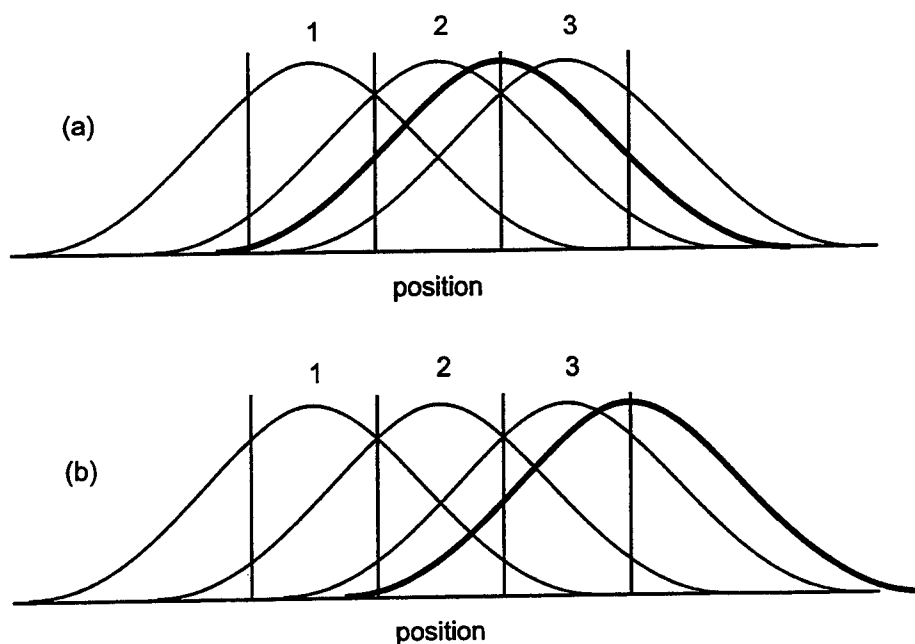


Figure 3-6. Schematic diagrams of output focal plane for a heterodyne DG channelizer. The spot due to the (monochromatic) optical input is shown with a heavy line, the LO comb spots are shown with lighter lines, and the vertical lines indicate the boundaries of the detector array elements. There is a frequency shift between the signal and LO spots, such that if a signal spot coincides with an LO spot, the resulting photocurrent oscillates at the IF frequency.

The relevant response at this signal frequency is the integral of the product of the signal spot with the LO₂ spot over detector 2. Part b shows the configuration for calculating crosstalk into channel 2, since the signal spot is centered on the far edge of channel 3. The relevant response is the integral of the product of the signal spot with the LO₃ spot over detector 2. As we did for the FP channelizer, we assume an IF filter is present after the detector to eliminate the out-of-band signal \times LO₂ into detector 2 contribution from the part b configuration.

For a DG channelizer, we can express crosstalk, ripple and loss in the following manner. Let

$$g(x) = \left(\frac{2}{\pi w^2} \right)^{1/4} \exp \frac{-x^2}{w^2} \quad (3.2-4)$$

be the field profile for the Gaussian spots we assume in the output focal plane. The field profile $g(x)$ is normalized so that the integral of $g^2(x)$ over all x is unity. Here both the position x and the Gaussian radius w are understood to be measured in units of the detector array element spacing, which corresponds to the channel spacing by our assumptions. This scaling of position is convenient, and is similar to the frequency scaling we employed for the FP analysis. By assuming an ideal detector array (i.e. no electrical crosstalk, zero gap between detector array elements, spatial uniformity of array element responsivity), we obtain the following simple expressions for the loss, ripple and crosstalk of a direct detection DG channelizer:

$$l_D = \left[\int_{-1/2}^{1/2} g^2(x) dx \right]^{-2}, \quad r_D = \left[\frac{\int_{-1/2}^{1/2} g^2(x) dx}{\int_{-1/2}^{1/2} g^2(x-0.5) dx} \right]^2, \quad x_D = \left[\frac{\int_{-1/2}^{1/2} g^2(x-1.5) dx}{\int_{-1/2}^{1/2} g^2(x) dx} \right]^2, \quad (3.2-5)$$

where l_D , r_D and x_D are now the loss, ripple and crosstalk respectively of a direct detection DG channelizer. The parallel with Eqs. 2 is evident. For a heterodyne DG channelizer, the results are almost as simple:

$$l_H = \left[\int_{-1/2}^{1/2} g^2(x) dx \right]^{-2}, \quad r_H = \left[\frac{\int_{-1/2}^{1/2} g^2(x) dx}{\int_{-1/2}^{1/2} g(x-0.5)g(x) dx} \right]^2, \quad x_H = \left[\frac{\int_{-1/2}^{1/2} g(x-1.5)g(x-1) dx}{\int_{-1/2}^{1/2} g^2(x) dx} \right]^2. \quad (3.2-6)$$

All of the integrals in (3.2-5) and (3.2-6) can be explicitly evaluated in terms of the error function, which was done in the calculations. Since $g(x)$ only depends on the single

parameter w (ratio of physical Gaussian radius to detector element spacing), we immediately obtain the ripple and loss vs. crosstalk trades shown in Figure 3-7. The ripple-crosstalk trade for an optical DG channelizer is much more favorable than the same trade for an optical FP channelizer, since it is possible, in principle, to obtain low crosstalk and an acceptable level of ripple simultaneously. The ripple-crosstalk trade for a heterodyne channelizer is significantly different than for a direct detection channelizer, and it is not difficult to see why. For the direct detection case, the ripple is due to the division of optical power between adjacent detectors, so in the limit of small spot size where the loss goes to zero, the ripple must approach 6.02 dB as seen in Figure 3-7(a). For a heterodyne channelizer, the overlap between a signal spot at the edge of the detector and an LO spot centered on the detector decreases without limit as the spot size decreases, as seen in Figure 3-7(a). Figure 3-7(b) shows the channelization loss entailed by designs providing various levels of crosstalk, and Figure 3-8 gives the w required to obtain various levels of crosstalk.

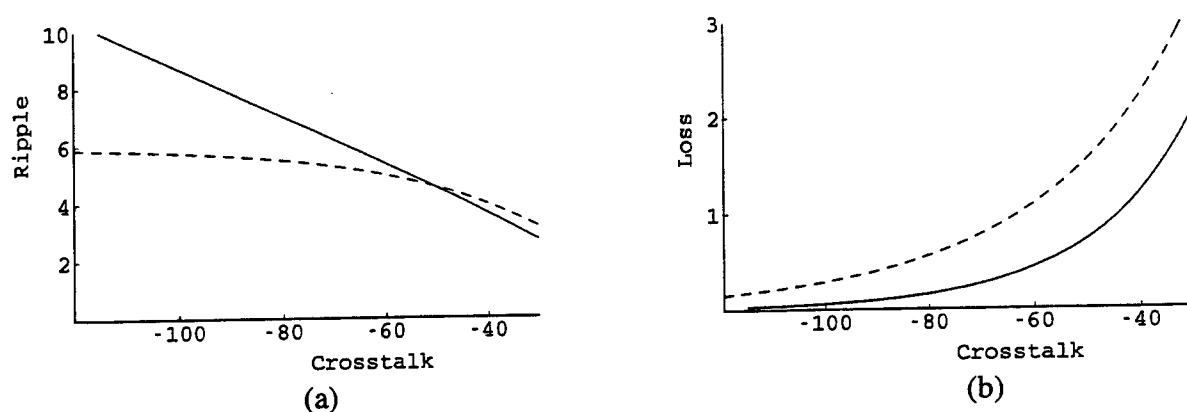


Figure 3-7. Ripple (a) and loss (b) trades vs. crosstalk for direct detection (dotted line) and heterodyne (solid line) free space diffraction grating optical channelizer.

In Figure 3-8 we see that a smaller spot size is required for the heterodyne channelizer than for a direct detection channelizer to obtain a specified level of crosstalk, as can also be inferred from (3.2-5) and (3.2-6). This difference in spot size leads to the lower loss seen in Figure 3-7(b) for the heterodyne case vs. the direct detection case.

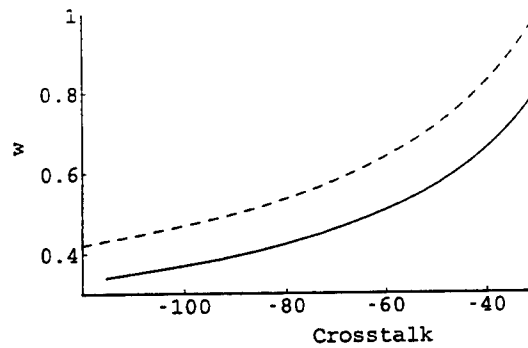


Figure 3-8. w parameter (Gaussian radius/array element spacing) for direct detection (dotted line) and heterodyne (solid line) DG optical channelizers

3.2.3 Additional issues for free-space, diffraction grating channelizer

In the previous section, we saw that a DG channelizer can, in principle, provide low crosstalk and reasonably low ripple simultaneously. The basic reason that good performance can be obtained is the exponential behavior assumed in (3.2-4). Since the idealized analysis led to a favorable conclusion, we refine the analysis to provide more support for this conclusion. Three topics will be considered in this section. The first is the effect of a finite grating length, the second is the effect of gaps between detector array elements and the third is the potential for reducing ripple by allowing the signal and LO spots at the detector array to be of different sizes. In the following three subsections, only the heterodyne case will be considered, since that is the case we are implementing.

To make the following considerations more concrete, we discuss most of these effects as they pertain to the specific example of a heterodyne channelizer designed to have a crosstalk of -70 dB. For this example, the required w is 0.46, and the resulting ripple and loss are 6.17 dB and 0.26 dB respectively. Recall that $w = 0.46$ means that the Gaussian spot radius is 0.46 times the array element spacing. To obtain maximum insight, and to simplify the presentation, these three topics will be considered individually, even though a detailed design would need to consider their combined effect.

3.2.3.1 Finite grating aperture

The effect of the finite grating aperture on the channelizer performance needs to be included in the analysis since otherwise there is, in principle, no way to determine the physical size of the diffraction grating required to achieve a specified level of

channelization performance. We assume the field distribution of the signal and LO is exactly Gaussian at the diffraction grating, and is centered on the grating. We also assume the field distribution is imaged onto the output focal plane without aberration by the camera lens of the spectrograph. Under these assumptions, the finite grating aperture symmetrically truncates the field distributions imaged by the camera lens, and so the resulting output field distribution is the Fourier transform of a truncated Gaussian. Specifically, we have

$$h(x) = \left(\frac{2}{\pi w^2} \right)^{1/4} \operatorname{Re} \left\{ \operatorname{erf} \left(\frac{b}{2} + i \frac{x}{w} \right) \right\} \exp \frac{-x^2}{w^2}, \quad (3.2-7)$$

for the field distribution at the output focal plane, where b is the ratio of grating length to the Gaussian spot radius *at the grating*, and $\operatorname{erf}(z)$ is the error function. In Figure 3-9, we plot $h^2(x)$ (solid line) and $g^2(x)$ (dotted line) for $w = 0.46$ (our nominal example) and $b = 3$, which means the grating length is three times the Gaussian spot radius at the grating. Even though $b = 3$ is quite a large aperture by most standards (e.g. the power loss due to $b = 3$ truncation is only 0.27%), we see that this level of truncation greatly increases the intensity at points one to two channel spacings away from the spot center.

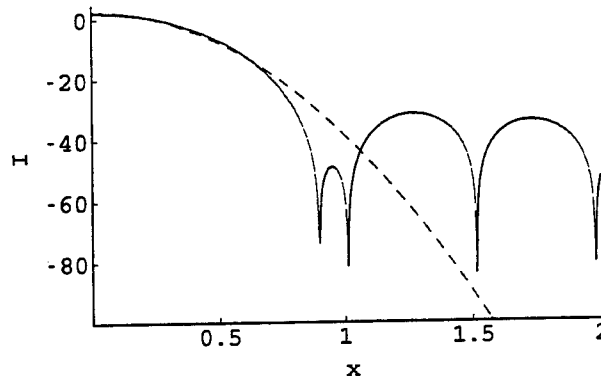


Figure 3-9. Output intensity ($I = h^2$) distribution due to finite grating length ($b = 3$) for $w = 0.46$. Dotted line is intensity distribution from an infinitely long grating, for comparison. The units of position are channel spacings, so this plot shows the intensity distribution for a spot centered on detector 0 where the detector edges are at 0.5, 1.5, 2.5 etc.

It is clear the behavior shown in Figure 3-9 can significantly increase channelizer crosstalk, if the aperture is too small. We can directly calculate the crosstalk in the presence of a finite aperture from (3.2-6) where $g(x)$ is replaced with $h(x)$ from (3.2-7).

For this case, the integrations must be performed numerically. Figure 3-10 shows the result of such a calculation for the nominal -70 dB crosstalk design ($w = 0.46$), and we see the crosstalk increases by over 9 dB for $b = 3.3$ which corresponds to a truncation loss of less than 0.1 %. The aperture has to increase to the range $b > 5.5$ before the aperture has no visible effect on the crosstalk level. Fortunately, in the range $4.3 < b < 5.5$, the crosstalk is actually slightly less than the -70 dB design value, so if we require $b > 4.3$, the aperture will not significantly increase the crosstalk. It is possible to adopt a different design strategy, where the spot size is chosen so that the nominal crosstalk is -73 dB (or some other convenient value less than -70 dB), and the finite grating length crosstalk is required to be < -70 dB. This approach would require a smaller grating, typically, but the price paid would be an increase in ripple due to the smaller spot size.

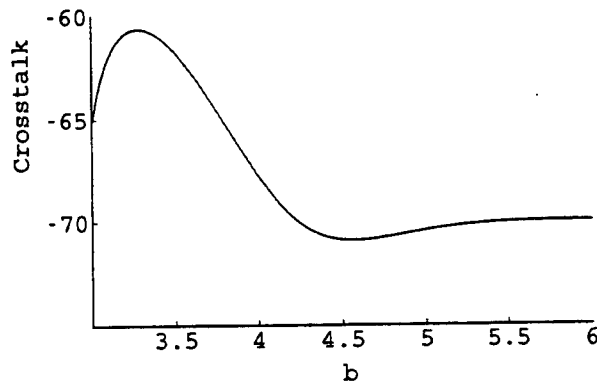


Figure 3-10. Crosstalk vs. grating aperture for -70 dB crosstalk example. b is the ratio of grating length to Gaussian spot radius at the grating.

Up until now, we have not considered the effect of the overlap of the LO spots, as shown schematically in Figure 3-6. The reason for this delay is that a discussion of LO overlap that does not incorporate the finite grating aperture is misleading. In principle, every LO spot makes some contribution to the total optical field seen by each detector. After detection, the photocurrent due to these LO overlaps has "spurs" at all integer multiples of the channel spacing. Recall we are assuming an IF bandpass filter follows the detector. If the IF filter rolls off between the center and edge of the nominal IF band, it will contribute to ripple. We require the IF filter to make no contribution to the ripple. Thus we require the IF filter transmission characteristic to be flat over the range $f_i - 0.5 < f < f_i + 0.5$, where f_i is the intermediate frequency and the unit of frequency is taken to be the channel spacing, as before.

Under these assumptions, the IF filter will typically pass only one of the LO overlap spurs, so our analysis can focus on individual spurs. Since $f_1 > 1.5$ is required to achieve proper spectral separation of the heterodyne and direct detection photocurrents, $f = 2$, $f = 3$, etc., are the relevant LO overlap spurs with the lowest frequencies. If we choose to pass the $f = 2$ spur, we have $1.5 < f_1 < 2.5$, and if we choose to pass the $f = 3$ spur, we have $2.5 < f_1 < 3.5$, etc. Thus a calculation of the $f = 2$ and $f = 3$ spurs will provide a basis for choosing the range in which the intermediate frequency must fall: either $1.5 < f_1 < 2.5$, or $2.5 < f_1 < 3.5$ or $3.5 < f_1$. We assume that operation at the lowest possible f_1 reduces the burden on the post-detection electronics as much as possible, so we focus on the lowest two intermediate frequency ranges.

The calculation of the $f=2$ and $f=3$ spurs is not completely straightforward, since each spur is the sum of a large number of terms. In the finite grating case, it seems necessary to empirically include enough terms so that the results no longer change significantly when another term is added. Each $LO_i \times LO_j$ term makes a contribution to the total photocurrent at $f = i-j$ whose phase depends on the relative phase between LO_i and LO_j . We calculate a worst case estimate for the total spur power by adding up the magnitude of each contribution and then squaring, since it is unrealistic to design for a specific set of LO relative phases. More specifically, we calculate

$$s_2 = \left[\left| \int_{-1/2}^{1/2} h(x-1)h(x+1)dx \right| + 2 \sum_{j=1}^N \left| \int_{-1/2}^{1/2} h(x-1+j)h(x+1+j)dx \right| \right]^2 \quad (3.2-8)$$

$$s_3 = \left[2 \sum_{j=0}^N \left| \int_{-1/2}^{1/2} h(x-1+j)h(x+2+j)dx \right| \right]^2$$

where s_2 and s_3 are the worst case $f = 2$ and $f=3$ spur powers respectively, and N is the number of terms to be considered. (3.2-8) exploits the symmetry of the problem ($LO_{+x} \times LO_{-y}$ equivalent to $LO_{-x} \times LO_{+y}$) to avoid duplicate calculation of integrals. In Figure 3-11, numerical results for s_2 and s_3 as a function of b are given for our -70 dB crosstalk example, and it was found that $N = 5$ seemed to give enough terms. From Figure 3-10, we see that s_2 essentially reaches its limiting value of -82 dB for $b > 5.7$, while s_3 does not reach its limiting value over the plotted range of apertures. This difference is due to the very low limiting value of s_3 as aperture increases, namely -185 dB, which is reached

for $b > 9$. The unrealistically large apertures required to bring s_2 and (especially) s_3 to their limiting values is the reason an analysis of LO overlap that neglects the finite grating aperture is misleading.

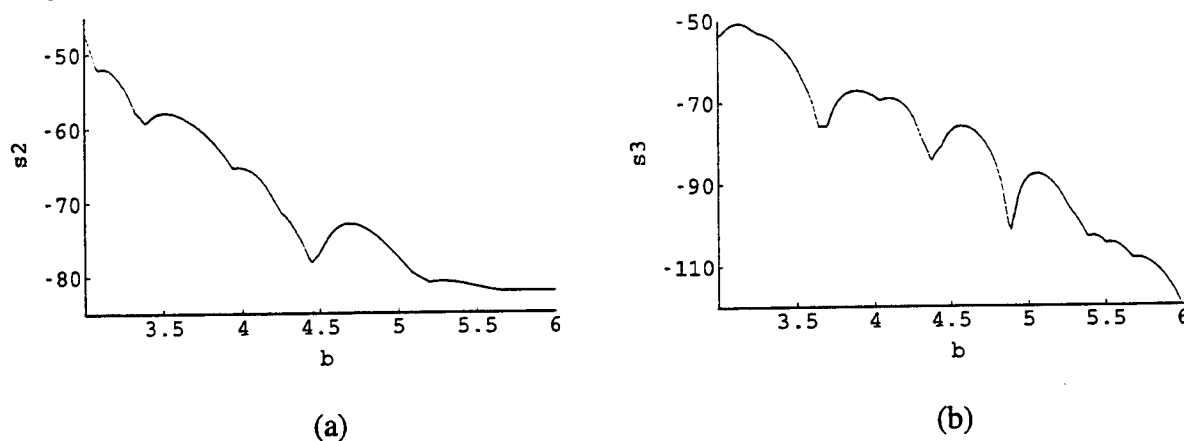


Figure 3-11. s_2 (a) and s_3 (b) vs. b (the grating aperture) for a heterodyne DG channelizer with -70 dB of crosstalk.

The requirements to be placed on s_2 and/or s_3 depend on the implementation and application of the channelizer, so only a simple example will be given here. Suppose our requirement on the LO spur is that its power be less than the additive noise power into some bandwidth B , and that the only significant additive noise terms are LO shot noise and thermal noise. This can be expressed quantitatively by

$$2r^2 P_1^2 s < \left(4kT/R_L + 2qrP_1/\sqrt{l_H} \right) B, \quad (3.2-9)$$

where s is the relevant LO overlap term ((3.2-8) gives s_2 and s_3), q is the electron charge, R_L is the load resistance seen by the detector, k is Boltzmann's constant, P_1 is the LO power (per LO spot) at the detector array, r is the detector responsivity [A/W], and l_H is the heterodyne channelization loss given by (3.2-6) with $h(x)$ substituted for $g(x)$. Typically the effect of l_H is negligible, as it is for our -70 dB crosstalk example. For the following typical numbers: $r = 0.7$ A/W, $B = 40$ MHz, $T = 300$ K, $R_L = 50 \Omega$, $l_H = 1$, and P_1 in the range $10 \mu\text{W}$ to 1 mW, we obtain a requirement on s ranging from $s < -38$ dB ($P_1 = 10 \mu\text{W}$) to $s < -76$ dB ($P_1 = 1$ mW). The requirement on s gets more demanding as P_1 increases, since the spur power increases with increasing power more rapidly than the noise, as seen in (3.2-9). Note that B is assumed to be significantly less than our nominal channel spacing of 1 GHz, which is appropriate for significant post-detection electronic

processing, such as further channelization. As B decreases, the requirement on s also becomes more stringent, since it becomes easier for the electronics to "see" the LO overlap spur. In this particular example, the combination of these requirements with Figure 3-11 provides information on what aperture and/or IF range is required to satisfy the LO overlap requirement. More specifically, we see that if P_1 is at the low end of its range, the LO overlap effect is negligible if $b > 3$, which is already ensured by the crosstalk-driven requirement that $b > 4.3$. If P_1 is at the high end of its range, we need $b > 5$ to bring s_2 within specification, and $b > 4.7$ to bring s_3 within specification, and either of these aperture requirements is more stringent than the crosstalk-driven requirement. To summarize, we considered two effects which depend critically on the grating size --- crosstalk and LO overlap. For our -70 dB crosstalk example, $b > 4.3$ is required to avoid increased crosstalk. There is an additional requirement on the aperture for our example based on the LO overlap calculation (Figure 3-11) that depends on several additional parameters as seen in (3.2-9). In practice, of course, it is necessary to choose an aperture which satisfies both the crosstalk and LO overlap requirements.

3.2.3.2 Gaps between detector array elements

Thus far we have assumed the detector array performs in a very idealized manner. Specifically that there is no electrical crosstalk between array elements, every array element has a spatially uniform response with the same responsivity, and that there is no gap between array elements (i.e. the fill factor is unity). These are all assumptions that will not be obtained in practice, so it is important to relax them as much as possible in the analysis. It should be noted that the "detector array" need not be an array of detectors in close physical proximity. In fact, it may well be that a configuration of that type leads to insuperable electrical crosstalk problems. An alternative approach that will reduce electrical crosstalk is to place an array of waveguides so that the spectrograph images signal and LO spots onto an array of waveguide end faces. These waveguide end faces thus define the channels, since they will only admit light that is incident on the waveguide cores, roughly speaking. The waveguides then fan out to detectors that can be spatially separated to whatever degree is necessary to reduce electrical crosstalk to acceptable levels. An issue of major concern for this optical waveguide array approach is

that the effective fill factor is likely to be much less than the fill factor of a detector array, since the waveguide cores must be far enough apart that waveguide-waveguide coupling is negligible. Therefore, our analysis of nonideal detector array behavior will focus on the effect of decreasing the fill factor, motivated primarily by the low fill factor expected of an optical waveguide array approach, and secondarily by the difficulty of adequately modeling electrical crosstalk or nonuniform element response in terms of a suitably small number of parameters.

Recall that (3.2-6) for the loss, ripple and crosstalk of a heterodyne channelizer are based on the assumption that the relevant detector covers the range $-0.5 < x < 0.5$, where the unit of distance is the array element spacing. We can allow for a nonunity fill factor simply by assuming the active region of the detector now covers the range $-0.5\eta < x < 0.5\eta$, where η is the fill factor. The required equations follow from the corresponding modification to the limits of integration in (3.2-6). If η is decreased while holding w fixed, the qualitative effect on loss, ripple and crosstalk is clear. The loss will increase, since more of the spot will miss the array element; the ripple will also increase, since at the relevant frequency the signal spot will be centered on a larger "hole" in the detector array; and the crosstalk will decrease, since the edge of the array element is farther from the centers of the spots that cause crosstalk.

Since crosstalk depends on only the fill factor and the spot size, we can calculate a plot showing the w parameter required to obtain crosstalk of -70 dB vs. the fill factor. Such a plot is shown in Figure 3-12, and we see that as the fill factor decreases, the w parameter (i.e. the spot size) increases to keep the crosstalk at the specified level of -70 dB.

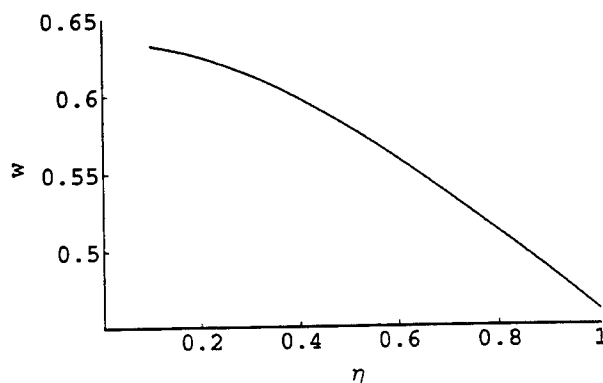


Figure 3-12. Spot size vs fill factor for heterodyne DG channelizer with -70 dB crosstalk

Our standard -70 dB crosstalk example is the $\eta = 1$ point on this plot.

Next we calculate the loss and ripple vs. η , where the crosstalk is held at -70 dB by varying w as shown in Figure 3-13. The resulting curves are shown in Figure 3-13, where part (a) gives the ripple and part (b) gives the loss. Somewhat surprisingly, the ripple actually *decreases* as the fill factor decreases, although this decrease is just a few tenths of a dB. The explanation for this result is that even though decreasing η opens up physical holes in the detector array that act to increase ripple, decreasing η also leads to larger spot sizes to keep crosstalk at -70 dB, and larger spot sizes tend to decrease ripple. In the case shown in Figure 3-13(a), these two effects nearly cancel.

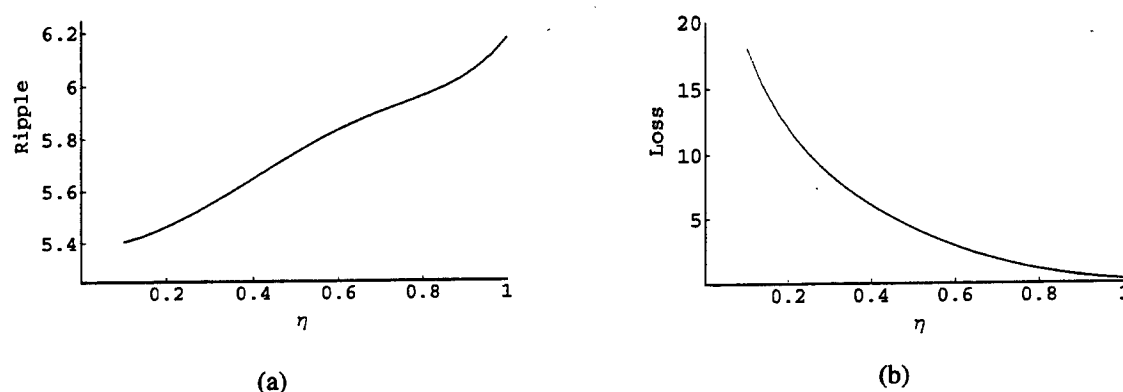


Figure 3-13. Ripple (a) and loss (b) vs. detector array fill factor for heterodyne DG channelizer with -70 dB crosstalk.

Since the effect of fill factor on ripple (for fixed crosstalk) is rather small, the primary effect of reduced fill factor is an increase of channelization loss, as seen in Figure 3-13(b). Since ripple is a more critical issue than loss (i.e. a few extra dB of ripple is typically worse than the same amount of extra loss), the behavior of a heterodyne channelizer as the fill factor decreases is relatively benign. Even fill factors as low as 50% only lead to a few extra dB of loss.

3.2.3.3 Unequal carrier and L.O. spot sizes

Up to this point, we have assumed the carrier (or signal) spot and the LO spots are the same size at the detector array. There is no reason in principle why we cannot have unequal carrier and LO spots at the detector array, if some advantage can be gained by doing so. If the dispersion is performed by a grating spectrograph, all that is required to

make the output spot sizes unequal is an appropriate modification of the carrier and/or LO inputs to the spectrograph. The improvement we are seeking by making the carrier and LO spot sizes different is a reduction of the ripple for a given level of crosstalk (i.e. -70 dB in our example). In Figure 3-14 we give the LO (part a) and carrier (part b) w parameters vs. ripple for a constant crosstalk level of -70 dB. These calculations are based on (3.2-6) modified by letting $g_C(x)$ differ from $g_{LO}(x)$. As the ripple is reduced, we see that the LO spot gets smaller and the carrier spot gets larger. This behavior is expected, since ripple is due to a change in carrier-LO overlap as the position of the carrier spot is moved. The larger the carrier spot is, the less variation we expect in this overlap. From Figure 3-14, we see that significant reduction in the ripple is possible, although the required modification of the spot sizes will have a major impact on the design. For example, to reduce the ripple to 3 dB requires w_L to be roughly 0.23, which is half the value for the nominal -70 dB crosstalk design with equal carrier and LO spots. Thus the physical size of the channelizer will basically need to double (for the same channel spacing) in order to realize the reduced ripple.

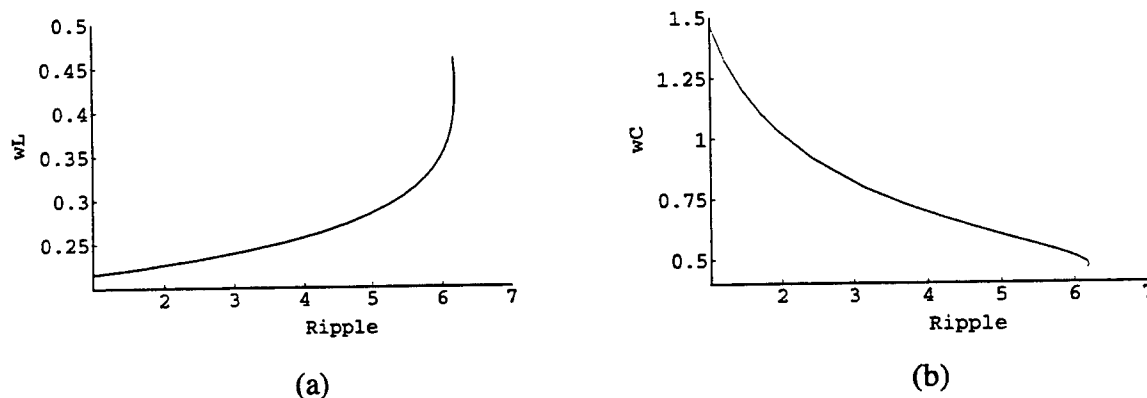


Figure 3-14. LO (a) and carrier (b) w parameters vs. ripple for a heterodyne DG channelizer with -70 dB crosstalk

There are two additional issues to consider when evaluating designs with unequal spot sizes. The first issue is the extra loss due to the larger carrier spot, as mentioned above. The second issue is a requirement that is placed on the IF filter that follows the detector. Recall that the crosstalk into detector 0 is assumed to come from the product of LO_1 with the carrier and that the (larger) product of LO_0 with the carrier is assumed to be

suppressed by the IF filter. Let $T_{IF}(f)$ be the (power) transmission function of the IF filter. Then the above suppression requirement is expressed quantitatively by

$$\frac{T_{IF}(f_I - 1.5)}{T_{IF}(f_I - 0.5)} \ll \left[\frac{\int_{-1/2}^{1/2} g_C(x - 1.5) g_{LO}(x - 1) dx}{\int_{-1/2}^{1/2} g_C(x - 1.5) g_{LO}(x - 0) dx} \right]^2 \equiv q, \quad (3.2-10)$$

where we have defined the RHS of the inequality to be equal to q for convenience, and $g_C(x)$ and $g_{LO}(x)$ are the carrier and LO field distributions respectively, from (3.2-4) with $w = w_C$ and $w = w_L$ respectively. (3.2-10) ensures that after the IF filter, the carrier \times LO_0 crosstalk term is much less than the carrier \times LO_1 crosstalk term we have been concerned with. For our purposes a plot of q will provide adequate information on the variation of the IF filter requirement, since we assume the IF filter suppression is required to be some fixed factor times q . Figure 3-15 gives plots of the loss and q parameter vs. ripple for a fixed crosstalk level of -70 dB. We see that the loss increases by roughly 1 dB for every dB the ripple decreases, which is basically a favorable trade. The effect of reducing ripple on q (i.e. the IF filter requirement) is much stronger, as see in Figure 3-15(b), where the q parameter goes from trivial (i.e. $q = -7$ dB) to substantial (i.e. $q = -43$ dB) as the ripple is reduced from 6 dB to 3 dB.

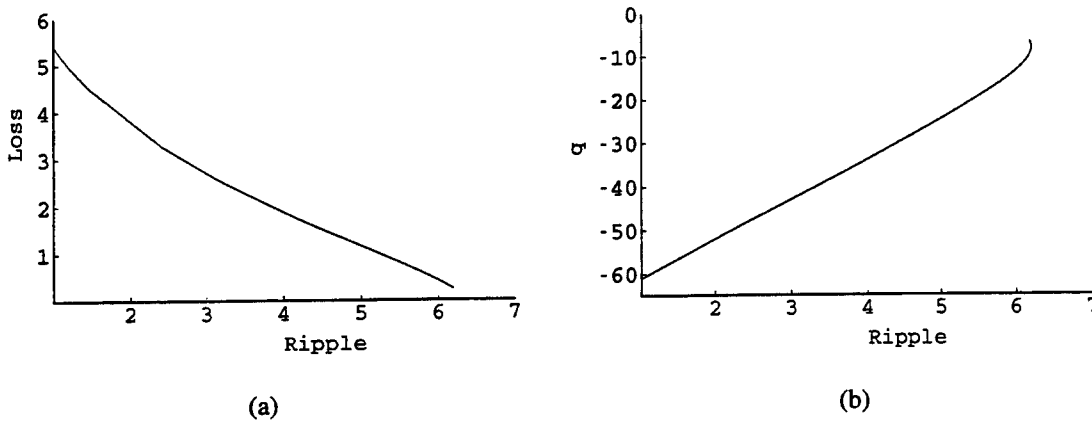


Figure 3-15. Loss (a) and q (b) vs. ripple for heterodyne DG channelizer with -70 dB crosstalk

4 OPTICAL CARRIER TRACKING

An important consideration in any heterodyne receiver is the need to mitigate the reduction of signal fidelity caused by additive phase noise due to the relative phase incoherence between the carrier and local oscillator. This is a particularly pressing problem in optical heterodyne systems because of the generally broad phase noise spectrum of the optical sources. In the RF regime carrier tracking, wherein the local oscillator is made to be phase coherent with the signal carrier, is a mature, well understood technology. For the case where the carrier and local oscillator are operating at optical frequencies the solutions to this problem are not as clear. During the course of this program we analyzed and performed experimental investigations of two techniques for performing optical carrier tracking, namely optical phase-locked loops and optical injection locking. In this section we present a highly detailed analysis that includes a review of the theory of random processes and noise. We then present analyses of the optical phase-locked loop and optical injection locking approaches to carrier tracking, along with our experimental results for both approaches.

4.1 GENERAL NOISE BACKGROUND

Since we need to employ the spectral analysis of random processes in several of the following sections, we begin with a collection of some of the basic definitions and general results of this analysis that forms a general background section for reference.

4.1.1 Definitions and notation

4.1.1.1 Wide-sense stationary random process

A random process $y(t)$ is treated as a statistical ensemble of $y_j(t)$, where each y_j is an unknown, but deterministic, function of time. The properties of a random process are statistical properties of the ensemble as a whole, and therefore do not pertain to any of the y_j individually. The fundamental description of a random process is in terms of probabilities $p_1(y_1, t_1) dy_1$ for y to take on a value in (y_1, y_1+dy_1) at time t_1 , $p_2(y_1, y_2, t_1, t_2) dy_1 dy_2$ for y to take on a value in (y_1, y_1+dy_1) at t_1 and to take on a value in (y_2, y_2+dy_2) at time t_2 and an infinite number of higher order probability density functions.

While this description of a random process is complete, it is too elaborate for practical use. The quantities of greatest interest for a random process are the mean $\mu_y(t_1)$ and the covariance $K_{yy}(t_1, t_2)$ which are defined as follows:

$$\begin{aligned}\mu_y(t_1) &= E[y(t_1)] \\ K_{yy}(t_1, t_2) &= E[y(t_2)y^*(t_1)]\end{aligned}\tag{4.1-1}$$

where E is the statistical expectation operator, and the $*$ superscript indicates complex conjugation.

A random process $y(t)$ is stationary if all the probability densities p_j needed to fully describe the process are unchanged when all times t_k are shifted together by some T . So a stationary process essentially has statistical properties that do not change in time. A process $y(t)$ is wide-sense stationary (WSS) if the mean and covariance given in (4.1-1) are unchanged when t_1 and t_2 are shifted together by some T . A stationary process must also be WSS, but a WSS process need not be stationary. For a WSS process $y(t)$, the mean and covariance are given by

$$\begin{aligned}\mu_y &= E[y(t)] \\ K_{yy}(\tau) &= E[y(t+\tau)y^*(t)]\end{aligned}\tag{4.1-2}$$

so the mean is time-independent and the covariance is a function of $\tau = t_2 - t_1$ only.

4.1.1.2 Power spectral density

If $y(t)$ is a random process, its Fourier transform cannot be defined as the average over the Fourier transforms of the y_j , since these transforms do not exist. Therefore, a different approach is needed to define the spectrum of a random process. Let $y(t)$ be a random process, and let y_T be obtained from y by truncation, so that y_T vanishes outside $(-T/2, T/2)$. Then every member of y_T has finite energy and thus has a Fourier transform S_{jT} . The power spectral density (PSD) of y_T is given by $S_T(f) = E[|S_{jT}(f)|^2] / T$.

If the truncated process y_T is "representative" of the original process y , then we expect S_T to be similarly "representative" of the PSD of y . Clearly, at least some of the statistical properties of y must be time-independent for $(-T/2, T/2)$ to be a "representative" interval, and it turns out that the necessary and sufficient condition is that $y(t)$ be WSS. For a WSS process, it can be shown (Weiner-Khintchine theorem) [5] that

$$S_{yy}(f) = \lim_{T \rightarrow \infty} S_T(f) = \int_{-\infty}^{\infty} K_{yy}(\tau) e^{-j2\pi f\tau} d\tau \quad (4.1-3)$$

$$K_{yy}(\tau) = \int_{-\infty}^{\infty} S_{yy}(f) e^{j2\pi f\tau} df$$

where $S_{yy}(f)$ is the power spectral density (PSD) of the WSS process $y(t)$. Thus the covariance and the PSD for a WSS process are a Fourier transform pair.

The PSD $S(f)$ as defined in (4.1-3) is a “two-sided” spectral density, since the total power in the process is obtained by integration of the PSD from $-\infty$ to ∞ . For a real WSS process $y(t)$, $K_{yy}(\tau)$ is a real, even function of τ , which implies that $S_{yy}(f)$ is a real, even function of f . For this special case, the negative frequency part of $S_{yy}(f)$ provides no additional information, so it has become common engineering usage to define a “one-sided” spectral density $W_{yy}(f)$ via

$$W_{yy}(f) = 2S_{yy}(f)u(f) \quad (4.1-4)$$

where $u(f)$ is the unit step function ($u(f) = 1$ for $f > 0$, $u = 0$ for $f < 0$) so that only positive frequencies need be considered for a real process. Although the two-sided density S is preferable for general developments, it can be useful to give results for real processes in terms of W , since the expressions often simplify. To reduce confusion, our notation will be consistent: $S(f)$ for a two-sided PSD and $W(f)$ for a one-sided PSD.

4.1.1.3 Sum/difference of random processes

Let $z(t) = x(t) \pm y(t)$, where $x(t)$ and $y(t)$ are both WSS, and assume $x(t)$ and $y(t)$ are also jointly WSS so that their cross-covariance, K_{xy} , is given by

$$K_{xy}(\tau) = E[x(t+\tau)y^*(t)] \quad (4.1-5)$$

We define the cross-spectral density (CSD) of two jointly WSS random processes as the Fourier transform of $K_{xy}(\tau)$, so it is given by

$$S_{xy}(f) = \int_{-\infty}^{\infty} K_{xy}(\tau) e^{-j2\pi f\tau} d\tau \quad (4.1-6)$$

The CSD does not have a physical interpretation as a power density, since it is generally complex. However, the CSD does satisfy the identity

$$S_{xy}(f) = S_{yx}^*(f) \quad (4.1-7)$$

which follows from the definition of $K_{xy}(\tau)$. With these definitions, the PSD of the sum/difference process $z(t)$ is given by

$$S_{zz}(f) = S_{xx}(f) + S_{yy}(f) \pm S_{xy}(f) \pm S_{yx}(f) \quad (4.1-8)$$

and we see that (4.1-8) ensures that S_{zz} is real. We also see that if two processes are uncorrelated, so that their CSD is zero, then the PSD of the sum or difference process is simply the sum of the PSDs of the two processes. This important result is frequently employed to express a total noise PSD as the sum of the PSDs of various independent contributions to the noise.

4.1.1.4 Gaussian process

A random process $x(t)$ is Gaussian if, for every finite set of times t_n , the random variables $x(t_n)$ have a Gaussian joint probability density function. To obtain some of the following results, it will be necessary to assume certain random processes are Gaussian. When this is done, the Gaussian assumption will always be stated.

4.1.2 Linear filtering of noise

Let $y(t)$ be the output of a linear, time-invariant system with transfer function $H(f)$, driven by a random WSS input $x(t)$. Then it can be shown that [5]

$$\begin{aligned} S_{xy}(f) &= S_{xx}(f)H^*(f) \\ S_{yy}(f) &= S_{xy}(f)H(f) = S_{xx}(f)|H(f)|^2 \end{aligned} \quad (4.1-9)$$

(4.1-9) shows the basic results for the effect of a linear system on noise, and one of the main purposes of the development to this point is to provide background for these results. If $u(t)$ is obtained by passing WSS $x(t)$ through system $H(f)$ and $v(t)$ is obtained by passing WSS $y(t)$ thorough system $G(f)$, then we have

$$S_{uv}(f) = H(f)G^*(f)S_{xy}(f) \quad (4.1-10)$$

provided $x(t)$ and $y(t)$ are also jointly WSS.

4.1.3 Passband to baseband transformation [5]

It is frequently useful to express a signal, especially a narrowband signal, in terms of a complex envelope modulating a carrier as follows:

$$x(t) = \text{Re}\{z(t) = x(t) + jy(t) = w(t)\exp j2\pi vt\} = a(t)\cos 2\pi vt - b(t)\sin 2\pi vt \quad (4.1-11)$$

where $w(t) = a(t) + jb(t)$ is the complex envelope, which is slowly varying if $x(t)$ is narrowband about the carrier frequency v . The representation of (4.1-11) is ambiguous, in the sense that two signals, $a(t)$ and $b(t)$, are to be used to represent the given signal $x(t)$.

If $a(t)$, $b(t)$ and $x(t)$ are all deterministic signals, there are clearly many ways to choose $a(t)$ and $b(t)$ so that (4.1-11) holds.

If $x(t)$, $a(t)$ and $b(t)$ are WSS random processes, there is less freedom to choose $a(t)$ and $b(t)$ in (4.1-11). By requiring the RHS of (4.1-11) to be WSS, and making use of symmetries due to $a(t)$, $b(t)$, $x(t)$ and $y(t)$ all being real, we obtain the following relations among the PSDs and CSDs:

$$\begin{aligned} 4S_{xx}(f) &= 4S_{yy}(f) = S_{zz}(f) + S_{zz}(-f) \\ j4S_{xy}(f) &= S_{zz}(-f) - S_{zz}(f) \\ 4S_{aa}(f) &= 4S_{bb}(f) = S_{ww}(f) + S_{ww}(-f) \\ j4S_{ab}(f) &= S_{ww}(-f) - S_{ww}(f) \end{aligned} \quad (4.1-12)$$

and, in addition, $x(t)$, $a(t)$ and $b(t)$ must all be zero-mean processes. The process $y(t)$ is also WSS and zero-mean.

Even though the relationships in (4.1-12) significantly reduce the ambiguity inherent in the representation of (4.1-11), they do not lead to a unique representation. The standard (analytic signal) representation is obtained by assuming $y(t)$ can be obtained from $x(t)$ by linear filtering with transfer function $H(f)$. From (4.1-12), we have the following conditions on $H(f)$:

$$\begin{aligned} |H(f)| &= 1 \\ H(f) &= -H(-f) \\ \text{Re}\{H(f)\} &= 0 \end{aligned} \quad (4.1-13)$$

where the first condition follows from $S_{xx} = S_{yy}$, the second from $S_{xy}(f) = -S_{xy}(-f)$, and the third from $\text{Re}\{S_{xy}\} = 0$. The simplest (i.e. smallest number of discontinuities) $H(f)$ that satisfies (4.1-13) is $H(f) = \pm j \text{sgn}(f)$, where $\text{sgn}(f)$ is the sign function ($\text{sgn}(x) = 1$ for $x > 0$, $\text{sgn}(x) = -1$ for $x < 0$). We take $H(f) = -j \text{sgn}(f)$ which leads to the following relations which uniquely specify the representation:

$$\begin{aligned} S_{xy}(f) &= j \text{sgn}(f) S_{xx}(f) \\ S_{zz}(f) &= 4u(f) S_{xx}(f) \\ S_{aa}(f) &= S_{bb}(f) = S_{xx}(v+f)u(v+f) + S_{xx}(v-f)u(v-f) \\ S_{ab}(f) &= j[S_{xx}(v+f)u(v+f) - S_{xx}(v-f)u(v-f)] \end{aligned} \quad (4.1-14)$$

where we have employed the relation $S_{ww}(f) = S_{zz}(v+f)$, which follows from (4.1-3). The powers of the various signals are related by $P_x = P_y = P_a = P_b = P_z/2 = P_w/2$. Together,

these processes $a(t)$ and $b(t)$ are called the baseband representation of the process $x(t)$. The specification of $a(t)$ and $b(t)$ is simpler in terms of one-sided PSDs:

$$W_{aa}(f) = W_{bb}(f) = W_{xx}(\nu + f) + W_{xx}(\nu - f) \quad (4.1-15)$$

One application of this representation that will be useful later on is the effect of additive noise on the amplitude and phase of a carrier. Let

$$V(t) = A_0 \cos(2\pi\nu t) + x(t) = \text{Re}\{A(t)e^{j\phi(t)}e^{j2\pi\nu t}\} \quad (4.1-16)$$

where $x(t)$ is zero-mean WSS additive noise which will be represented as in (4.1-11).

Solving for $A(t)$ and $\phi(t)$, the amplitude and phase of the carrier, gives

$$\begin{aligned} A(t) &= \sqrt{(A_0 + a(t))^2 + b^2(t)} \approx A_0 + a(t) \\ \phi &= \tan^{-1}\left(\frac{b(t)}{A_0 + a(t)}\right) \approx \frac{b(t)}{A_0} \end{aligned} \quad (4.1-17)$$

where $a(t)$ and $b(t)$ are the baseband representation of $x(t)$, and the approximate forms on the right are valid for low noise conditions. In this case, we see that $a(t)$ (the “in phase” component) gives rise to amplitude noise on the carrier, and $b(t)$ (the “quadrature” component) gives rise to phase noise on the carrier. From (4.1-17) and (4.1-15), we have the following result for the phase noise PSD of a noiseless carrier + additive noise $x(t)$:

$$W_{\phi\phi}(f) = \frac{1}{A_0^2} [W_{xx}(\nu + f) + W_{xx}(\nu - f)] \quad (4.1-18)$$

where A_0 is the amplitude of the carrier and W_{xx} is the additive noise PSD. This result will be useful when considering the effect of additive noise in a phase locked loop.

4.1.4 Phase noise spectra and units

There are many equivalent ways to specify a phase (or frequency) noise spectrum. We will mainly be concerned with two quantities: $W_{\phi}(f)$, the phase noise PSD (units rad^2/Hz), and $W_f(f)$, the frequency noise PSD (units Hz^2/Hz). To relate these two quantities, it is convenient to briefly consider the angular frequency noise PSD $W_{\omega}(f)$ (units $\text{rad}^2/\text{s}^2\text{Hz}$). Since angular frequency is the derivative of phase, we have $W_{\omega}(f) = 4\pi^2 f^2 W_{\phi}(f)$ from (4.1-9), and since $\omega = 2\pi f$, we have $W_{\omega}(f) = 4\pi^2 W_f(f)$. By combining these two relations, we obtain

$$W_f(f) = f^2 W_{\phi}(f) \quad (4.1-19)$$

4.1.5 Phase modulation of a carrier by noise

Since phase noise is a critical issue for coherent optical systems, we collect certain basic results here for reference and later use. Consider a carrier with a noisy phase

$$V(t) = A \cos[2\pi\nu t + \theta + \phi(t)] \quad (4.1-20)$$

where the amplitude A is assumed to be constant, and $\phi(t)$ is the phase noise process (assumed real and WSS). The quantity θ is a time-independent random variable, distributed uniformly on $[0, 2\pi)$, which is introduced into (4.1-20) to make $V(t)$ a WSS process. The covariance of $V(t)$ is

$$K_{VV}(\tau) = \frac{A^2}{2} \text{Re}\{\exp(j2\pi\nu\tau) E[\exp j(\phi(t+\tau) - \phi(t))]\} \quad (4.1-21)$$

In general, the expectation in (4.1-21) is difficult to evaluate, but if we assume $\phi(t)$ is a Gaussian process, then the expectation can be easily evaluated. The relevant result for Gaussian random variables is

$$E[\exp(j\mathbf{a} \cdot \mathbf{x})] = \exp(-\mathbf{a}^T \mathbf{K} \mathbf{a} / 2) \quad (4.1-22)$$

where \mathbf{x} is a real Gaussian random vector, \mathbf{K} is the covariance matrix of \mathbf{x} , and \mathbf{a} is an arbitrary vector of real coefficients. We assume $\phi(t)$ is a Gaussian process, so that the covariance of V can be evaluated using (4.1-22) in (4.1-21) to obtain

$$K_{VV}(\tau) = \frac{A^2}{2} \exp[-[K_{\phi\phi}(0) - K_{\phi\phi}(\tau)] \cos 2\pi\nu\tau] \quad (4.1-23)$$

From (4.1-23), the PSD of the noise-modulated carrier is given by

$$S_{VV}(f) = \frac{A^2}{2} \int_0^\infty \exp[-[K_{\phi\phi}(0) - K_{\phi\phi}(\tau)] \cos 2\pi(\nu + f)\tau + \cos 2\pi(\nu - f)\tau] d\tau \quad (4.1-24)$$

which shows that the two-sided PSD of $V(t)$ is peaked at or near $f = \pm \nu$ as expected. In practice, the carrier frequency ν is typically much larger than the bandwidth of the phase noise sidebands, and in this case, we can simplify (4.1-24) by giving an approximate result for the one-sided PSD:

$$W_{VV}(f) \approx A^2 \int_0^\infty \exp\left[-\int_0^\infty (1 - \cos 2\pi z\tau) W_{\phi\phi}(z) dz\right] \cos 2\pi(\nu - f)\tau d\tau \quad (4.1-25)$$

where (4.1-3) has been used to express $K_{\phi\phi}$ in terms of $W_{\phi\phi}$. In (4.1-25), the portion of the peak centered at $f = -\nu$ that extends into the region $f > 0$ is assumed to be negligible. From (4.1-25) we see that the relation between phase noise spectrum and carrier spectrum

is quite complicated, even after making the simplifying assumption that the phase noise is a Gaussian process.

4.1.6 Special cases for phase modulation of a carrier by noise

Since (4.1-25) relating the phase noise spectrum to the carrier spectrum is so complicated, we concentrate on the most relevant special cases.

4.1.6.1 White frequency noise

Suppose the frequency noise is white, with a frequency-independent PSD W_f [Hz²/Hz]. From (4.1-19) the phase noise PSD is then given by $W_\phi f^2$, and substituting this spectrum into (4.1-25) gives the following result:

$$W_w(f) = A^2 \frac{W_f}{(\pi W_f)^2 + 4(\nu - f)^2} \quad (4.1-26)$$

The resulting carrier spectrum is Lorentzian, with FWHM linewidth given by $\Delta\nu = \pi W_f$ [Hz]. This model is frequently used for laser phase noise, since $W_\phi = W_f/f^2$ is the spectrum of a random walk, so (4.1-26) is relevant for much of the later material.

4.1.6.2 Small phase variance

Another special case of great practical significance is when the phase variance is small. This usually cannot be assumed for the output of a free-running laser, since in that case the phase variance is usually infinite. However, if a phase locked loop, or any other frequency control/stabilization technique is employed, the residual phase noise in the loop (or equivalent) will typically have a small variance if the stabilization system is performing properly. The relevant result is obtained from (4.1-25) by performing a first order expansion of the exponential and evaluating the resulting integrals, which gives

$$W_w(f) \approx \frac{A^2}{2} \left[(1 - \sigma_\phi^2) \delta(\nu - f) + \frac{W_{\phi\phi}(|\nu - f|)}{2} \right] \quad (4.1-27)$$

where σ_ϕ^2 is the phase variance, and $\delta(f)$ is the Dirac delta function. In this case, the noisy carrier still has a discrete line at the carrier frequency, with sidebands around the line which are replicas of the phase noise PSD. The factor of 0.5 multiplying $W_{\phi\phi}$ ensures that the total power of the carrier is unchanged by this small-variance phase modulation, which is the expected behavior for phase modulation in general. It can be

shown that (4.1-27) also holds for non-Gaussian phase statistics, provided the phase variance remains small [6].

A commonly employed notation for the RF spectrum due to phase noise is $L(f)$, which is by definition the RF noise PSD at an offset $\pm f$ from the carrier frequency due to phase noise only, divided by the total power. The usual units for $L(f)$ are thus dBc/Hz, and for this special case, we have

$$L(f) \equiv 10 \log_{10} \left[\frac{W_{vv}(v \pm f)}{\int_0^\infty W_{vv}(f) df} \right] \approx 10 \log_{10} \left[\frac{W_{\phi\phi}(f)}{2} \right] \quad (4.1-28)$$

for $L(f)$, where the first form given is its general definition, and the second form applies to the present case. It is common to report the results of phase noise measurements in terms of $L(f)$, so (4.1-28) provides an important relation between the measured spectrum ($L(f)$), and the underlying phase noise spectrum ($W_{\phi\phi}(f)$).

4.2 OPTICAL SIGNALS AND NOISES

In the analyses of this report, we will make use of the following signal and noise models, which are collected here for reference and consistency.

4.2.1 Photocurrent

The photodetector is treated as a current source driving a load resistance (R). Typically, the load resistance is 50Ω in an RF system, to properly impedance match to the rest of the system, and in such a matched system, only half of the total power from the detector is delivered to the rest of the RF system, while the other half is dissipated in the load R . The signal and noise analysis can be done either in terms of available power (power delivered to the rest of the RF system), or in terms of total power, as long as it is done consistently. We do the analysis in terms of total power for simplicity. The photocurrent is given by

$$I = rP(t) + i_{th}(t) + i_s(t) + i_R(t) + i_A(t) \quad (4.2-1)$$

where r is the detector responsivity [A/W], $P(t)$ is the optical power [W], $i_{th}(t)$ is the thermal noise current, $i_s(t)$ is the shot noise current, $i_R(t)$ is the noise current due to laser relative intensity noise (RIN), and $i_A(t)$ is the noise current due to optical amplification (if an optical amplifier is present). We assume these additive noise processes are

independent, so that the total additive noise PSD is the sum of the PSDs of the individual processes.

Frequently we will be concerned with the case where the optical field is generated by two lasers that deliver constant optical powers P_1 and P_2 to the detector whose frequency difference $f_0 = f_2 - f_1$ is well within the detector bandwidth. In this case, we have

$$P(t) = P_1 + P_2 + 2\eta\sqrt{P_1P_2} \cos(2\pi f_0 t + \phi_2(t) - \phi_1(t)) \quad (4.2-2)$$

where $\eta \leq 1$ is the heterodyne efficiency, which depends on the degree of mode and polarization overlap between the two lasers at the detector, and $\phi_1(t)$ and $\phi_2(t)$ are the phase noise processes of lasers 1 and 2 respectively. Since the photocurrent phase is given by $\phi_2 - \phi_1$, reduction of this phase difference directly, as opposed to reducing both ϕ_1 and ϕ_2 , is typically the most effective coherent detection phase noise reduction approach. The following noise models will be given assuming two lasers are present, since we are mainly concerned with the coherent detection case. These expressions differ from those appropriate for the analysis of an optical channelizer, since such a channelizer performs significant noise filtering in the optical domain.

4.2.2 Thermal noise

The PSD of the process $i_{th}(t)$ is given by

$$W_{th} = \frac{4kT}{R} \quad (4.2-3)$$

where T is the absolute temperature, k is Boltzmann's constant (1.38×10^{-23} J/K) and R is the load resistance (usually 50Ω).

4.2.3 Shot noise

We assume the PSD of the process $i_s(t)$ is given by

$$W_s = 2e(P_1 + P_2) \quad (4.2-4)$$

where e is the electron charge (1.6×10^{-19} C). To obtain (4.2-4), we have assumed that the time variation in $P(t)$ is only a small fraction of $P_1 + P_2$, which is a good approximation for most analog direct detection links, and for coherent systems where one laser is much stronger at the detector than the other. For coherent systems with high heterodyne efficiency where the laser powers are comparable at the detector (or for

digital systems), the time-varying level of the shot noise can be accounted for with an improved model.

4.2.4 Laser RIN

We assume the PSD of the process $i_R(t)$ is given by

$$W_R = r^2 (P_1^2 10^{RIN_1/10} + P_2^2 10^{RIN_2/10}) \quad (4.2-5)$$

where RIN_1 and RIN_2 are the specified RIN values for lasers 1 and 2 respectively (e.g. -160 dB/Hz). In reality, the RIN spectrum of a laser is approximately white over a range of frequencies limited on the low frequency side by $1/f$ noise and limited on the high frequency side by the relaxation resonance. Since a single number (the RIN value) is frequently the only information available for a laser, we use the simple model of (4.2-5). If the laser RIN spectrum is known, it is not difficult in principle to incorporate that information into these analyses. If two lasers are present, we assume their respective intensity noise processes are independent, so that each laser contributes to W_R independently as shown in (4.2-5). This assumption may not be valid if the two lasers are phase locked via injection locking or in a PLL.

4.2.5 Optical amplifier noise

We assume the PSD of the process $i_A(t)$ is given by

$$W_A = 2r^2 h\nu (P_1 + P_2) (F_1 G_1 (1 - L_1) + F_2 G_2 (1 - L_2)) \quad (4.2-6)$$

where $F_{1,2}$, $G_{1,2}$ and $L_{1,2}$ are the noise figures, optical power gains and transmission losses of paths 1 and 2 respectively, $h = 6.6 \times 10^{-34}$ Js is Planck's constant and ν is the optical frequency (assumed approximately equal for the two lasers). When (4.2-6) is expanded, it has four terms which account for the mixing of two "signals" with two "noises". To obtain (4.2-6), we assume the amplifiers are operating in the high gain limit, so that signal \times ASE noise dominates, and in this limit, the noise figures F_1 and F_2 must be ≥ 3 dB (quantum limit). We also assume that paths 1 and 2 are amplified by two distinct amplifiers, so that the ASE in the two paths is uncorrelated. Our final assumption is that optical amplification is performed before transmission losses are incurred (the most favorable case).

4.2.6 Laser phase noise

From (4.1-22), we have

$$W_{\phi\phi}(f) = \frac{\Delta\nu}{\pi f^2} \quad (4.2-7)$$

for the phase noise PSD $W_{\phi\phi}$ [rad²/Hz] of an idealized laser (Lorentzian lineshape, FWHM linewidth = $\Delta\nu$ [Hz]). Real laser phase noise PSDs may or may not be well approximated by (4.2-7), so we need to consider reported experimental results for phase noise of the relevant lasers for this work — i.e. diode-pumped monolithic Nd:YAG lasers, and monolithic semiconductor lasers.

In reference [7], a phase noise spectrum of

$$W_{\phi\phi}(f) = 10^7/f^4 + 1.5 \times 10^4/f^3 + 0.2/f^2 \quad (4.2-8)$$

was found for a diode-pumped monolithic Nd:YAG laser of the same basic type as we used in our experiments. The measured FWHM linewidth for this laser was 6 kHz, which comes completely from the $1/f^3$ and $1/f^4$ terms in (4.2-8), since the linewidth would be < 1 Hz if only the $1/f^2$ term in (4.2-8) were present. We see that for this type of laser, the model of (4.2-7) is not even approximately applicable, and a measured phase noise spectrum must be used instead.

In reference [8], a phase noise spectrum of

$$W_{\phi\phi}(f) = 5.8 \times 10^{11}/f^3 + 9.4 \times 10^5/f^2 \quad (4.2-9)$$

was measured for a monolithic DFB semiconductor laser. For this phase noise spectrum, the measured linewidth (self-heterodyne technique) is 5 MHz, while the linewidth obtained from just the $1/f^2$ term in (4.2-9) is 3 MHz. So, for this particular laser, (4.2-7) provides a rough approximation for the phase noise PSD, but inclusion of $1/f$ term(s) is necessary to obtain quantitative results. We expect this case to be representative of the applicability of (4.2-7) to monolithic semiconductor lasers in general, since it is known[9] that spontaneous emission phase noise is described by (4.2-7), and typically spontaneous emission noise dominates in these lasers due to their small size and low cavity Q.

Although the DFB linewidth in this case was roughly 10^3 times the linewidth of the Nd:YAG laser, we see from (4.2-8) and (4.2-9) that the phase noise PSD of the DFB is roughly 10^6 to 10^7 times larger than the phase noise PSD of the Nd:YAG, especially at

high frequencies. So the ratio of linewidths greatly understates the underlying difference in the phase noise PSDs of the two lasers.

4.3 PHASE LOCKED LOOP - THEORY

4.3.1 PLL transfer functions

One of the standard methods of reducing phase noise is to use a phase lock loop to lock a noisy oscillator to a reference with better noise properties. This technique has been applied to the generation of RF tones from the heterodyne of two lasers, as in [10]. Before considering the results of [10], we develop a PLL model that is appropriate for this application.

In Figure 4-1, we have a schematic block diagram of a heterodyne optical phase lock loop. The optical outputs of lasers 1 and 2 (shown by heavy lines) are coherently superposed and detected. The resulting RF photocurrent is mixed with the output of an RF mixer, and if the loop is locked, the mixer output is proportional to the phase difference between the reference and the photocurrent. The phase difference is then filtered through the loop filter and used as a control input to laser 2 which thus plays the part of a voltage (or current) controlled oscillator.

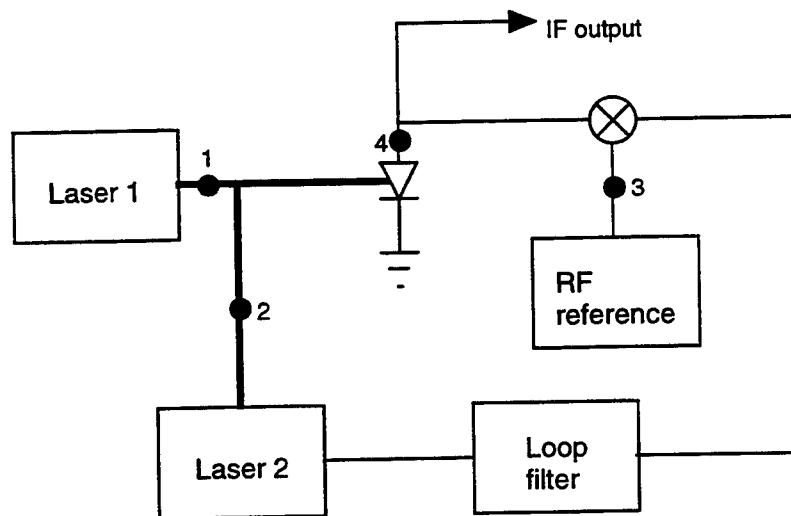


Figure 4-1. Block diagram of an optical phase lock loop

In comparing the model of Figure 4-1 to the standard references, e.g. [11], note that the RF VCO in this system is the combination of the two lasers and photodiode, and that the

RF reference enters the loop the way the signal does in the standard loop. The reason we can think of these three blocks as a single “VCO block” is simply that we expect the frequency of the RF photocurrent to be proportional to the loop filter output voltage. If this approximation does not hold with sufficient accuracy, then a more accurate model is necessary. As a result of the composite nature of the VCO in this PLL, the fundamental loop equation is written as follows:

$$\theta_2 = G(s)(\theta_{ref} - \theta_2 + \phi_1) \quad (4.3-1)$$

where $G(s)$ is the open loop gain from the RF mixer input to the controlled phase output of laser 2, and ϕ_1 and θ_2 are the phases of lasers 1 and 2 respectively. We employ a notation where θ is used for the basic PLL state variables (e.g. θ_2 and θ_{ref}) and ϕ is used for other variables (i.e. the various noise inputs).

The signs in Eq. 0 ensure a negative feedback action where the phase difference between θ_{ref} and $\theta_2 - \phi_1$ tends to be driven to zero by varying θ_2 . The closed loop transfer function, $H(s)$, follows from Eq. 0 by solving for θ_2 , which gives

$$\theta_2 = \frac{G(s)}{1 + G(s)}(\theta_{ref} + \phi_1) \equiv H(s)(\theta_{ref} + \phi_1) \quad (4.3-2)$$

Since $H(s)$ is a lowpass, unity DC gain filter, we see that the PLL forces the phase of laser 2 to follow the sum of the phases of the RF reference and laser 1. Standard forms for $H(s)$ for first and second order loops are given by

$$H(s) = \frac{K_v}{s + K_v} \quad (4.3-3)$$

$$H(s) = \frac{K_v(2\zeta\omega_n s + \omega_n^2) - \omega_n^2 s}{K_v(s^2 + 2\zeta\omega_n s + \omega_n^2)} \approx \frac{2\zeta\omega_n s + \omega_n^2}{s^2 + 2\zeta\omega_n s + \omega_n^2}$$

where ω_n is the natural frequency of the loop, ζ is the damping factor, and K_v is the DC gain of the loop. The approximate form given for the second order loop is valid in the high gain limit, where $K_v \gg \omega_n/2\zeta$. Although the high gain limit is commonly employed in PLL analyses, we will see that the calculation of noise spectra usually requires the exact form of the transfer function.

In many PLL applications, second order loops are preferred because the independence of ω_n and K_v allows the construction of a loop capable of tracking a signal over a much wider range of frequencies than the loop bandwidth. The first order loop has essentially

the same bandwidth and tracking ranges, and is inappropriate in cases where a narrow bandwidth and large tracking range are desired. For our application, the locking of one laser to another, a large bandwidth and tracking range are required, so both types of loop are worth consideration.

4.3.2 Stability

Before we consider the noise filtering properties of a PLL, we investigate the stability of the system, since the linear properties of an unstable system are irrelevant. The transfer functions in (4.3-3) have poles in the left half of the s-plane, and are thus unconditionally stable. However, if there is a significant loop propagation delay, the transfer functions in (4.3-3) must be modified as shown below, and it is possible for these systems to be unstable.

$$H(s) = \frac{K_v}{se^{s\tau} + K_v} \quad (4.3-4)$$

$$H(s) \approx \frac{2\zeta\omega_n s + \omega_n^2}{s^2 e^{s\tau} + 2\zeta\omega_n s + \omega_n^2}$$

Here τ is the loop time delay. For the systems in (4.3-4), it is more convenient to use the Bode criterion for unconditional stability, where the gain of the open loop transfer function $G = H/(1-H)$ is required to be less than unity at any frequency at which the phase shift of G is π . This procedure leads to the following conditions on τ that ensure stability:

$$\tau < \pi/2K_v$$

$$\omega_n \tau < \frac{\tan^{-1} \left[2\zeta \sqrt{2\zeta^2 + \sqrt{4\zeta^4 + 1}} \right]}{\sqrt{2\zeta^2 + \sqrt{4\zeta^4 + 1}}} \quad (4.3-5)$$

for first and second order loops respectively. For $\zeta = 0.707 = 1/\sqrt{2}$ (critical damping), the RHS of (4.3-5) reduces to 0.736, which is close to its maximum value (0.741 @ $\zeta = 0.639$) as a function of ζ . Thus $\zeta = 0.707$ is quite appropriate in cases where the delay time is a significant issue, such as [10]. We see that the stability requirement on the time delay gets more stringent as the loop bandwidth is increased. This time delay issue is the main reason it is difficult to obtain very large loop bandwidths in a PLL.

4.3.3 Noise filtering

We have indicated on Figure 4-1 four places where noise can enter this PLL. Laser phase noise enters in at points 1 and 2, RF reference phase noise enters in at 3, and all additive noises effectively enter the loop at 4. If deterministic signals are applied to these extra inputs, (4.3-1) gives

$$\theta_2 = G(s)(\theta_{ref} + \phi_3 - \theta_2 - \phi_2 + \phi_1 - \phi_4) \quad (4.3-6)$$

since the relation of phase detector inputs to VCO phase must remain the same, even in the presence of additional noise inputs. Note that ϕ_2 does not appear on the LHS of (4.3-6), since the PLL acts by controlling θ_2 , not $\theta_2 + \phi_2$. The phase of the photocurrent in the PLL is given by

$$\begin{aligned} \theta_{IF} &= \theta_2 + \phi_2 - \phi_1 + \phi_4 \\ &= H(s)(\theta_{ref} + \phi_3) + (1 - H(s))(\phi_2 - \phi_1 + \phi_4) \end{aligned} \quad (4.3-7)$$

For nondeterministic signals, we work in terms of the phase noise power spectral density W (the subscript $\phi\phi$ from previous sections is dropped here), take $\theta_{ref} = 0$ without significant loss of generality, and assume all noise inputs are independent to obtain, using (4.1-6), (4.1-9) and (4.3-7):

$$W_{IF}(f) = |H(f)|^2 W_3(f) + |1 - H(f)|^2 (W_1(f) + W_2(f) + W_4(f)) \quad (4.3-8)$$

where $W_{IF}(f)$ is the photocurrent phase noise PSD, $W_1(f)$ and $W_2(f)$ are the phase noise spectra of the *free-running* lasers 1 and 2 respectively, $W_3(f)$ is the RF reference phase noise PSD, and $W_4(f)$ is the phase noise contributed by additive noise in the loop. Here we see that the PLL strongly suppresses the effect of laser phase noise on the heterodyne beat phase noise, since $1-H(f)$ is a highpass filter and $W_1(f)$ and $W_2(f)$ typically have $1/f$ type spectra. We also see that a high quality RF reference is required, since the RF reference phase noise contribution to $W_{IF}(f)$ is lowpass filtered.

The PSD $W_4(f)$ gives the phase noise induced by additive noise in the loop, so we must employ our earlier result from (4.1-18) to relate $W_4(f)$ to W_a , the PSD of the additive noise itself. Since our additive noise models are all white (for simplicity), we have

$$W_4(f) = \frac{2W_a}{I_{RF}^2} = \frac{2}{I_{RF}^2} \left[\frac{4kT}{R} + 2er(P_1 + P_2) + r^2(P_1^2 10^{RIN_1/10} + P_2^2 10^{RIN_2/10}) \right] \quad (4.3-9)$$

where we have employed the signal and noise models of section 4.2, defined the RF photocurrent amplitude $I_{RF} = 2r\eta\sqrt{P_1P_2}$ for convenience, and assumed $f < f_0$, where f_0 is the RF heterodyne beat note frequency. We have also neglected additive noise due to the loop electronics, since it will depend on details of the loop construction. If the noise due to loop electronics is known, it can easily be included in this analysis. Since we expect $W_1(f)$, $W_2(f)$ and $W_3(f)$ to decrease with increasing frequency, the high frequency photocurrent phase noise is $L(f) = W_4/2$ at sufficiently high frequencies.

We give illustrative plots of this phase noise floor vs $P_{RF} = I_{RF}^2 R/2$ for various levels of laser RIN in figures 4-2 and 4-3. In these figures, the detector responsivity is taken to be 0.7 A/W (56% quantum efficiency at 1.55 μm), the load resistance is 50 Ω , and the RIN specifications of the two lasers are assumed to be equal. In figure 4-2, we assume $P_1 = P_2$, and in figure 4-3 we consider the unequal case $P_1 = 0.01 P_2$.

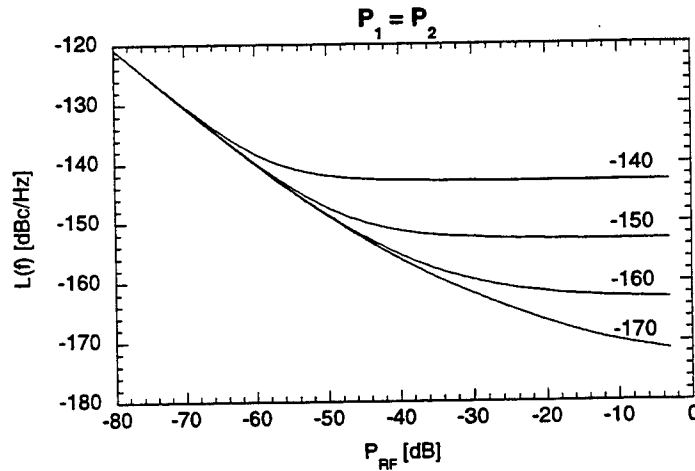


Figure 4-2. Additive phase noise in PLL with $r = 0.7$ A/W, $P_1 = P_2$ and $RIN_1 = RIN_2$. The curves are labeled with the laser RIN [dB/Hz]

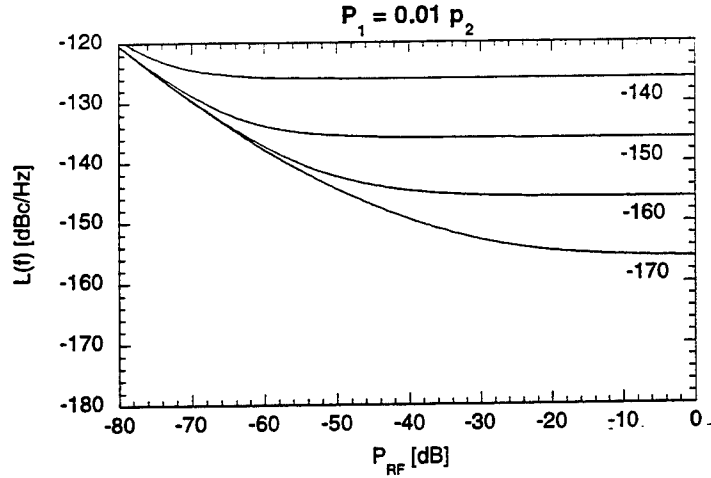


Figure 4-3. Additive phase noise in PLL with $r = 0.7 A/W$, $P_1 = 0.01 \cdot P_2$ and $RIN_1 = RIN_2$. The curves are labeled with the laser RIN [dB/Hz]

Figure 4-2 shows the expected behavior, where the phase noise floor decreases as P_{RF} increases, until a limit is reached that depends on the RIN of the lasers. In figure 4-3, where the optical power at the detector from the two lasers differs by a factor of 100 (as may occur in a strong LO, weak carrier scenario), we see the same qualitative pattern, where noise decreases as P_{RF} increases until the RIN-dependent limit is reached. However, comparison of figures 4-2 and 4-3 shows that the contribution of RIN to phase noise is greatly increased when the optical powers at the detector differ significantly. Let $P_2 = x P_1$. The RIN limit of W_4 is then given by

$$W_{RIN} = \left(\frac{1 + x^2}{2x} \right) 10^{RIN/10} \quad (4.3-10)$$

for $RIN_1 = RIN_2 = RIN$, which shows that the optimal value of x is 1, and that the phase noise increases by roughly a factor of $\max(x, 1/x)/2$ for large (or small) x , which is consistent with the 17dB shift seen between figures 2 and 3. The reason for this behavior is that as P_1 and P_2 become increasingly unequal, while keeping I_{RF} constant, the RIN increases relative to I_{RF} , leading to increased photocurrent phase noise in the RIN-limited regime.

4.3.4 External time delay

It is instructive to consider the phase noise spectra of the lasers individually, assuming a PLL has been implemented as above. Since laser 1 sees no input from the PLL, its noise

spectrum is not altered by the PLL, so the locked and free-running phase noise spectra of laser 1 are the same. The output phase of laser 2 is given by

$$\psi_2 = \theta_2 + \phi_2 = H(\theta_{ref} + \phi_3 + \phi_1 - \phi_4) + (1-H)\phi_2 \quad (4.3-11)$$

which leads to the following results pertaining to S_{LL} , the phase noise PSD of laser 2 under locked conditions, and S_{1L} , the phase noise CSD between lasers 1 and 2 under locked conditions:

$$\begin{aligned} S_{LL} &= |H|^2(S_3 + S_1 + S_4) + |1-H|^2 S_2 \\ S_{1L} &= H^* S_1 \end{aligned} \quad (4.3-12)$$

where we have made use of (4.1-9) for filtering of noise by a linear system. We see that under locked conditions, the phase noise PSD of laser 2 is roughly the same as that of laser 1, if S_3 and S_4 are negligible, and $|1-H|^2 S_2$ is also negligible. These assumptions are equivalent to an assumption of good locking performance. The PLL does not necessarily act to reduce the linewidth of laser 2 (recall that S_1 could be larger than S_2 , which would mean the PLL actually increases the linewidth of laser 2 when locked). Instead, a correlation, S_{1L} , is induced between the two lasers, such that the phase noise on the heterodyne beat is greatly reduced (as seen above for W_{IF}).

To see how this works out more explicitly, suppose we tap off a portion of the outputs of the lasers in Figure 4-1 to be combined and mixed on a separate detector than the one in the PLL, as indicated schematically in figure 4-4. This configuration is not a purely academic exercise, since it is relevant to distribution of RF tones by the optical heterodyne of phase locked lasers [12].

Also indicated on Figure 4-4 are the relevant time delays in this problem: t_{1P} and t_{2P} , the delays from lasers 1 and 2 respectively to the PLL detector, and t_{1E} and t_{2E} , the delays from lasers 1 and 2 respectively to the external detector. The effect of the total time delay within the PLL (t_{2P} is part of this total delay) is assumed to be included in the PLL transfer function $H(f)$, as in (4.3-4).

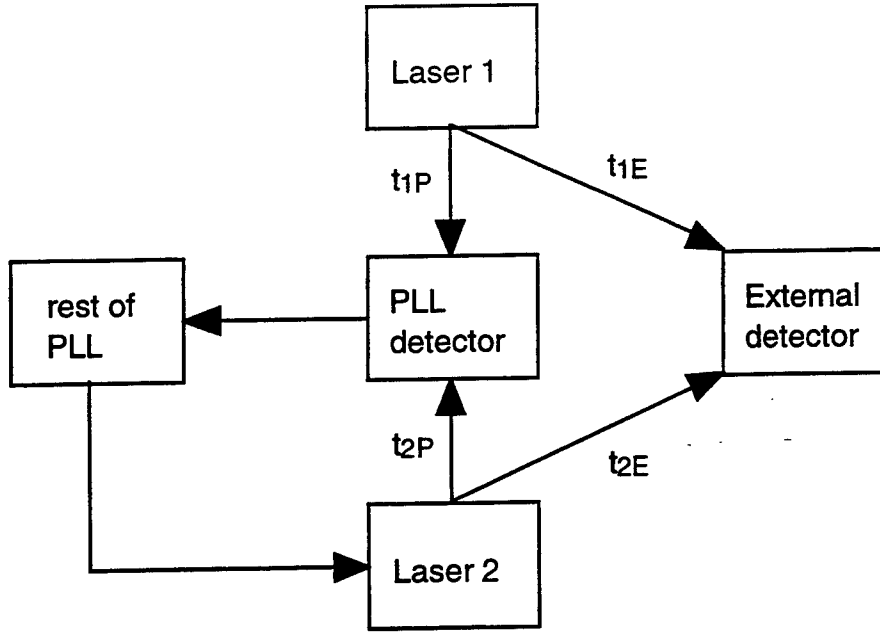


Figure 4-4. Schematic block diagram for external heterodyne of PLL-locked lasers

Since $H(f)$ for a time delay τ is given by $H = e^{-j2\pi f\tau}$, Figure 4 leads to the following relations between the CSD of lasers 1 and 2 at various places in the system (the PSDs of lasers 1 and 2 are not affected by external time delays, since $|H|^2 = 1$)

$$\begin{aligned} S_{1L} &= e^{-j2\pi f t_{1P}} e^{j2\pi f t_{2P}} S_{1L}|_{LASER} \\ S_{1L}|_{EXT} &= e^{-j2\pi f t_{1E}} e^{j2\pi f t_{2E}} S_{1L}|_{LASER} \end{aligned} \quad (4.3-13)$$

where (4.1-10) has been employed to relate the delayed CSDs to the undelayed CSD. Recall that S_{1L} is the CSD at the PLL detector, which follows from (4.3-7). (4.3-13) allows us to relate S_{1L} to $S_{1L}|_{EXT}$ at the external detector as follows:

$$S_{1L}|_{EXT} = \exp j2\pi f [(t_{2E} - t_{1E}) - (t_{2P} - t_{1P})] S_{1L} \equiv e^{j2\pi f T} S_{1L} \quad (4.3-14)$$

where we have introduced the net external delay T . Now we define $z(t)$ to be the heterodyne phase at the external detector, which has the following PSD

$$\begin{aligned} S_z(f) &= S_{LL}(f) + S_1(f) - S_{1L}(f)|_{EXT} - S_{L1}(f)|_{EXT} \\ &= |1 - H e^{-j2\pi f T}|^2 S_1(f) + |1 - H|^2 S_2(f) + |H|^2 (S_3(f) + S_4(f)) \end{aligned} \quad (4.3-15)$$

which follows from (4.3-14) and (4.1-8). Note that if S_{L1} and S_{1L} were zero, the phase noise on laser 1 would contribute to S_{zz} as $(1+|H|^2)S_1$, which shows that the correlations are responsible for the reduced contribution from laser 1 to the heterodyne phase noise

S_{zz} . Comparison of the external heterodyne phase noise PSD (S_{zz}) with the photocurrent phase noise PSD in the PLL (W_{IF} from (4.3-8)) shows two differences. The first is that the additive noise contribution (from W_4) to W_{IF} and S_{zz} are highpass and lowpass filtered respectively. This is expected, since the PLL reduces the effect of W_4 within the loop by impressing this noise onto laser 2 so that it is suppressed in the heterodyne mixing leading to W_{IF} . As a result, we see lowpass filtered PLL additive noise in an external detector, and the results shown in Figure 4-2 and 4-3 will give the low frequency phase noise floor, provided the laser and RF reference phase noise contributions are less than the additive noise floor.

The second difference between W_{IF} and S_{zz} is that the net time delay T affects the contribution of laser 1 phase noise to S_{zz} . The condition $T = 0$ can be rewritten as $t_{2E} - t_{1E} = t_{2P} - t_{1P}$, which means $T = 0$ if the difference in the time delays from the lasers to the PLL detector and from the lasers to the external detector are the same. If T is nonzero, then the contribution to S_{zz} from W_1 is altered as indicated in (4.3-15) (typically this leads to increased noise). The physical reason for this effect is that the correlation between two samples of the output phase of laser 1 that are delayed relative to each other by τ decreases as τ increases, which is just another way of saying laser 1 has phase noise. The PLL operates by forcing laser 2 to track laser 1 at the PLL detector, so if lasers 1 and 2 are heterodyned with a different relative delay than that present at the PLL detector, laser 2 will effectively be tracking a time-shifted (delayed or advanced) version of laser 1 at the external detector, and this time shift alters the correlation between the lasers at the external detector and thus the external heterodyne phase noise as can be seen from (4.3-14) and (4.3-15).

Additional insight into the physical significance of the net time delay T can be obtained by supposing the phase of laser 1 varies much slower than the loop bandwidth and that the other noises in the loop are negligible. In this case, we expect laser 2 to track laser 1 very well, as seen in (4.3-11). For sufficiently low frequencies, $H(f)$ for a first or second order loop (with or without the internal time delay τ) is given by

$$H_{LF}(f) \approx 1 - j2\pi f / K_v \quad (4.3-16)$$

Since a time delay of $1/K_v$ has a low frequency limit identical to $H_{LF}(f)$, we can interpret (4.3-16) as the statement that laser 2 perfectly tracks the low frequency fluctuations of

laser 1 up to a positive time delay $1/K_v$. That is, $\psi_2(t) = \phi_1(t - 1/K_v)$ in the low frequency limit. Since no physical process can respond instantaneously, this is the best possible tracking that can be expected on general grounds. Now we can see that the net external time delay T simply adds to the "intrinsic" time delay $1/K_v$ in the low frequency limit. For example, if $T = -1/K_v$, the low frequency phase fluctuations of laser 1 are tracked perfectly by laser 2 at the external detector. It is not necessarily a good idea to deliberately introduce an external time delay equal to $-1/K_v$, since the high frequency performance may be degraded.

4.4 PHASE LOCKED LOOP – EXPERIMENT

4.4.1 Phase-Locked Loop (PLL) Testbed

A PLL testbed was constructed to address the basic coherent detection issue, that is synchronization of an optical local oscillator to an optical carrier. A functional block diagram of the testbed is shown in figure 4-5. We used solid state Nd:YAG lasers that were off-the-shelf from Lightwave Electronics. The lasers were nominally identically, with the model LWE 122 being equipped with a fast tuning option compatible with the PLL circuitry. The components shown in the double-lined box are all contained in a Laser Offset Locking Accessory (LOLA) that is sold by the laser manufacturer.

There were two specific goals that we intended to accomplish with the testbed. First, we wanted to measure and understand phase noise as a function of received optical carrier power. Since the channelized receiver uses a low-biased Mach-Zehnder modulator, there will be a high degree of carrier suppression. If the level of residual carrier is inadequate it may be necessary to employ a second fiber in the transmit-receive link to transport the carrier-bearing complimentary output of the modulator. Second, by using low-noise, Nd:YAG lasers we wish to verify our prediction that locked beat tone phase noise can be reduced to RF state-of-the-art levels.

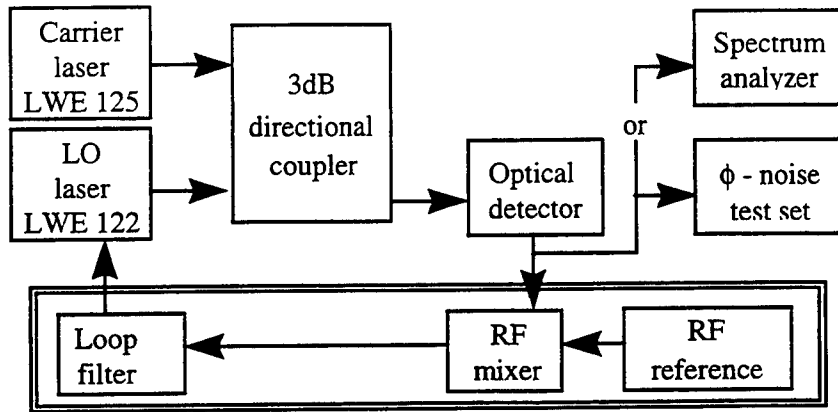


Figure 4-5. PLL testbed block diagram

4.4.2 Experimental Results

Our initial experiments were performed with a LOLA that was loaned to us by the manufacturer, Lightwave Electronics. Locking was obtained and spectrum analyzer traces were taken to characterize the noise. Typical signal levels used for the experiments were about 1mW for the LO laser and the carrier power was varied between 1μW and 1mW, both power levels being measured at the detector. In general the performance was within published specifications (-80dBc/Hz @ 10kHz offset). A peak in the noise spectrum occurred at ~2kHz offset. This differed from the expected 50 to 70kHz offset that was predicted from our modeling of the loop electronics. The reason for this difference is not well understood. There was significant structure (i.e. 10-20dB spurs) in the noise sidebands. It seems likely that this structure was mostly due to corresponding structure in the RIN spectrum of one of the two lasers (the Lightwave 122), as evidenced by direct measurement. Unfortunately the loaner LOLA unit failed in service, losing its ability to lock, just as a phase noise test set became available, so it was not possible to obtain phase noise spectra for this unit. We replaced the noisy laser with another LWE 125 that we had on hand. Also, by this time the LOLA unit that had been ordered for the program came in and was incorporated in the measurement setup. We measured phase noise performance using a Hewlett-Packard phase noise test set and the results are shown in figure 4-6. The high frequency phase noise is relatively low, as was expected with the narrow-linewidth Nd:YAG lasers. The strong peak at 10KHz offset is an artifact of yet another problem with the LOLA. We found that with the new unit loop stability was

marginal. We were able to obtain locking at only a few reference frequencies (the unit is specified to operate at any reference frequency up to 1GHz) and then it was a very difficult to obtain consistent performance. Subsequently we solved the marginal locking problem with our LOLA unit and obtained stable locking at all specified reference frequencies. Our latest results are shown in Figure 4-7. The solid dots in the figure are the typical high-performance synthesizer requirements from our receiver architecture study. These results demonstrate that this technique is capable of producing state-of-the-art electronic phase noise levels from our photonic system.

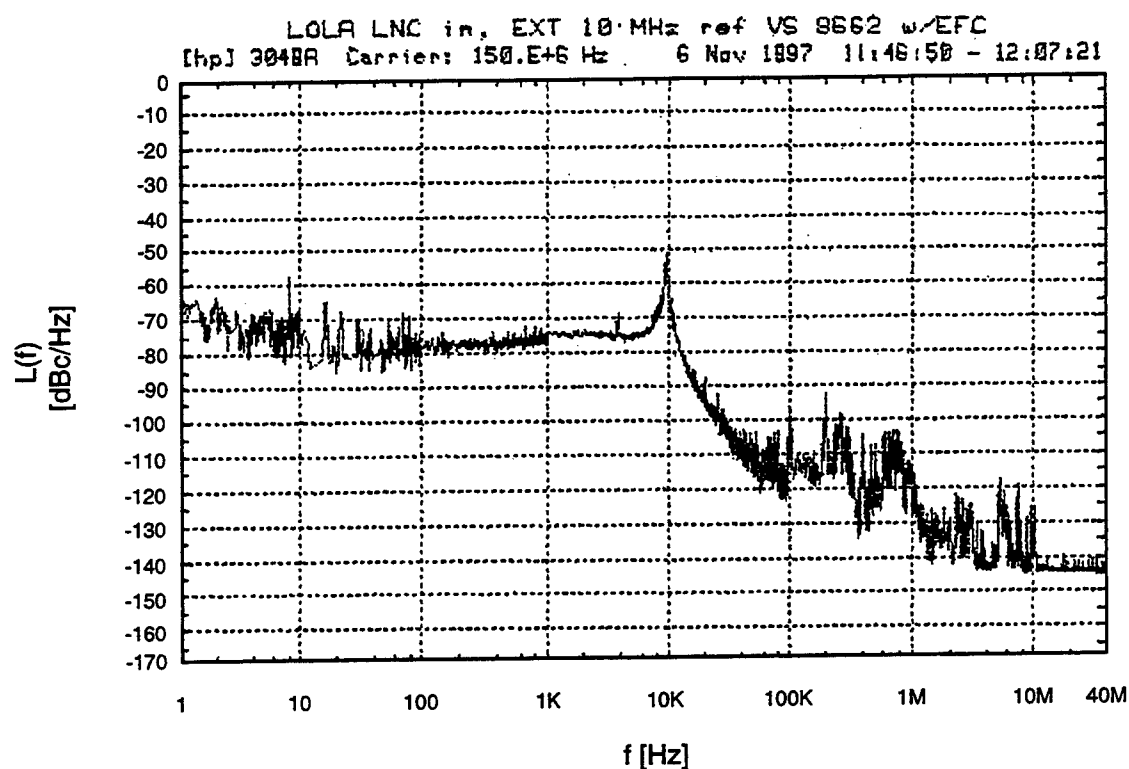


Figure 4-6. Preliminary phase noise measurement from PLL testbed

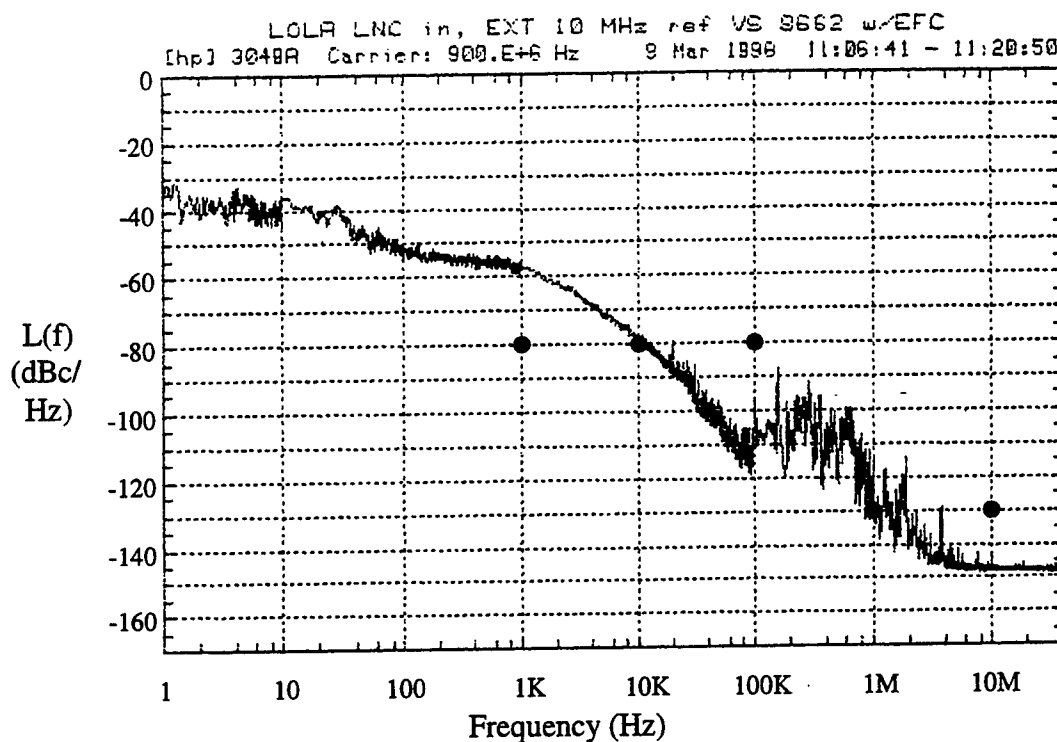


Figure 4-7. Phase noise measurement from PLL testbed

4.5 INJECTION LOCKING (CW LASERS) - THEORY

Optical injection locking of lasers is easily achieved by using the output of the master laser and injecting it into the slave laser as illustrated in Figure 4-8. The spectral properties of the slave laser can be forced to follow that of the master laser. Adequate isolation between the master and slave laser is needed to prevent mutual coupling. The injected electric field acts to force the electric field of the slave to follow that of the master as illustrated in the phasor diagram of Figure 4-8. Phase and frequency control at optical frequencies can be established by optical injection locking (OIL) without the use of high-speed electronics and phase-locked loops.

In this section we determine how phase (and amplitude) noise is transferred from the master laser to the slave laser in the process of optical injection locking. We are principally concerned with semiconductor lasers, so we will allow for phase-amplitude coupling in the model. We then present the results of our experimental investigation of injection locking.

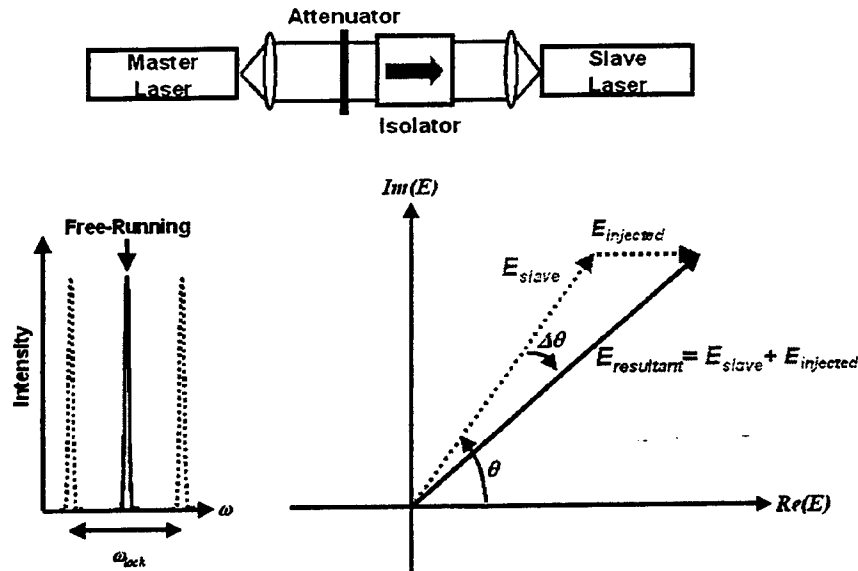


Figure 4-8. Optical injection locking phasor diagram

4.5.1 Summary

High performance coherent optical receivers require the establishment of a high degree of correlation between the phase noise of the signal laser and the phase noise of the LO laser, so that significant phase noise cancellation is obtained upon heterodyne detection. The conventional method of performing this function is to construct a phase lock loop where the beat note between the signal and LO lasers is phase locked to a low noise RF reference source. The PLL approach should enable demanding performance requirements to be met if low noise lasers are used (e.g. Nd:YAG monolithic nonplanar ring oscillator), but it appears unlikely that these requirements can be met by semiconductor DFBs in a PLL, due to stringent requirements on loop bandwidth and loop time delay.

Optical injection locking provides an alternative method for obtaining optical phase coherence that can be pushed to higher bandwidths more easily than a PLL. For example, it will be shown in the following work that, under the appropriate conditions, injection locking of semiconductor lasers gives phase coherence identical to that provided by a first order PLL with bandwidth Δf given by

$$\Delta f = \sqrt{\frac{P_i}{P_f}} \frac{v_g}{4\pi L} \ln \frac{1}{R} \quad (4.5-1)$$

where P_i is the injected power, P_f is the free-running power, L is the cavity length of the slave, v_g is the group velocity in the cavity, and R is the power reflectivity of the mirrors (symmetric cavity assumed). We see that semiconductor lasers offer the potential for large Δf due to the combination of short round trip time and low R . For example, if $v_g = c/3$, $L = 300 \mu\text{m}$, $R = 0.3$, and $P_i/P_f = 0.01$, we obtain $\Delta f = 3.2 \text{ GHz}$, which is a substantial bandwidth for a PLL.

In the remainder of this section, we will develop a simple model for injection locking that supports the above result and shows what assumptions have to be made along the way.

4.5.2 Semiconductor laser rate equations

Laser injection locking noise analysis can generally be performed by linearizing an appropriate set of coupled differential equations for the population inversion, cavity mode amplitude, and medium polarization. For the case of semiconductor lasers, we can reduce the complexity of the problem by assuming the driving polarization P of the gain medium is related to the cavity mode amplitude by

$$P = \epsilon \chi(n) E_n \quad (4.5-2)$$

where E_n is the amplitude of the relevant cavity mode, χ is a susceptibility which is assumed to be an instantaneous function of n , the number of e-h pairs, and ϵ is the background dielectric constant (assumed approximately uniform for simplicity). For this assumption to be valid, the frequency of the fluctuations of n and E_n must be much smaller than the reciprocal of the intraband thermalization time. Since this time is on the order of 1 ps in a semiconductor laser, and the fluctuation frequencies of interest are $\ll 1 \text{ THz}$, this assumption is valid for semiconductor lasers.

Accordingly, only two differential equations are required, one for the cavity mode amplitude and the other for the carrier population. It is convenient to take the semiclassical slowly varying envelope equations in Siegman [13] as a starting point, employ (4.5-2) to eliminate P , and renormalize E_n to simplify the results. The resulting equations are given by

$$\frac{dE}{dt} + \left[\frac{\gamma_c}{2} + j(\omega - \omega_c) \right] E = \frac{-j\omega \chi(n)}{2} E + \gamma_c E_i \quad (4.5-3)$$

$$\frac{dn}{dt} + R(n - N) + \omega \chi_i(n) \frac{|E|^2}{\gamma_e \hbar \omega} = 0 \quad (4.5-4)$$

Here γ_e is the output coupling rate, defined as the ratio of output power to stored energy for the cavity mode of interest. E is the cavity mode wave amplitude, renormalized such that $|E|^2$ is the output power of the laser. The injected power is $|E_i|^2$ (so E_i is also a wave amplitude), and we assume for simplicity that this external signal is injected into the output port of the laser. The total cavity energy loss rate is $\gamma_c = \gamma_o + \gamma_e$, where γ_o is the loss rate due to all other mechanisms besides output coupling, the cold cavity resonant frequency is ω_c , and ω is the assumed frequency of both E and E_i . The carrier recombination rate is R , the steady state carrier number in the absence of lasing is N , and subscript r or i on χ indicates real or imaginary part respectively. Note that n and N are carrier numbers, not (average) carrier concentrations.

To clarify the interpretation of (4.5-3) and (4.5-4), some simple special cases will be briefly considered. First we consider (4.5-3) in steady state, with $\chi = 0$ and $\omega = \omega_c$, which immediately gives $E = 2\gamma_e E_i / \gamma_c$. Let $P_i = |E_i|^2$ be the injected power, and let P_d be the power dissipated inside the cavity. Then we have

$$\begin{aligned} P_i - P_d &= |E_i|^2 - \gamma_o |E|^2 / \gamma_e \\ &= \left(\frac{\gamma_o - \gamma_e}{\gamma_o + \gamma_e} \right)^2 P_i \end{aligned} \quad (4.5-5)$$

where the first line in (4.5-5) follows from our definitions (cavity energy = $|E|^2 / \gamma_e$), and the second follows from the on-resonance steady state solution of (4.5-3). Since the difference $P_i - P_d$ must logically be the power reflected from the cavity, we see that this formalism gives the proper result for the on-resonance cavity power reflectivity (by power conservation), even though the reflected wave is not explicitly present in the formalism. This example indicates that the injected power $P_i = |E_i|^2$ is the power launched toward the cavity, as opposed to the power that gets into the cavity.

From the right side of (4.5-3), we see that $\omega \chi_i$ is the energy growth rate due to material gain (since γ_c on the left side is the cavity loss rate). From this, we see that the last term in (4.5-4) is the cavity energy times the energy growth rate divided by the transition

energy, which is the expected form for the stimulated emission rate. Also as expected, the stimulated emission term is always a negative contribution to dn/dt .

Since (4.5-3) and (4.5-4) are a system of coupled nonlinear differential equations, significant approximations will be required in order to obtain simple results. The first step is to assume that the time dependence of the injected field consists of small perturbations about a constant amplitude and phase. Therefore, we define

$$\begin{aligned} E &= (A_0 + \delta a) \exp j(\delta \phi) \\ E_i &= (A_i + \delta i) \exp j(\delta \phi_i - \phi_0) \\ n &= n_0 + \delta n \end{aligned} \quad (4.5-6)$$

where A_0 and n_0 are the steady state amplitude and carrier density in the presence of a constant injected signal of amplitude A_i , and δa , $\delta \phi$ and δn are the amplitude, phase and carrier density fluctuations caused by the injected amplitude and phase fluctuations δi and $\delta \phi_i$. The notation introduced in (4.5-6) is that all quantities with a δ in them are both small and time-varying, while the non- δ quantities are not time-varying and are not assumed to be small.

The DC phase of the cavity mode is taken to be the overall phase reference, so the DC phase offset between slave and master is accounted for by the constant ϕ_0 . We will see that the value of ϕ_0 has a critical effect on all injection locking properties in the course of this analysis. We have assumed in writing (4.5-6) that the injected signal is close enough in frequency to the free-running frequency of the slave laser that locking occurs. Later on, we will obtain an expression for the frequency detuning in the low-level injection limit, but it is important to realize that we have not yet assumed A_i is small.

We substitute (4.5-6) into (4.5-3) and (4.5-4), and linearize with respect to the small fluctuations to obtain:

$$\begin{pmatrix} s + \frac{A_i \gamma_e \cos \phi_0}{A_0} & A_i \gamma_e \sin \phi_0 & -A_0 \omega \xi_i / 2 \\ -A_i \gamma_e \sin \phi_0 / A_0 & A_0 s + A_i \gamma_e \cos \phi_0 & -A_0 \omega \alpha \xi_i / 2 \\ \frac{2(A_0 \gamma_c - 2A_i \gamma_e \cos \phi_0)}{\gamma_e \hbar \omega} & 0 & s + R + \frac{A_0^2 \xi_i}{\gamma_e \hbar} \end{pmatrix} \begin{pmatrix} \delta a \\ \delta \phi \\ \delta n \end{pmatrix} = \begin{pmatrix} \gamma_e \cos \phi_0 \\ -\gamma_e \sin \phi_0 \\ 0 \end{pmatrix} \delta i + \begin{pmatrix} A_i \gamma_e \sin \phi_0 \\ A_i \gamma_e \cos \phi_0 \\ 0 \end{pmatrix} \delta \phi_i \quad (4.5-7)$$

(4.5-7) has been Laplace transformed, so s is the complex frequency variable. We have also introduced the differential susceptibility $\xi = d\chi/dn$, evaluated at $n = n_0$, and the linewidth enhancement factor α , which is equal to $-\xi_r/\xi_i$. α as defined here is typically a positive quantity in semiconductor lasers, on the order of 1 to 10. The reason we end up with three equations is that (4.5-3) is complex, so its real and imaginary parts have been written as separate equations.

Most of the coefficients in (4.5-7) (e.g. α , ξ_i , A_0 , ϕ_0 or ω) depend on the operating point around which the linearization has been performed. The operating point equations corresponding to (4.5-7) are a system of nonlinear algebraic equations given by

$$\begin{aligned} A_0(2\omega_c - \omega\chi_r(n_0) - 2\omega) &= A_i\gamma_e \sin \phi_0 \\ A_0\omega\chi_i(n_0) + 2A_i\gamma_e \cos \phi_0 &= \gamma_c A_0 \\ \frac{A_0(A_0\gamma_c - 2A_i\gamma_e \cos \phi_0)}{\gamma_e \hbar \omega} + n_0 R &= RN \end{aligned} \quad (4.5-8)$$

(4.5-8) shows how the operating point of the laser (n_0 , A_0 and ϕ_0) depends on the inputs (A_i , ω , N), provided ω is close enough to ω_c for a solution to exist (i.e. ω is within the locking range).

4.5.3 Low level injection locking

In many practical cases, the injected power is only a small fraction of the laser output power. In this case, the equations from the preceding section (which are valid for arbitrary injection levels) can be significantly simplified. It is convenient to express later results in terms of the relaxation resonance parameters (frequency and damping rate) of the free-running laser, so the first step is to define these parameters. (4.5-7) for a free running laser (i.e. no injection) has poles in the s -plane at $s = 0$ and $s = -\gamma_r \pm j\omega_r$, where γ_r and ω_r (the relaxation damping rate and frequency respectively) are given by

$$\begin{aligned} \gamma_r &= \frac{\gamma_e \hbar R - A_f^2 \xi_i}{2\gamma_e \hbar} \\ \omega_r &= \frac{\sqrt{4A_f^2 \gamma_c \gamma_e \hbar \xi_i - (A_f^2 \xi_i + \gamma_e \hbar R)^2}}{2\gamma_e \hbar} = \sqrt{\frac{A_f^2 \gamma_c \xi_i}{\gamma_e \hbar} - \gamma_r^2} \end{aligned} \quad (4.5-9)$$

where A_f is the amplitude of the free-running slave laser and ξ_i is evaluated at n_f . In low level injection, we assume $A_i \ll A_f$, so that the steady state effect of injection is to perturb the free-running slave amplitude, frequency and carrier number as follows:

$$\begin{aligned} A_0 &= A_f + A_i \\ n_0 &= n_f + n_i \\ \omega &= \omega_f + \omega_i \end{aligned} \quad (4.5-10)$$

By substituting (4.5-10) into (4.5-8) we can obtain the following first order approximation to the perturbations A_i , ω_i , and n_i :

$$\begin{aligned} A_i &= \frac{A_i \gamma_e (\gamma_e \hbar R + A_f^2 \chi_i) (2\omega_c \cos \phi_0 - \gamma_c \sin \phi_0)}{A_f^2 \gamma_c \chi_i (\alpha \gamma_c + 2\omega_c)} \approx \frac{2A_i \gamma_e \gamma_r \cos \phi_0}{\gamma_r^2 + \omega_r^2} \\ n_i &= \frac{2A_i \gamma_e (\gamma_c \sin \phi_0 - 2\omega_c \cos \phi_0)}{A_f \omega_f \chi_i (\alpha \gamma_c + 2\omega_c)} \approx \frac{-2A_f A_i \gamma_e \cos \phi_0}{\hbar \omega_f (\gamma_r^2 + \omega_r^2)} \\ \omega_i &= \frac{-2A_i \gamma_e \omega_f (\alpha \cos \phi_0 + \sin \phi_0)}{A_f (\alpha \gamma_c + 2\omega_c)} \approx \frac{-A_i \gamma_e (\alpha \cos \phi_0 + \sin \phi_0)}{A_f} \end{aligned} \quad (4.5-11)$$

where the simplified forms on the far right of the equations follow from (4.5-9), and the relations $\omega_c \approx \omega_f \approx \omega_i$ (to zeroth order) and $\gamma_c \ll \omega_c$. The quantities ξ_i and α are evaluated at n_f .

The interpretation of (4.5-11) is particularly simple if $\phi_0 = 0$. In this case, we see that the output is increased and the carrier density is decreased, exactly as one would expect from a simple physical picture of the injected signal "helping" the slave laser. Since the carrier density has decreased due to injection, the refractive index seen by the lasing mode has increased (less free carrier screening). In order for this mode to still satisfy the cavity resonance condition, its frequency must be slightly less than the free-running frequency (increased index \Rightarrow increased optical length \Rightarrow increased resonant wavelength \Rightarrow decreased resonant frequency). Consistent with this physical argument, the last equation in (4.5-11) predicts a negative frequency shift when injection locking with $\phi_0 = 0$, and this shift is proportional to α , as expected. (4.5-11). is basically consistent with standard semiconductor laser injection locking theory [14].

As ϕ_0 varies throughout the range 0 to 2π , we see from (4.5-11) that the frequency shift ω_i varies from $-\sqrt{1+\alpha^2} A_i \gamma_e / A_f$ to $\sqrt{1+\alpha^2} A_i \gamma_e / A_f$ so we conclude that the difference

between the injected frequency and the free-running frequency of the slave must be within this range for injection locking to occur. Since γ_e is typically small compared to an optical frequency, we have the basic result that injection locking can only occur if the fractional detuning of the master from the slave is very small. The injection locking range is further reduced in practice, since (4.5-7) is not stable for all ϕ_0 in the range $[0, 2\pi]$.

Taking $A_0 \approx A_f$ and $A_i \ll A_f$ in (4.5-7), the poles of the system matrix are given by

$$\begin{aligned} p_1 &= \frac{A_i \gamma_e}{A_f} (\alpha \sin \phi_0 - \cos \phi_0) \\ p_2 &= -\gamma_r - \frac{A_i \gamma_e}{2A_f} (\cos \phi_0 + \alpha \sin \phi_0) - j \left(\omega_r + \frac{A_i \gamma_e \gamma_r}{2A_f \omega_r} (5 \cos \phi_0 + \alpha \sin \phi_0) \right) \\ p_3 &= p_2^* \end{aligned} \quad (4.5-12)$$

to first order in small quantities, where we have assumed $\gamma_r \ll \gamma_e$ and $\omega_r^2 \ll \gamma_e \gamma_r$ to simplify the results. The second approximation is used only to simplify the imaginary parts of p_2 and p_3 , so if it is not valid for a particular device, the stability analysis (which only depends on the real parts of the poles) will not be affected. By applying the usual stability condition (all poles located in left half of the s plane) to (4.5-12), we obtain the following conditions for stable injection locking:

$$\begin{aligned} \cos \phi_0 - \alpha \sin \phi_0 &> 0 \\ \cos \phi_0 + \alpha \sin \phi_0 &> \frac{-2A_f \gamma_r}{A_i \gamma_e} \end{aligned} \quad (4.5-13)$$

In early work on injection locking of Fabry-Perot (FP) semiconductor lasers, e.g. [15], an additional stability requirement is obtained. This requirement is that the carrier density (i.e. gain) must not increase due to the injected signal. That is, $n_2 < 0$ in (4.5-11), which leads to the condition $\cos(\phi_0) > 0$. The reason for this additional requirement is that a positive n_2 is likely to bring a side mode above threshold and cause mode hopping or other undesirable behavior, since the side mode suppression in a FP laser is so weak. We are more concerned with DFB lasers, in which the side mode suppression is assumed to be large enough that we can operate stably with positive n_2 . Accordingly, we do not require $\cos(\phi_0) > 0$ for stability in our analysis.

For low level injection, the second inequality in (4.5-13) is always satisfied, so the low level injection locking range can be obtained from the first inequality alone as follows:

$$\tan^{-1}(1/\alpha) - \pi < \phi_0 < \tan^{-1}(1/\alpha) \quad (4.5-14)$$

From (4.5-11), we see that the endpoints of the frequency tuning range correspond to the limits of the phase range in (4.5-14), as one would expect, and so a symmetric tuning range of $2\Delta\omega\sqrt{\alpha^2 + 1}$ about $\delta\omega = 0$ is obtained, where

$$\Delta\omega = \frac{A_i \gamma_e}{A_f} \quad (4.5-15)$$

In (4.5-15), we have defined $\Delta\omega$, which is a useful measure of the injection locking level and/or bandwidth, and we will use this definition to simplify later results.

For higher levels of injection, both inequalities in (4.5-13) must be considered to obtain the stable locking range. To see the effects of (4.5-13), some plots will be useful

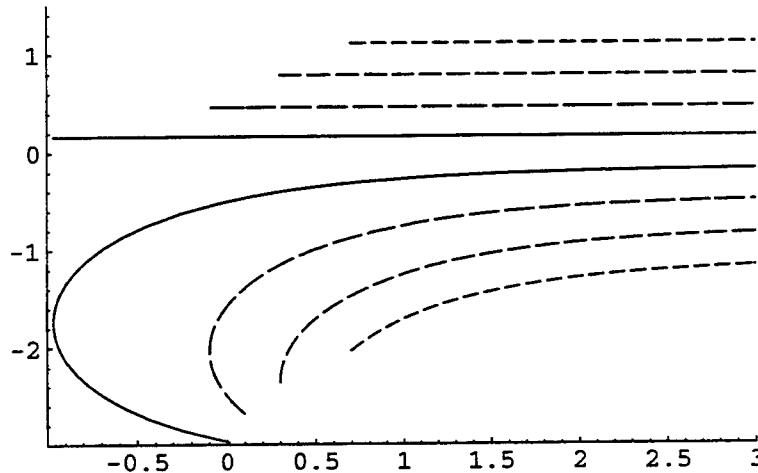


Figure 4-9. Stable regions in the phase/injection plane. Injection level ρ is on the horizontal axis, and the relative phase ϕ_0 is on the vertical axis. The various curves correspond to $\alpha = 0.5, 1, 2$, and 6 , where as α increases, the curves generally move to the left and closer to $\phi_0 = 0$. For each α there are two lines which give the stability region (patterns correspond on plot), and a point is stable if it is below the upper line and to the left of the lower line. Points below the lowest point of the lower curve are not stable.

In Figure 4-9, we show the stability conditions on the phase versus the normalized injection level ρ which is defined to be

$$\rho \equiv \log_{10} \left(\frac{\Delta\omega}{2\gamma_r} \right)^2 \quad (4.5-16)$$

Thus ρ is the ratio of the injection "rate" to the relaxation damping rate, which we would expect to be the relevant parameter for the excitation of relaxation oscillations by optical injection, which is the physical mechanism underlying the second inequality in (4.5-13). As an example of how to interpret Figure 4-9, consider the case $\alpha = 6$ (solid line). For arbitrarily low levels of injection, the whole range given by (4.5-14) is stable. For $-1 < \rho < 0$ (roughly), the region of stability is divided into two parts, one near $\phi_0 = 0$, and the other near $\phi_0 = -\pi$. For $\rho > 0$, the stable region near $\phi_0 = -\pi$ has disappeared, and the only stable region is the one near $\phi_0 = 0$, which is significantly narrower than the nominal range given by (4.5-14).

Another way of looking at the same information, which is more widely used in the literature, is to give the frequency detuning on the vertical axis, instead of the relative phase as shown in Figure 4-10.

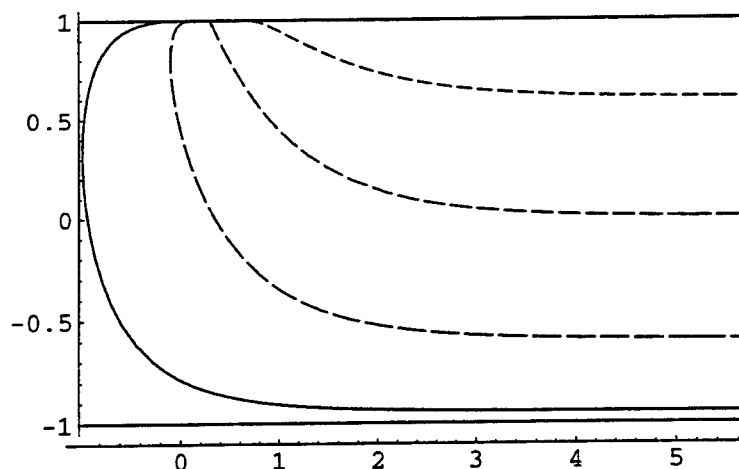


Figure 4-10. Stable regions in the detuning/injection plane. Injection level is on the horizontal axis, and the normalized detuning is on the vertical axis. Regions below (or to the left of) the lines and between $y = 1$ and $y = -1$ are stable. The various curves correspond to $\alpha = 0.5, 1, 2$, and 6 , where as α increases, the curves move down and to the left.

Here we have plotted stability curves in the detuning/injection level plane, where the vertical axis is normalized detuning $= \delta\omega / \Delta\omega\sqrt{\alpha^2 + 1}$, and the horizontal axis is ρ , as before. We see that for low level injection, the tuning range is symmetric about $\delta\omega = 0$, but as the injection level increases, a nonzero α causes a significant preference for negative detuning. From figures 4-6 and 4-7 we obtain two important conclusions: the

operating point $\phi_0 = 0$ is always within the stable locking region, while the $\delta\omega = 0$ operating point may or may not be stable. Accordingly, we will simplify the following discussion by assuming operation at or near the $\phi_0 = 0$ operating point.

4.5.4 Transfer functions for $\phi_0 = 0$ injection locking

Since the laser rate equations have been linearized, we can obtain transfer functions relating inputs to outputs. The inputs we are interested in are the master phase and amplitude, and the outputs are the slave phase and amplitude. We assume, for simplicity, that the noise present in the current source driving the slave is negligible. We also assume, based on the preceding stability analysis, that we are operating at the $\phi_0 = 0$ operating point, which is guaranteed to be stable. At this operating point, it turns out to be possible to give relatively simple results that are valid for an arbitrary injection level, so we will do so.

For arbitrary injection level and $\phi_0 = 0$, the poles of (4.5-7) are given by $-A_i\gamma_e/A_0$ and $-\Gamma_r \pm j\Omega_r$, where

$$\Gamma_r = \frac{2A_i\hbar\gamma_e + 2A_0\hbar R + \epsilon_0 A_0^3 \xi_i}{4A_0\hbar}$$

$$\Omega_r = \frac{\sqrt{8A_0\hbar\tau(2A_i\hbar\gamma_e R\tau + \epsilon_0 A_0^3 \xi_i - \epsilon_0 A_0^2 A_i\gamma_e \tau \xi_i) - \tau^2(2A_i\hbar\gamma_e + 2A_0\hbar R + \epsilon_0 A_0^3 \xi_i)^2}}{4A_0\hbar\tau} \quad (4.5-17)$$

Here Γ_r and Ω_r are the relaxation oscillation damping rate and frequency in the presence of an injected signal. We can obtain transfer functions directly from (4.5-7), and we express our results in terms of Γ_r and Ω_r to simplify the expressions. We have

$$H_{\phi\phi} = \frac{A_i\gamma_e}{A_0s + A_i\gamma_e}$$

$$H_{\phi a} = \frac{-\alpha_0\gamma_e(A_0^2\Gamma_r^2 - 2A_0A_i\Gamma_r\gamma_e + A_i^2\gamma_e^2 + A_0^2\Omega_r^2)}{A_0^2(A_0s + A_i\gamma_e)(s^2 + 2\Gamma_r s + \Gamma_r^2 + \Omega_r^2)} \quad (4.5-18)$$

$$H_{a\phi} = \frac{A_i\gamma_e s(A_0s + 2A_0\Gamma_r - A_i\gamma_e)}{(A_0s + A_i\gamma_e)(s^2 + 2\Gamma_r s + \Gamma_r^2 + \Omega_r^2)} \phi_0 \quad \phi_0 \ll 1$$

$$H_{aa} = \frac{\gamma_e(A_0s + 2A_0\Gamma_r - A_i\gamma_e)}{A_0(s^2 + 2\Gamma_r s + \Gamma_r^2 + \Omega_r^2)}$$

The first subscript on a transfer function is the output, and the second is the input. For example, $H_{\phi a}$ is the master amplitude to slave phase transfer function, and $H_{a\phi}$ is the

master phase to slave amplitude transfer function. Since $H_{a\phi}$ is zero at $\phi_0 = 0$, we give an expression valid for small ϕ_0 for completeness.

There are a number of interesting results in (4.5-18). The first is that the master to slave phase transfer function, $H_{\phi\phi}$, is first order, which means that a first order PLL (or Adler equation) model with appropriate parameters is applicable for arbitrarily high levels of injection, provided $\phi_0 = 0$. Some care is needed with the model parameters for high level injection. In particular, $A_0 \approx A_f$ cannot be assumed, and we also have $A_i/A_0 < 1$, which establishes an absolute upper limit on effective loop bandwidth for a given γ_e .

4.5.5 Noise

In this section, we will make the basic connections between the transfer functions derived in the previous sections and laser noise theory. Our goal is to obtain expressions for the phase PSD of the slave laser, and the master-slave phase cross spectral density, since these are the quantities we need to know in order to obtain the RF phase noise spectrum of the beat note.

Following ref [16], we now add a noise term

$$(\Delta_r + j\Delta_i) \exp j(\omega_i t + \phi_0) \quad (4.5-19)$$

to the right side of (4.5-3), where Δ_r and Δ_i are the real and imaginary parts of the complex, slowly varying, noise amplitude Δ . For simplicity, we will continue to assume $\phi_0 = 0$. Since Δ is assumed to be small, it simply acts as a source on the RHS of the linearized system (4.5-7), and so we can obtain transfer functions as we did before. We obtain

$$\begin{aligned} |G_{\phi r}(\omega)|^2 &= \frac{1}{4\omega_i^2(A_i^2\gamma_e^2 + A_0^2\omega^2)} \\ |G_{\phi i}(\omega)|^2 &= \frac{1}{4\omega_i^2(A_i^2\gamma_e^2 + A_0^2\omega^2)} \frac{\alpha^2(A_0^2\Gamma_r^2 - 2A_0A_i\Gamma_r\gamma_e + A_i^2\gamma_e^2 + A_0^2\Omega_r^2)^2}{A_0^4(\omega^2 - 2\omega\Omega_r + \Omega_r^2 + \Gamma_r^2)(\omega^2 + 2\omega\Omega_r + \Omega_r^2 + \Gamma_r^2)} \end{aligned} \quad (4.5-20)$$

where $G_{\phi r}$ is the ratio of $\delta\phi$ to Δ_r and $G_{\phi i}$ is the ratio of $\delta\phi$ to Δ_i . Only the square magnitude of these transfer functions is given, since the inputs Δ_r and Δ_i are random processes. Let $W_r(f)$ and $W_i(f)$ be the PSD of Δ_r and Δ_i respectively. Since Δ is the complex envelope of the real spontaneous emission noise process, we necessarily have $W_r(f) = W_i(f)$.

We can make a connection with standard laser noise theory by setting $A_i = 0$ in (4.5-20) and taking the low frequency limit. In this limit, we have

$$W_f(f) = f^2 W_\phi \approx \frac{W_r(1 + \alpha^2)}{16\pi^2 A_0^2 \omega_i^2} \quad (4.5-21)$$

for the frequency noise spectrum $W_f(f)$ of the laser. By making the usual assumption that W_r is white, we see that the laser frequency noise W_f is also white, which implies a Lorentzian lineshape, as seen earlier, and that the FWHM linewidth ($= \pi W_f$) is increased by a factor of $1 + \alpha^2$ for nonzero α .

Assuming that the injected field does not significantly change the spontaneous emission rate into the lasing mode (i.e. that injection does not significantly change the carrier density), the (two-sided) phase noise PSD for the slave laser is given by

$$S_{s\phi}(f) = |G_{\phi\phi}(f)|^2 S_{m\phi}(f) + \left(|G_{\phi r}(f)|^2 + |G_{r\phi}(f)|^2 \right) S_r \quad (4.5-22)$$

where all the transfer functions G_{xx} have been given above, $S_{m\phi}$ is the phase noise PSD of the master, and $S_r = W_r/2$ is the spontaneous emission PSD. The two terms in (4.5-22) account for the slave phase noise due to input phase noise from the master, as well as noise due to the slave's own spontaneous emission. We use two sided PSDs (S instead of W) because we need to deal with a cross spectral density. The injection locking process establishes a correlation between the master and slave phase noise given by

$$S_{ms}(f) = G_{\phi\phi}^*(f) S_{m\phi}(f) \quad (4.5-23)$$

In (4.5-22) and (4.5-23) we have neglected phase-amplitude coupling terms between the two lasers for simplicity. Upon heterodyne detection, the photocurrent phase is the difference between the phases of the master and slave lasers, and we assume there is no relative time delay as the master and slave laser beams propagate to the detector. If a time delay is present, it can be treated the same way the external time delay was treated in the PLL analysis. Using (4.5-22) and (4.5-23), we obtain

$$W_y(f) = |1 - G_{\phi\phi}(f)|^2 W_{m\phi}(f) + \left(|G_{\phi r}(f)|^2 + |G_{r\phi}(f)|^2 \right) W_r \quad (4.5-24)$$

where $W_y(f)$ is the (one sided) phase noise PSD of the photocurrent (neglecting all other noise sources). We can obtain a simpler result by assuming ω and A_i are both small enough that $|G_{\phi i}|^2 \approx \alpha^2 |G_{\phi r}|^2$. In this case, we obtain

$$W_y(f) \approx |1 - G_{\phi\phi}(f)|^2 (W_{m\phi}(f) + W_{s\phi}(f)) \quad (4.5-25)$$

where $W_{s\phi}(f)$ is the free-running slave laser phase PSD. Thus the photocurrent phase noise PSD is simply the combined phase noise PSD of both lasers, passed through the high pass filter $1 - G_{\phi\phi}$.

This is the basic result that supports our view that injection locking basically acts like a (high bandwidth) first order PLL to reduce the phase noise of the heterodyne beat note of the master and slave lasers.

4.6 INJECTION LOCKING (CW LASERS) - EXPERIMENT

4.6.1 Injection locking testbed

The setup shown in Figure 4-11 was used to measure the locking range and noise performance of injection locked semiconductor lasers. The output of the master laser is split using a 3dB coupler. One arm is attenuated and then injected into the slave laser via the optical circulator. Fiber to slave laser coupling is measured to be 60%. The other arm is frequency shifted 55 MHz using a fiber pigtailed acousto-optic frequency shifter and recombined with the slave laser output for heterodyne detection.

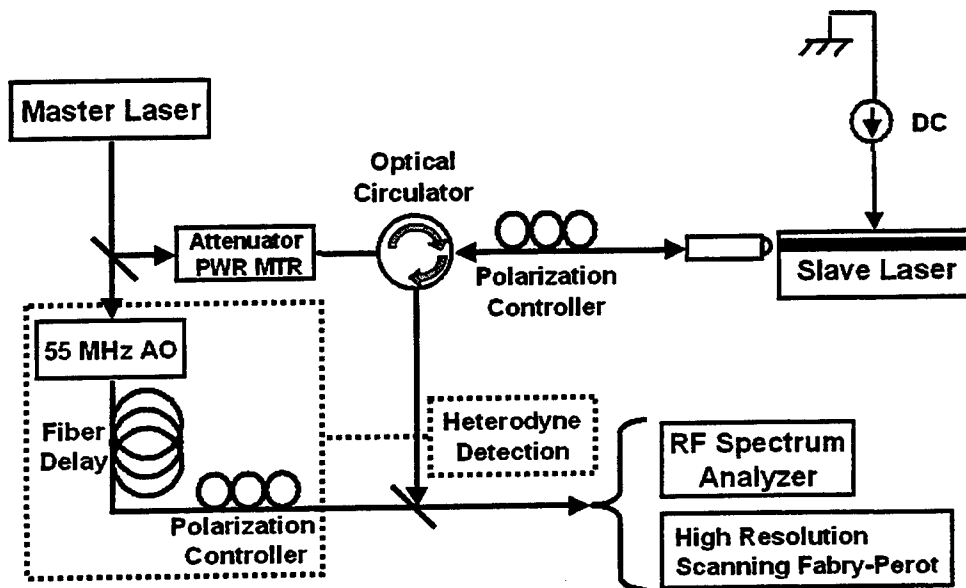


Figure 4-11. Experimental setup for optical injection locking of CW lasers

When the two lasers are injection locked a strong tone at 55 MHz is observed using a photodetector and RF spectrum analyzer. Due to the residual reflectivity on the facet of

the slave laser, a 55 MHz tone is still present even when the two lasers are not injection locked. However, the power in this unlocked tone will be decreased by approximately 10dB. Injection locking is also verified with a high resolution scanning Fabry-Perot with a resolution of 40 MHz.

The master laser was a commercial, external cavity laser (ECL), tunable from 1530 nm to 1570 nm with a side mode suppression ratio greater than 40 dB. Coarse tuning of wavelength is achieved by manually rotating the external grating, while fine tuning was achieved by varying the voltage of the piezo actuator. The slave laser is an unpackaged monolithic distributed feedback laser (DFB) with a cavity length of 150 μm . To ensure high side-mode suppression, the DFB laser was anti-reflection coated on both sides to less than 5% to achieve a side mode suppression greater than 40 dB at current levels as high as three times threshold. This is shown in Figure 4-12.

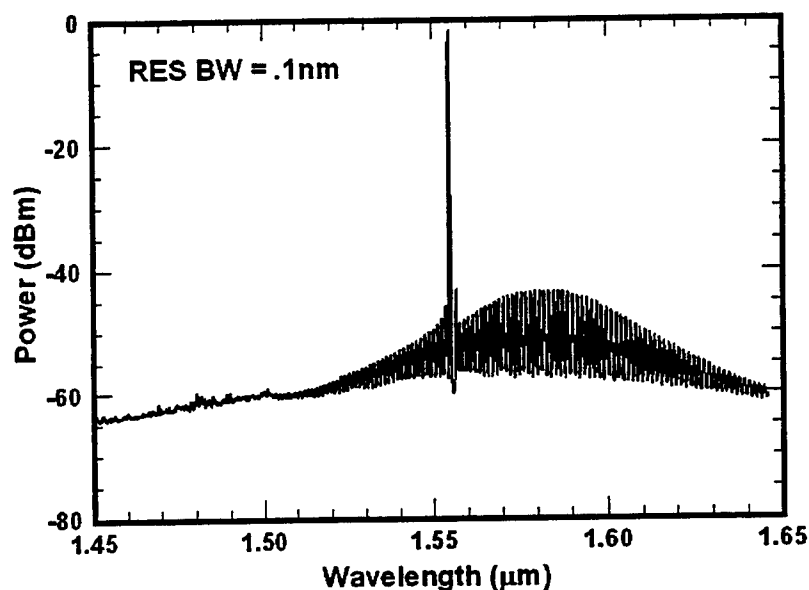


Figure 4-12. Optical spectrum of DFB slave laser

4.6.2 Injection locking characteristics

The linewidths of the external cavity laser and the free-running DFB laser are 20kHz and 1.2 MHz respectively. Measurement of linewidth is made using a time delay much less than the coherence time of the lasers. A 52 m length of standard single mode fiber (SMF-

28) is used to produce a time delay of 250 nsec. The detected tone seen in a self heterodyne system of arbitrary time delay, τ_d , is given by [17]:

$$S_R(\omega) = 2I_1 I_2 e^{-\tau_d/\tau_c} \delta(\omega - \omega_m) + \frac{(2I_1 I_2 \tau_c)/\pi}{1 + (\omega - \omega_m)^2 \tau_c^2} \left[1 - e^{-\tau_d/\tau_c} \left(\cos((\omega - \omega_m) \cdot \tau_d) + \frac{\sin((\omega - \omega_m) \cdot \tau_d)}{(\omega - \omega_m) \cdot \tau_c} \right) \right] \quad (4.6-1)$$

where the linewidth is related to the coherence time by $\Delta\nu = \frac{1}{2\pi\tau_c}$, ω_m is the angular

modulation frequency used for the frequency shift, and I_1 and I_2 are the intensities in each arm respectively. Figures 4-13 and 4-14 show the measured heterodyne tone and the curve fit; the delta function is removed for curve fitting purposes.

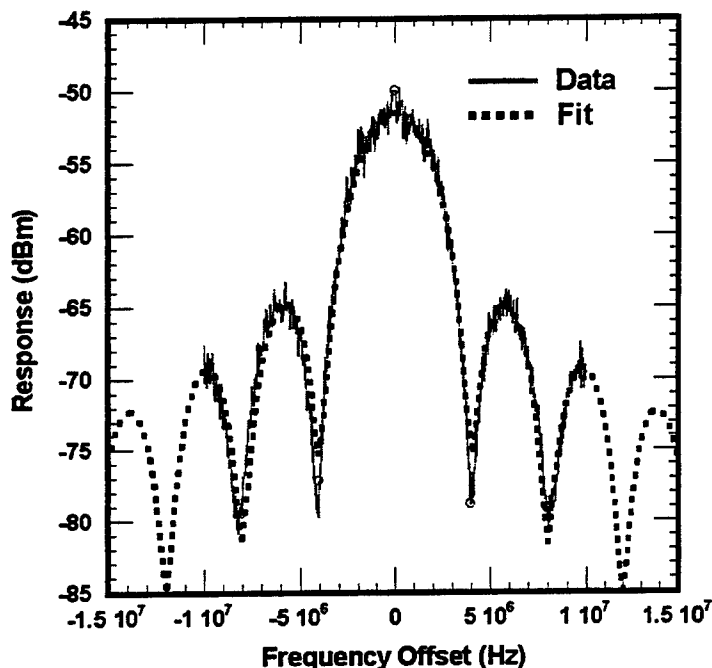


Figure 4-13. Linewidth of SDL external cavity laser measured with 250 nsec delay

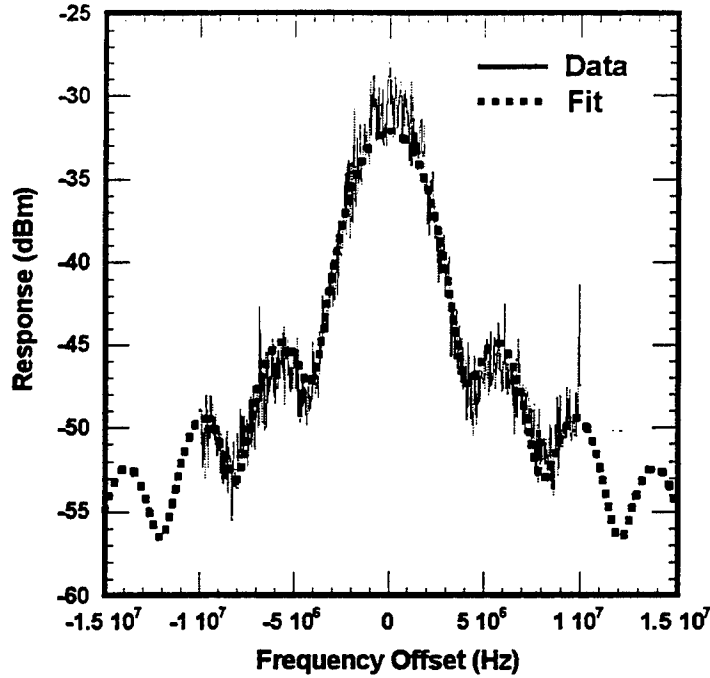


Figure 4-14. Linewidth of free-running DFB laser measured with 250 nsec delay

It is important to note that the delta function is only present when the two arms are coherent. If two free running lasers are mixed on a photodiode, the generated RF spectrum will simply be a Lorentzian with twice the linewidth of the lasers, no delta function is seen indicating that the two lasers are not coherent. The ripples due to the cosine and sine terms represent a decorrelation due to time delay. In the limit when the delay is large ($\tau_d \gg \tau_c$), the ripples in the RF spectrum will be minimized and the width of the heterodyne tone will be approximately given by twice the Lorentzian linewidth of the laser with the addition of the delta function at ω_m :

$$S_R(\omega) = 2I_1 I_2 e^{-\tau_d/\tau_c} \delta(\omega - \omega_m) + \frac{(2I_1 I_2 \tau_c)/\pi}{1 + (\omega - \omega_m)^2 \tau_c^2} \quad \text{for } \tau_d \gg \tau_c \quad (4.6-2)$$

When the injected signal is outside the locking range, two signals are observed on the optical spectrum analyzer: the free running slave laser and the injected light due to the residual reflection of the slave laser facet. On an RF spectrum analyzer, the 55 MHz heterodyne tone is still present due to the residual reflection. In addition, a beat tone is observed at the offset frequencies of the two lasers. When injection locked, the slave laser is pulled significantly from the free running frequency to the frequency of the

master laser and the heterodyne tone shows a significant increase in power in the detected tone at 55 MHz, typically greater than 10 dB. Linewidth narrowing is also observed when the slave laser is injection locked to the master laser. The linewidth of the slave is reduced from 1.2 MHz to 50 kHz; measurement is achieved using the delayed self heterodyne technique with 20 meters of fiber delay corresponding to a time delay of 100 nsec. (Figure 4-15)

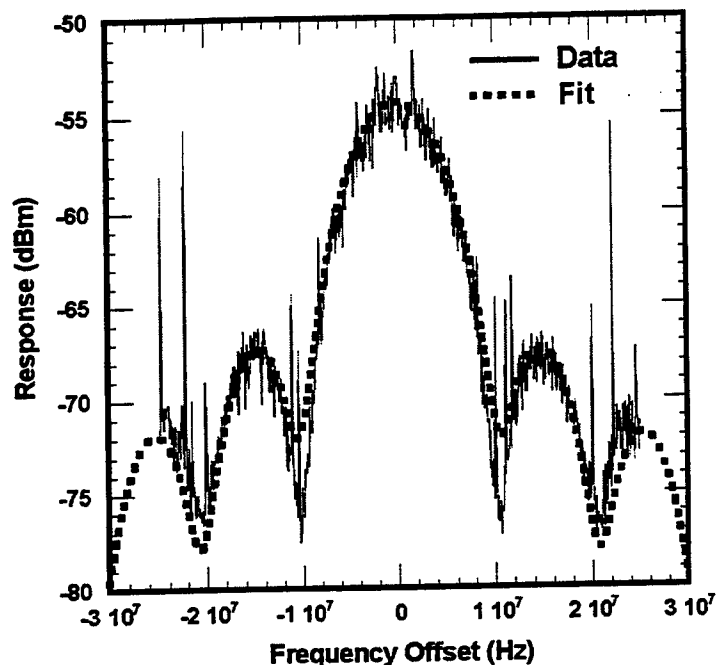


Figure 4-15. Linewidth of injection locked DFB slave laser measured with 100 nsec delay

Since the setup is completely fiber coupled, there is no complication with matching beam sizes for each individual laser as in a free space system. Thus, the optical injection parameter of choice is the ratio of the injected power to the slave output power. Injected optical power is monitored using a fiber coupled inline power meter. For our purpose of measuring phase noise of the injection locked semiconductor laser, we only need to measure the total useful locking range. For coherent optical systems, operation in the center of the locking range is desired. Figure 4-16 is the total stable locking range versus the injection ratio for various bias currents. Measurement is made with the master laser centered at the free-running frequency of the slave laser, then the master laser is tuned to lower frequencies until slave laser is unlocked. Next the master laser is returned

to the free-running frequency of the slave laser and tuned to higher frequencies until locking is lost. The locking range is determined using this methodology since the locking bandwidth is known to have hysteresis [18]. Tuning in from an unlocked frequency and into the locking range will produce a smaller locking bandwidth due to the bistable region. Locking bandwidth is also slightly skewed to the lower frequencies and is smaller for positive frequency detuning.

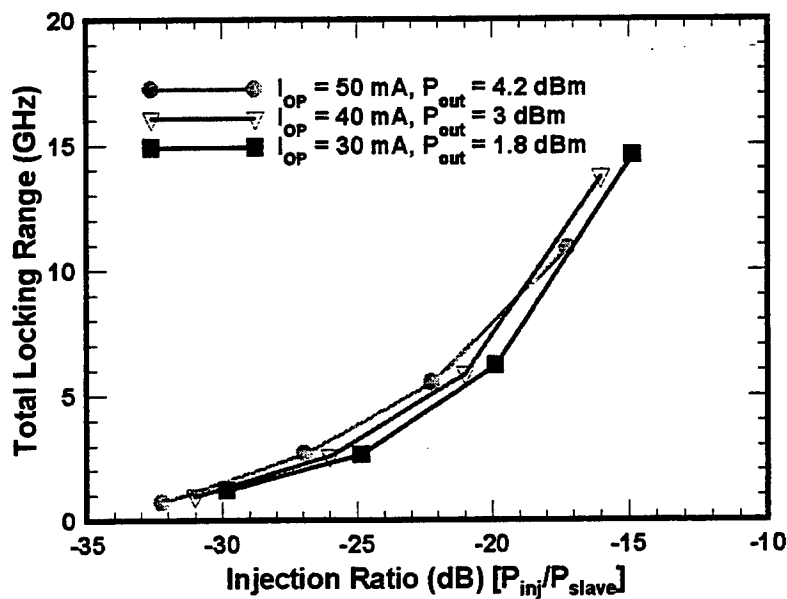


Figure 4-16. Total locking range at various bias currents

4.6.3 RF performance of injection locked lasers

Injection locking is proposed to establish phase coherence between the signal carrier and the local oscillator. Phase noise measurement is made on the 55 MHz tone to determine how well the two lasers can be locked to each other. Phase noise performance is independent of the frequency of the heterodyne tone, therefore tones generated by offset injection locked lasers are expected to have the same phase noise performance. A delay line is introduced in the heterodyne measurement to compensate for decorrelation effects due to the path length difference of the heterodyne arms that lead to higher phase noise [19]. Figure 4-17 shows the injection locked heterodyne tone with a path length difference greater than 20 meters of single mode fiber. In a heterodyne detection scheme the spectrum of the tone is given by (4.6-2). By balancing the path length, the delay

between the arms is set to zero which will minimize the ripples and maximize the delta function at 55 MHz.

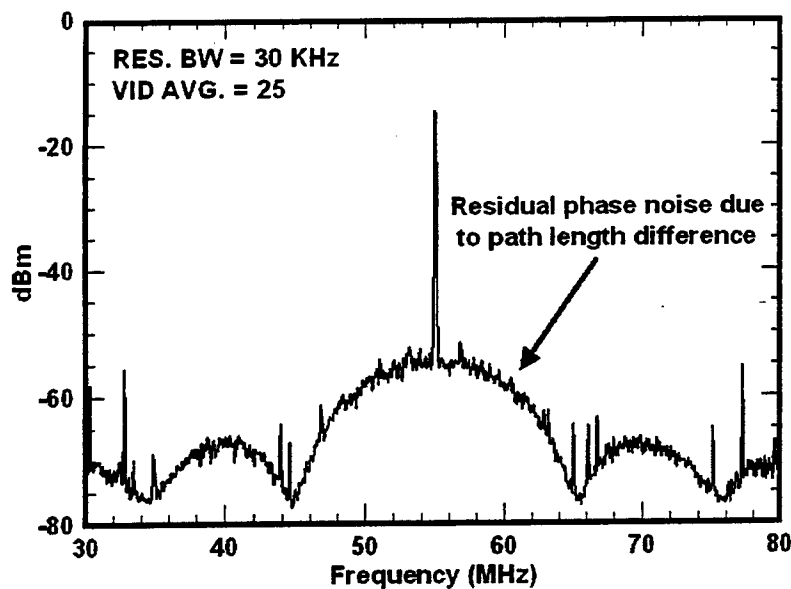


Figure 4-17. Heterodyne tone of injection locked semiconductor laser

The tone generated by the heterodyne of the optical beams will have noise side-bands which consist of both intensity noise and phase noise. To decouple these two noise sources from the detected tone, a HP 3048 phase noise measurement system is used. Currently there are two techniques to decouple amplitude noise and phase noise [20]: (1) Use a RF delay line with a very high intrinsic loss. (2) Phase shift one arm such that the two signals combine in quadrature, such that amplitude noise will cancel out. The HP 3048 uses the second method.

Recall that the injection locking process approximates a first order phase locked loop. The noise performance can be estimated from this and measured versus injection ratio and detuning frequency. Figure 4-18 shows the phase noise of the 55 MHz injection locked tone, the injection ratio was -15 dB. By tuning the master laser within the locking range, no significant change in the phase noise is observed. When the slave laser falls out of the locking range the noise in the tone increases significantly and no measurement of phase noise can be achieved due to the limited locking bandwidth of the HP 3048 test system. The phase noise floor is measured at offsets larger than 10 kHz for various injection ratios. At offsets less than 10 kHz, a sudden increase in phase noise is seen

which is attributed to acoustics in the fiber system. Similar noise is seen in other fiber systems and fiber lasers [21]. The phase noise is shown to decrease linearly with increased injection levels (Figure 4-19); this agrees well with the theory that injection locking is a first order phase locked loop.

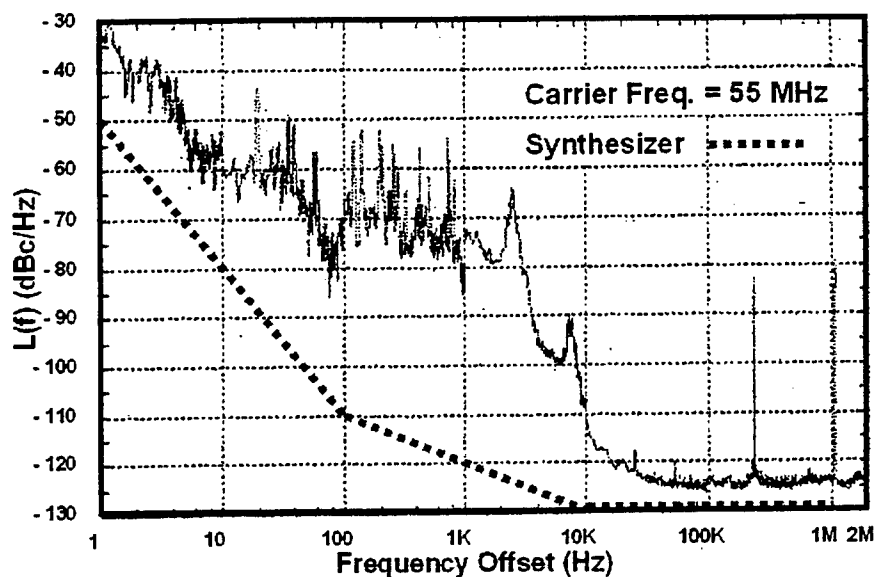


Figure 4-18. Injection locked phase noise, -15 dB injection ratio

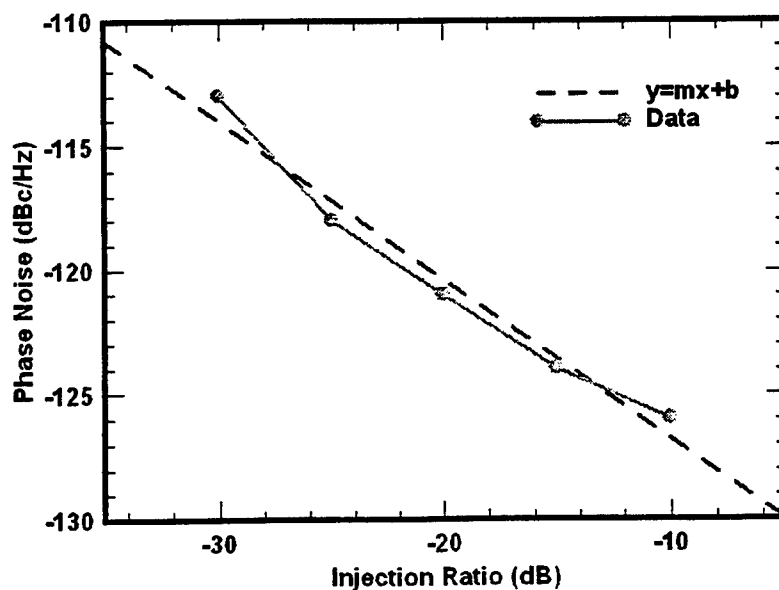


Figure 4-19. Phase noise at various injection levels

As shown in Figure 4-18, the phase noise of an injection locked semiconductor laser is quite comparable to the phase noise a commercial RF synthesizer. The phase noise performance is as good as any electronic phase locked loop to date [22]. The frequency shifter is driven with an HP 8662A, which has the lowest phase noise for any commercially available synthesizer. The phase locking characteristics make injection locking a viable alternative to electronic phase locked loops for synchronizing relatively low coherence lasers. With adequate injected optical power from generated sidebands, injection locking can generate low phase noise tones at frequencies above 50 GHz [23].

4.6.4 RF modulation of injection locked semiconductor lasers

Further research work on CW injection locking of semiconductor lasers revealed the benefits of increased modulation bandwidth and decreased modulation distortion of the slave laser at strong injection levels [24,25]. The setup shown in Figure 4-11 was used to measure the modulation bandwidth of the slave laser, a network analyzer was employed to measure the frequency response. The free-running slave laser had a relaxation peak near 4 GHz and modulation response dropped off quickly beyond 5 GHz, under injection locking the relaxation peak shifted out to 13 GHz and a flatter frequency response was obtained. Figure 4-20 shows the increase in modulation bandwidth of the slave laser under strong optical injection locking, the injection ratio is -8dB .

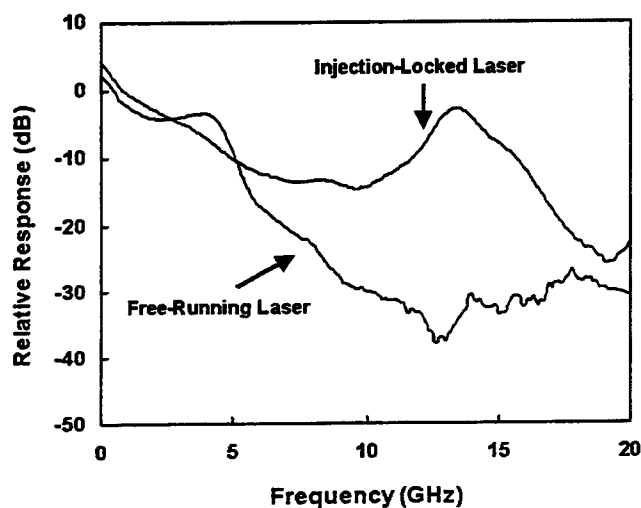


Figure 4-20. Increased modulation bandwidth of slave laser under injection locking

Using the same setup, the slave laser was directly modulated at various frequencies while free-running and injection locked. Figure 4-21 shows the decrease in the second harmonic at various modulation frequencies. These benefits offer an alternative to externally modulated RF photonic links.

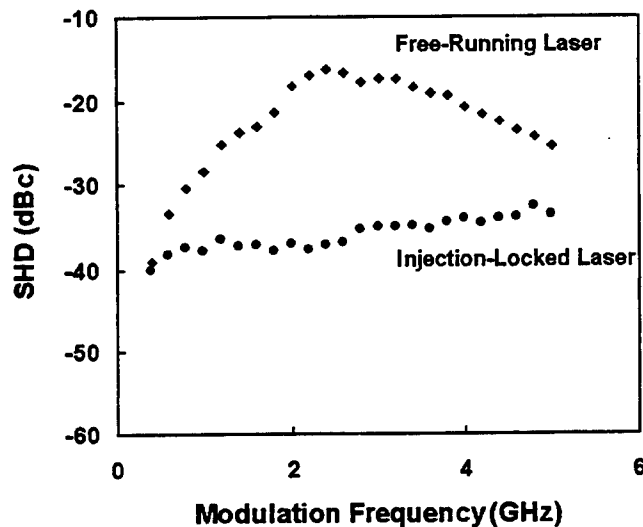


Figure 4-21. Second harmonic distortion suppression under injection locking at various modulation frequencies

Injection locking of lasers is not only limited to locking of CW semiconductor lasers; optical injection locking of mode-locked semiconductor lasers opens up many interesting possibilities relevant to our application. Currently there are four variants of injection locking of semiconductor lasers: 1) CW master to CW slave; 2) mode-locked master to mode-locked slave; 3) CW master to mode-locked slave; and 4) mode-locked master to one or more CW slave lasers. In the following sections we will discuss our results on the third variant and show injection locking of the mode-locked laser can perform carrier tracking for the channelizer receiver.

5 OPTICAL FREQUENCY COMB GENERATION

The coherent optical receiver engineering (CORE) program employed a diffraction grating approach to “spectrally slice” broadband signals into smaller more manageable bands for signal processing, this process is often referred to as channelization. The chosen approach taken in the program is illustrated in Figure 5-1.

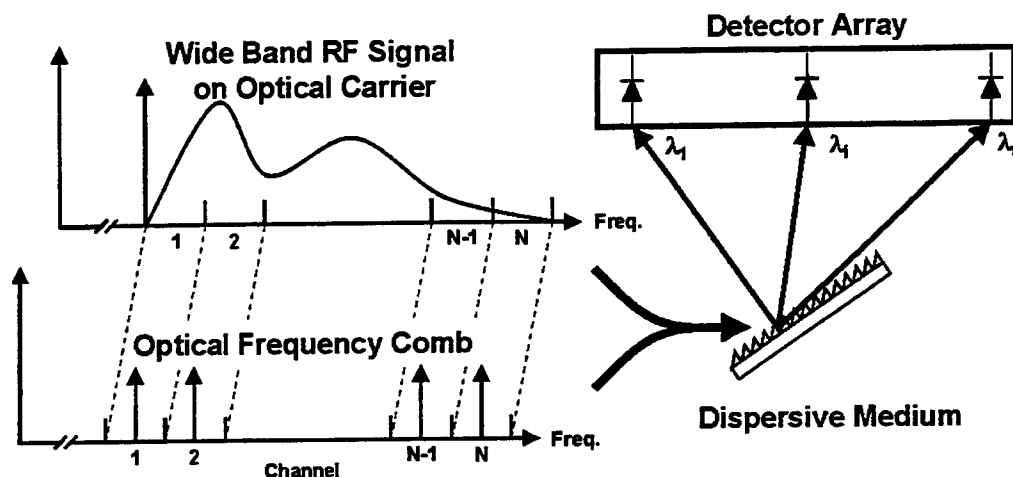


Figure 5-1. Coherent optical channelizer concept

An RF signal is imposed on an optical carrier and dispersed onto a detector by the diffraction grating. Additionally an optical frequency comb (OFC) is dispersed onto the detector array to provide the local oscillators necessary to downconvert the individual channels for signal processing. For efficient heterodyne detection of the RF signal, the local oscillator OFC must be phase locked to the optical carrier.

A principal task of the UCLA subcontract called for the development of an optical frequency comb generator suitable for use as the local oscillator for the coherent channelizer. The external cavity mode-locked laser was chosen due to its flexibility and simplicity. In the early stage of the project some investigation was done on other methods used to generate the OFC, the drawback of other approaches will be discussed. Towards the end of the program an external cavity hybrid mode-locked laser was delivered to TRW and incorporated into the channelizer testbed for demonstration purposes. The results learned from frequency comb generation were then combined with the CW injection locking results to investigate injection locking of a mode-locked laser,

which fulfills the role of establishing phase coherence between the signal and frequency comb.

Due to the availability of a phase-noise-measurement test setup, the injection locking experimental setup was transported to TRW for accurate phase noise measurements.

5.1 METHODS FOR OPTICAL FREQUENCY COMB GENERATION

Methods used to generate an OFC include the resonant waveguide modulator, where the modulator is made resonant at a particular frequency to enhance the modulation depth [26]. A single frequency laser is used as a source and is externally modulated to create the many sidebands. The output will then consist of harmonics spaced at multiples of the modulation frequency and are phase coherent with the carrier frequency of the laser. However, the sidebands generated usually drop off rather quickly, making higher order tones many orders of magnitude below the carrier frequency. Since the modulator is made resonant at a particular frequency changing the frequency is rather difficult, and the required RF power is still quite large.

An alternative method for comb generation is to use an Erbium doped fiber amplifier (EDFA) to amplify and recirculate the output of a phase modulator [27]. The use of the EDFA will help increase the power of the sidebands generated. However, the recirculating loop forms a ring cavity, which requires the comb spacing to be an integral multiple of the mode spacing. An extension of this approach is the mode-locked fiber laser, which incorporates an EDFA to form a ring cavity and an electro-optic intensity modulator to achieve mode locking. In a mode-locked laser, the longitudinal modes are phase locked together and interfere with each other to generate pulsed output intensity with a repetition rate equal to that of the mode spacing [28]. A typical length of an EDFA is on the order of 20 meters or more, corresponding to a mode spacing on the order of 10 MHz. Therefore, to generate a comb spacing of 1 GHz would require the suppression of 99 modes between the teeth of the OFC, typical mode suppression is on the order of 27 dB optically [29]. (Figure 5-2) These side modes will limit the dynamic range of the channelizer since the tones will generate spurs in the channel. This approach also requires a relatively large RF power to drive the modulator, and is rather bulky due to the EDFA. However, the optical spectrum of a mode-locked laser is relatively uniform making it the ideal source for an optical frequency comb.

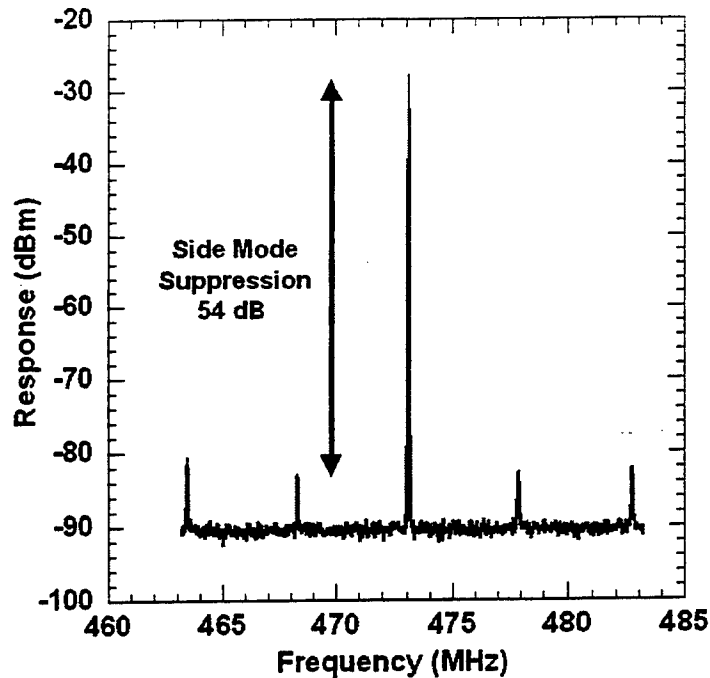


Figure 5-2. Side mode suppression of a harmonic mode-locked fiber laser

An external cavity mode-locked semiconductor laser is chosen to be the ideal candidate for the optical frequency comb due to its versatility and compact form. The cavity length can be continuously controlled and made substantially shorter than a fiber laser, therefore fundamental operation can be achieved at frequencies above 1 GHz. The mode-locking elements can also be incorporated onto the monolithic device.

5.2 MODE-LOCKED LASER EXPERIMENTAL SETUP

To generate the desired frequency comb, a hybrid mode-locked external cavity semiconductor laser is constructed with a 15 cm cavity length to give mode spacing of 1 GHz. (Figure 5-3) A multi-quantum-well, etched mesa buried heterostructure (EMBH) laser is anti-reflection (AR) coated with a multi-layer dielectric coating on one facet to less than 1%. An aspheric lens with a numerical aperture of 0.4 is used to couple the output into an external cavity and a plane metal mirror is used as an end reflector for the external cavity. Wavelength tuning is achieved using an intracavity etalon with a full width half maximum of 5 nm. The EMBH laser is metallized with three separate gain sections (Figure 5-4), the longest section is used as the gain, and the two small sections

are either reverse biased as a saturable absorber or modulated with a synthesizer. The AR coating typically increases the threshold current 1.5 to 2 times. Estimated reflectivity is less than 1% by comparing L-I curves before and after coating. Alignment of the external cavity is achieved by biasing all three sections of the laser slightly below threshold while tilting the external mirror until maximum output power is achieved. Because of the high inherent gain of semiconductor lasers, a small amount of feedback can cause the external cavity laser to lase.

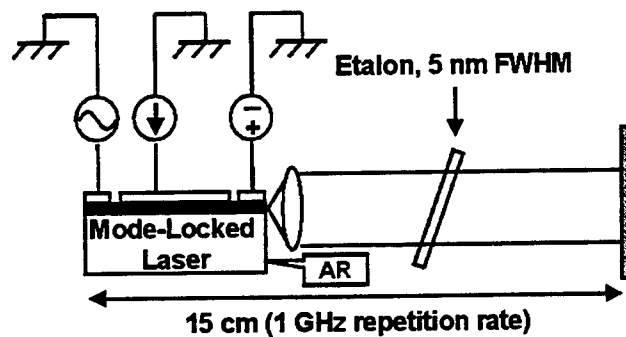


Figure 5-3. External cavity mode-locked laser configuration

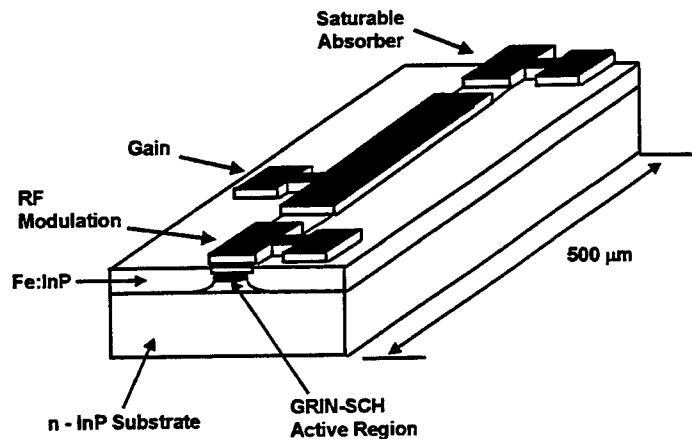


Figure 5-4. EMBH multi-quantum well three section laser

To ensure there was no double pass in the external cavity, a network analyzer is used to verify the cavity resonance of 1 GHz as shown in Figure 5-5 and 5-6. Due to the feedback from the external mirror, the frequency response of the laser will exhibit

resonances at multiples of the longitudinal mode spacing. The effect of a double pass external cavity is to double the cavity length which will give a cavity resonance of 500 MHz (Figure 5-7).

CW output power in the external cavity configuration is typically 1 mW centered at 1550 nm. By angle tuning the intracavity etalon the center wavelength can be tuned to shorter wavelengths from 1580 nm to 1540 nm. The etalon also allows wavelength tuning without a significant change in cavity length as opposed to using a tilted grating end reflector. The etalon also limits the large bandwidth of the semiconductor laser (typically > 30 nm). Limiting the bandwidth will concentrate the energy of the pulse into a narrower wavelength span, thus increasing the power per mode, which is important for channelizer applications. A smaller bandwidth helps prevent incomplete mode-locking (also known as mode-locking in clusters), where certain groups of the spectrum are phase locked, but not phase locked together as a whole which give rise to the coherence spikes in the autocorrelation trace that we see in Figure 5-8 [30-32].

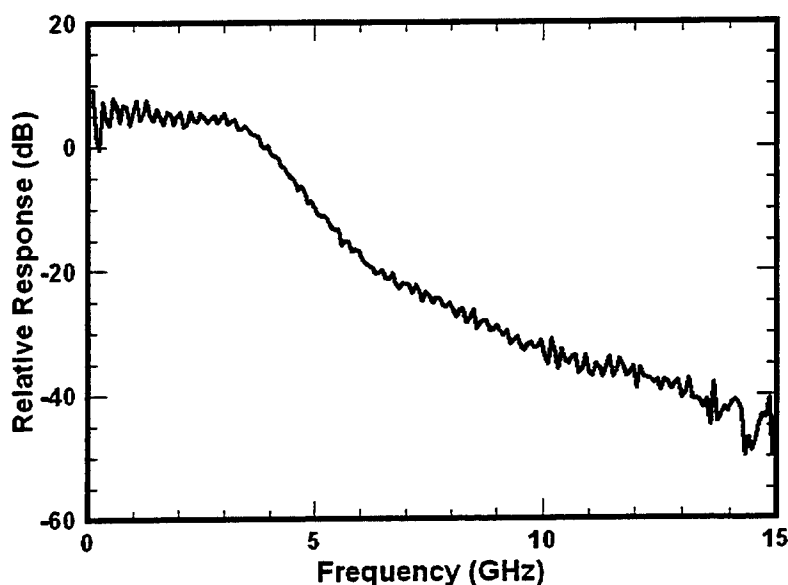


Figure 5-5. Frequency response of monolithic external cavity without external feedback

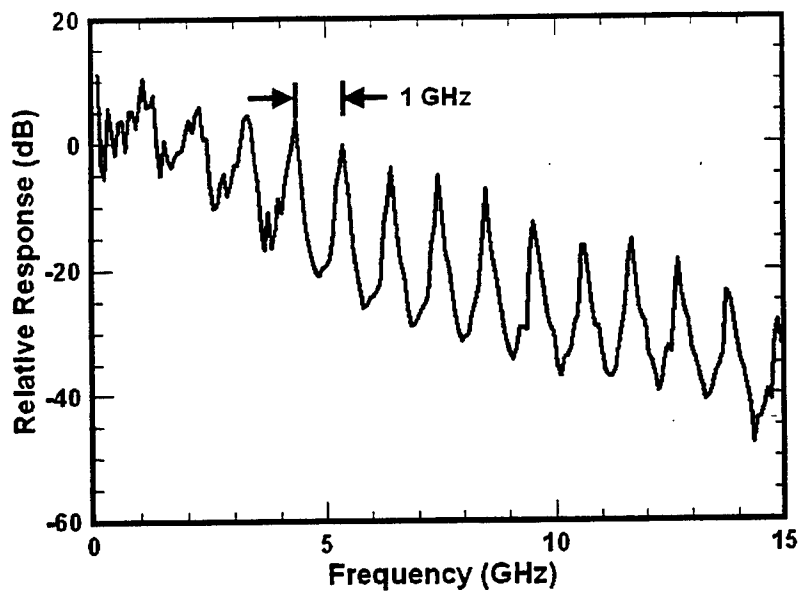


Figure 5-6. Frequency response of a 1 GHz external cavity

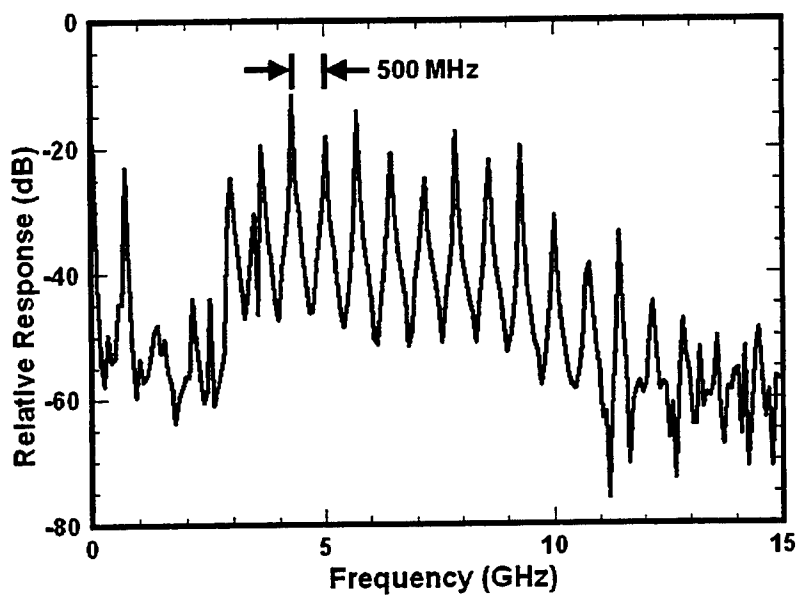


Figure 5-7. Frequency response of a double pass external cavity

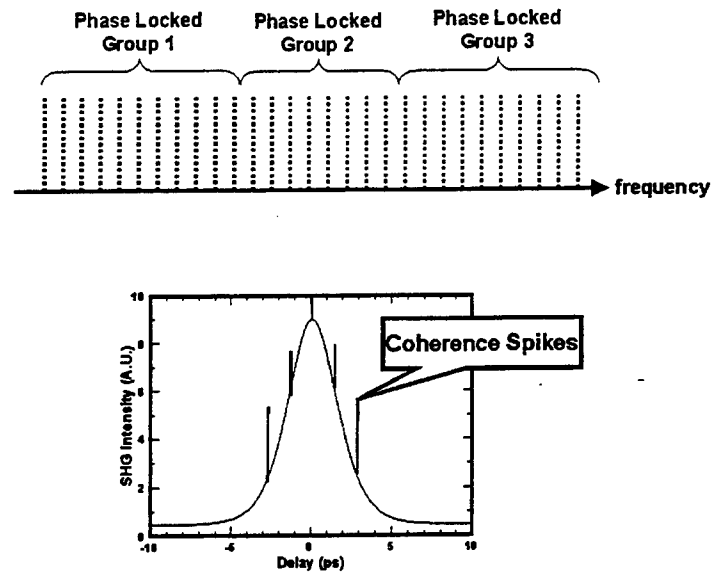


Figure 5-8. Incomplete mode-locking and coherence spikes

Mode locking of the external cavity laser is achieved using the hybrid mode-locking technique, where both a saturable absorber and loss modulation are utilized [33-36]. In a hybrid mode-locked laser, the saturable absorber does the majority of the mode locking and the RF modulation is used to provide a timing reference. Passively mode-locked lasers tend to have large timing jitter due to the lack of an external reference. By introducing a modulation section the timing jitter can be reduced. Typical modulation power needed for an actively mode-locked, semiconductor laser is greater than 25 dBm and produces highly chirped pulses. Whereas, in a hybrid mode-locked scheme a relatively low power of 5 dBm is adequate. The hybrid method provides us with the advantages of both techniques: minimally chirped pulses with low timing jitter and low RF power.

5.3 MODE-LOCKED LASER EXPERIMENTAL RESULTS

The output of the hybrid mode-locked external cavity laser is measured with a non-collinear autocorrelator. Figure 5-9 shows the autocorrelation scan of the pulses with a deconvolved pulsewidth of 2.4 ps. The bandwidth of the pulse is 134 GHz centered at a nominal wavelength of 1550 nm. This is shown in Figure 5-10. This corresponds to a time-bandwidth product of .319, slightly above the transform limit of .3148 for a sech^2

pulseshape [37]. By angle tuning the intracavity etalon the center wavelength will shift towards shorter wavelengths, a tuning range larger than 20 nm can be achieved while maintaining nearly transform limited pulsewidths of less than 3 ps. (Figure 5-11).

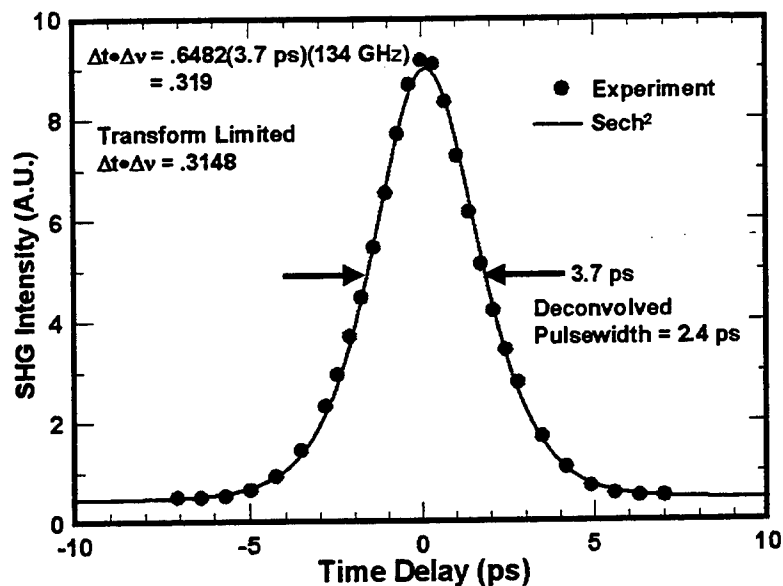


Figure 5-9. Autocorrelation trace of external cavity hybrid mode-locked laser

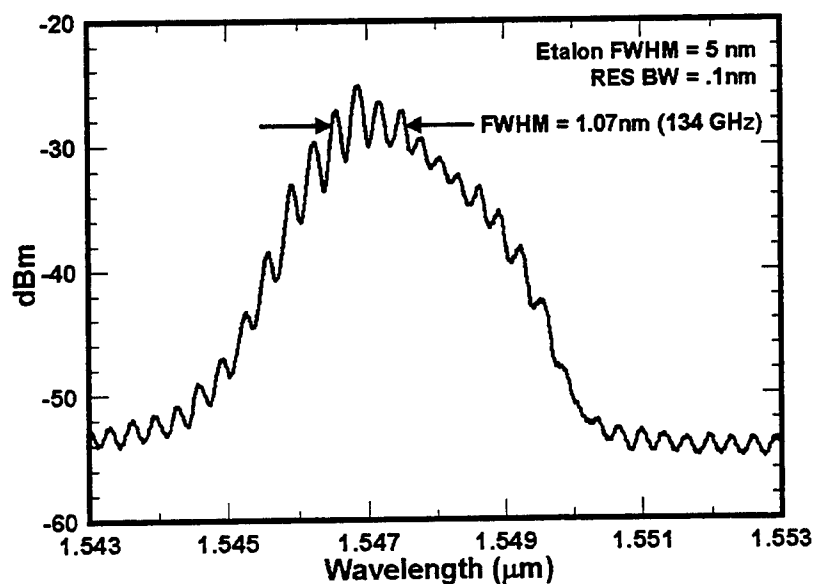


Figure 5-10. Optical spectrum of hybrid mode-locked laser

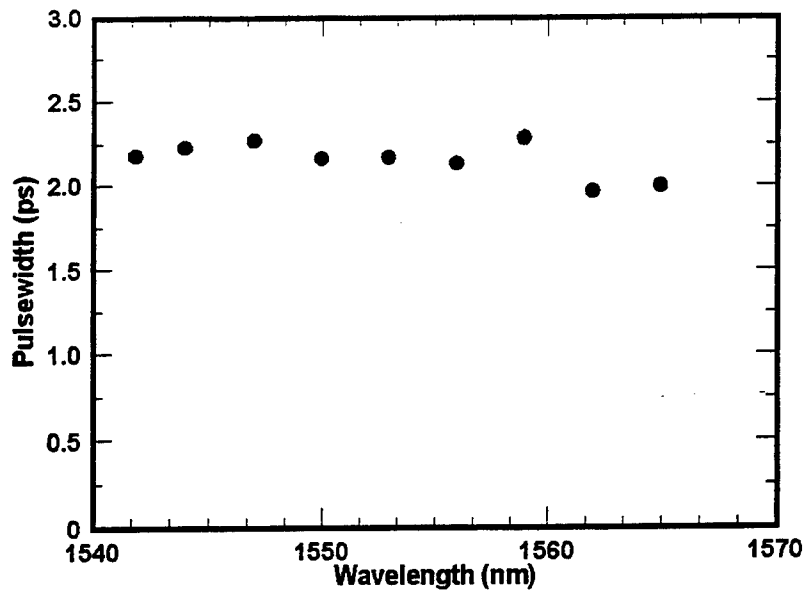


Figure 5-11. Pulsewidth at various center wavelengths

Using a high resolution scanning Fabry-Perot the optical spectrum is resolved and is shown to be modulated by the monolithic cavity mode spacing of 40 GHz. (Figure 5-12) This modulation of the optical spectrum is also evident in Figure 5-10. An imperfect AR coating causes the modulation of the gain spectrum by the monolithic mode spacing, this translates to trailing pulses via Fourier transform [30]. Due to the inherent high gain in semiconductor lasers, it has been estimated that reflectivities as low as .5% are adequate to generate trailing pulses with approximately 50% of the main pulse energy [38]. Current state of the art AR coatings can be as low as 10^{-4} using in-situ monitoring, whereas angled waveguide lasers offer a viable alternative to such high performance coatings. A couple cavity effect is also observed due to the imperfect AR coating. The small reflection of the inner facet forms two coupled cavities: one formed by the external mirror and the output facet, the external mirror and the coated inner facet form the other. Since the lengths of the two cavities are different, the cavity modes of each cavity will be at different frequencies. This is seen clearly in Figure 5-13. The longer cavity modes will have higher power due to the higher cavity Q. By adjusting the lengths each cavity such that the modes overlap at the same frequency these coupled cavity modes can be eliminated. Fine tuning of the monolithic cavity length can be achieved by changing the

bias on the individual sections of the laser. These coupled cavity modes will introduce additional spurious tones in the 1 GHz channels, which can decrease the dynamic range. The imperfect AR coating also increases the likelihood of exciting higher order supermodes which lead to pulse break up and long pulsewidths [30].

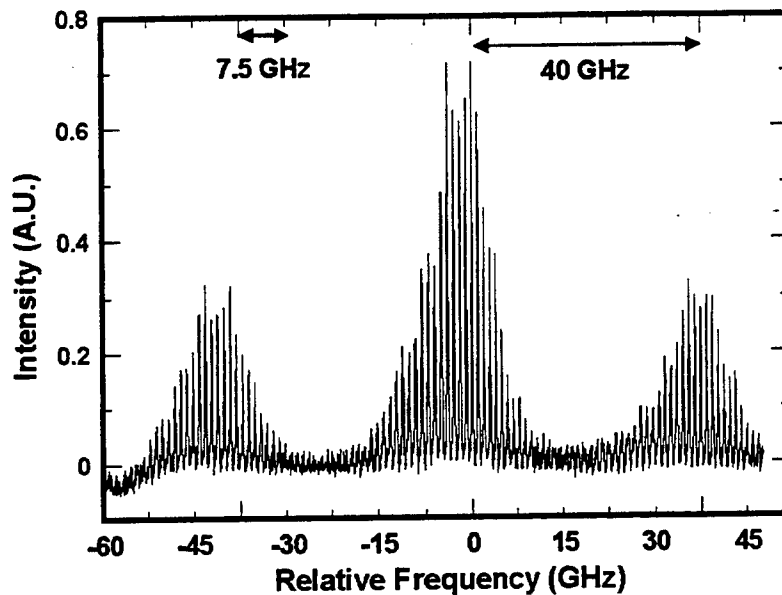


Figure 5-12. Resolved modes of the hybrid mode-locked laser

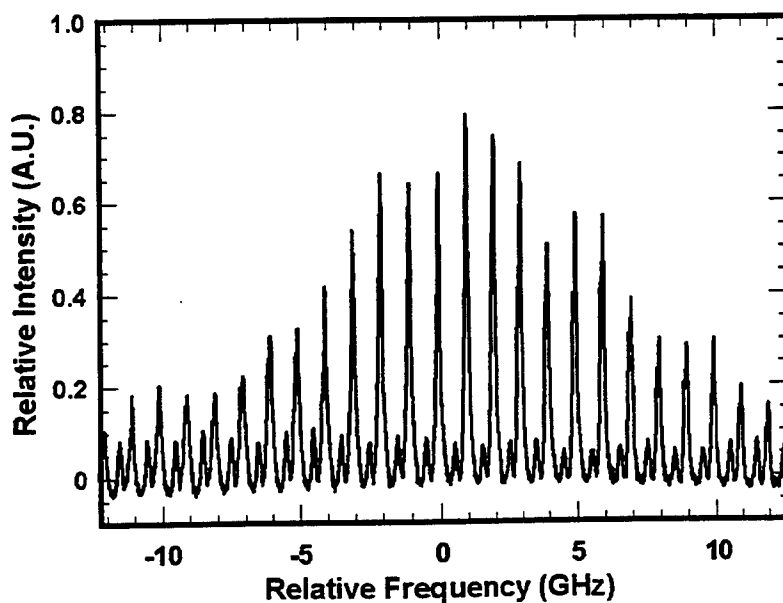


Figure 5-13. Coupled cavity effect due to imperfect AR coating

5.3.1 Linewidth of an external cavity hybrid mode-locked laser

The modes of the mode-locked laser are resolved by a high resolution scanning Fabry-Perot spectrometer and are shown to have a linewidth of 170 MHz per mode. (Figure 5-14) The resolution of the scanning Fabry-Perot is 40 MHz. An average mode-locked power of -9 dBm was achieved, this corresponds to a power of $1\text{ }\mu\text{W}$ per mode. Under CW operation at the same operating current the output power was 0 dBm. This rather broad linewidth is attributed to the low saturation power of the saturable absorber, typically on the order of 1 pJ . With a higher saturation power, the laser can be operated higher above threshold and a narrower linewidth can be achieved. CW operation of the external cavity laser at an output power level of -9 dBm indicates that the laser is slightly above threshold.

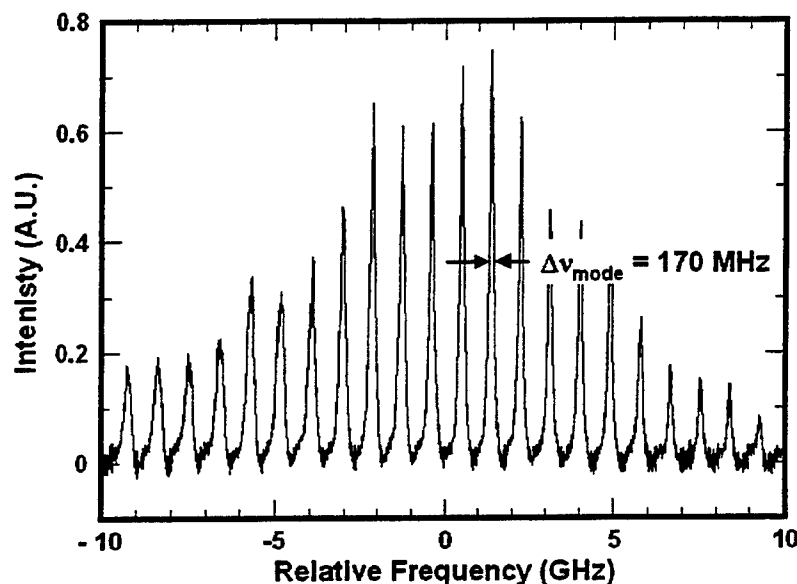


Figure 5-14. Linewidth of hybrid mode-locked, external cavity laser

It has been shown that an actively mode-locked laser will have a linewidth per mode equal to that of CW operation at the same output power [39]. (A mode-locked laser with an average power of 0 dBm will have the same linewidth per mode as if the laser were operating CW at an output power level of 0 dBm.) The effect of the modulator is to distribute the energy of the single mode into many cavity modes that are phase locked together. This modulation diffuses the spontaneous emission of one mode among the

many modes of the mode-locked spectrum. The modulation tends to broaden the optical spectrum whereas the gain will tend to narrow the spectrum due to gain saturation. Semiconductor materials have low energy storage potential therefore they tend to saturate at lower intensities compared to other materials such as chemical dyes and solid state crystals. The pulse energy in a hybrid mode-locked laser is similar to that of a passively mode-locked laser and is limited by the saturation energy of the integrated monolithic saturable absorber, typically on the order of 1 pJ. High saturation energies have been achieved with semiconductor quantum well saturable absorbers mirrors (SESAM), with saturation energies on the order of 10 μJ . Keller has demonstrated passive mode-locking of a Ti:Sapphire laser with an external anti-resonant quantum well saturable absorbers with very high peak powers [40,41]. By incorporating a saturable absorber within an anti-resonant cavity, a higher incident intensity would be required to reach saturation. (Figure 5-15) SESAM's have been used to generate average mode-locked powers as high as 500 mW from Cr:LiSAF lasers [42]. Tsuda has extended this principle into a distributed saturable Bragg reflector (SBR), where a single quantum well saturable absorber is placed in a region of low intensity within the Bragg mirror [43]. (Figure 5-16) The use of a thin absorber layer helps decrease the insertion loss of the device. An average mode-locked power of 42 mW has been demonstrated from a diode pumped Cr:LiSAF laser. With the laser operating CW an output power of 55 mW was obtained, substantiating the low loss introduced by the SBR. Power is also shown to scale with increasing pump power.

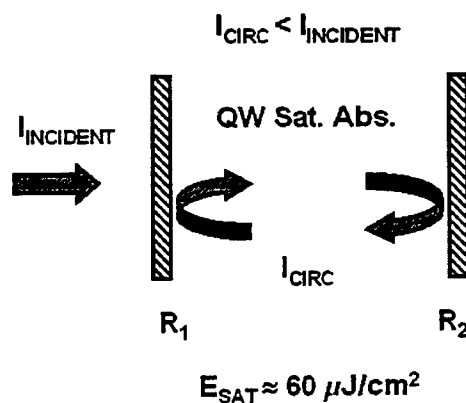


Figure 5-15. Anti-resonant fabry perot saturable absorber (AFP-SA)

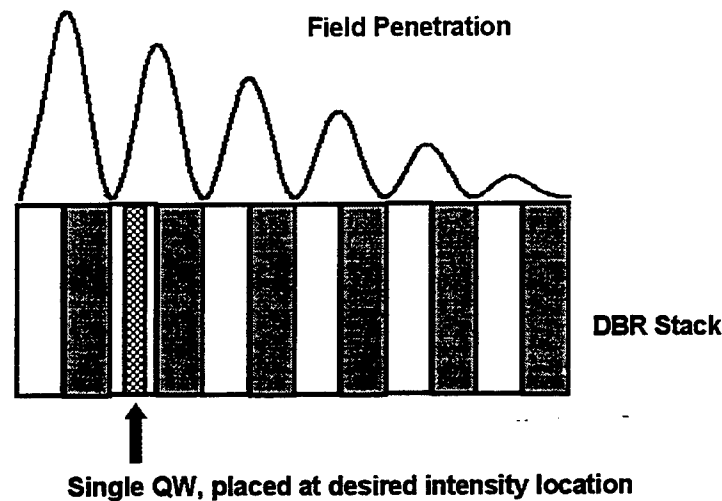


Figure 5-16. Saturable Bragg reflector (SBR)

In the current external cavity configuration of Figure 5-3, the placement of the saturable absorber is not in the most effective position and contributes to modulation of the gain spectrum which can lead to different repetition rates [35]. The ideal hybrid mode-locked laser will have both mode-locking components at the ends of the cavity to efficiently couple the cavity modes and be as thin as possible [45-47]. By replacing the external mirror with the SBR, the saturable absorber can be placed in its most effective position, as well as increasing the saturation energy resulting in higher peak powers. This will in turn produce a narrower linewidth per mode.

Mode locking of an external cavity semiconductor laser using a SBR has been demonstrated using an absorber obtained from Cornell University. The external cavity configuration is shown in Figure 5-17. A 20 times focusing lens is used to focus the external cavity beam to achieve the proper saturation intensity on the SBR. Figures 5-18 and 5-19 show the pulse bandwidth and pulsewidth at various stages of pulse compression using single mode fiber, respectively. Pulsewidths as short as 570 fs with a time bandwidth product of .496 have been achieved [48]. As seen in Figure 5-20 the edges of the pulse do not correspond very well to the sech^2 fit. This is due to higher order chirp in the pulse.

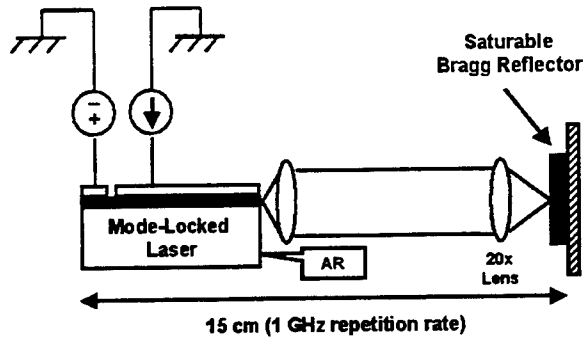


Figure 5-17. External cavity mode-locked semiconductor laser using SBR.

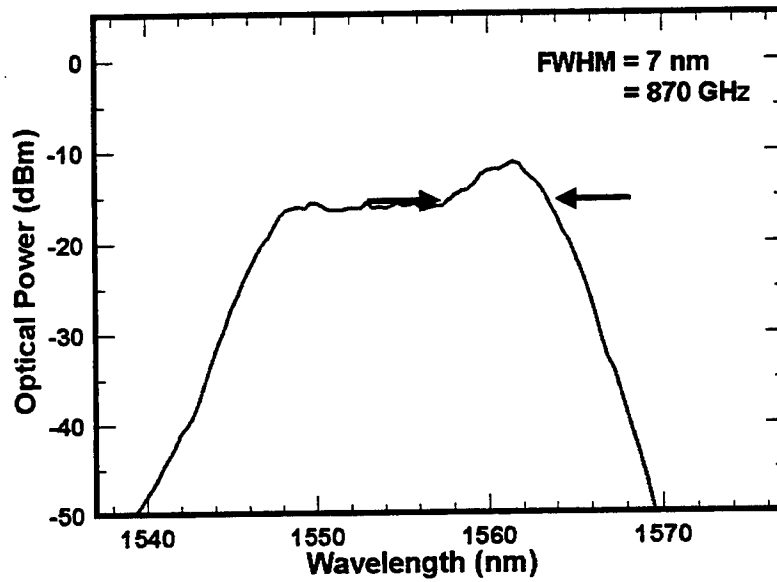


Figure 5-18. Optical spectrum of passively mode-locked external cavity laser using a SBR

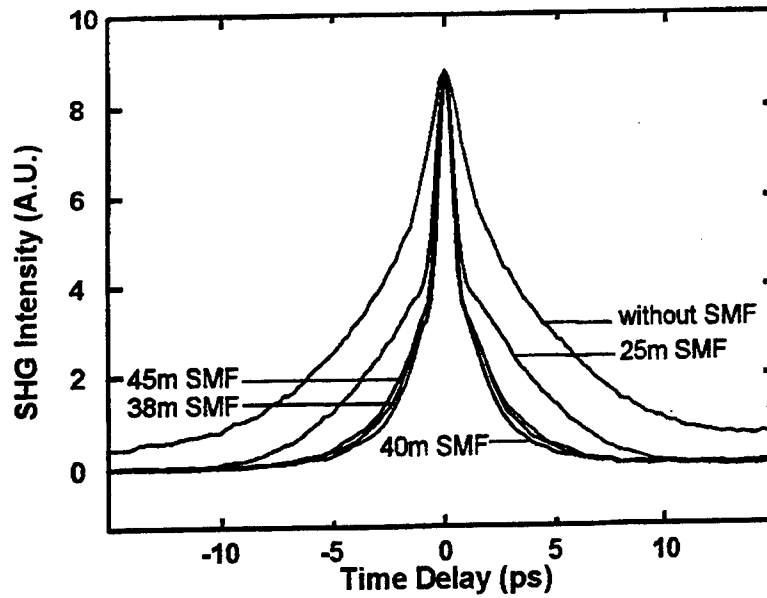


Figure 5-19. Compressed pulsewidths at various stages of pulse compression using single mode fiber

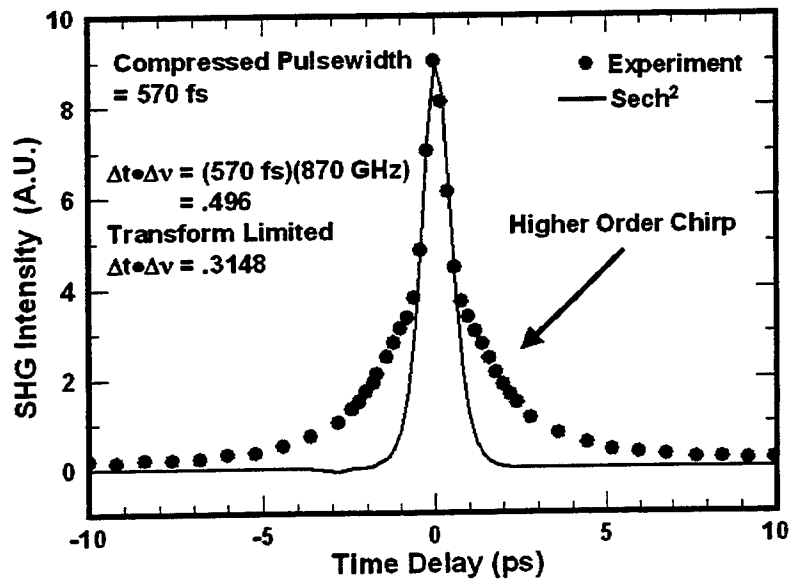


Figure 5-20. 570 fs compressed pulsewidth using 40 meters of single mode fiber

5.3.2 Noise of a Mode-Locked Laser

The noise of a mode-locked laser is determined by timing jitter and intensity noise. Timing jitter is referred to the variation in time between pulses (this can be shown to be related to the instantaneous incoherent phase between the individual modes), and intensity noise is referred to as the variation in energy of each pulse. These two noise parameters can be extracted from the harmonics seen on a high speed photodetector and a RF spectrum analyzer [49]. The pulse train of a perfectly mode-locked laser with no noise can be represented as:

$$I_0(t) = \sum_k i(t + kT_R) \quad (5.3-1)$$

where $i(t)$ is the temporal intensity of an individual pulse (typically Gaussian or sech^2), T_R is the repetition rate, and k is an integer from minus to plus infinity. Noise of the pulse train can be described by adding an amplitude noise and timing jitter to (5.3-1);

$$I(t) = I_0(t) + I_0(t) \cdot A(t) + T_R \cdot J(t) \cdot \frac{\partial I_0(t)}{\partial t}, \quad (5.3-2)$$

where $A(t)$ describes the amplitude fluctuation and $J(t)$ describes the temporal jitter. Taking the Fourier transform and using the following definitions:

$$G_I(\tau) = \langle I(t + \tau) I(t) \rangle, \quad (\text{Autocorrelation}) \quad (5.3-3)$$

and

$$P_I(\omega) = \frac{1}{2\pi} \int_{-\infty}^{\infty} G_I(t) e^{j\omega t} dt, \quad (\text{Power Spectral Density}) \quad (5.3-4)$$

gives the following result.

$$P_I(\omega) = P_{I_0}(\omega) * [\delta(\omega) + P_A(\omega)] + [(\omega T_R)^2 P_{I_0}(\omega)] * P_J(\omega). \quad (5.3-5)$$

$P_A(\omega)$ and $P_J(\omega)$ represent the amplitude noise and timing jitter noise power spectral density, respectively. $P_{I_0}(\omega)$ is the detected power spectrum for a perfectly mode-locked pulse train without any noise, and is given by

$$P_{I_0}(\omega) = \frac{2\pi}{T_R^2} \cdot |\tilde{i}(\omega)|^2 \cdot \sum_k \delta\left(\omega - \frac{2\pi}{T_R} k\right) \quad (5.3-6)$$

(5.3-6) indicates that with an ideal photodetector and RF spectrum analyzer, the detected spectrum would be delta functions spaced at multiples of the repetition frequency, with a

3 dB bandwidth half of that of the spectral intensity profile, $|\tilde{i}(\omega)|^2$. With the addition of energy fluctuations and timing jitter the detected power spectrum is then given by

$$P_I(\omega) = \frac{2\pi}{T_R^2} |\tilde{i}(\omega)|^2 \cdot \sum_k [\delta(\omega_k) + P_A(\omega_k) + (2\pi k)^2 P_J(\omega_k)], \quad (5.3-7)$$

where $\omega_k = \omega - \frac{2\pi}{T}k$, represents the harmonic number. Additional noise power spectral density terms P_A and P_J are centered around each delta function at frequency ω_k . (5.3-7) indicates that the power spectrum for amplitude noise is constant with harmonic number k , whereas timing jitter (phase noise) scales with harmonic number k^2 .

As shown in Figure 5-20, when the output of a mode-locked laser is seen on a photodetector and RF spectrum analyzer, harmonics are observed at multiples of the repetition frequency. These tones are due to the beating of the longitudinal modes of the mode-locked laser. Nearest neighbor modes beat with each other to generate the 1 GHz tone, second nearest neighbor modes beat with each other to generate the 2 GHz. Modes farther apart are less coherent than modes closer together, therefore phase noise increases with harmonic number squared. When these tones are amplified and observed with a narrower span (Figure 5-21), the measured tones are placed on top of a pedestal of noise below it. This pedestal of noise consists of both amplitude noise and phase noise.

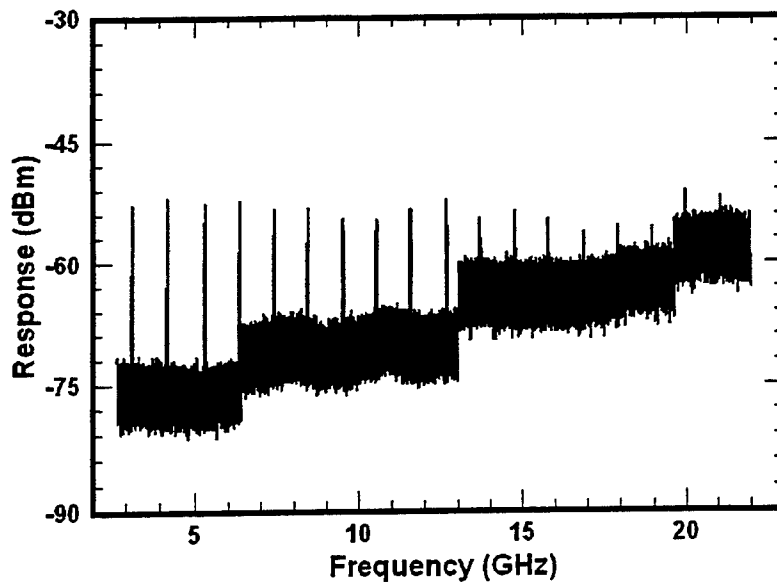


Figure 5-21. Detected RF spectrum of hybrid mode-locked laser

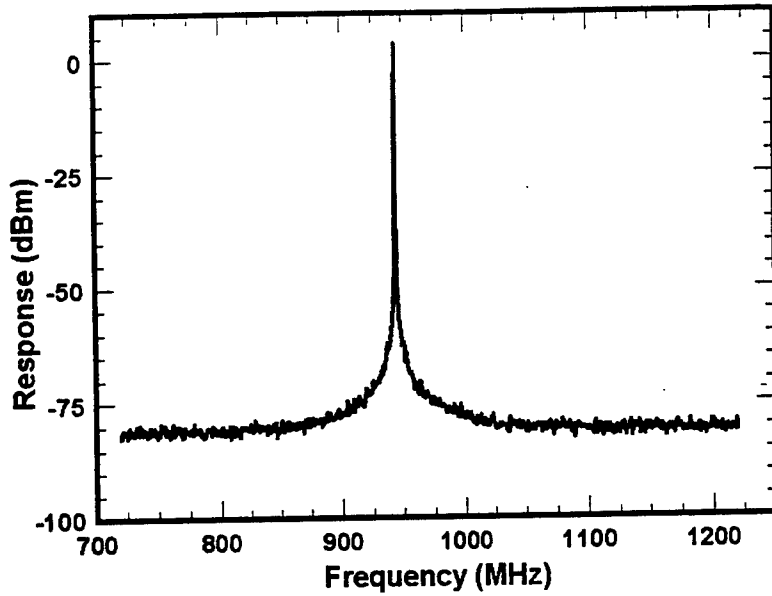


Figure 5-22. Fundamental tone of external cavity hybrid mode-locked laser

From the digitized data, the timing jitter and pulse energy fluctuations of a mode-locked laser can be calculated from the following equations [50].

$$\frac{\Delta T_r}{T_r} = \frac{1}{2\pi k} \left[\int_{-f_2}^{-f_1} L_p(f) + \int_{f_1}^{f_2} L_p(f) \right]^{1/2}, \quad (5.3-8)$$

and

$$\frac{\Delta E}{E} = \left[\int_{-f_2}^{-f_1} L_a(f) + \int_{f_1}^{f_2} L_a(f) \right]^{1/2}, \quad (5.3-9)$$

where T_r is the cavity round-trip time (repetition time), k is the harmonic number, $L_p(f)$ is the single side band phase noise power spectral density (PSD) with respect to the carrier power, $L_a(f)$ is the amplitude noise power spectral density with respect to the carrier. Amplitude noise usually dominates at offsets larger than 1 MHz from the measured mode-locked fundamental frequency [51]. An upper bound for the amplitude noise is estimated from the fundamental tone to be less than 3% at offsets between 1 MHz and 50 MHz. Using a RF spectrum analyzer to determine the phase noise of the mode-locked laser would require a measurement of the single side band noise for many harmonics to extrapolate the phase noise, which increases with harmonic number squared. This

method is rather difficult and inaccurate because the amplifier and photodetector response will drop at higher frequencies, and the spectrum analyzer noise floor increases at higher frequencies. An alternative approach to measure the phase noise is to use the HP 8048 phase noise test set, similar to the measurement used in injection locking of two CW lasers as described in section 4.

5.3.3 Residual phase noise of an actively mode-locked laser

Residual phase noise of an actively mode-locked laser is defined as the excess phase noise the mode-locked laser introduces at the fundamental harmonic relative to the phase noise of the driving synthesizer. Actively mode-locked lasers usually have the lowest timing jitter and amplitude noise, however spontaneous emission is always present and contributes to the noise of the laser. Much of the noise in a mode-locked laser can also be attributed to cavity acoustics where the cavity length is modulated by low frequency vibrations; this is very significant in fiber lasers where the typical length of fiber used is between 15 and 50 meters.

The HP 8048 phase noise test set is used to measure the phase noise of the 1 GHz fundamental tone of the external cavity mode-locked laser. A 1 GHz low pass filter is used after the photodetector to minimize noise contribution from the second harmonic at 2 GHz. The measured phase noise is shown in Figure 5-23. The phase noise of the HP 8662A synthesizer used to drive the mode-locked laser is also shown for comparison, the difference of the two plots is the additional noise the mode-locked laser contributed. In an actively mode-locked laser the phase noise performance can be as good as the driving source [51]. The phase noise plot shows a leveling off of the phase noise past a 10 kHz offset, and levels down to -100 dBc/Hz at 40 MHz offset. This flat noise floor is attributed to the restoring gain dynamics of the semiconductor laser and spontaneous emission [52]. Using (5.3-8), the estimated RMS timing jitter is 2.2 ps measured at offsets of 10 Hz to 10 MHz from the carrier. It is important to note that the synthesizer itself introduces 172 fs of jitter.

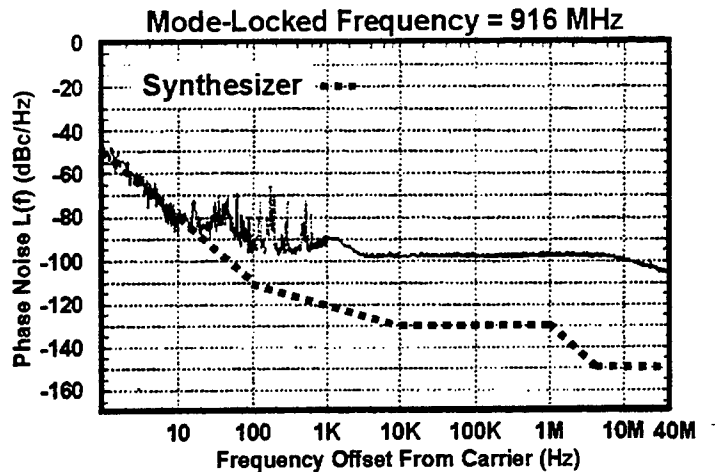


Figure 5-23. Phase noise hybrid mode-locked laser fundamental tone

Increasing the RF drive will also force the laser to follow the spectral purity of the RF source used. For a 3 dB increase in RF drive, the phase noise is shown to decrease by approximately 10 dB. This measurement is shown in Figure 5-24. Increasing the RF drive changes the operating condition of the laser and requires a slight change in driving frequency to achieve complete mode-locking. Ultimately, the lowest phase noise will be obtained with active mode-locking.

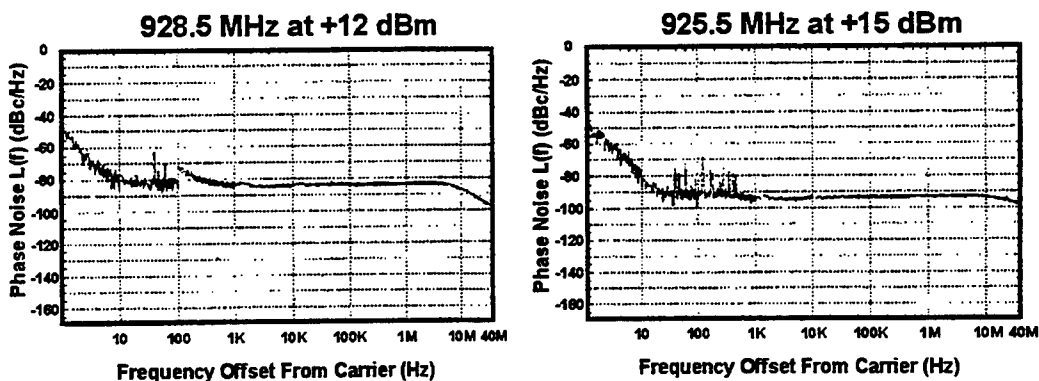


Figure 5-24. Phase noise with increased RF drive power

5.3.4 Locking Bandwidth of a Mode-Locked Laser

Active mode-locking offers a larger range of repetition rates than passive mode-locking for a fixed cavity length [30,31]. Since the gain is driven periodically by the driving RF source, it can compensate for pulses that arrive later or earlier by either amplifying the

trailing edge or the leading edge as illustrated in Figure 5-25. When the arrival of the pulse is outside of the locking range the pulse will be distorted and mode-locking is not achieved. In the frequency domain model, this can be viewed as contraction or expansion of the cavity mode spacing.

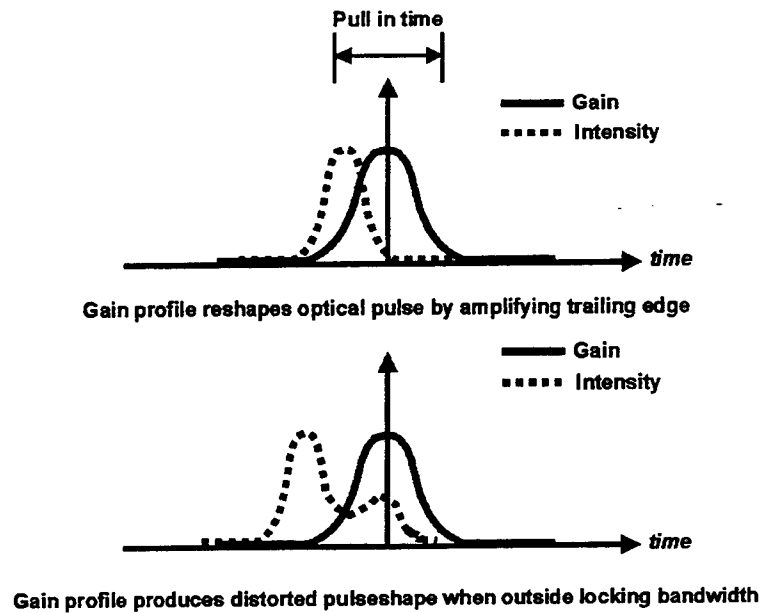


Figure 5-25. Pulse shaping process for detuning a mode-locked laser

For hybrid mode-locking, a locking range of 17 MHz is achieved which corresponds to a pull in time of 20 ps [53]. In Figure 5-26 and 5-27 the pulsewidth and the phase noise floor measured at a 10 kHz offset show little change across the RF locking range. RF modulation power is set constant at 6 dBm. This locking range is expected to vary depending on how much mode locking the saturable absorber is doing compared to the modulator.

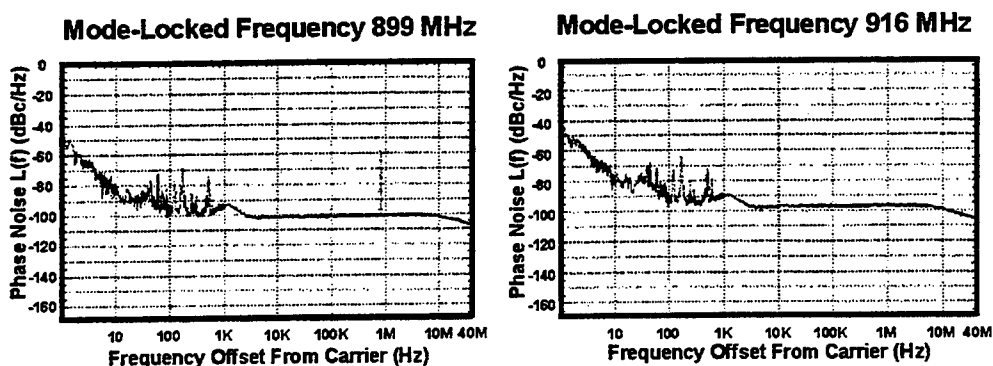


Figure 5-26. Phase noise measured at various mode-locked frequencies

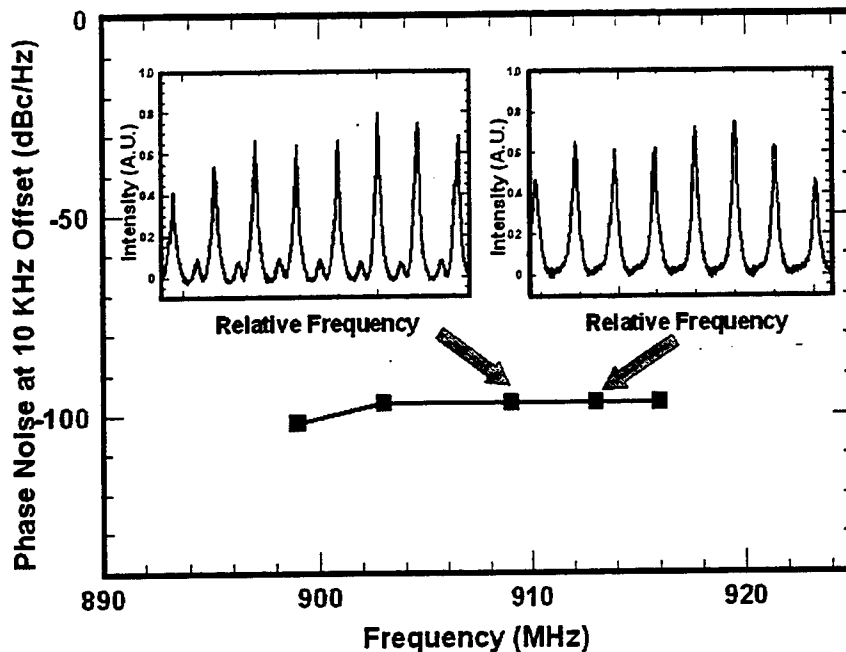


Figure 5-27. Phase noise floor measured at frequencies 10 kHz offset across the detuning range

It is important to note that the RF locking range that produces a sech^2 pulseshape does not always produce perfect spectral qualities of the mode-locked laser. Due to the imperfect AR coating, a coupled cavity configuration exists as shown previously in Figure 5-13. The external cavity modes can be made to coincide with the monolithic laser modes by carefully adjusting the external cavity length or varying the modulation frequency. The monolithic mode spacing is 40 GHz for a 500 μm device, whereas the external cavity has a mode spacing on the order of 1 GHz. By varying the RF drive frequency across the locking range, the coupled cavity effect can be eliminated as shown in Figure 5-27.

5.4 CARRIER TRACKING

5.4.1 Injection locking of a hybrid mode-locked semiconductor laser

To establish phase coherence with the optical frequency comb, optical injection locking is used. Figure 5-28 shows a schematic layout of the experimental setup used similar to that used for CW injection locking. An external cavity laser is used as the master laser. The output is split with one arm directed to an acousto-optic frequency shifter, and the

other arm is attenuated and then injected into the mode-locked slave laser via optical circulator. Polarization controllers are utilized at the injection arm and at the detection arm. A delay line is introduced into the heterodyne arm to minimize the excess phase noise found in heterodyne detection schemes [19].

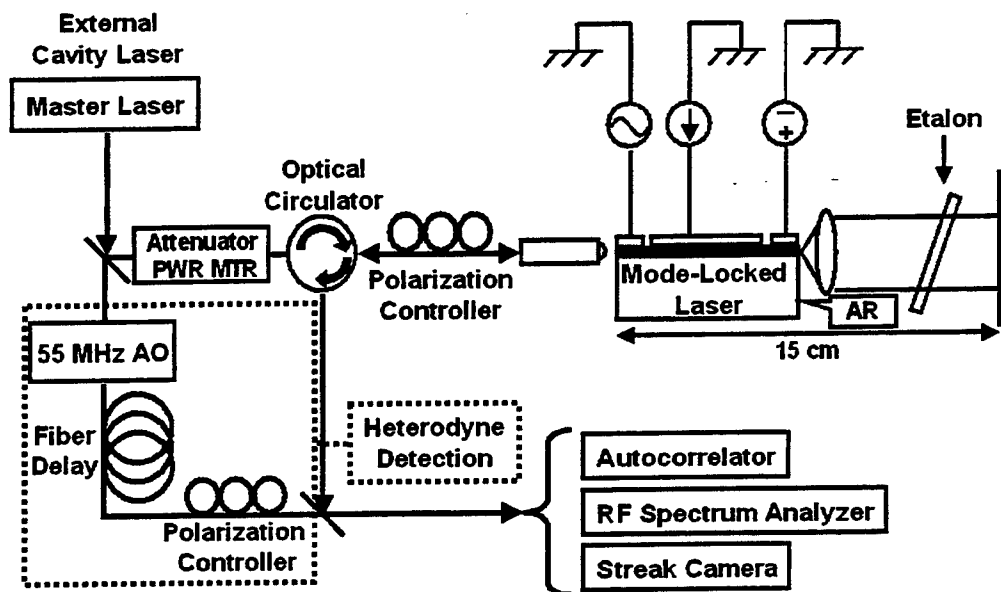


Figure 5-28. Experimental setup for injection locking of a mode-locked semiconductor laser

When the output of the mode-locked laser is detected on a high speed photodetector, harmonics at 1 GHz, 2 GHz, and so forth can be seen. If the modes of the laser were not phase locked, the incoherent beating of the modes would generate beat noises and would not resemble the strong coherence represented by the delta function. When the master laser is injected into one of the modes of the slave, phase coherence is established between the master and the particular mode. However, in a mode-locked laser all the modes are phase coherent therefore the whole frequency comb is phase coherent with the slave laser. The modes of the slave laser can also be slightly pulled away from the free running frequency. To detect this phase coherence and mode-pulling the heterodyne detection scheme of Figure 5-29 is used.

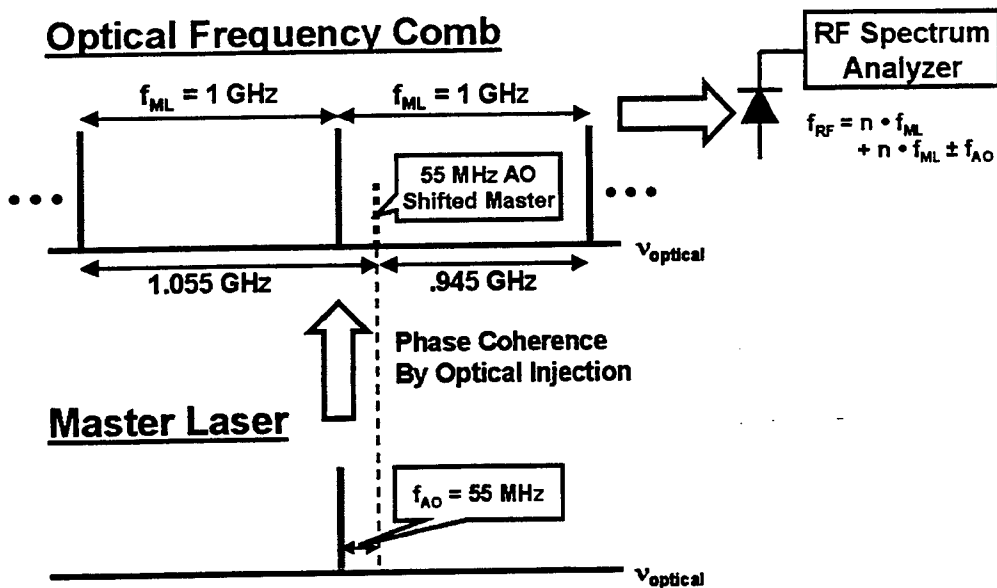


Figure 5-29. Heterodyne detection of injection locked mode-locked laser

When detected with a high-speed photodetector and RF spectrum analyzer, harmonics of the mode-locked laser can be seen. In addition, tones spaced 55 MHz apart from the harmonics are observed as shown in Figure 5-30. These tones are due to the beating of the frequency-shifted master with the modes of the mode-locked laser.

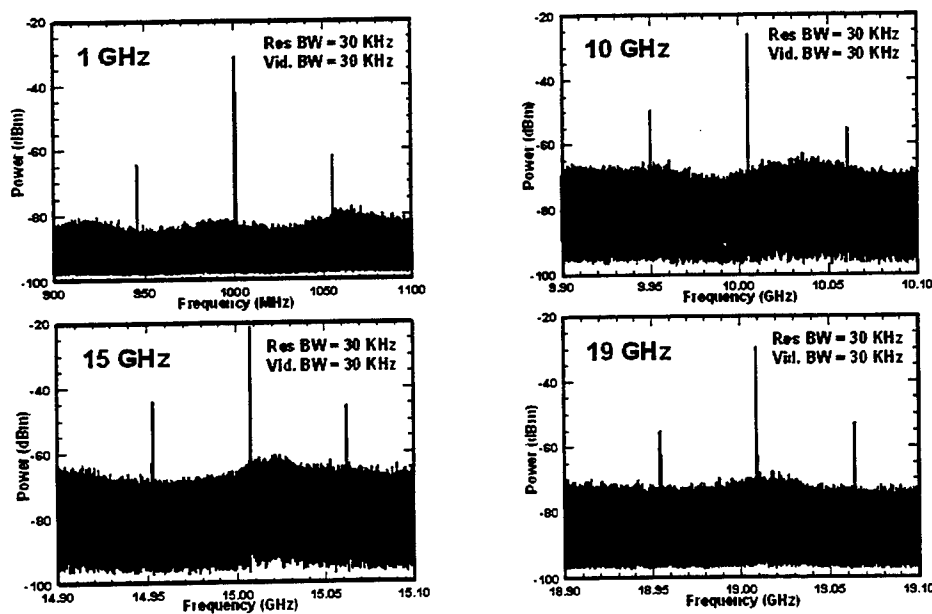


Figure 5-30. Heterodyne tones of injection locked mode-locked laser

In Figure 5-30, tones at 945 MHz and 1055 MHz indicate that the modes adjacent to the injected mode are phase coherent with the master laser. Tones at 9.945 GHz and 10.055 GHz indicate that modes 10 GHz to the left and right of the injected mode are phase coherent with the master laser. These tones can be seen up to 19 GHz indicating that the modes 19 GHz away from the injected mode are also phase coherent with the master laser. This corresponds to the supermode behavior where the optical spectrum of a mode-locked laser operates as a quasi-single mode [39,54].

5.4.2 Pulse Characteristics of an Injection Locked Mode-Locked Laser

The first parameter of interest is how the pulse characteristics change with injected optical power. When the laser is well mode-locked using the hybrid technique, the autocorrelation trace in Figure 5-31 shows 100% modulation depth in the pulses. Trailing pulses are still evident due to the imperfect AR coating. Taking the autocorrelation trace over a full scan of 100 ps shows that there is also no slowly varying substructure. The master laser is then centered to the center wavelength of the mode-locked laser, and adjusted such that injection locking is seen on the RF spectrum analyzer. Autocorrelation traces are then taken at various injected optical powers while injection locked. The pulsewidth and pulse shape show little change at low optical injection levels. At injected optical powers comparable to the average mode-locked power, the pulse shape begins to distort and shows a significant increase in substructure due to the optical DC bias on the saturable absorber. This can be seen in the autocorrelation traces shown in Figures 5-31 through 5-33. The plot of pulsewidth as a function of injection level presented in Figure 5-34 also shows that the pulses broaden at high optical injection levels. This DC bias will tend to force the laser to operate in a single mode, and the saturable absorber has little effect in spreading the energy over many modes in the optical spectrum.

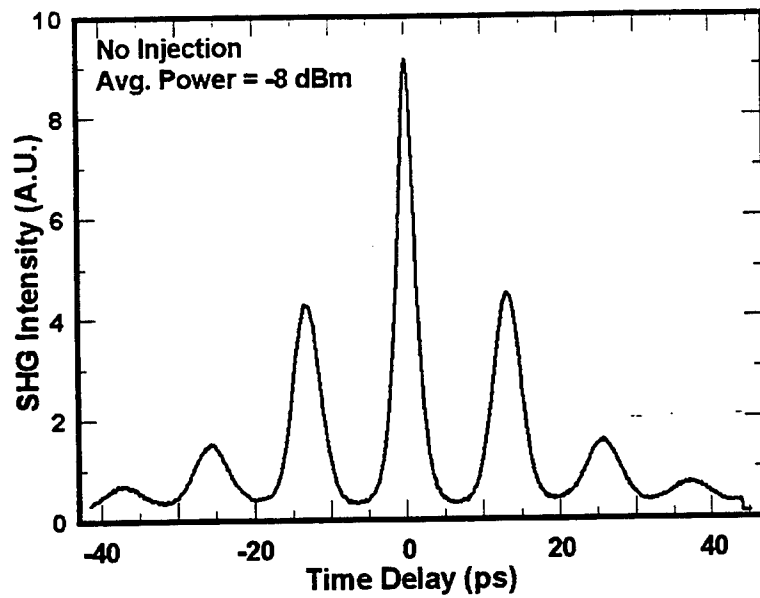


Figure 5-31. Autocorrelation of mode-locked laser with no injection

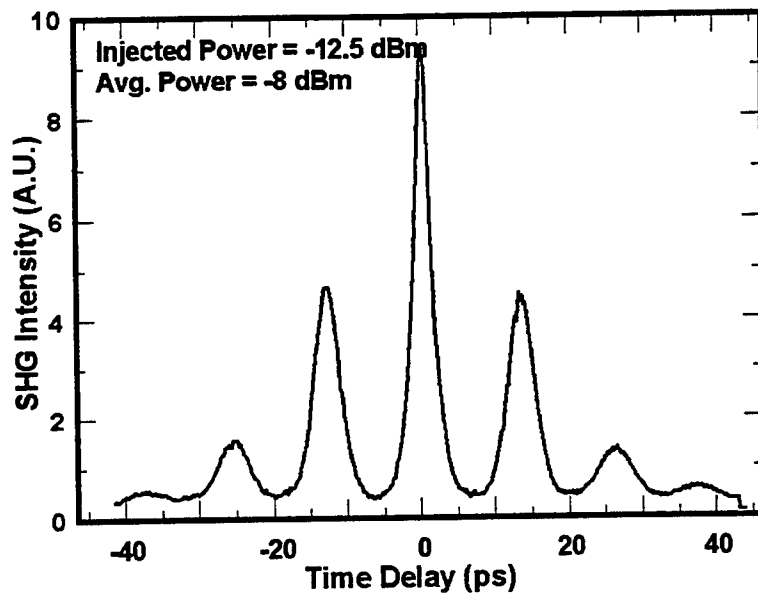


Figure 5-32. Autocorrelation trace of mode-locked laser with -12.5 dBm injection

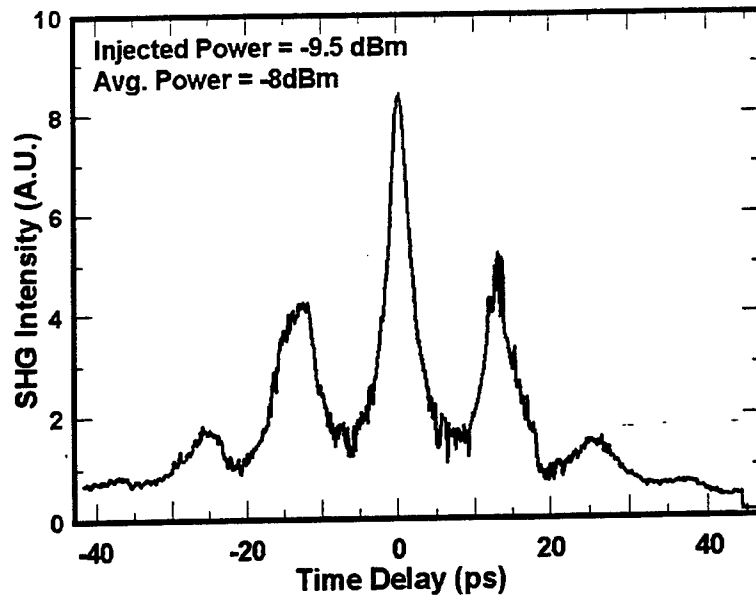


Figure 5-33. Autocorrelation trace of mode-locked laser with -9.5 dBm injection

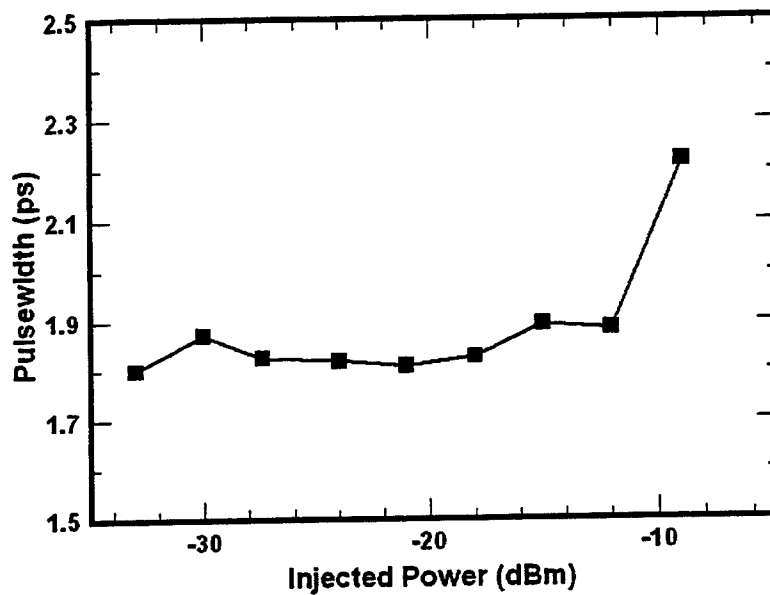


Figure 5-34. Pulsewidth at various injection levels

5.4.3 Physics of injection locking of a mode-locked laser

Active mode locking is achieved by using a modulator to couple the individual modes of the laser. The modulator modulates the cavity modes at approximately the cavity mode spacing and generates sidebands. These sidebands will couple into the adjacent cavity modes and create phase coherence throughout the spectrum [45-47]. (Figure 5-35) Similarly, when the master laser is injected into a mode of the slave laser, phase coherence is established with that particular mode. This mode is then modulated to generate side bands which are phase coherent with the master laser. These sidebands then couple into adjacent modes throughout the spectrum to establish phase coherence between the mode-locked slave laser and master laser. The evidence of sideband generation can be observed using a high resolution scanning Fabry-Perot. Figure 5-36 shows the injected light that is far away from a cavity mode and thus not injection locked. The sidebands generated by the modulation of the injected light are shown and have comparable power due to the inherent gain in the medium.

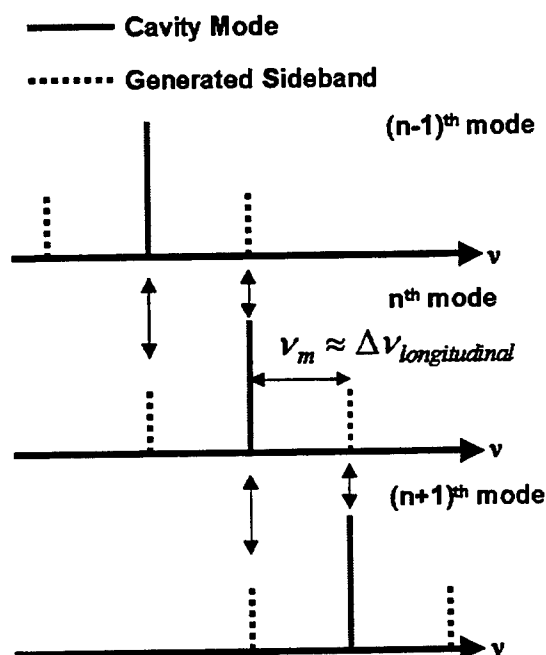


Figure 5-35. Sideband generation in a mode-locked laser

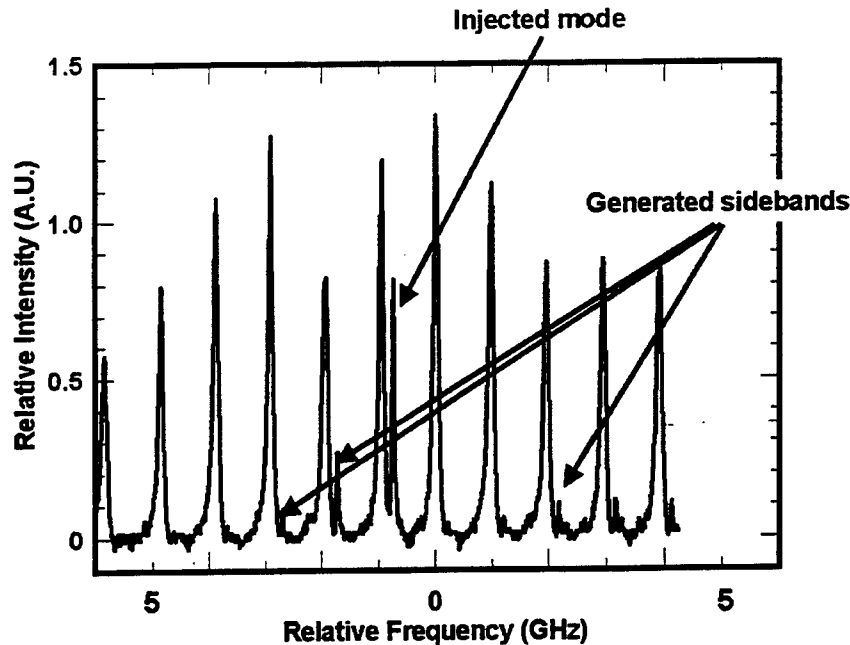


Figure 5-36. Generation of sidebands from injected mode

Similar results have been published in [55], where a double side-band suppressed carrier (DSB-SC) signal is used to stabilize a passively mode-locked DBR laser. The time domain model indicates that the intensity-modulated light will modulate the carrier concentration, which will temporally synchronize the window of net gain in the passively mode-locked laser. In the frequency domain model, the DSB-SC signal will inject into two modes of the mode-locked laser and establish phase coherence. Also, the frequency spacing of the DSB-SC signal will pull the slave laser mode spacing and alter the repetition rate. Figure 5-36 shows similar results where the modulation section of the monolithic laser does the sideband generation. Figure 5-37 shows a comparison between these two methods and where the sidebands are generated. As shown, the integrated hybrid mode-locked scheme offers a more compact system, and does not require an external electro-optic modulator. It is also important to note that the injected master laser is first passed through the modulation section of the three section laser, thus the sideband generation is different from that with the saturable absorber and modulation positions switched. In the case where the saturable absorber is at the output facet, the injected light will serve more as an optical DC bias and the generated side bands will be expected to be less significant.

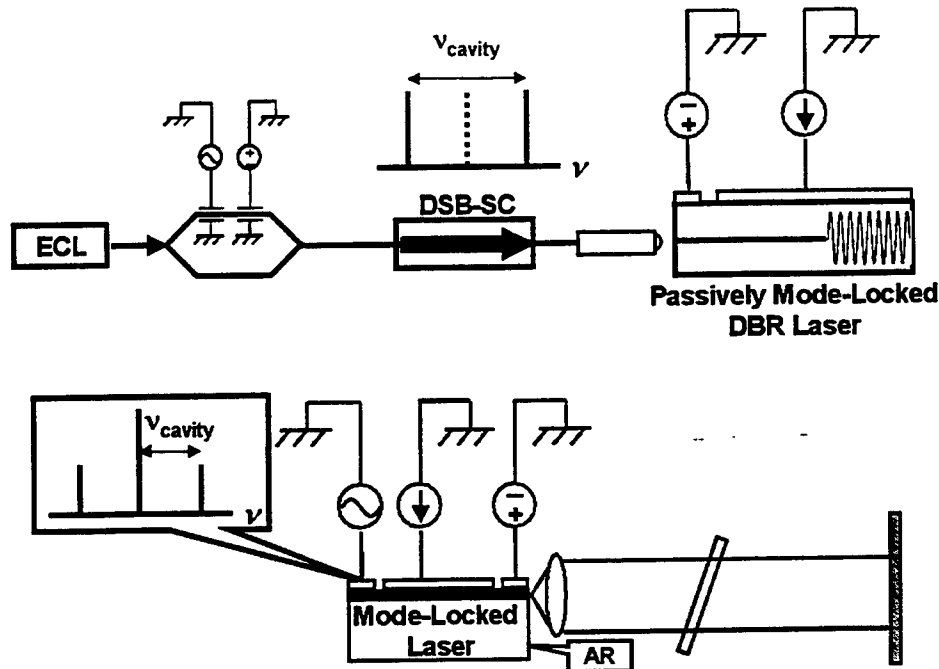


Figure 5-37. Generation of sidebands for various injection locking schemes

By tuning the wavelength of the master laser, the locking bandwidth can be determined by monitoring the heterodyne tones on the RF spectrum analyzer. The locking bandwidth is defined as the tuning range such that injection locking tones can be seen up to 5 GHz. By monitoring the heterodyne tones at frequencies up to 5 GHz, the generated sidebands from the injected mode would not contribute to the heterodyne tones in Figure 5-30, since powers of higher harmonics drop off rapidly with harmonic number. Therefore, the heterodyne tones are due to the beating of the frequency comb with the frequency-shifted master, not with the generated sidebands. Figure 5-38 shows the total locking range at various injection levels, and is shown to increase with increased injected optical power, as in the case of CW injection locking. During the course of the program various Japanese groups have reported similar results on CW injection locking of a mode-locked semiconductor laser [56,57].

The entire frequency comb does not pull uniformly, modes far away are not affected significantly by the injected light. This is evident in the heterodyne detection RF spectrum, the tones at 19 GHz are much more sensitive to tuning of the master laser; indicating modes far away are not well locked. Due to the imperfect AR coating ($\approx 1\%$),

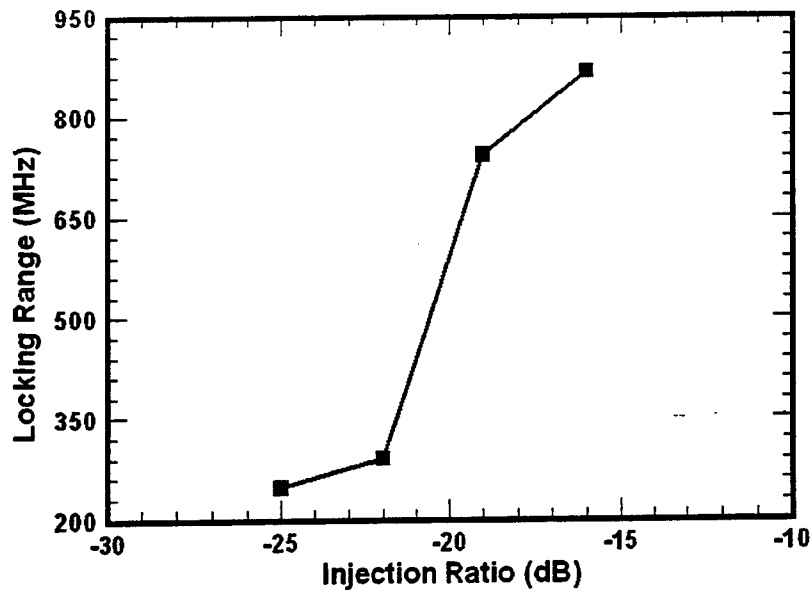


Figure 5-38. Locking range at various optical injection ratio

the gain profile is modulated by the monolithic mode spacing and gives rise to multiple supermodes.

Figure 5-39 shows the pulling of the frequency comb. With an injection ratio of -15 dB, the modes can be pulled approximately 400 MHz, which gives a locking range of 800 MHz. The locking range cannot be larger than the mode spacing since any mode of the mode-locked laser is within 500 MHz of the injected signal. Locking range appears to be symmetric, whereas injection locking of CW lasers results in an asymmetric locking range. A larger mode spacing, to eliminate the effects of neighboring modes, is required to determine the exact symmetry of the locking range. This can be achieved with monolithic mode-locked semiconductor lasers. The locking range is also expected to be a function of the cavity Q and the operating point of the laser. The low average power of the mode-locked laser indicates that the laser is slightly above threshold and is limited by the saturation intensity of the monolithic saturable absorber. Also shown in Figure 5-39 is an increase in power of the injected mode due to optical injection. Linewidth narrowing has also been observed by other groups [58]. At sufficiently high optical injection levels, this single mode will dominate and the mode-locking process will breakdown.

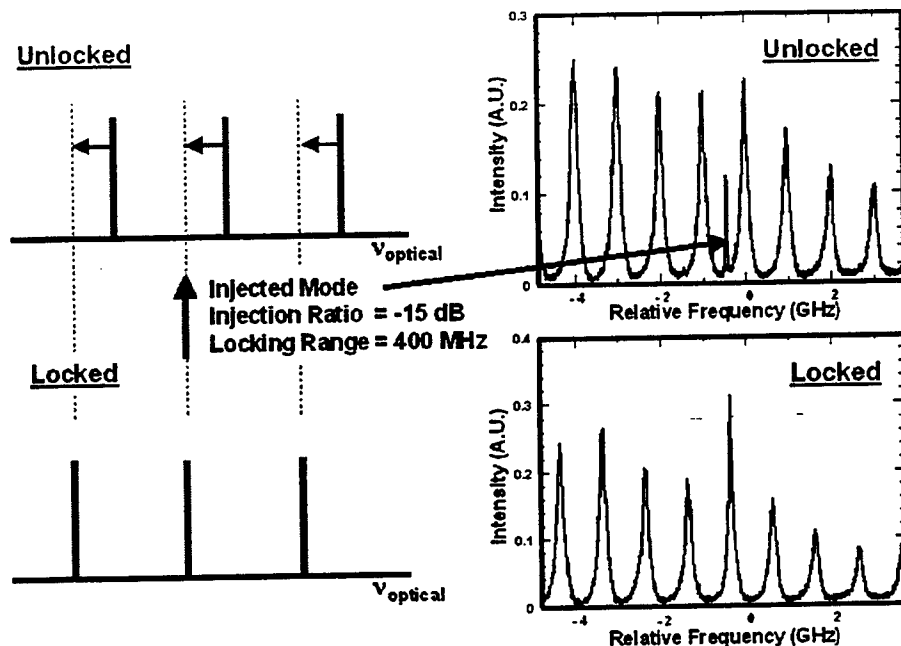


Figure 5-39. Pulling of mode-locked laser modes

Since the laser is hybrid mode-locked it is difficult to characterize how much pulse shaping the saturable absorber is doing compared to the modulator section. To achieve mode-locking, the reverse bias on the saturable absorber is increased until nearly 100% modulation depth of the pulses is observed in the autocorrelation trace. When this was obtained an RF drive of less than +10 dBm is applied to help stabilize the pulses. Due to the large impedance mismatch between the microwave probe and the laser (measured $Z_{in} = 5+j25$), less than 25% of the RF power is used to drive the laser. A larger spectral pulling range is expected for passively mode-locked lasers than for actively mode-locked lasers, since the modes pacing of an actively mode-locked laser are fixed precisely by the RF source.

An attempt was made to determine how well the slave laser is locked to the CW master laser, a modified setup shown in Figure 5-40 is used. An Erbium doped fiber amplifier (EDFA) is used to amplify the power per mode and a fiber Fabry-Perot (FFP) with a resolution of 1 GHz is used to filter out a single mode of the mode-locked laser. Significant power from adjacent modes is passed through due to the relatively wide 3 dB bandwidth of the FFP. (Figure 5-41) The filtered mode and the master laser are then detected on a photodetector. The RF spectrum analyzer shows a beat tone centered near

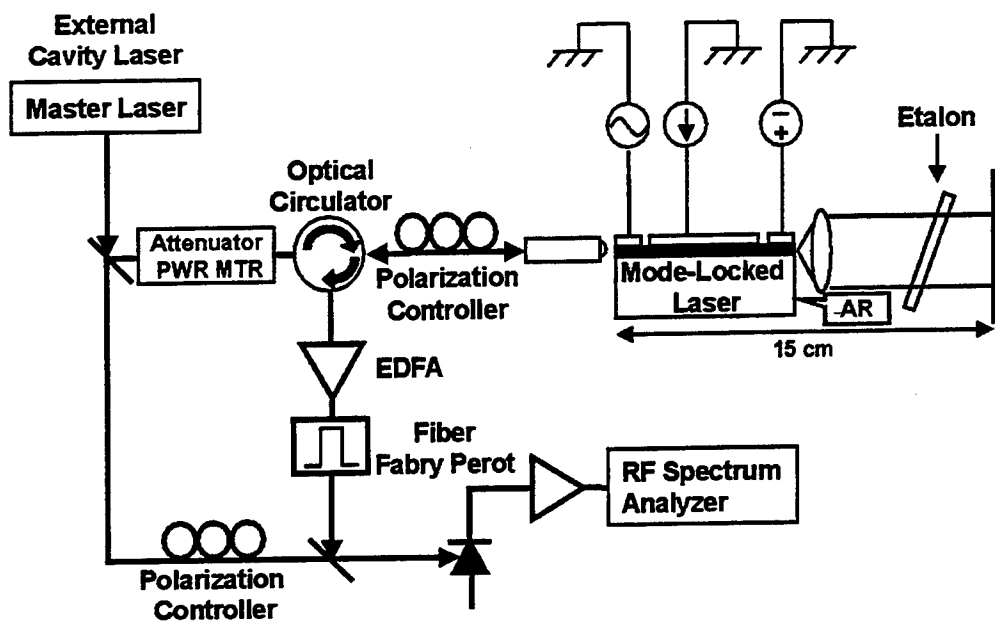


Figure 5-40. Experimental setup to filter the output of the mode-locked laser

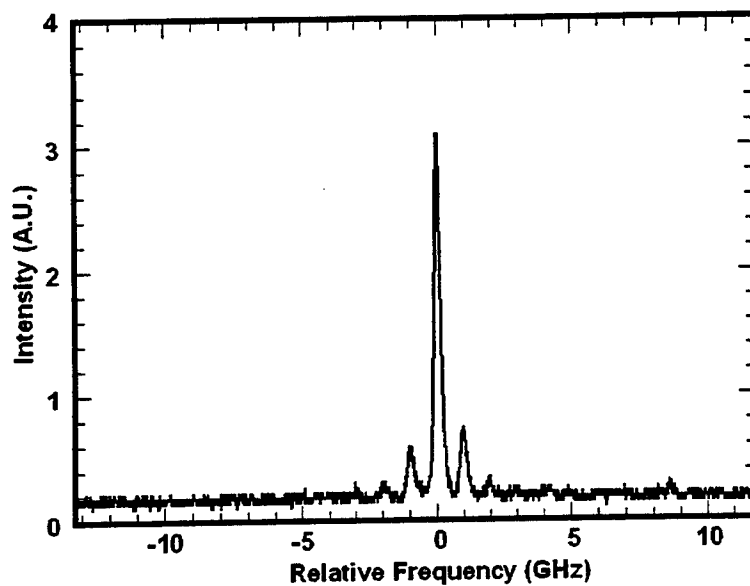


Figure 5-41. Filtered modes of the external cavity mode-locked laser

15 GHz, indicating that the 15th mode away from the injected mode is phase coherent with the master laser. A cluster of tones is seen near 15 GHz indicating that the 14th and 16th mode are also transmitted through the FFP. (Figure 5-42) The beating of the modes passing through are also evident at harmonics of the mode-locked laser. At low injection levels (≈ -40 dB), the heterodyne tones do not exhibit the sharp delta function as in Figure 5-41; instead a relatively broad beat tone is observed in Figure 5-43, indicating a low degree of coherence.

It is important to note that the detected tones will be similar to that of Figure 4-17. No attempt was made to balance the unknown path length difference in the heterodyne detection. The path length of the EDFA used is estimated to be between 18 and 25 meters.

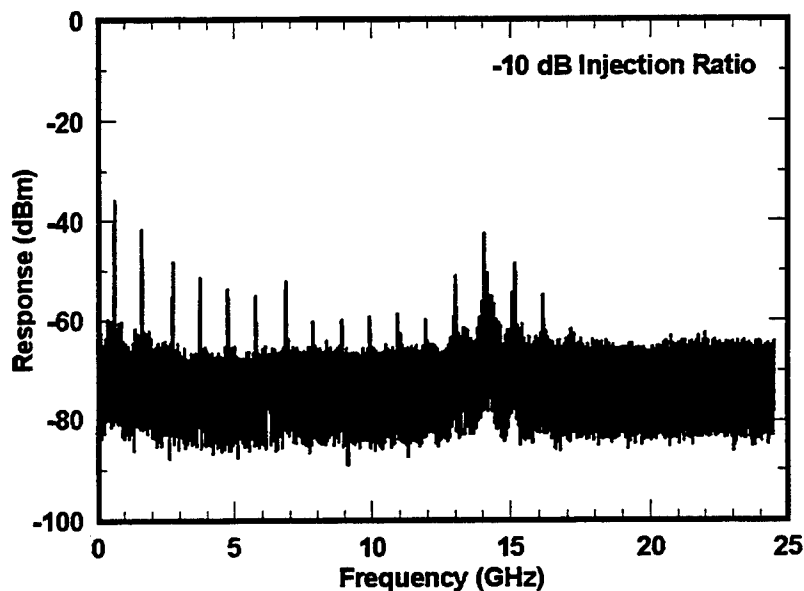


Figure 5-42. Heterodyne detection of filtered mode-locked laser modes and master laser

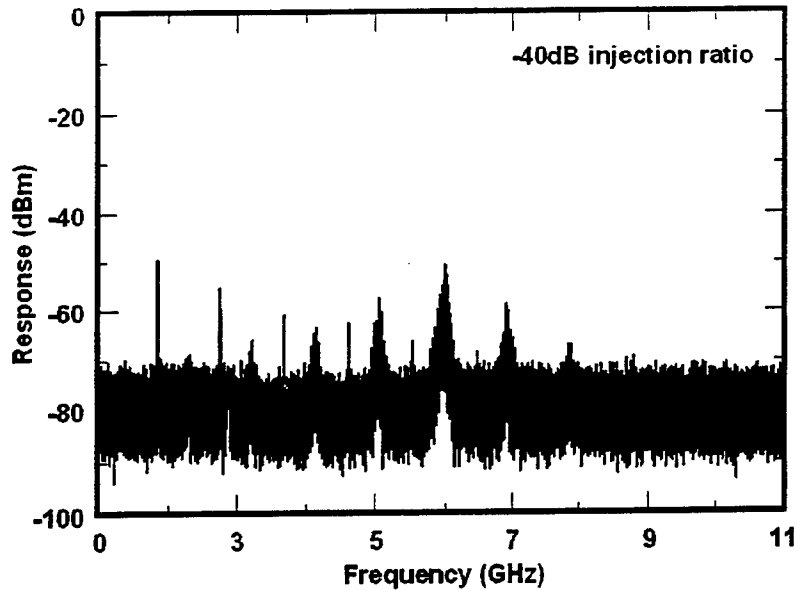


Figure 5-43. Heterodyne detection of filtered mode-locked laser modes and master laser under low injection

5.5 CONCLUSIONS

In conclusion, we have demonstrated that CW injection locking of a mode-locked external cavity semiconductor laser can provide a local oscillator source for an ultra-wide band coherent optical channelizer. Nearly transform limited pulses were obtained over a tuning range of 24 nm. Pulsewidths obtained were less than 2.5 ps, this corresponds to a signal bandwidth which can process signals with bandwidths greater than 100 GHz. Phase coherence between the incoming carrier signal and the local oscillator is achieved by optical injection locking. The coherence between the carrier laser and the optical frequency comb is dependent on how well the longitudinal modes of the mode-locked laser are phase locked. Preliminary results from injection locking of two CW lasers indicate that the phase noise can be as low as -125 dBc/Hz at a 10 kHz offset. Injection locking is also shown to be able to pull the optical frequency comb by as much as 400 MHz (corresponding to a total locking range of 800 MHz), which allows the local oscillator to track frequency drifts in the carrier signal. Only at injection levels comparable to the average power of the mode-locked laser do the pulses begin to distort and break up.

Optical injection locking of mode-locked semiconductor lasers opens up many new applications in optical communication systems. This technique is not limited to the use

of semiconductor lasers, and is expected to be observable in other laser systems. By replacing the external cavity semiconductor laser with a actively mode-locked fiber laser, higher power per mode can be accomplished. The side mode suppression can be increased by using coupled cavities and intra-cavity filters. A fiber laser also alleviates the need for high performance AR coatings; and because the light is guided inside a fiber, the laser is very tolerant to environmental disturbances. By removing the modulation of the gain spectrum, a more uniform pulling of the spectrum and better phase coherence is expected since only one supermode will dominate. Active mode-locking can also give a higher degree of coherence among the modes in the spectrum, therefore modes far away from the injected mode is expected to have a higher degree of coherence with the master laser. Another alternative for a local oscillator laser source would be the new micro-chip lasers utilizing a diode pumped Er:Glass gain medium. The use of a compact gain medium allows relatively short cavities for fundamental operation at a frequency of 1 GHz, and eliminates the problem of side mode suppression in harmonic mode-locking.

6 OPTICAL CHANNELIZER TESTBED

At the outset of the program it was felt that the optical channelizer would take on one of two forms: a high-resolution grating spectrograph-based channelizer, or a fiber optic-based filter bank, in particular a set of fiber Fabry-Perot filters. It was clearly evident as a result of our analysis that the latter approach was incapable of delivering the RF performance demanded by the intended application. The typical passband response for the fiber Fabry-Perot rolled off far too slowly to make it viable in terms of channel response uniformity. The channel response characteristic could be made more favorable by serially connecting several (upwards of 7 to 10) filters, but in addition to the obvious complexity implications a serious drawback is that the channelizer's optical throughput would suffer greatly. On the other hand, we found that a properly designed grating channelizer could provide the desired performance. In this approach a diffraction grating is used as a spatially dispersive element to channelize the RF spectrum in a single parallel operation. A mode-locked laser generates the local oscillator set that is injected onto the same grating but at an offset angle to define the IF frequency. The RF modulated optical spectrum and the offset local oscillator spectrum are imaged onto a detector array or alternatively, onto an array of optical waveguides that routes the spectral components to the detector elements.

A channelizer testbed was designed to provide a means for characterizing key aspects of the coherent optical receiver performance, including optical heterodyne frequency translation and wideband channelization with a passive dispersive element. Figure 6-1 shows the functional layout of the channelizer testbed. In summary, the original channelizer test plan called for the performance the following experiments:

1. Observe an RF signal's spectrum on an infrared imaging device at the channelizer's focal plane.
2. Introduce the (single frequency) optical L.O. beam and observe the heterodyne signal in the photo-detector.
3. Apply multi-tone signals to the modulator and perform multi-channel detection at the photo-detector by changing the L.O. frequency.
4. Insert a mode-locked laser into the system. Observe the L.O. spectrum on the focal plane imager.

In addition to performing these tasks we measured the critical RF performance characteristics of the system and verified that this approach was capable of providing the performance required of future EW receiver systems.

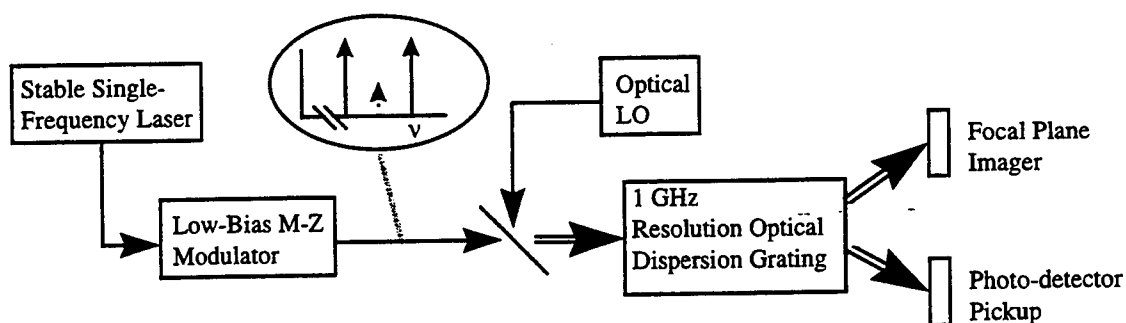


Figure 6-1. The channelizer testbed is a powerful tool for characterizing coherent optical receiver performance.

In this section we describe the design and construction of the channelizer testbed, which encompasses the rationale leading to the selection of the specific components used in the testbed and the evolutionary development of the optical layout. Also we present the results of the optical characterization of the testbed's components. Finally we describe the experiments that were performed and relate the results to our model-based calculations.

6.1 CHANNELIZER DESIGN

Table 6-1 lists those design goals, which were established at the outset of the program, that are pertinent to the design of the optical channelizer.

Table 6-1. Nominal channelizer RF performance requirements

Parameter	Performance Specification
Instantaneous Bandwidth	100 GHz
Channel Bandwidth	1 GHz
Spur-Free Dynamic Range	>50 dB
IF Output Frequency	~5 GHz
Crosstalk	< -70 dB
Channel Response Uniformity	< 3 dB

These requirements primarily were derived from the RF requirements for a “typical” high-performance electronic support measure (ESM) receiver.

The actual design process of the channelizer followed the flow path shown in figure 6-2. The key component in this type of channelizer is the diffraction grating. Since the scope of this phase of the program was for proof-of-concept and not form fit and function, we did not undertake to design and fabricate the optimal custom diffraction grating. This would have been prohibitively expensive and added no value to the program. Therefore our system was based primarily on an “off-the-shelf” grating that could be built into a system to provide the desired resolution. This turned out to be a not too severe constraint, but it did require that we select the best candidate available and design the spectrometer around it. Once a suitable grating was identified the optical layout was designed. This determined the sizes of the optical beams and the system’s dispersion, which when considered with the RF requirements dictated the configuration of the input/output (I/O) optics. The I/O optics comprise two entities: (1) the focal plane layout, which is where the signal-bearing (carrier) and L.O. beams are introduced into the system and where the signal spectrum is observed; and (2) the channelizer lens which collimates the input beams and images the signal spectrum onto the output focal plane.

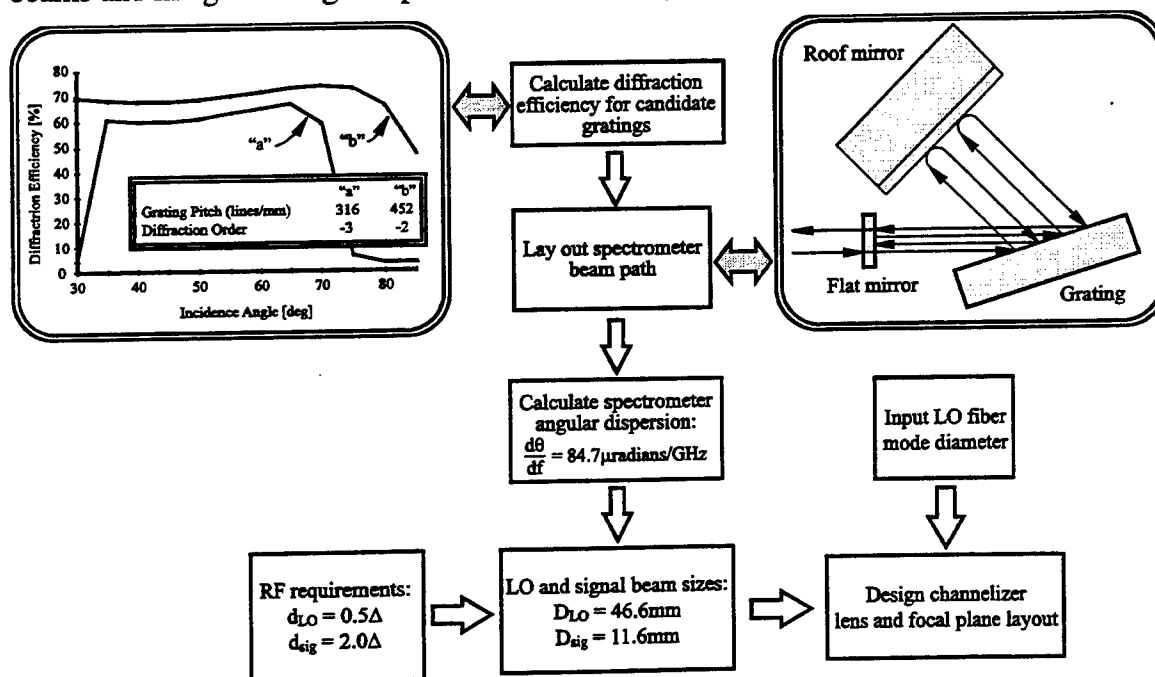


Figure 6-2. The channelizer design is based on a suitable off-the-shelf diffraction grating and the RF performance requirements.

6.1.1 Grating selection

As mentioned above we elected to choose a grating off-the-shelf and work the design of the channelizer around the selected grating. There are several criteria relevant to choosing an appropriate grating. Among them are the grating's resolving power, the grating's diffraction efficiency at the operating wavelength, and to a lesser degree of importance for our purposes, the overall size of the grating and the resulting optical system. Our selection pool was drawn from the catalog of Richardson Laboratories, a well-known and highly regarded source for diffraction gratings used in a number of applications.

Two factors determine the resolving power of a grating. First is the theoretical resolution capability that can be expressed as

$$\mathcal{R} = \lambda / \Delta\lambda = mN, \quad (6-1.1)$$

where λ is the operating wavelength, $\Delta\lambda$ is the resolvable wavelength, m is the diffraction order, and N is the number of grating grooves illuminated by the optical beam. \mathcal{R} is the standard Rayleigh resolution, in which the grating (assumed infinite in extent in the direction parallel to the grooves) is illuminated by a uniform beam. Assume that the input beam comprises only two frequency components, then $\Delta\lambda$ is the difference in wavelength that will cause the peak of the far-field pattern for one of the diffracted wavelengths to coincide with the first null of the far-field pattern for the other diffracted wavelength.

(6-1.1) can be rewritten with the help of the following grating equation.

$$k \sin\theta_i + k \sin\theta_d = mK, \quad (6-1.2)$$

where $k = 2\pi / \lambda$ is the optical k-vector and $K = 2\pi / \Lambda$ is the grating k-vector, Λ is the grating period. θ_i and θ_d are the optical beam's angles of incidence and diffraction respectively, measured with respect to the grating normal. As shown in Figure 6-3, the relationship between these angles is determined from the phase-matching condition for Bragg diffraction. Using the expressions for k and K in (6-1.2) leads to the following expression for the grating's resolution.

$$\mathcal{R} = N\Lambda (\sin\theta_i + \sin\theta_d) / \lambda = W (\sin\theta_i + \sin\theta_d) / \lambda, \quad (6-1.3)$$

where $W = N\Lambda$ is the width of the grating illuminated by the optical beam.

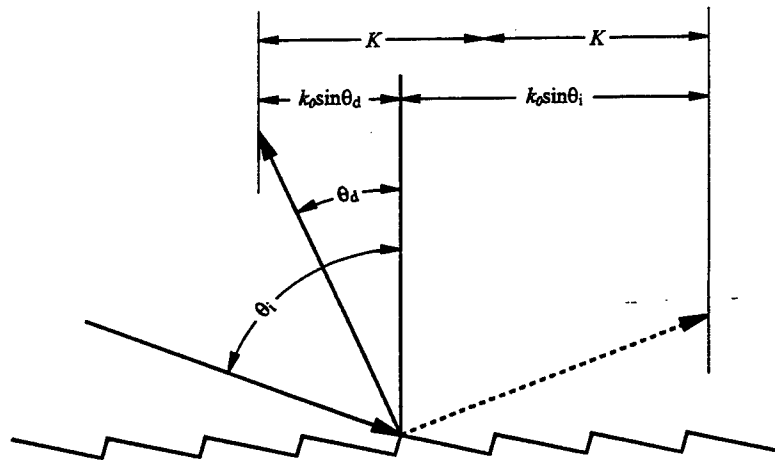


Figure 6-3. k -vector diagram for Bragg diffraction from a grating. We have illustrated the case of diffraction order $m = 2$.

Second, the degree to which the theoretical resolving power can be attained depends on the optical quality of the grating surface and the uniformity of the groove spacing. Any departure greater than $\lambda/10$ from flatness for a plane grating will result in a loss of resolving power. Also the grating groove spacing must be kept constant to within about 1% of the wavelength. These effects generally are specified by the grating manufacturer as an aggregate diminution of the grating's resolving power.

The actual requirement for resolving power is determined by the desired RF resolution of 1GHz at an operating wavelength of $1.55\mu\text{m}$. We have

$$\mathcal{R} = \lambda/\Delta\lambda = \nu/\Delta\nu = c / (\lambda \Delta\nu) \approx 2 \times 10^5, \quad (6-1.4)$$

where c is the speed of light in vacuum. We anticipated that our RF performance specifications would impose a more demanding requirement on our optical system than the standard Raleigh criterion so we adopted a target value of 10^6 as our resolution goal. As it turned out, this was very nearly the resolution we needed to meet our program objectives. In order to achieve this resolution we narrowed our search space to a group of large astronomical gratings that are designed for use near our operating wavelength of $1.55\mu\text{m}$. Two gratings in particular appeared to be viable candidates. The first was a grating with 316 grooves per mm, ruled over an area of 309mm high by 370mm wide.

We refer to the direction parallel to the grooves as the grating height. The second candidate had 452 grooves per mm on an area of 209mm high by 310mm wide. The use of either of these gratings required a multi-pass layout in order to achieve the desired resolution. In Figures 6-4 and 6-5 we show some early layouts based on these gratings. The layout in Figure 6-4 uses the 316 groove per mm grating. Gratings #1 and #2 are used in third order while grating #3 is arranged in a Littrow configuration and is also used in third order. A total of five passes on the gratings are accomplished with this relatively compact folded geometry. The overall dimensions of this layout are about 75cm by 40cm.

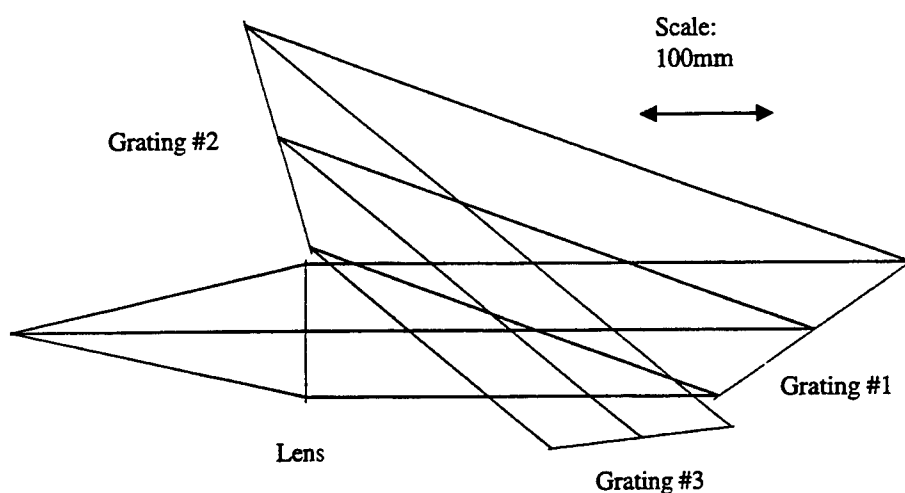


Figure 6-4. Channelizer layout using gratings with 316 grooves per mm

The layout in Figure 6-5 uses the 452 groove per mm grating. This layout is analogous to that in Figure 6-4 except here all of the gratings are used in second order. The overall dimensions of this layout are slightly larger at about 90cm by 45cm.

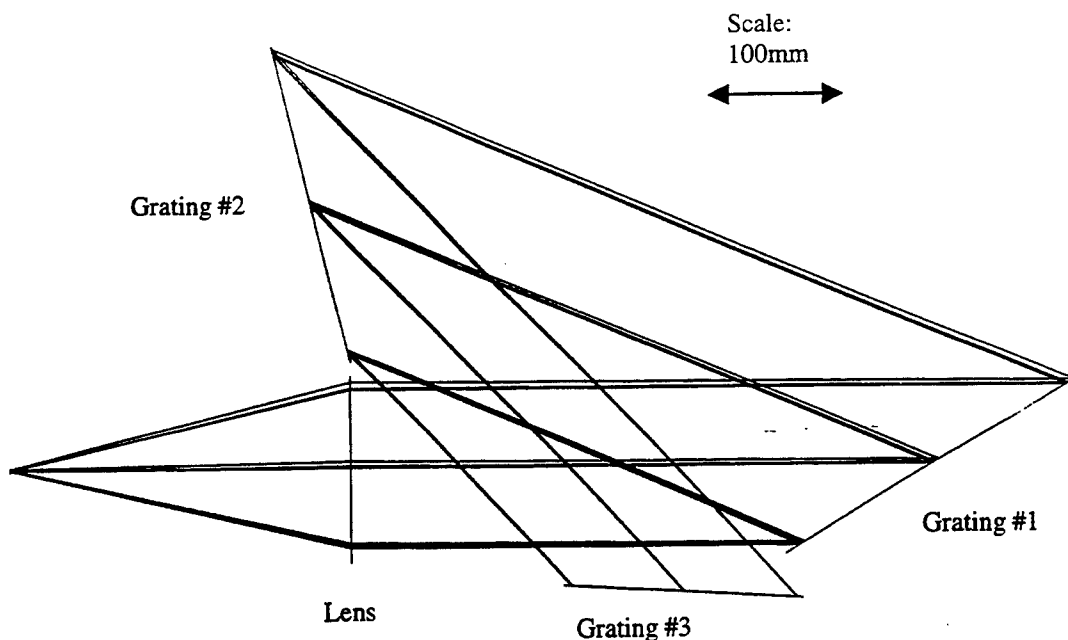


Figure 6-5. Channelizer layout using gratings with 452 grooves per mm

The sizes of the gratings for the two systems are given in Table 6-2. It can be seen that their sizes preclude the cutting of two or more of the gratings from a single master, which in itself would be an enormously risky venture. Thus for either of the layouts three separate gratings would have to be purchased, at about \$40,000 to \$50,000 each, with much of the gratings' areas unused.

Table 6-2. Grating sizes for two channelizer layouts

Candidate grating	grooves per mm	#1 and #2 widths	#3 width
"A"	316 (Figure 6-4)	223 mm	165mm
"B"	452 (Figure 6-5)	231mm	186mm

In order to use the available area of a grating more efficiently and to minimize the cost of the system, the layout shown in figure 6-6 was devised. In this layout a total of four passes are made at a single full-sized grating by using a roof mirror and a plane mirror. The actual optical path through the system can be seen in the figure.

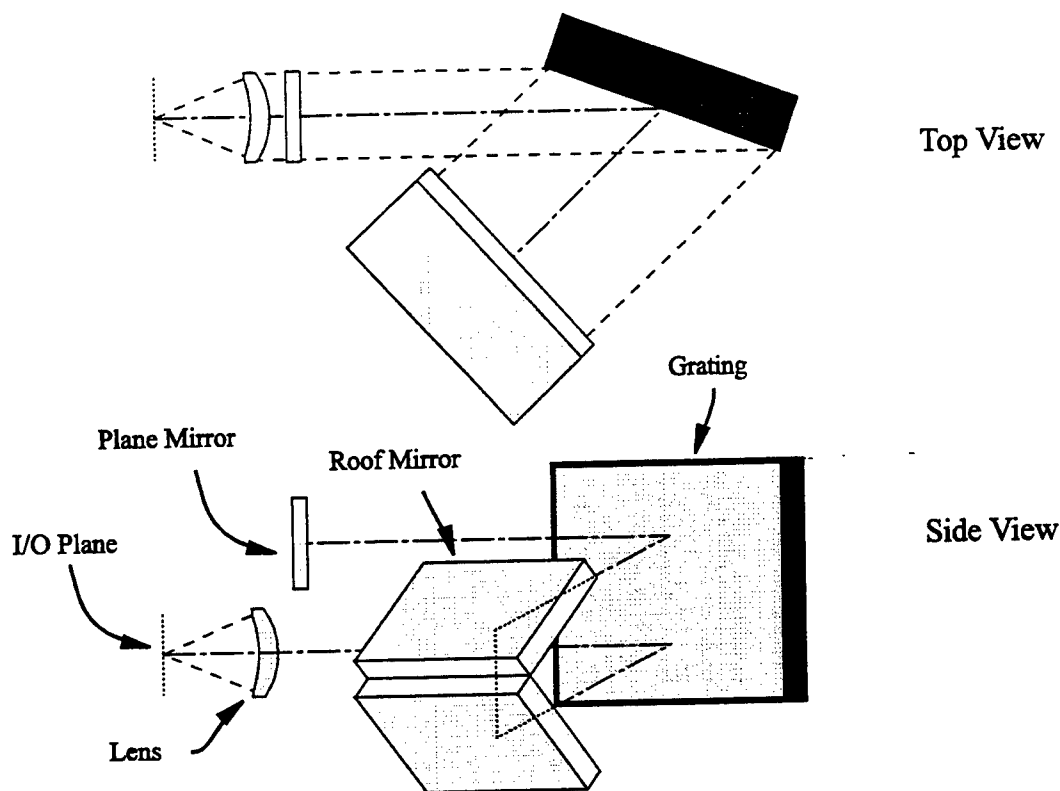


Figure 6-6. Channelizer optical layout that uses a single diffraction grating

In order to determine which of the two grating candidates would best suit our needs we calculated their diffraction efficiencies at an optical wavelength of $1.55\mu\text{m}$ for the allowed range of beam incident angles. By allowed angles we mean those incident angles that diffract into the desired order ($m=3$ for 316 grooves per mm or $m=2$ for 452 grooves per mm) in accordance with (6-1.2). We performed the computation for P-polarized light and S-polarized light, where in grating parlance the P components of the incident and diffracted beams are polarized parallel to the grating grooves and the S components are polarized perpendicular to the P components. This is in contrast to the standard definition of P and S, which are determined with respect to the plane spanned by the incident and reflected beams. Our calculations showed that the P-polarized efficiency was negligible for these gratings. A surprising result of the calculation was that the highest efficiency was obtained when the incident beam was directed at the "back" side of the grating teeth in the manner depicted in Figure 6-3. We define this as the reverse orientation. With the grating rotated 180° to the forward orientation the diffraction efficiency was reduced considerably. This result was confirmed independently by

measurements made on a 452 grooves per mm grating by the supplier. The results of our calculations are presented in Figures 6-6 and 6-7.

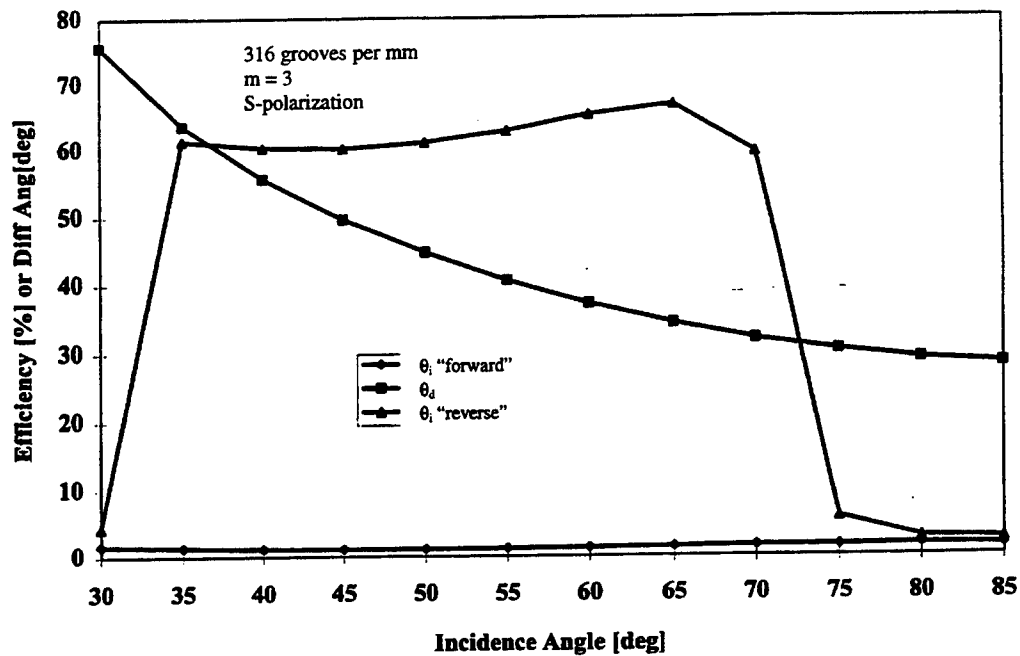


Figure 6-7. Diffraction efficiency as a function of incident angle for grating "A".

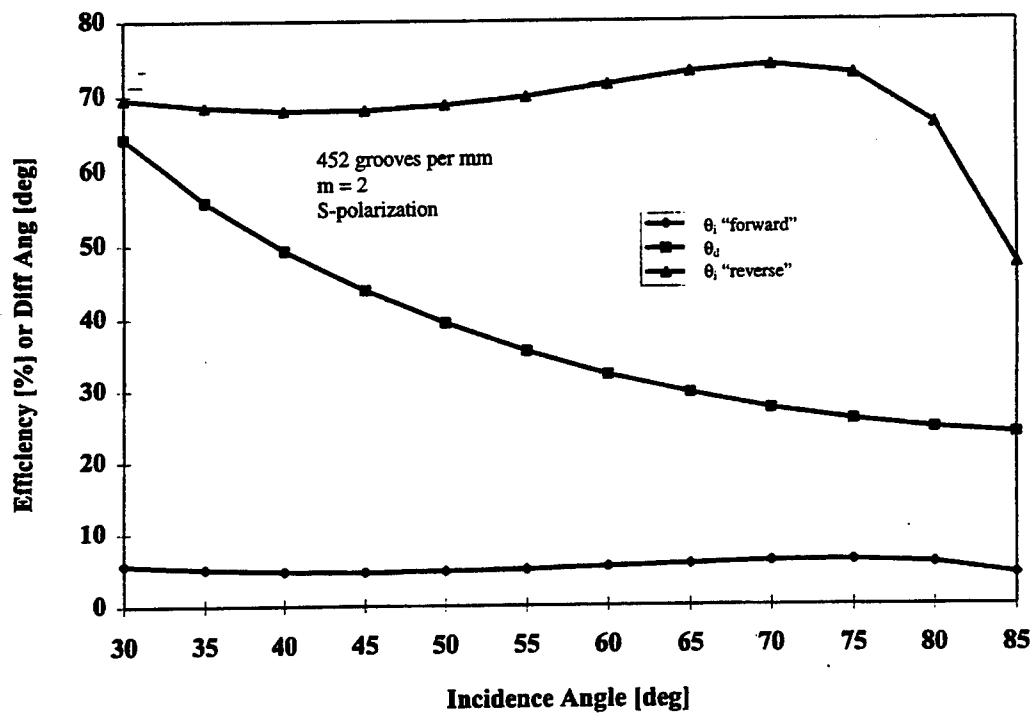


Figure 6-8. Diffraction efficiency as a function of incident angle for grating "B".

The overall diffraction efficiency for grating "B" is nearly 10% higher than that for grating "A". In our system requiring four passes on the grating this equates to a 70% greater throughput. Also the range of high-efficiency angles is broader for grating "B". This provides for additional flexibility in the layout of the optical path. For these reasons we selected grating "B" to build the channelizer.

We then performed a tolerance analysis, which entailed calculating the diffraction efficiency for variations of the grating tooth profile from the profile specified by the manufacturer. Refer to Figure 6-9 for the definition of the tooth parameters. The specified face angle is $FA = 15^\circ$, and the tooth apex angle is $AP = 90^\circ$. Figure 6-10 shows the diffraction efficiency as a function of incidence angle for several combinations of FA and AP. These results reveal only a mild dependence of the grating performance on the tooth profile. All of the calculations performed to this point assumed that the grating was overcoated with a standard aluminum reflectance coating. Richardson Labs provides a gold reflectance coating, and when applied on gratings used in their intended configuration these coatings offer superior performance in the infrared. In order to determine if gold would improve the performance of our grating, which is being used in a decidedly non-standard configuration, we performed calculations on a gold-coated grating and our results indicated that the diffraction efficiency is increased by about 5% over the aluminum-coated grating, therefore we specified a gold coating on the grating we purchased.

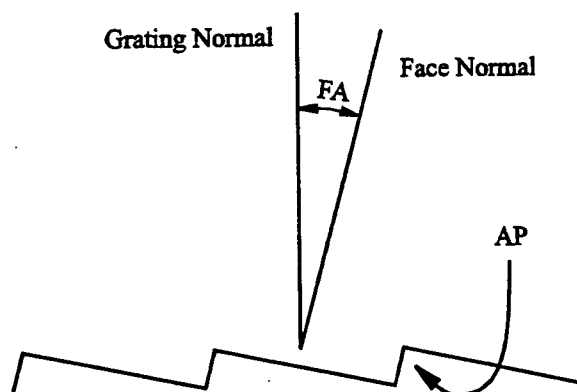


Figure 6-9. Diffraction grating tooth profile

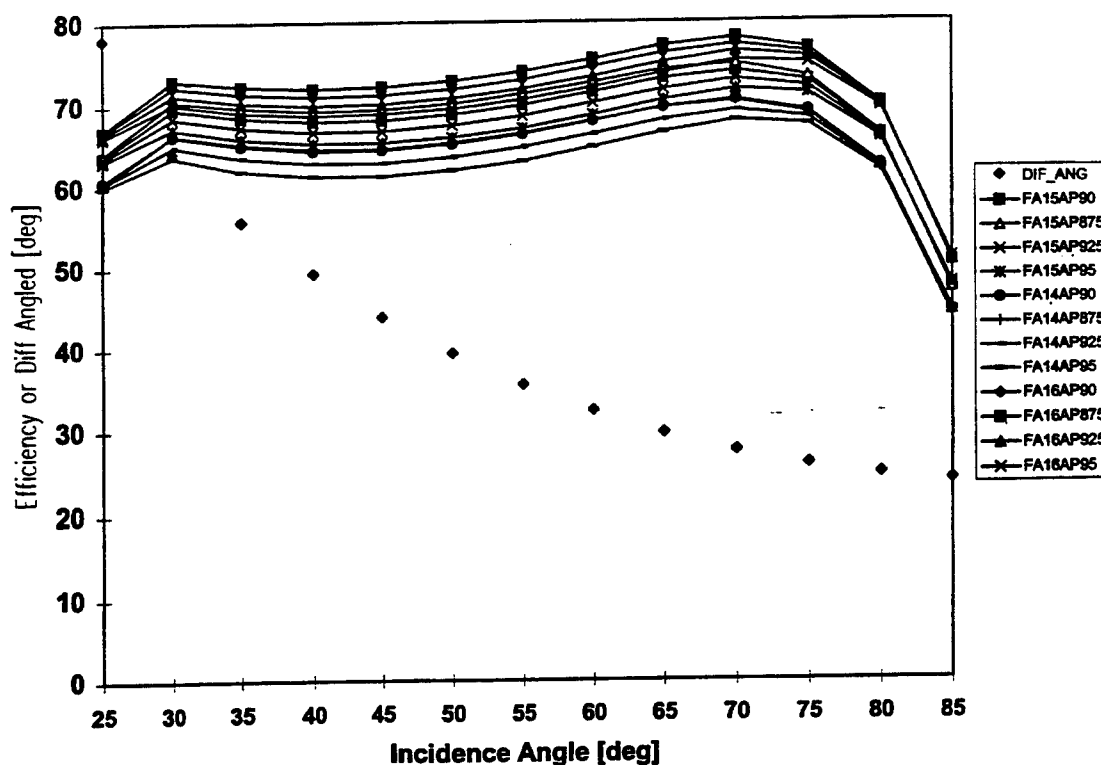


Figure 6-10. Diffraction efficiency for grating "B" various tooth profiles
Specified tooth angles: FA = 15°
AP = 90°

6.1.2 Channelizer angular dispersion and optical beam diameter

From Figure 6-8 we see that the grating efficiency peaks at an incident angle of about 70°. As the incident angle is decreased the efficiency drops off slowly until we reach the Littrow condition at just under 45°. As we decrease the incident angle further, the efficiency returns to a second maximum at about 27.5°, which is seen from (6-1.2) to be the diffraction angle for 70°. This behavior would be expected from a symmetry argument. Choosing $\theta_i = 70^\circ$ essentially sets the optical layout of the channelizer and we can now calculate the angular dispersion for the channelizer. We define angular dispersion as the incremental change in the optical beam's exit angle, $\delta\theta$, as a result of an incremental change in the optical frequency, $\delta\nu$. Referring to figure 6-11 we derive an expression for the angular dispersion of a multi-pass system as follows. Consider an incident beam at optical frequency ν (solid line) that is diffracted by the grating. The diffracted beam is reflected by the mirror back along its original path where it undergoes

a second diffraction and exits the system contralinear with the incident beam. If the optical frequency is increased by $\delta\nu$, the beam will follow the path given by the dotted line.

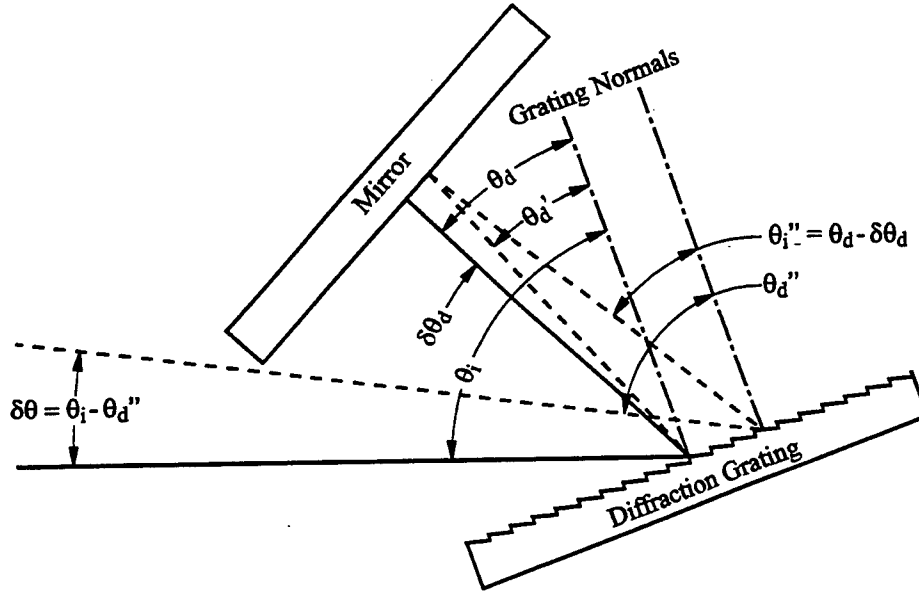


Figure 6-11. Angular dispersion in a multi-pass geometry

We rewrite (6-1.2) as

$$\sin\theta_d = m\lambda/\Lambda - \sin\theta_i. \quad (6-1.5)$$

Since θ_i is fixed we differentiate and get

$$\begin{aligned} \cos\theta_d \delta\theta_d &= (m/\Lambda) \delta\lambda \\ &= - (m\lambda^2/c\Lambda) \delta\nu, \end{aligned} \quad (6-1.6)$$

which gives us

$$\delta\theta_d = - (m\lambda^2/c\Lambda) (1/\cos\theta_d) \delta\nu. \quad (6-1.7)$$

From the construction in Figure 6-11 we can see that the diffracted beam at frequency ν is reflected back towards the grating and is incident at $\theta_i'' = \theta_d$, and diffracted at $\theta_d'' = \theta_i$.

For the second diffraction the grating equation gives us

$$\sin\theta_d'' = m\lambda/\Lambda - \sin\theta_i''. \quad (6-1.8)$$

We now differentiate (6-1.8) and note that θ_i'' does not remain constant.

$$\begin{aligned} \cos\theta_d'' \delta\theta_d'' &= (m/\Lambda) \delta\lambda - \cos\theta_i'' \delta\theta_i'' \\ \cos\theta_i \delta\theta &= (m/\Lambda) \delta\lambda - \cos\theta_d \delta\theta_i'' \end{aligned} \quad (6-1.9)$$

We also see from the figure that $\delta\theta_i'' = -\delta\theta_d$, so we can write (6-1.9) as

$$\begin{aligned}\cos\theta_i \delta\theta &= (m/\Lambda) \delta\lambda + \cos\theta_d \delta\theta_d \\ &= 2(m/\Lambda) \delta\lambda.\end{aligned}\tag{6-1.10}$$

This gives us

$$\delta\theta = -2(m\lambda^2/c\Lambda) (1/\cos\theta_i) \delta\nu.\tag{6-1.11}$$

In the case of the channelizer, we pass through the identical system a second time, which leads to the result

$$\delta\theta_{\text{channelizer}} / \delta\nu = -4(m\lambda^2/c\Lambda) (1/\cos\theta_i).\tag{6-1.12}$$

For $\lambda = 1.55\mu\text{m}$, $\Lambda = 2.212\mu\text{m}$, $c = 3 \times 10^8\text{m/s}$, and $m = 2$ we have for the angular dispersion of the channelizer

$$\delta\theta_{\text{channelizer}} / \delta\nu = 84.7\mu\text{radians} / \text{GHz}.\tag{6-1.13}$$

We now wish to determine the sizes of the L.O. and carrier beams. In section 3 we arrived at the conclusion that the sizes of the focussed L.O. and carrier spots necessarily must be unequal in order to achieve the desired RF channel response characteristics. Recall that our analysis assumed that each of the beams is a Gaussian distribution, which is a good approximation for a single-mode fiber's mode profile. In this section when we refer to the sizes of the focussed spots and beam sizes we are talking about the $1/e^2$ diameters. Guided by our analysis of Section 3, we chose to make the L.O. spot diameter, $d_{\text{L.O.}}$, equal to one half the detector spacing that corresponds to 1GHz in the focal plane, Δ . This dictated that a carrier spot of about twice the detector spacing was required to ensure a crosstalk specification of about -70dB. This combination of spot sizes delivered less than 3dB of ripple and loss, which are considered well within the acceptable range.

Now consider the L.O. beam. Assume we are using a lens with focal length, fl . Then the spacing in the lens focal plane corresponding to 1GHz in optical frequency is given by

$$\Delta = fl \times (\delta\theta_{\text{channelizer}} / \delta\nu) \times (1\text{GHz}) = fl \times 84.7 \times 10^{-6}.\tag{6-1.14}$$

We want the L.O. spot size to be half of this,

$$d_{\text{L.O.}} = fl \times 42.35 \times 10^{-6}.\tag{6-1.15}$$

The general relationship between a collimated Gaussian beam size and its focussed spot size is

$$D = (4 fl \lambda) / (\pi d).\tag{6-1.16}$$

Substituting (6-1.15) into (6-1.16) and solving for $D_{L.O.}$ leads to the following for the size of the L.O. beam propagating in the channelizer.

$$D_{L.O.} = (4 \lambda) / (\pi \times 42.35 \times 10^{-6}) = 46.6\text{mm} \quad (6-1.17)$$

Similarly we find for the carrier beam,

$$D_c = (4 \lambda) / (\pi \times 169.4 \times 10^{-6}) = 11.6\text{mm} \quad (6-1.18)$$

Another consideration that was explored during our analysis was the extent to which diffraction sidelobes due to finite beam size compromised the crosstalk performance. We determined that for the case where $d_{L.O.} = 0.46 \times \Delta$, which is essentially our design point, it was necessary to truncate the local oscillator beam at about twice its $1/e^2$ diameter to insure -70dB crosstalk. Consider the grating that we selected for the channelizer and a 70° angle of incidence. The 310mm grating width projects back to a maximum input beam diameter of $310\text{mm} \times \cos 70 = 106.0\text{mm}$. This is well in excess of $2 \times D_{L.O.} = 93.2\text{mm}$ demanded by the crosstalk requirement.

6.1.3 Channelizer focal plane layout

The selected optical layout for the channelizer uses a single lens to perform two of the critical optical processes for the channelizer. The first is to expand and collimate the local oscillator and carrier beams and present them to the dispersive (grating) portion of the channelizer. The second function is to focus the spatially dispersed spectral components of those beams so that they may be resolved and detected. The focussed input and output beams must be separated in the lens's back focal plane sufficiently to minimize the possibility of crosstalk due to light leakage between input and output and to permit the placement of the physical means for launching and collecting the beams. This is accomplished by displacing the input beams from the system's optic axis. As a result the return beams will be displaced a like amount in the opposite sense. In the case of an actual receiver a natural choice to implement this would be an array of channel waveguides most likely fabricated on a silicon substrate. Several vendors provide glass-waveguide-on-silicon foundry services (e.g. Photonic Integrated Research, Inc. or Lucent Technologies). The waveguides would fan out from the focal plane to provide sufficient separation for coupling the outputs to an array of detectors and input-couple the optical fibers bearing the L.O. and carrier beams. This arrangement provides the added

advantage of not requiring a contiguous array of detectors, greatly mitigating the problem of suppressing the electrical crosstalk between the individual detectors.

For the purpose of satisfying the objectives of Phase I of the program it was not necessary to provide this level of component development. Recall that the primary purpose of the channelizer testbed was to demonstrate the essential receiver functions such as channelization and frequency translation. The most practical way to accomplish this was to launch the input beams directly from the cleaved or polished ends of single-mode fibers or as required, projecting a magnified image of the fiber's mode into the system. The focal plane layout we adopted actually displaced the inputs both horizontally and vertically from the optic axis as shown in Figure 6-12.

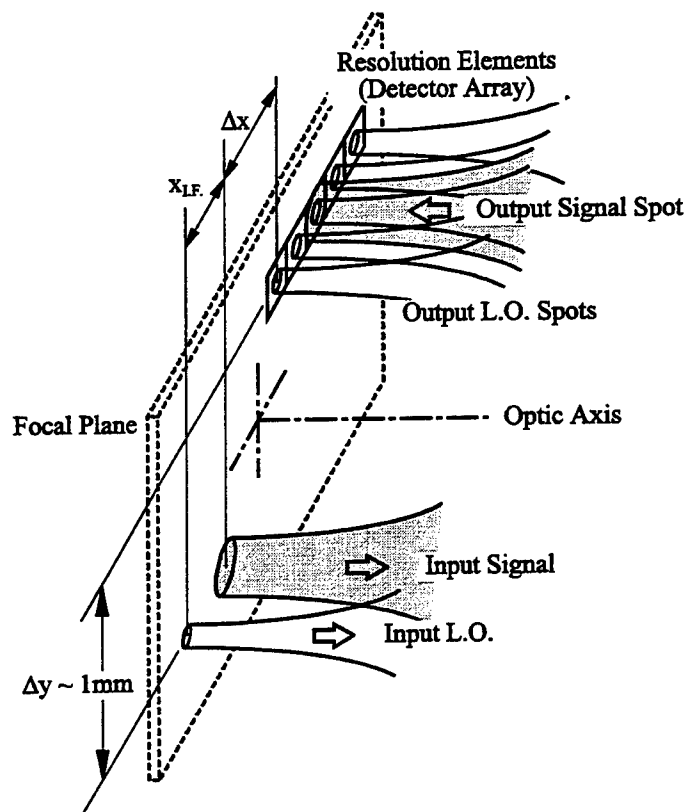


Figure 6-12. Channelizer testbed focal plane layout

The separation $\Delta y \sim 1\text{mm}$ was chosen to provide adequate separation to enable the use of off-the-shelf miniature optical components to deliver the input beams yet not be so large as to significantly increase the lens's field of view requirement. The separation, x_{LF} , between the input local oscillator and signal (carrier) beams is determined by the choice

of intermediate frequency. This distance, which is on the order of 50 μ m to 150 μ m, is too close to obtain directly without using a custom integrated optical circuit. We solved this problem by introducing a beamsplitter in the optical path. In so doing we provided duplicate optical paths leading to separate equivalent focal planes. Thus we were afforded considerable flexibility in physically positioning the various inputs and outputs. As it turned out the automated process we used to design the lens provided a convenient place to incorporate a beamsplitter in the lens itself. Details of the design will be provided in the following section. Obviously the beamsplitter causes a reduction of the optical throughput that would be unacceptable for a deployed receiver system, but that is not a critical issue with the testbed.

6.1.4 Channelizer testbed lens

6.1.4.1 Lens specifications

In a previous section we used the effect of the RF requirements on the spot sizes, coupled with the optical system dispersion to establish the collimated beam diameters, $D_{L.O.}$ and D_c , in the channelizer. We now factor in the mode radius of the fiber used for the L.O. input so we can determine the optical performance requirements for the channelizer's lens. The L.O. input spot size was used as the determinant for the following reason. Because it is smaller than the carrier spot we elected to launch the L.O. beam directly from the fiber output. This way the larger signal spot would be an expanded image of the fiber's output. Conversely, if the carrier spot were to be derived from the fiber directly then the L.O. spot would be a reduced image of the fiber's mode. This would have placed a severe burden on both the imaging optic used to obtain the reduced image and the channelizer lens. To illustrate, consider the arrangement shown Figure 6-13.

From the lens law we find that to perform a 4:1 reduction of the mode profile the lens focal length is 0.8 times the image distance, s_2 . The diameter of the Gaussian beam at the lens is given by

$$D = (4 s_2 \lambda) / (\pi d_2), \quad (6-1.19)$$

here d_2 is the image spot size.

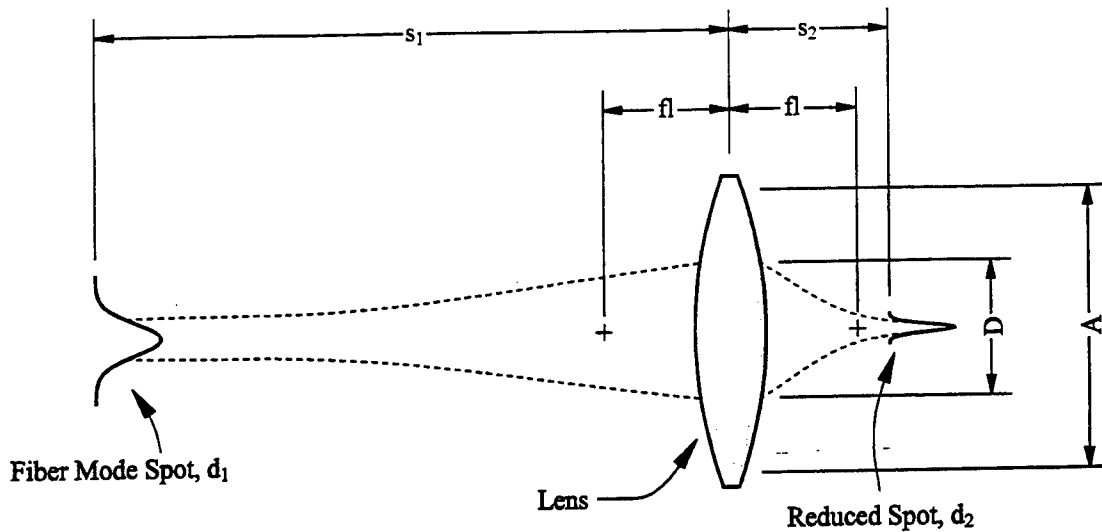


Figure 6-13. Reducing the size of the fiber mode spot requires a high-speed lens.

The lens aperture must be at least twice the Gaussian beam size, which leads to the following for the F-number of the lens.

$$\begin{aligned} F\# &= f_l / A = f_l / 2D = (0.8 s_2) (\pi d_2) / (8 s_2 \lambda) \\ &= (0.1 \pi d_2) / \lambda. \end{aligned} \quad (6-1.20)$$

The numerical aperture for the fiber is approximately

$$N.A. \approx D / 2 s_1 = D / 8 s_2 = \lambda / (2 \pi d_2). \quad (6-1.21)$$

By combining (6-1.20) with (6-1.21) and noting that typical single-mode fibers have a numerical aperture of about 0.1, we find that the required lens F# is

$$F\# = 0.1 / 2 N.A. = 0.5, \quad (6-1.22)$$

which is an extremely high-speed lens and very difficult to attain in practice.

For the purpose of designing the lens we used data provided by Fujikura Europe regarding the mode profile of their single-mode fiber. They measured the angular distribution of the far-field pattern for the fiber. We fit a Gaussian to the e^{-2} diameter of the measured data and calculated the equivalent Gaussian spot diameter of $10.06\mu\text{m}$ at the fiber. These results are shown in Figure 6-14. It can be seen that the measured profile deviates a little from the Gaussian as we move away from spot center. The variation is suggestive that the fiber mode is more like a truncated Gaussian, but overall the fit is adequate to use for the purposed of designing the lens.

We can determine the lens focal length, f_l , by rearranging (6-1.16).

$$f_l = (\pi D_{L.O.} d_{L.O.}) / \lambda = 237.6\text{mm} \quad (6-1.23)$$

The full aperture requirement is $A \geq 93.2\text{mm}$ leads to a nominal lens F# of F:2.5. These requirements were used to direct the design of the channelizer's lens.

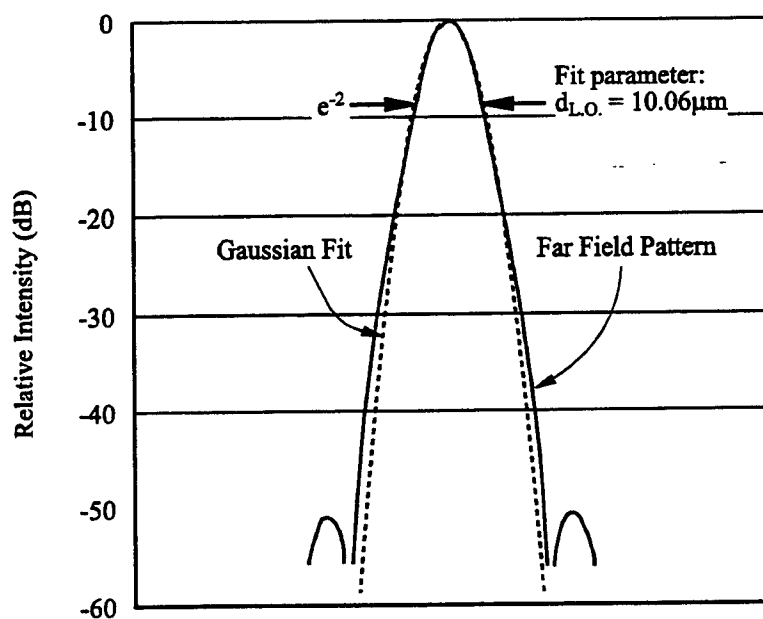


Figure 6-14. Far-field pattern for Fujikura single-mode fiber

6.1.4.2 Lens design

A mix of moderate and challenging requirements drove the design of the testbed lens. The lens F-number of 2.5 is certainly not a demanding figure in itself. Assuming the 100GHz output spectrum is displaced symmetrically about the optic axis, then the angular field-of-view is $\pm 84.7 \times 10^{-6} \times 50 = \pm 4.235 \times 10^{-3}$ radians = $\pm 0.243^\circ$. This too is not a severe design issue. We must qualify our assessment in that these are not difficult from the perspective of a standard imaging application such as a photographic lens. However when we demand near diffraction-limited performance over the field-of-view and further complicate the issue with the condition that the field angle (i.e. spot position in the focal plane) is wavelength dependent then the design exercise becomes quite formidable. An additional difficulty is presented by the rather limited range of refractive indexes and dispersion coefficients exhibited by optical materials at the wavelength of $1.55\mu\text{m}$.

We used CodeV optical design software to find a solution to our lens problem. The program utilized the full system optical layout to derive an optimum lens configuration. Table 6-3 is a summary of the requirements and specification used to design the lens. The reader is referred to Figure 6-6 to understand the meaning of some of the dimensions listed in the table.

Table 6-3. Lens design specifications

Parameter	Description	Value
Fl	Focal length	237.6mm
A	Exit aperture diameter	95.4mm
F#	Lens speed (fl/A)	2.49
λ_c	Carrier wavelength	1550nm
Δv	Optical bandwidth	100GHz
D	Input Gaussian beam diameter	10.06 μ m
$\Delta\theta$	Field-of-view	$\pm 0.243^\circ$
n_1	Refractive index of glass 1 – SFL6	1.76274
n_2	Refractive index of glass 2 – SF8	1.65821
L_1	Distance from exit pupil to grating (measured on optic axis)	325mm
L_2	Distance from grating to roof mirror	325mm
L_3	Distance from grating to flat mirror	340mm
H_1	Beam displacement height by roof mirror	110mm

CodeV generated the construct shown in Figure 6-15 to trace rays through the system and calculate the ray aberrations and ray intercepts in the focal plane. The program then conducted a search of parameter space until it arrived at a solution that satisfies program-internal or user-designated constraints. Parameters that were permitted to vary were the number of elements, the thickness of the elements, the radii of curvature of the lens surfaces, and the distance between lens elements. Figure 6-16 shows the final design and gives the values of the various thicknesses, lens spacings, and radii of curvature. Note that the surfaces denoted by radii r_{11} , r_{12} , and r_{21} , are concave, while the remaining surfaces are convex.

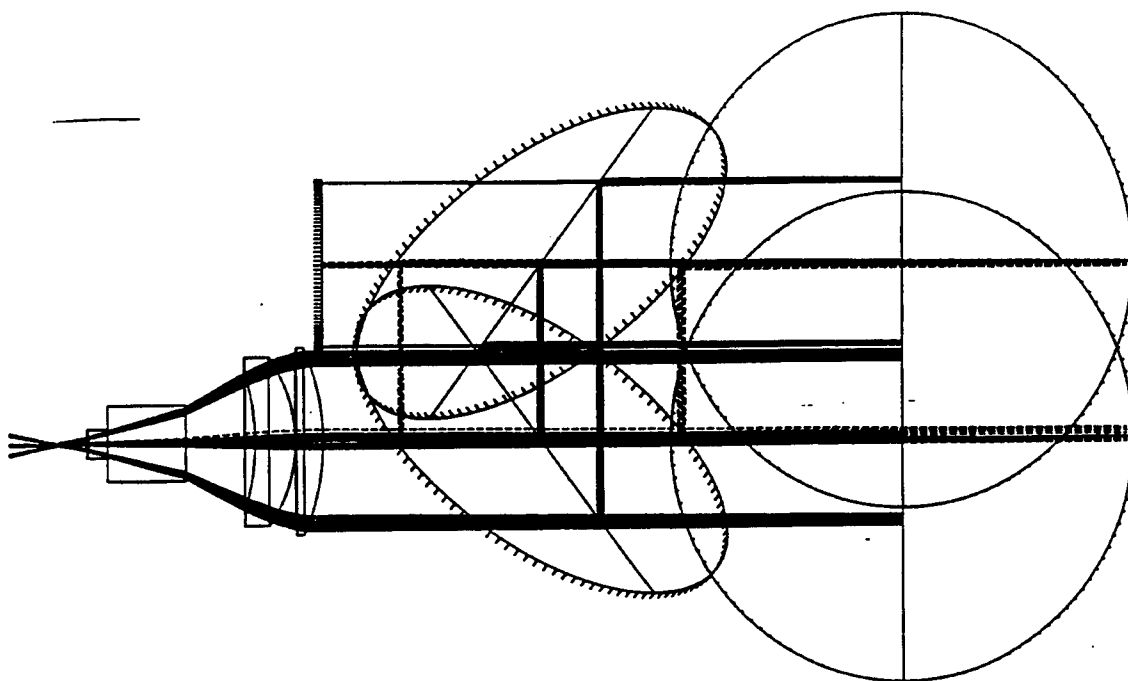
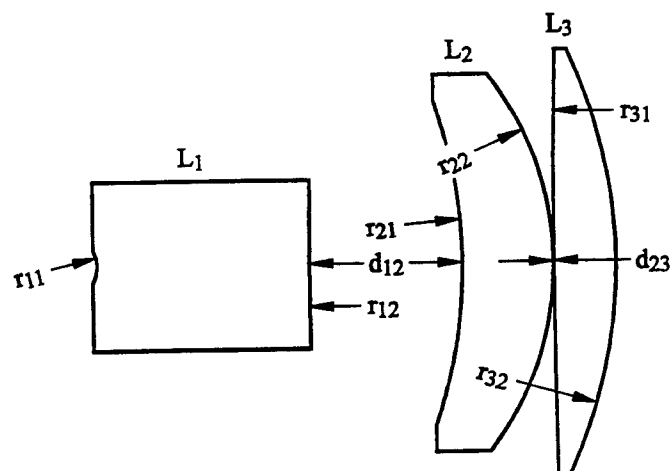


Figure 6-15. CodeV traces rays through the optical system to evaluate lens performance and optimize the lens design



Lens L ₁	Material: SFL6 d ₁₂ = 40.327mm	t ₁ = 56.388mm	r ₁₁ = 16.172mm	r ₁₂ = 2344.2mm
Lens L ₂	Material: SFL6 d ₂₃ = 0.100mm	t ₂ = 23.565mm	r ₂₁ = 130.94mm	r ₂₂ = 82.575mm
Lens L ₃	Material: SF8	t ₃ = 16.408mm	r ₃₁ = 2238.8mm	r ₃₂ = 132.68mm

Figure 6-16. Computer-optimized channelizer testbed lens comprises three elements manufactured from two glasses

The inter-lens spacings and the lens thicknesses are measured on the optic axis. Initially the number of elements was allowed to vary as CodeV designed the lens and the program produced some rather exotic multi-element (4 or more lenses). In the interest of maintaining a reasonable level of complexity, and thus fabrication difficulty and cost, we restricted the number of elements to a maximum of three.

All of the “good” three-lens designs included the very thick first element. This provided a convenient place to incorporate a beamsplitter, which is desirable to relieve congestion among the optical and mechanical components in the input/output focal plane. Figure 6-17 illustrates how the thick lens was reengineered to include the beamsplitter.

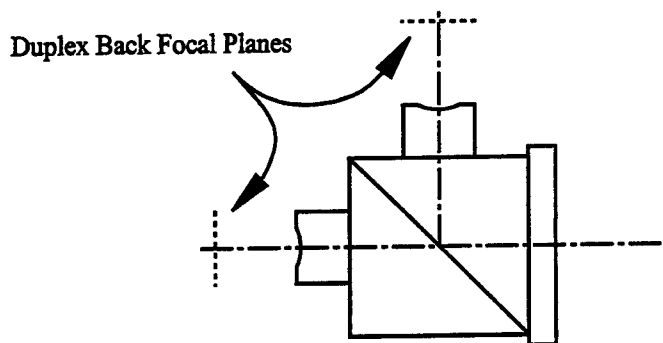


Figure 6-17. A beamsplitter was incorporated in the first lens element

6.1.4.3 Lens design verification

Before the lens was submitted to a manufacturer to be built we performed physical optics calculations on the design to verify that its performance would satisfy the channelizer's requirements. We also wanted to assess the design's tolerance to imperfections that naturally occur during the fabrication process.

The analysis involves tracing a set of rays through the system and plotting their intercepts in the output focal plane. Initially the rays are uniformly distributed in the input focal plane and amplitude weighted according to the intensity profile being analyzed, in our case the Gaussian approximation to the single-mode fiber's mode profile. In the following set of figures we show some examples of results of this calculation for several positions of the input beam. We also varied the frequency of the input beam by $\pm 50\text{GHz}$, which allowed us to determine the linearity of the system's dispersion and observe the lens performance throughout the channelizer's operational field-of-view. In Figure 6-18

we simply calculated the fiber's mode profile that was used as an input for the rest of the calculations. On the left, as is the case for all of these results, is the distribution of ray intercepts and on the right is an iso-intensity representation of the mode profile. The intensity contours are regularly spaced at intervals of about 0.04 (normalized to a value of 1 at the center) with the intensity of the outermost contour being about 0.02. This first calculation provided a sanity check on the technique and returned exactly the input Gaussian mode profile.

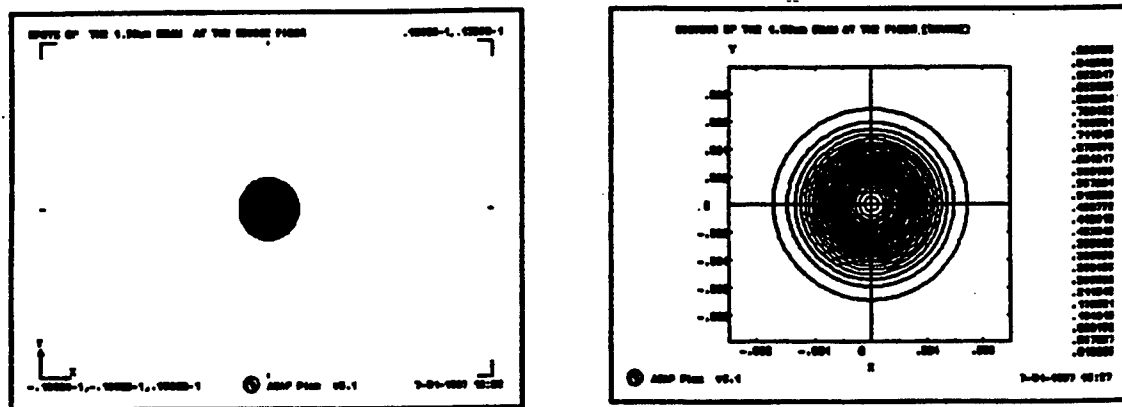


Figure 6-18. Physical optics calculation showing the output of a single-mode fiber and its mode profile.

In Figure 6-19 we launched the input mode on the optic axis and calculated the resulting reimaged spot. We can see some change in the ray intercept distribution from the uniform one in Figure 6-18, but this results in no perceptible change in the intensity pattern. Also as expected, the position of the image is centered on the optic axis at coordinates (0, 0). For reference, the size of the box surrounding the spot is always 20 μ m square unless otherwise noted.

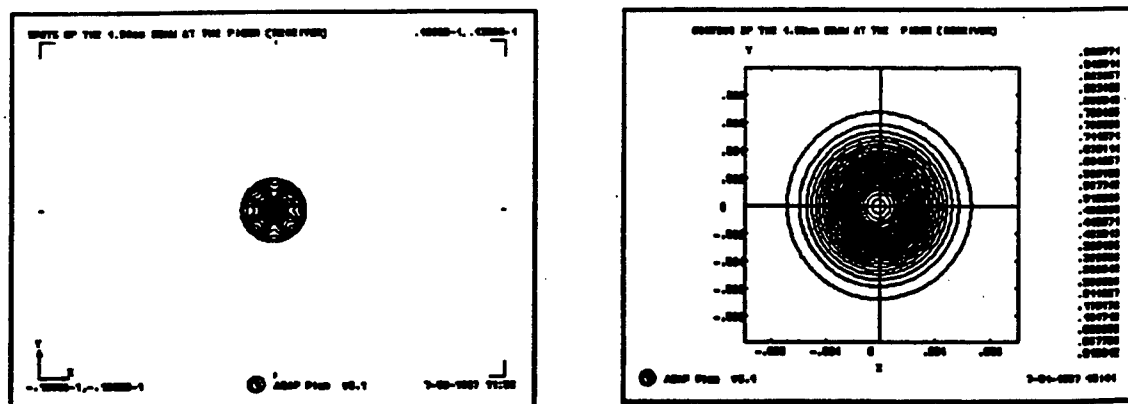


Figure 6-19. Physical optics calculation shows the image of the single-mode fiber in the output focal plane of the lens after propagating through the optical system. The position of the input is on the optic axis.

In Figures 6-20 and 6-21 we have launched the input on the optic axis but shifted the optical frequency first by +50GHz and then by -50GHz. The ray intercepts clearly show the onset of some aberrations but the effect on the intensity profiles is not too severe. The spots remain nearly circularly symmetric with some astigmatic spreading evident in the horizontal direction (parallel to the direction of grating-induced deflection). These results, and those to follow, show clearly that one cannot infer the lens's imaging properties from the ray intercepts alone.

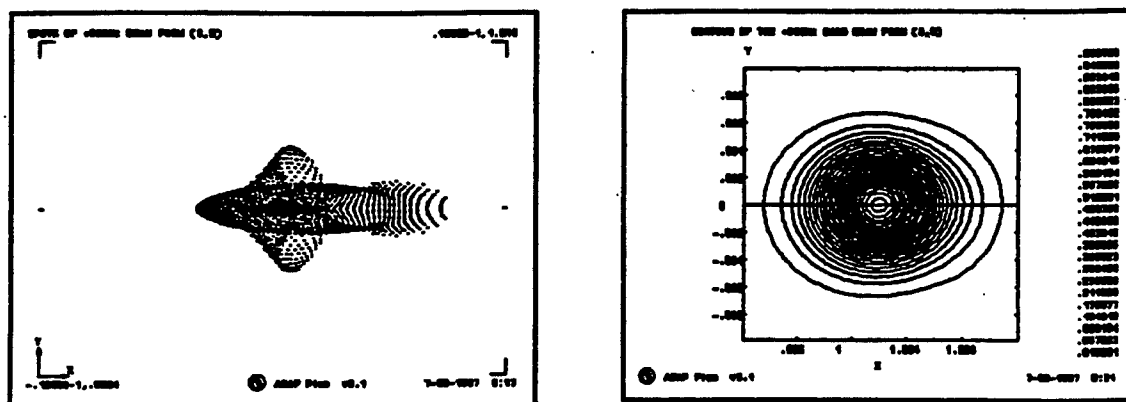


Figure 6-20. Output image of a +50GHz offset beam after propagating through the optical system. The location of the input is on the optic axis.

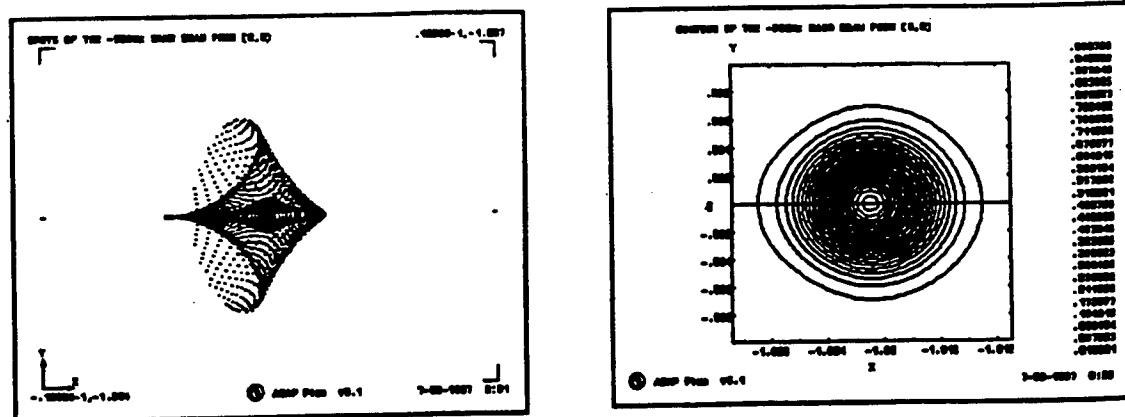


Figure 6-21. Output image of a -50GHz offset beam after propagating through the optical system. The location of the input is on the optic axis.

More significant is the asymmetric displacement of the spots from their expected positions. In accordance with the calculated dispersion, both frequency-shifted spots should be displaced 1.006mm from the optic axis. The analysis shows the +50GHz spot is at 1.002mm and the -50GHz spot is at -1.021mm. Further calculations showed that the optimum uniform array of detectors (or fanout waveguides) would be misaligned by as much as 4.5 μ m at several positions across the spectrum. The effect of this would be to produce an asymmetric channel response. As a result we might expect to see about 0.5dB increase in ripple on one side of the channel band. This will not be an issue if the waveguide fanout is used because the positions of the channel waveguides can be mapped to the positions of the uniform spectral grid.

We next considered the situation where the input is displaced by 0.5mm. The output spots will now appear 0.5mm above the optic axis as shown in figure 6-12. This is the more realistic configuration that was discussed in section 6.1.3 regarding focal plane layout. In Figure 6-22 we show the result for the case where the input is not frequency-shifted. The variation of the intensity profile from the input Gaussian is negligible. It is interesting to note that the spot is displaced horizontally from the center of the system. (The $x = 0$ position is given by the vertical line just inside the right edge of the box.) This is due to the small change of direction imparted on the beam in the vertical direction, which creates an ever so slight change to the angle of incidence in the grating equation. The net result is a nearly uniform translation of the entire spectrum by 9 μ m.

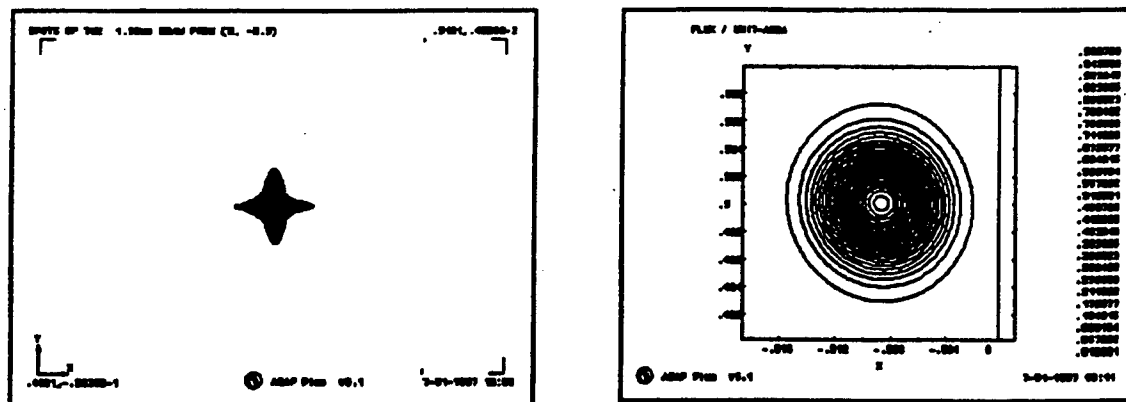


Figure 6-22. Output image of the single-mode fiber after propagating through the optical system. The input is 0.5mm off the optic axis.

Figure 6-23 shows the result for the -50GHz beam exhibiting a slight diagonal distortion to the focussed spot. Still, here the spread from the input spot shape is less than 10%. A similar result was obtained for the $+50\text{GHz}$ beam.

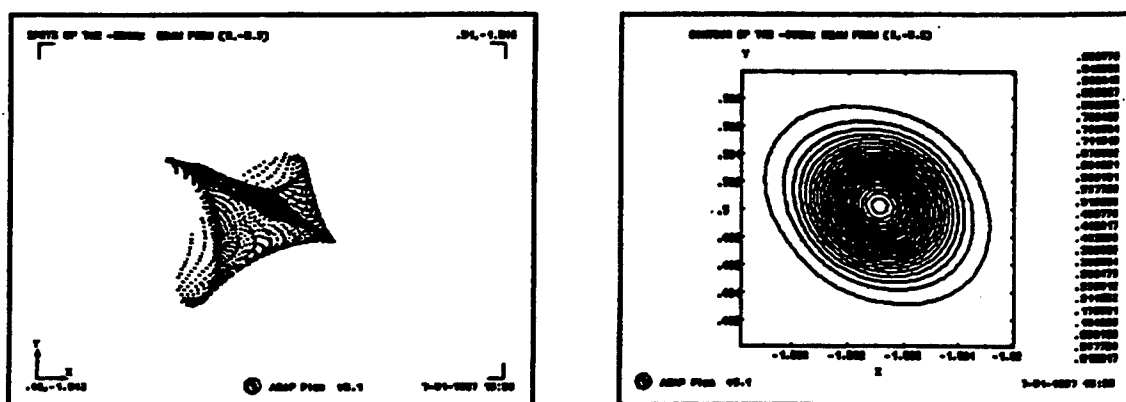


Figure 6-23. Output image of -50GHz offset beam after propagating through the optical system. The input is 0.5mm off the optic axis.

Figure 6-24 shows the output spot when the input is displaced by 1.0mm and frequency-shifted -50GHz . For this case the spot distortion is significant with the spread in the horizontal direction being about 45%.

These results showed that the lens design was capable of providing the optical performance required by the channelizer over the entire 100GHz bandwidth subject to the condition that the input and output axes were separated by 1mm or less.

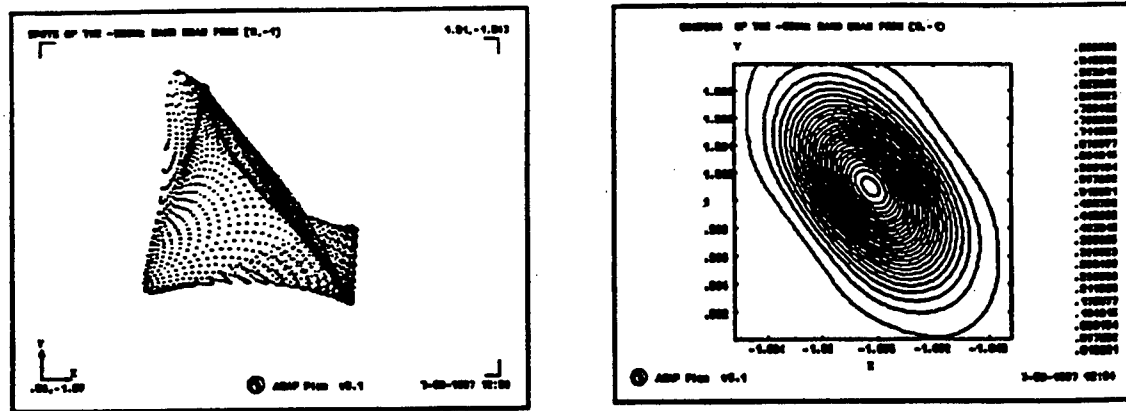


Figure 6-24. Output image of -50GHz offset beam after propagating through the optical system. The input is 1.0mm off the optic axis.

We performed additional analyses to determine how sensitive the lens's performance was to variations in the physical parameters that are used in the fabrication of the lens. This type of tolerance analysis is necessary in order to specify the precision with which the lens must be manufactured. It wouldn't make much sense to pursue a lens design that performs perfectly but is impossible to fabricate. The first thing we investigated was the tolerance to variations in the lens elements' radii of curvature. Not surprisingly, we found that the performance was most sensitive to changes in the most sharply curved surfaces. Seemingly insignificant changes in the radius from the design value produced severe degradation of the focussed spot. This is not as catastrophic a circumstance as one might think because in all cases the spot could be recovered adequately simply by moving the observation plane, or refocusing. This is illustrated in Figures 6-25 and 6-26 where we present the tolerance analysis as it applies to lens #2. On the left in these figures we show the spot produced by the perturbed system, as it would appear at the design focal plane. We show the refocused spot on the right side of the figure. For Figure 6-25 we have decreased the radius of curvature r_{21} (refer to the lens description in Figure 6-16) by 0.1% or 0.131mm, which results in the spot blowing up severely. By shifting the observation position 0.411mm we recover a nearly diffraction limited spot. Similar results can be obtained if we vary the radius r_{22} . The degradation caused by a 0.1% change in r_{22} (.083mm) is corrected by repositioning the observation position 0.940mm. These results are shown in Figure 6-26.

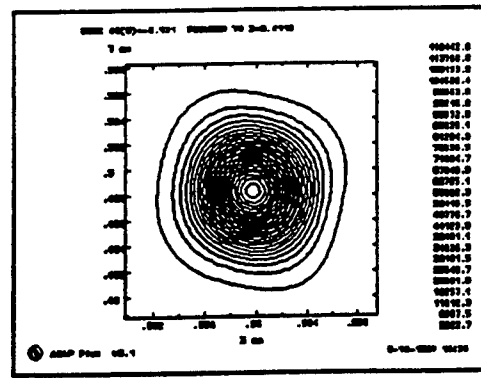
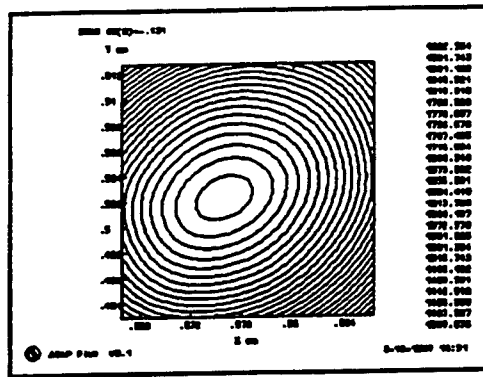


Figure 6-25. Refocusing can compensate for an error in the curvature r_{21} :
 $\Delta r_{21} = 0.131\text{mm}$; $\Delta z = 0.411\text{mm}$

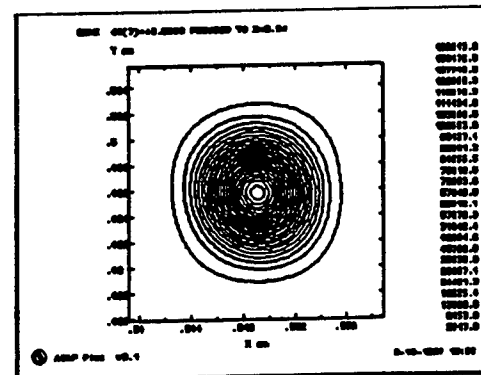
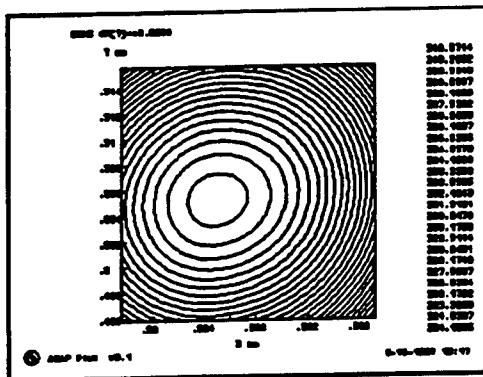


Figure 6-26. Refocusing can compensate for an error in the curvature r_{22} :
 $\Delta r_{22} = 0.083\text{mm}$; $\Delta z = 0.940\text{mm}$

We also calculated the effect of varying the lens thicknesses and inter-element spacing from their design values. We present an example in Figure 6-27. In this calculation we increased the air gap d_{12} by 0.01mm.

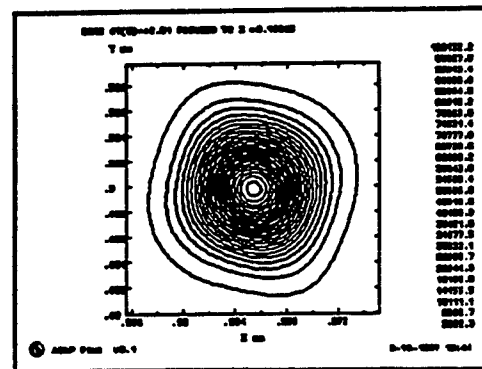
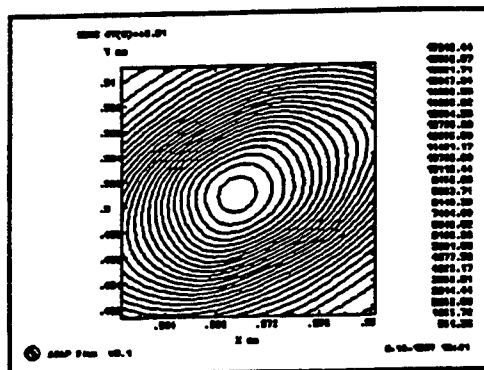


Figure 6-27. Refocusing can compensate for an error in the spacing d_{12} :
 $\Delta d_{12} = 0.01\text{mm}$; $\Delta z = 0.127\text{mm}$

As in the previous examples a simple refocusing produced an excellent output spot profile.

Based on the results of these calculations we concluded that our design provided near-diffraction-limited performance over the required field-of-view, and that reasonable manufacturing tolerances would be sufficient to maintain optimum performance. The design was submitted to Lightworks Optics to manufacture the lens. We specified a standard precision grade quality level that complied with our tolerance analysis.

6.1.4.4 Lens characterization

We evaluated the performance of the channelizer's lens assembly using the setup shown in Figure 6-28. In the figure we show the lens components without the support housing. We placed a flat mirror in front of the lens in contact with the rim of the support housing to ensure that the mirror's normal was parallel to the lens's axis of symmetry (optic axis). Light was launched into the system from a single-mode fiber through the face of the lens perpendicular to the primary optic axis. The light is partially reflected off the beamsplitter, exits the lens assembly as a collimated beam, and is reflected back on itself by the mirror. Upon traversing back through the lens the output pattern (mode profile) of the fiber is imaged in the back focal planes of the lens. We viewed the imaged spot in the focal plane as shown in the figure. We used a knife-edge technique to measure the intensity profile of the focussed spot. With this technique, illustrated in Figure 6-29, the total optical power that is transmitted past a knife-edge as it is scanned through the image spot is collected by a photodetector. The resulting temporal development of the photocurrent is proportional to the integrated intensity of the image. Numerical techniques are used to differentiate the result yielding the desired intensity profile. By repositioning the input fiber we were able to measure the image quality at three positions spanning the field of regard over which the lens was designed to operate. We measured the intensity profiles along horizontal and vertical axes at each measurement point.

The results from the first of the measurements, taken for the spot on the optic axis (corresponding to point #1 in Figure 6-28), are presented in Figure 6-30. The upper set of traces is for a horizontal scan and the lower set is for a vertical scan. In the left panel we show the photocurrent as a function on time, and the right panel shows the intensity profile obtained by differentiating the photocurrent data.

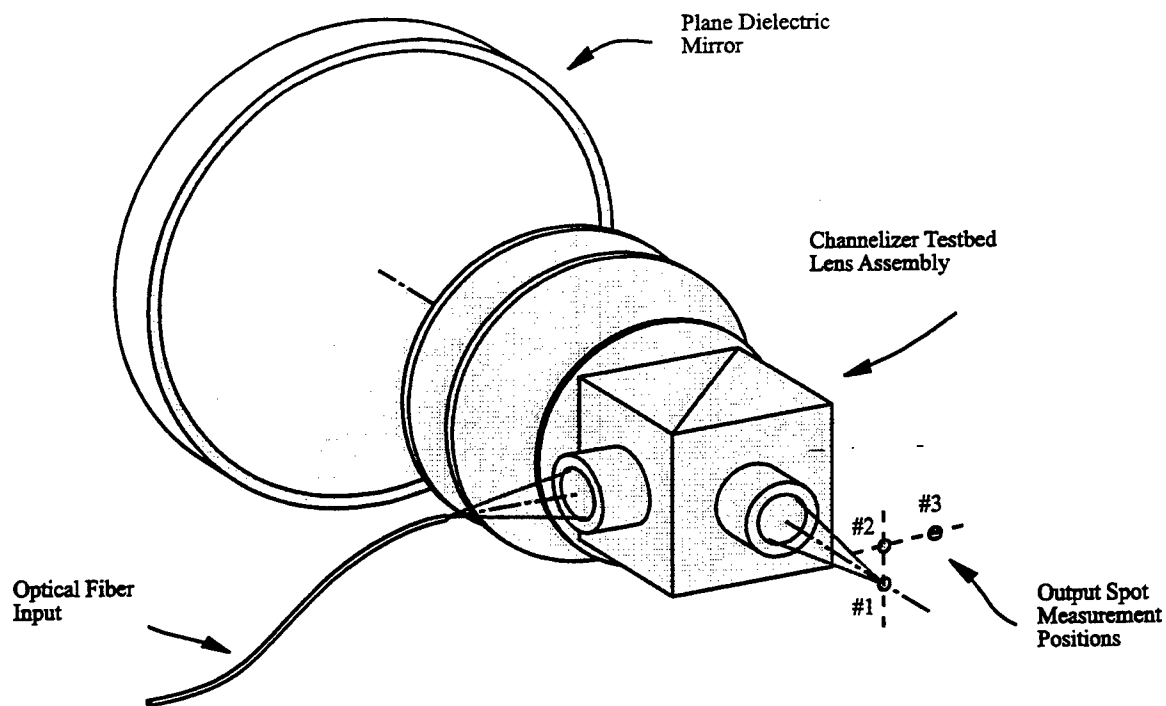


Figure 6-28. Setup for measuring the imaging properties of the channelizer's lens

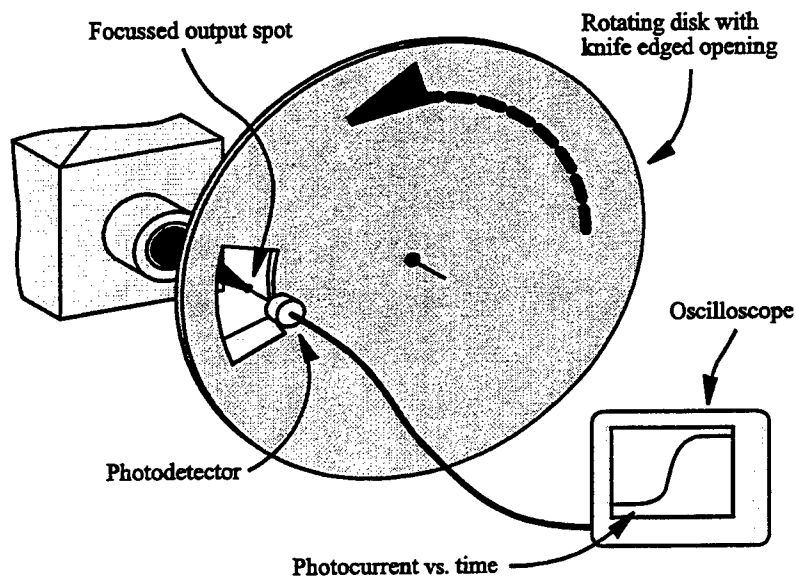


Figure 6-29. A scanning knife-edge technique was used to determine the intensity profiles of the imaged spots.

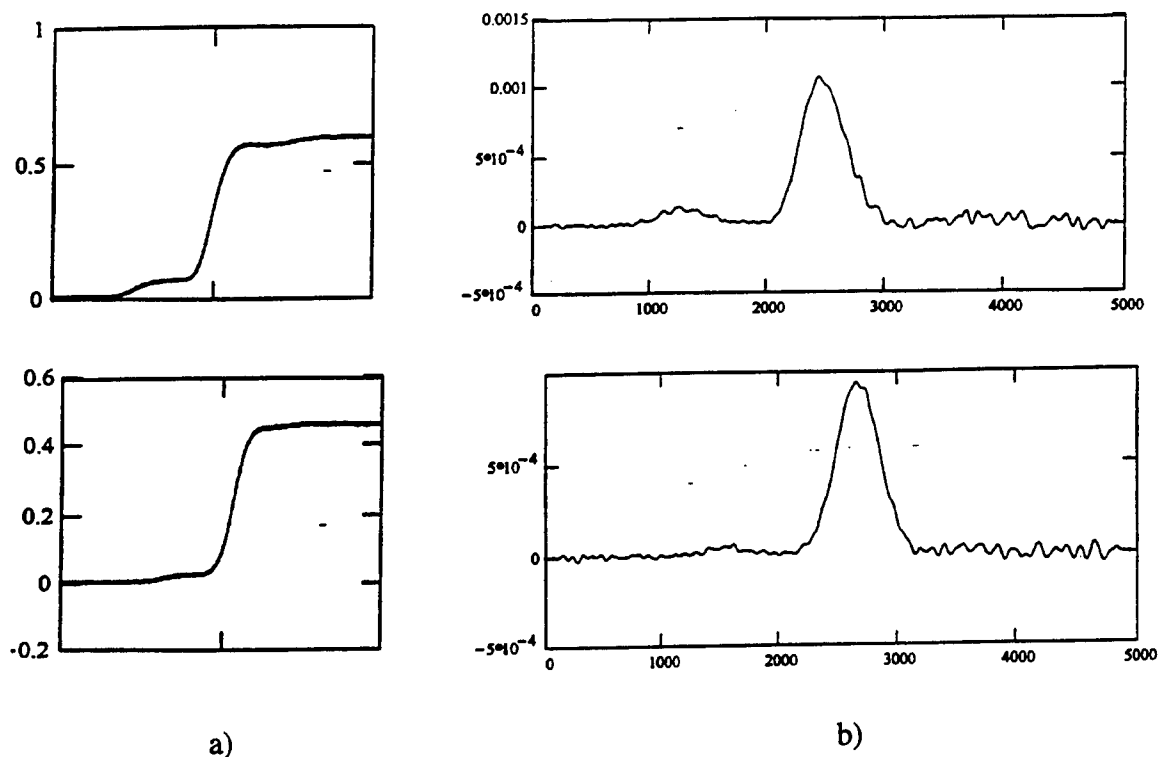


Figure 6-30. Measured intensity profile for spot on the optic axis

- a) Photocurrent vs. time
- b) Spot intensity profile

In Figure 6-31 we show the results of the measurements taken on spot #2, which was displaced vertically from the optic axis by 1mm. This spot was obtained by moving the input a like amount in the opposite sense. An additional horizontal translation of 1mm is introduced for the measurements at spot #3 shown in Figure 6-32.

We constructed contour plots of the spots' intensity profiles from the data. These are shown in Figure 6-33 versus their relative positions in the focal plane. A typical e^{-2} diameter for the spots is about $16\mu\text{m}$, which is somewhat larger than the diffraction-limited spot size we expected based on the data on the Fujikura fiber. Nevertheless these results verify our physical optics analysis in that they show that the image spot does not degrade significantly as the spot position varies throughout the field of regard.

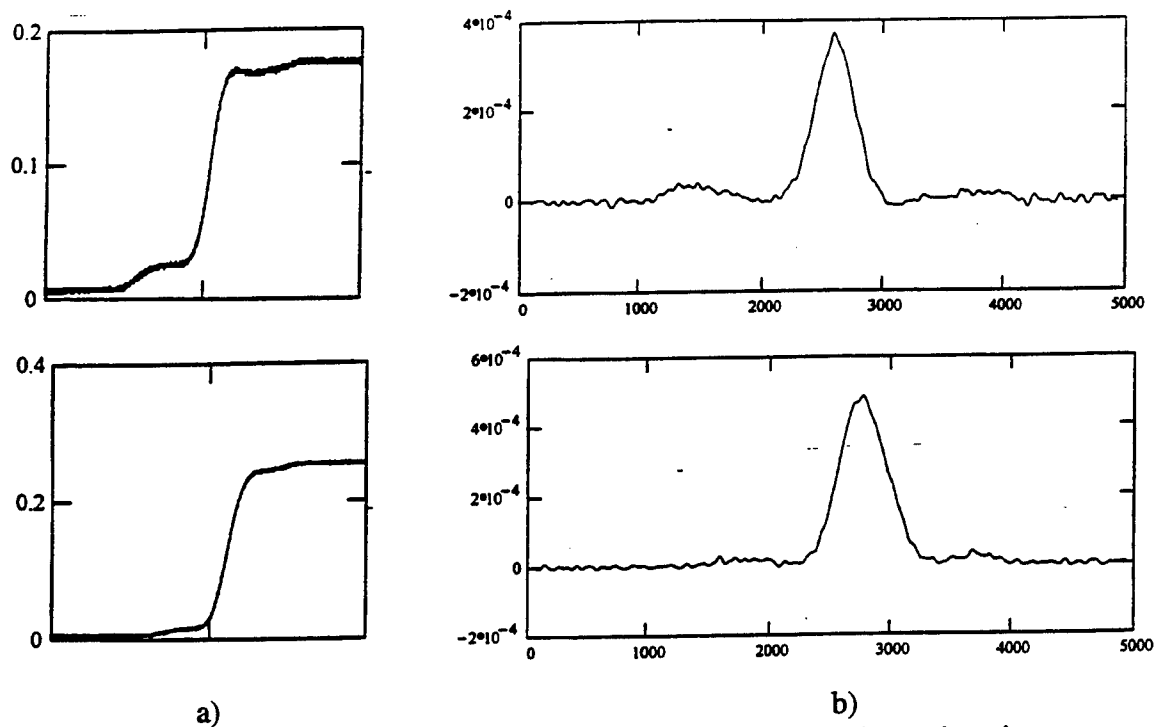


Figure 6-31. Measured intensity profile for spot above the optic axis

- a) Photocurrent vs. time
- b) Spot intensity profile

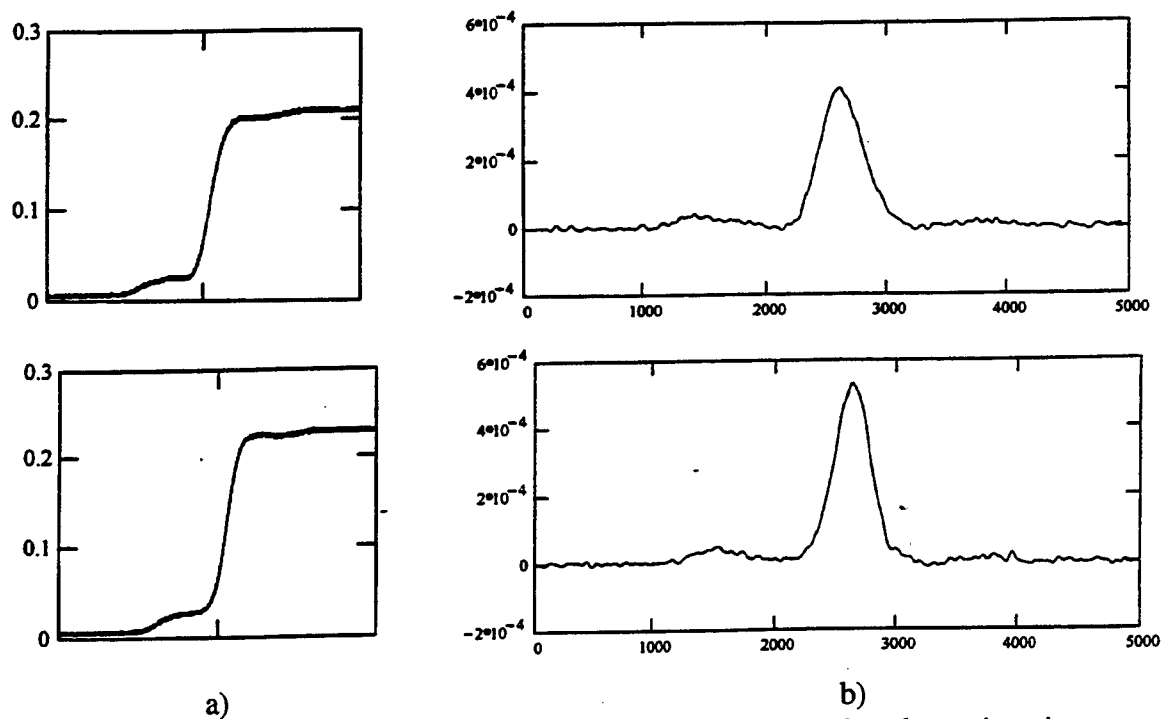


Figure 6-32. Measured intensity profile for spot diagonal to the optic axis

- a) Photocurrent vs. time
- c) Spot intensity profile

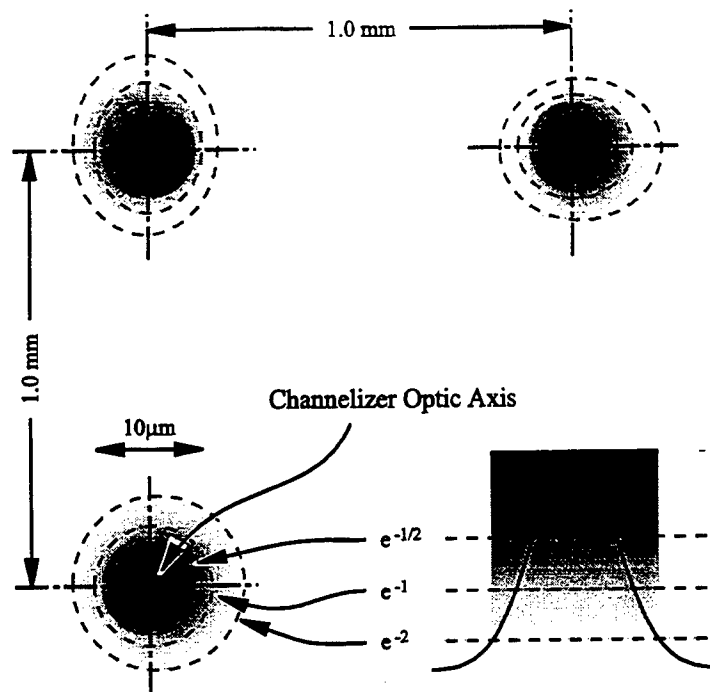


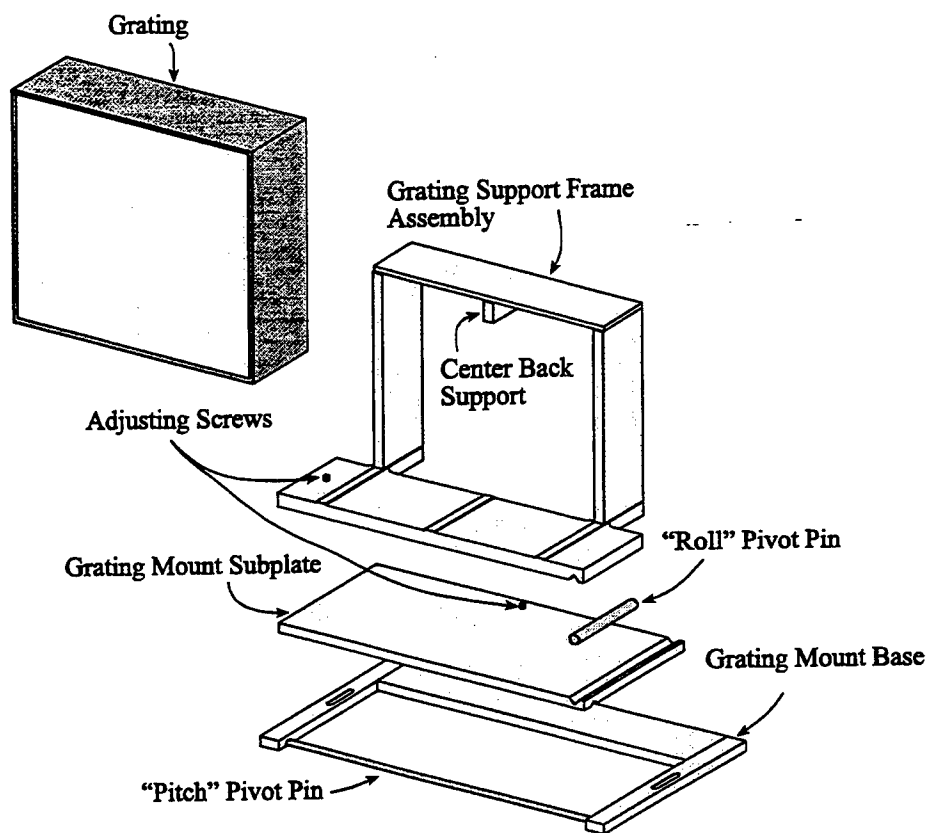
Figure 6-33. The channelizer lens point spread function was evaluated at three positions in the focal plane

6.2 CHANNELIZER TESTBED ASSEMBLY

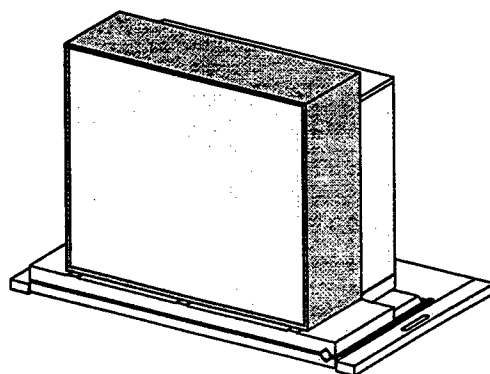
The channelizer testbed was assembled on an enclosed 4'x 8' Newport optical table. Most of the hardware with the exception of the grating, the lens and the roof mirror were purchased from various vendors' catalogs. The channelizer consists of four major optical components: (refer to Figure 6-6) the diffraction grating, the roof mirror, the channelizer lens, and the plane mirror.

Upon specification of the grating a purchase order was placed with Richardson Laboratories. While the grating order was being processed a special fixture to hold the grating in place was designed and fabricated. The fixture provided adjustments so that the grating could be oriented to make the grating grooves perpendicular to the table. An exploded view of the partially assembled fixture is shown in Figure 6-34. The grating was attached to the support frame with epoxy and silicone adhesive. Epoxy was applied along the center of the three ridges at the bottom and at the center back support. This provided a "hard" mount to fix the position of the grating in the support frame. The center back support is attached to a flexible cross-member, which allows thermal expansion in the vertical direction without transmitting stress to the grating. The grating

was bonded to the remaining bottom ridges and the two upright supports with silicone adhesive. This provides additional attachment security while the soft bond allows for a certain amount of thermal expansion mismatch between the aluminum fixture and the glass grating substrate.



(a) exploded view



(b) assembled view

Figure 6-34. Grating mounting fixture

The grating and support frame rest on the “roll” pivot pin, which is set in a v-groove in the mount subplate. The grating’s attitude about its roll-axis is then adjusted via the adjusting screw in the bottom plate of the support assembly. The mount subplate has a v-groove along its bottom side that engages the “pitch” pivot pin, which is positioned on the optical table and held in place by the two arms of the grating mount base. An adjusting screw in the mount subplate is used to adjust the grating’s attitude about its pitch-axis.

The roof mirror was manufactured to our specifications by PLX Incorporated. As seen in Figure 6-35 it comprises two large plane mirrors epoxy-bonded together and held at precisely 90° by the glass support pieces and mounted on an aluminum support structure. Each of the mirrors is 11.9” x 6.7” x 1.25”. They are polished flat to within $\lambda/10$ over their entire surface and coated for high reflectance for 45° incident light at $\lambda=1.55\mu\text{m}$.

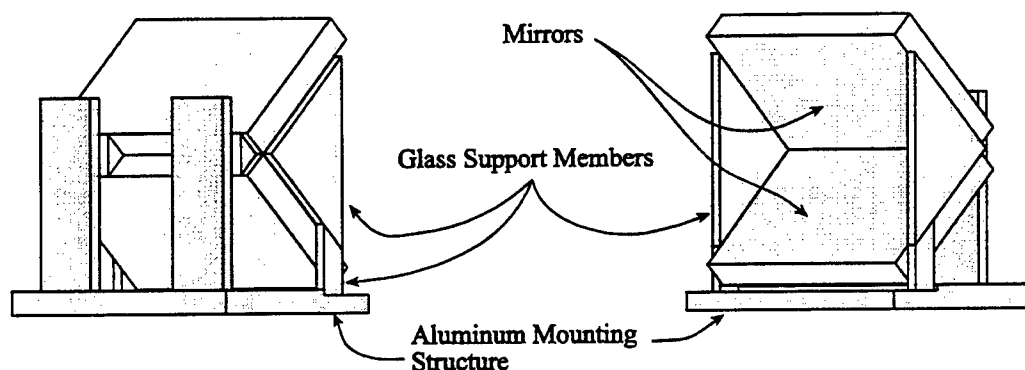


Figure 6-35. Custom roof mirror assembly

The channelizer lens assembly was manufactured by Lightworks Optics and it was mounted in a special housing shown in Figure 6-36. The housing was designed to permit the placement of the lens into the space available in the system and allow access to the lens’s input/output focal planes. An aluminum cradle was fabricated in-house to securely locate the lens in position on the optical table.

The plane mirror is a 4” diameter, $\lambda/20$ flat mirror that was ordered from Newport Corporation with a high-reflective coating for normal incident light at $\lambda=1.55\mu\text{m}$. It is mounted in a standard 4” mirror mount and positioned on a 1.5” diameter mounting post.

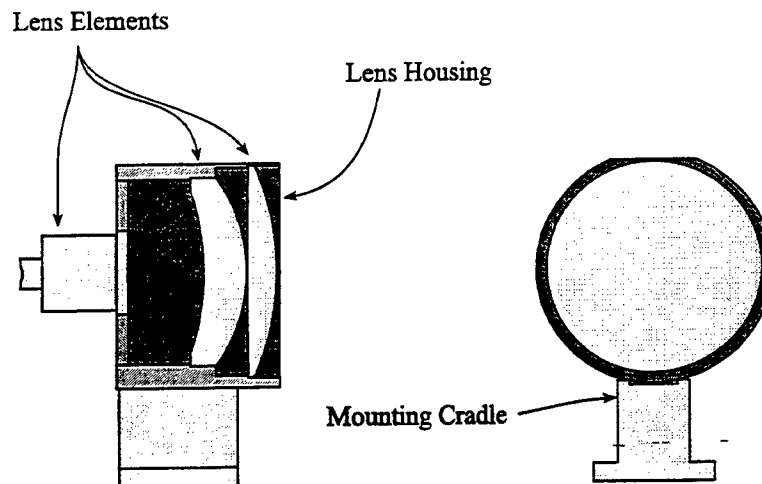


Figure 6-36. Channelizer lens mounting assembly

As discussed previously the lens design incorporated an optical beamsplitter as an integral part of the lens to provide some flexibility in the arrangement of the optical inputs and outputs. This is illustrated in figure 6-37, which is a scale drawing of the lens showing the beamsplitter and the basic arrangements of the optics used for most of our RF measurements.

The optical input for the local oscillator beam is obtained from the cleaved end face of a single-mode fiber. The fiber is positioned at a right angle to the optic axis and the beam is turned by a miniature right-angled prism mounted on the end of a specially modified fiber holder. For most of the measurements the signal (previously referred to as the carrier) input was provided by an optical fiber as shown in the figure. The fiber was replaced with a free-space, anamorphic beam-expansion imaging system for those measurements requiring different L.O. and signal spot sizes. Also depending on the measurement being made, either the multi-mode output fiber was made to sample the output directly or the output was reimaged onto a slit placed directly in front of the fiber. The reimaging optics and slit dimensions were configured to simulate one channel of a complete receiver. The input fibers are positioned with Newport precision XYZ positioners that are fitted with sub-micron resolution, electrostrictive actuators. The light source used in all of our measurements was a New Focus model 6328 tunable, external cavity diode laser. This laser can be scanned over the wavelength range of 1520nm to 1570nm and has a fine tuning resolution of better than 100MHz.

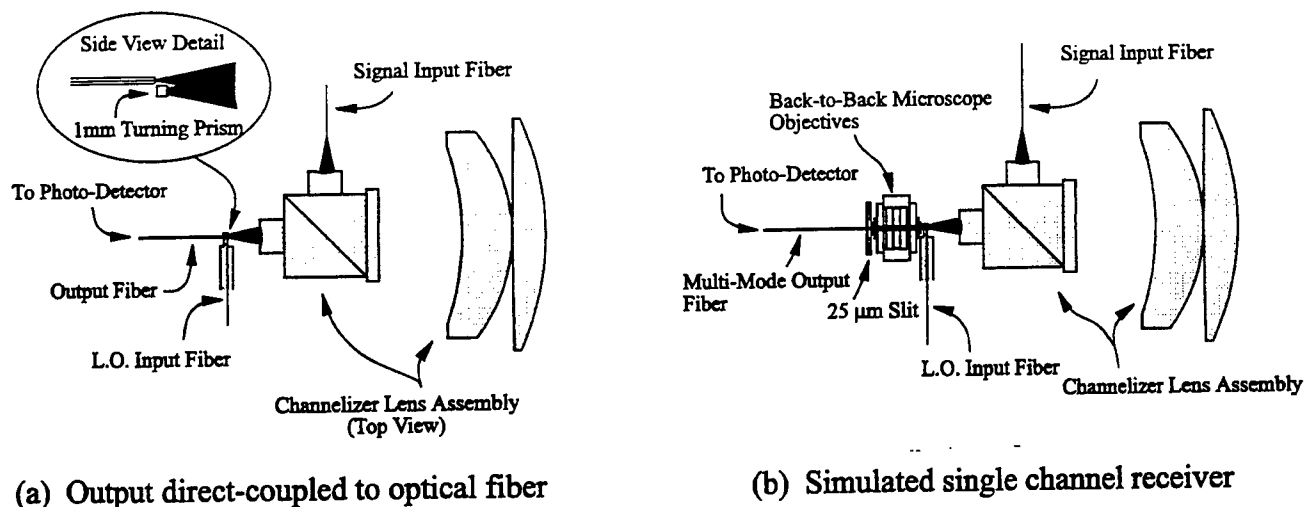


Figure 6-37. I/O optical layout for channelizer testbed

Figure 6-38 shows a scale drawing of the channelizer testbed layout as it was initially set up. The figure shows the relative placement of the optical components and the detailed configuration of some of the support structures. The portion of the testbed shown occupies an area of approximately 16" x 20" on the surface of the optical table, which is equipped with a pneumatic damping system to provide mechanical isolation. A plexiglass cover was fabricated that enclosed the optical components to prevent incident contact with and dust from settling on the grating and mirrors while other work was being performed within the table enclosure.

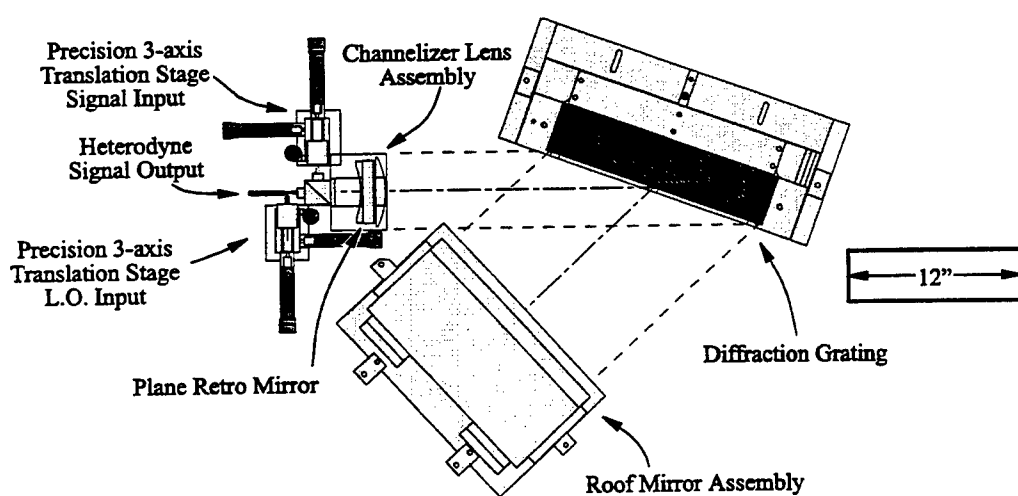


Figure 6-38. Scale drawing of the channelizer testbed layout on the optical bench

6.3 CHANNELIZER TESTBED EXPERIMENTAL RESULTS

Measurements were made to characterize the performance of the channelizer and to compare the RF performance with our model-based predictions.

6.3.1 Optical System Characterization

Once the channelizer was assembled we performed a series designed to determine the optical properties of the system.

6.3.1.1 Channelizer dispersion

In the first experiment the New Focus external-cavity diode laser was used for the input signal source. Its output ran through a Sumitomo Mach-Zehnder modulator and was launched into the system via a single-mode fiber and the miniature (1mmx1mmx1mm) turning prism that were positioned on the optic axis with the precision translation stage. We removed the signal-input fiber and took the system output at right angle off of the beamsplitter. The output was magnified by a relay objective and imaged onto an IR sensitive camera. The video image was viewed on a TV monitor. A photograph of the entire channelizer testbed is shown in Figure 6-39.

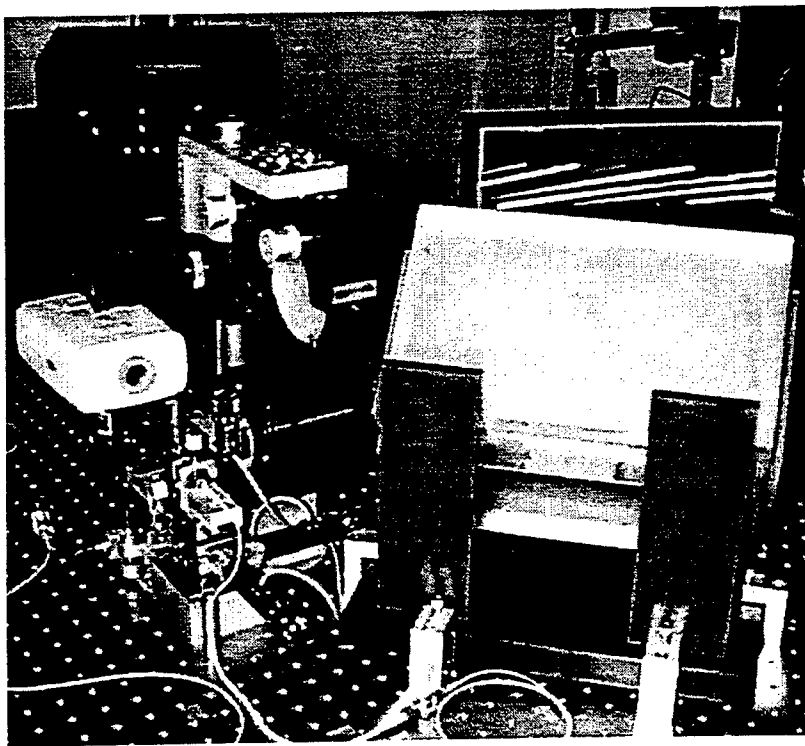
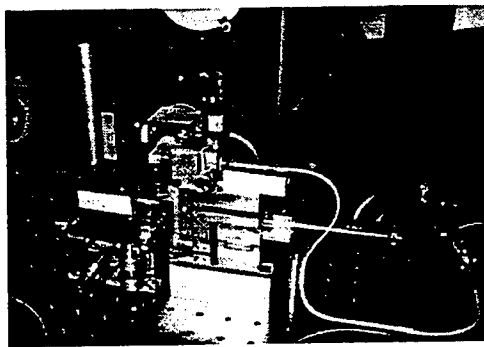
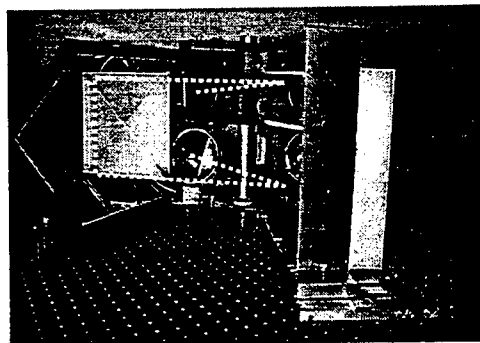


Figure 6-39. Photograph of the CORE channelizer testbed

We biased the modulator such that the residual carrier was about the same intensity as the modulated sidebands. The system's output can be seen on the monitor in the background of the figure. For illustrative purposes we have superimposed three spot distributions on the monitor. The lowest row of spots corresponds to a 1GHz tone being applied to the modulator. The center row corresponds to 4GHz and the upper row corresponds to 5GHz. The photo shows that the 1GHz spots are readily resolved, which is the expected result since by design the diffraction limited spot sizes should correspond to 0.45GHz. Figure 6-40 shows more detailed photographs of the RF channelizer. In 6-40(a) we show a view of the lens's focal plane with micropositioners for the signal and L.O. fibers. 6-40(b) is a picture of the grating and the mirrors used to fold the beams' paths, and provide the multiple reflections off of the grating. The dashed line traces the optical path through the system. The beams are collimated by the lens (at the lower central part of the picture) and are diffracted by the grating. The diffracted beams are directed to the right-angle roof mirror where they are elevated and redirected to the grating for a second diffraction. The twice-diffracted beams are then reflected by the circular mirror located directly above the lens, and the beams then retrace their route back along the identical path to the lens, through which they exit the system, ultimately being focused at the output of the channelizer.



(a) Channelizer's focal plane optics



(b) Beam path in the channelizer

Figure 6-40. CORE RF channelizer optical layout

We captured the image of a sideband spot with a frame grabber and this is shown in figure 6-41. In the figure we show an intensity profile taken through the center of the

spot in the horizontal direction (parallel to the spectral dispersion). The spot is clean with no sidelobes evident within the ~20dB dynamic range of the camera.

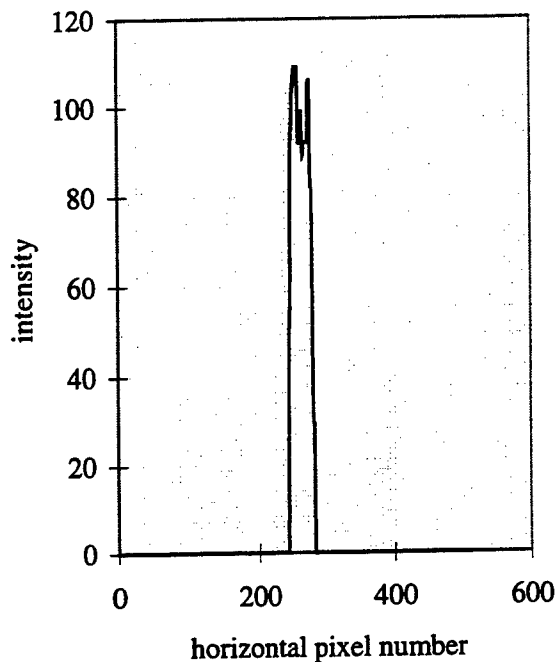


Figure 6-41. Channelizer testbed output spot intensity profile

6.3.1.2 Fiber mode profile measurement

We made measurements of the mode profile of the single-mode optical fiber used for the input signal beam. These measurements revealed that the fiber's mode profile differed significantly from the ideal Gaussian mode shape that we assumed for the purpose of designing the optical system. The mode was larger in diameter than expected as seen in the intensity scan shown in Figure 6-42. (Compare the measured diameter of 15.5 μm with the Fujikura data in Figure 6-14 showing a e^{-2} diameter of 10.06 μm .) We note although, that this measurement agrees well with the spot sizes measured when we evaluated the channelizer lens point spread function (see Figure 6-33), which is indicative that the lens performs near the diffraction limit. Of greater significance, the sidelobe levels were substantially higher than anticipated. This had a predictable influence on the RF performance of the channelizer; most notably the crosstalk suppression was somewhat compromised.

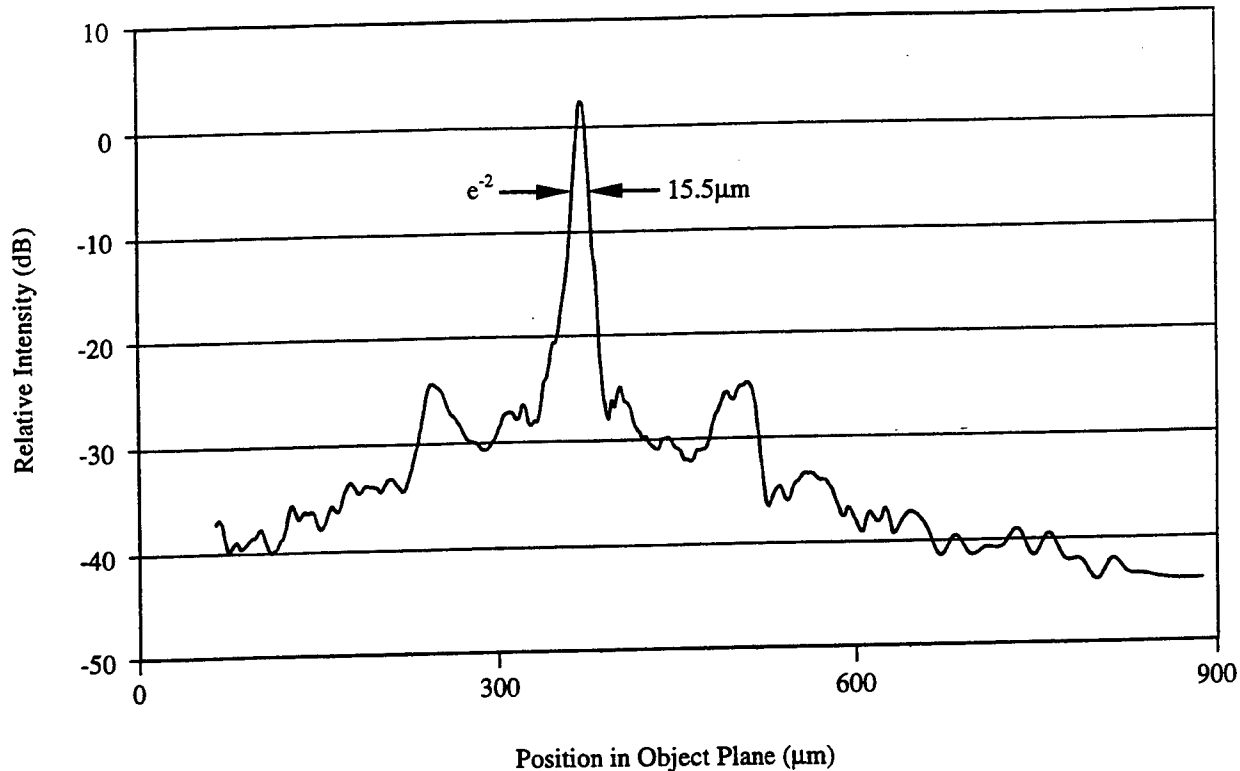


Figure 6-42. Measured mode profile for the single-mode fiber used in the channelizer

6.3.1.3 Channelizer throughput measurements

A tradeoff that was made to increase the testbed's flexibility was the inclusion of the beamsplitter in the optical path of the lens assembly. This provides a great deal of freedom in laying out the input and output configurations but it does introduce additional insertion loss that will influence the RF performance of the channelizer. We can quantify the impact of the beamsplitter with the help of the diagram shown in Figure 6-43, where T and R are the beamsplitter's intensity transmission and reflection coefficients respectively.

The quantity of interest is the strength of the heterodyne signal that is produced by the photodetector. Let's assume that we are taking the output from the left side of the beamsplitter, then the amplitude of the beat note is proportional to the product $T(TR)^{1/2}$. Further assume that the beamsplitter is lossless, then $R = 1 - T$ and it is straightforward to find that the value of T that maximizes the beat note is $T_{\text{optimum}} = 0.75$. A standard 50/50 unpolarized beamsplitter for $\lambda = 1.55\mu\text{m}$ is actually polarization dependent (they deliver

an average 50% beam split for unpolarized light) and typical values for T and R for our desired polarization are 0.85 and 0.15 respectively.

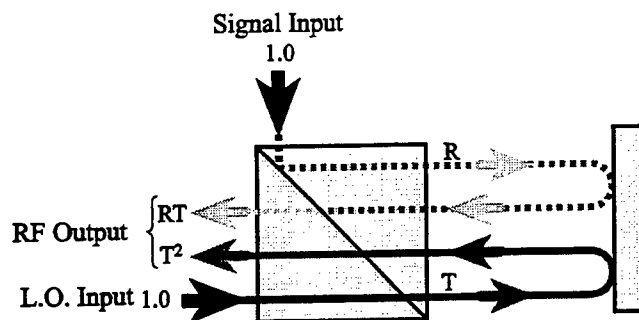


Figure 6-43. Channelizer testbed lens beamsplitter

These values yield a heterodyne signal strength that is about 0.5dB less than the maximum. Therefore, to avoid the expense of a specialized coating, we ordered the channelizer's lens with this type of a beamsplitter.

We measured the transmission and reflection of our beamsplitter for both polarizations and these results are presented in Table 6-4. The pertinent polarization state for our system's configuration is parallel. The data indicate that we are suffering about 10% loss in the beamsplitter independent of polarization. We also find that while the transmission for the desired polarization agrees well with what is expected, the reflection coefficient is down considerably.

Table 6-4. Performance of the channelizer lens's beamsplitter

Quantity	Measured Value	Specified Value
T_{parallel}	0.84	0.85
R_{parallel}	0.06	0.15
$T_{\text{perpendicular}}$	0.09	0.11
$R_{\text{perpendicular}}$	0.81	0.89

We next measured the net optical throughput for the channelizer using the arrangement shown in Figure 6-44. The measurement was made by plugging the fiber connector nearest each of the input points into an optical meter and comparing this input power level with the power measured at the output end of the multimode fiber. These results are summarized in Table 6-5. In the table the miscellaneous losses include fiber coupling losses, excess scattering and coupling losses, and any losses due to imperfect polarization

of the input beams. The R and T losses were taken from the previous measurement and the grating diffraction efficiency was measured directly.

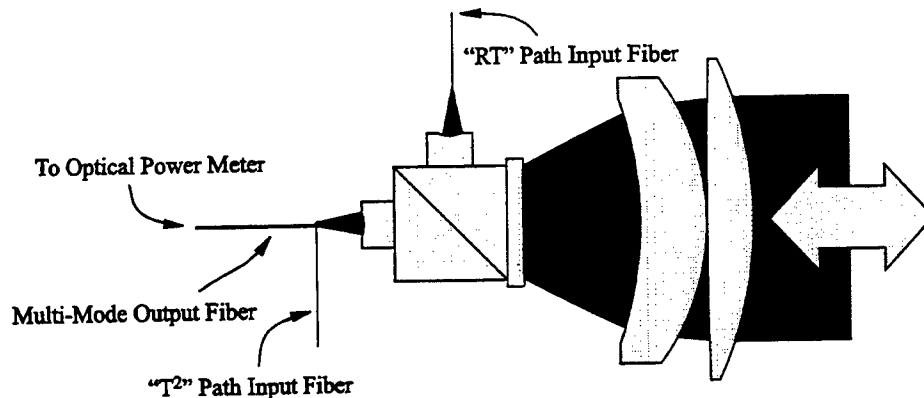


Figure 6-44. Fiber-to-fiber throughput was measured for both optical paths in the channelizer

Table 6-5. Channelizer optical throughput summary

	R	T	η_{grating}	miscellaneous	Total
"RT" path	.06	.84	$.49^d = .058$.53	.0015 (-28.1dB)
"T ² " path		$.84^2 = .71$	$.49^d = .058$.35	.0145 (-18.4dB)

The biggest surprise of this measurement is the low value of the grating's diffraction efficiency. Our calculations showed that η should have been greater than 70%. Measurement results provided to us by the grating supplier were in substantial agreement with our calculations. When we observed the distribution of optical power in all of the diffracted beams we found the relative strength of the diffracted beams to be in agreement with our calculations. We just found that there was about 30% optical loss at each bounce off of the grating. We were unable to determine the source of this loss.

6.3.2 RF Measurements

6.3.2.1 Optical heterodyne frequency translation

Figure 6-45 shows a functional block diagram of the setup used to observe the system's response to a single RF tone. The New Focus external-cavity diode laser was used for the input source. An erbium doped fiber amplifier (EDFA) was used to boost the power level to facilitate our measurement. A 3dB coupler divided the amplifier's output. One

of the outputs was launched into the system directly as the local oscillator and carefully positioned using the L.O. input translation stage. . The L.O. output spot was imaged on the multi-mode fiber and directed to a New Focus photodetector. The EDFA's other output was directed through a null-biased, Mach-Zehnder modulator, which was driven with a 5GHz CW tone, then launched into the system with the optical signal input translation stage. The optical modulation index (OMI) was about 50% with a RF driving power of 18 dBm and the DC bias was adjusted through the bias-T to suppress the optical carrier. We then positioned the signal-input fiber so that one of the modulated sidebands was imaged directly on the multimode fiber along with the L.O.

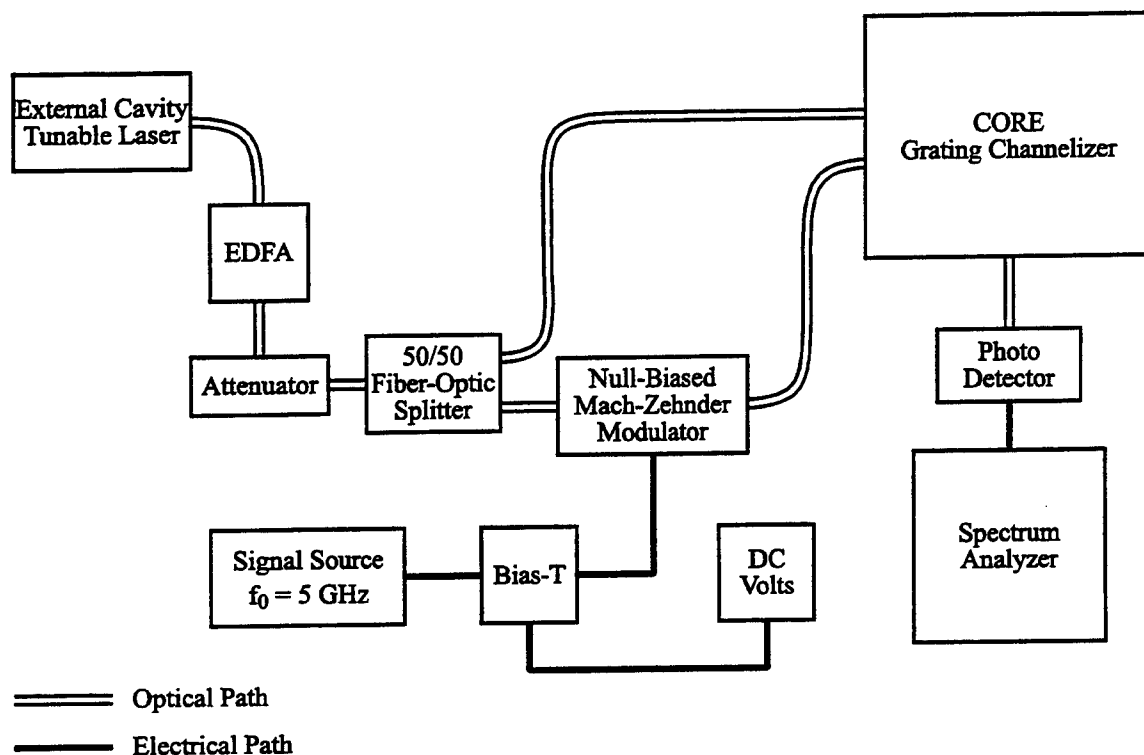


Figure 6-45. Block diagram of the basic RF characterization setup

Figure 6-46 shows the 5 GHz microwave signal that was recovered through heterodyne detection, amplified and displayed on a spectrum analyzer. The measured signal strength at the spectrum analyzer was about -4 dBm with a noise floor at about -70 dBm using a 1 MHz resolution bandwidth. Our initial calculations based on the observed optical power levels in the signal and L.O. beams, and assuming perfect heterodyne conversion, indicated that the measured RF power was about 10dB less than ideal.

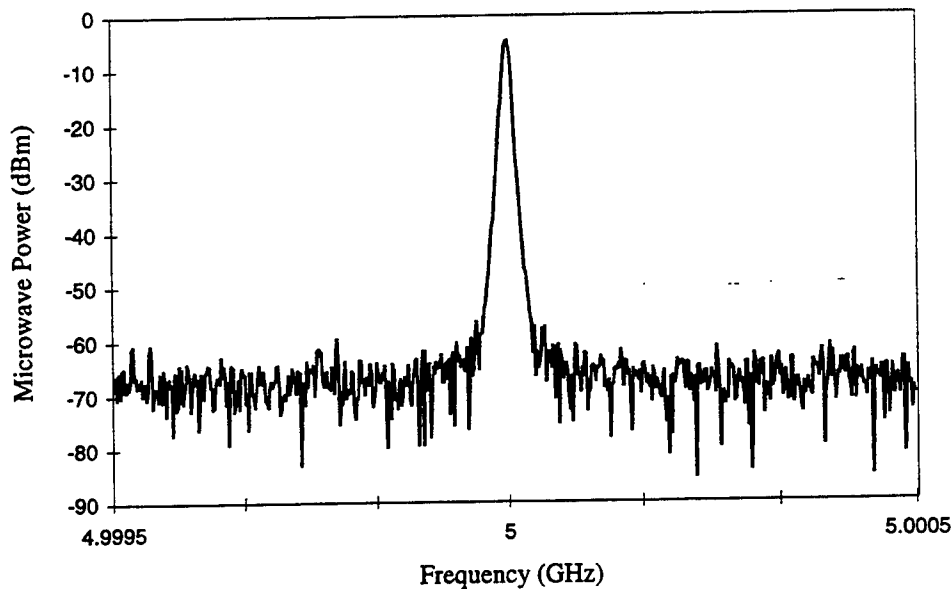


Figure 6-46. The measured 5 GHz microwave signal at the spectrum analyzer.

As one of the possible causes for this discrepancy we considered dispersion or wavefront distortion in the multimode fiber pigtail that was used as the focal plane pickup that transported the optical signals to the detector. To test this hypothesis we set up an experiment to measure heterodyne efficiency with single-mode fiber and multi-mode pigtails. For these experiments the optical output from the (ECL) was divided by a 3 dB coupler to feed the reference arm and the frequency shifted arm. The frequency-shifted tone was generated from a modulator at 5 GHz. The optical carrier and one side band were suppressed through proper bias control and a fiber Fabry-Perot (F-P) filter. The presence of only the single side band was confirmed and monitored through a super cavity scanning F-P fed by a 13dB coupler. The signal and the reference beams were combined in a polarization-maintaining (PM) 3 dB coupler, and fed directly through the single-mode PM fiber to a photodetector. The difference-frequency beat signal strength was measured with a spectrum analyzer. We compared the measured RF level with that calculated from the CW power levels from each arm. When we repeated the experiment with a multi-mode fiber our measurement indicated no observable degradation in the heterodyne efficiency.

We then reexamined our computation from our original experiment with the channelizer testbed and we discovered that we had used an incorrect circuit model to calculate the expected RF power in the heterodyne tone. This accounted for more than 6dB of the discrepancy.

6.3.2.2 Channel response characteristics

For the purpose of evaluating the channelizer's RF channel response we used the setup that was shown in Figure 6-37(b). We installed a pair of 40x diode laser objectives to reimage the output focal plane onto a 25 μ m wide precision air slit. A 50 μ m core-diameter, multi-mode fiber was positioned directly behind the slit to collect the transmitted beams. The slit defines the physical extent of the channel. Repositioning the lenses and slit/output-fiber can alter the magnification of the diode laser objective pair quite simply. This allowed us to control the RF channel bandwidth as desired. As shown in the figure, this setup provides equal-size spots for the signal and L.O. beams. The light source we used was the amplified output from the New-Focus external cavity laser that was split to the L.O. arm and the signal arm. The light in the signal arm went through a Mach-Zehnder modulator and was then sent to the signal input port of the channelizer, whereas the light in the L.O. arm is sent to the L.O. port directly. The L.O. output is centered on the channel and one of the signal sidebands is spatially overlapped with the L.O. at the center of the output port with some frequency, typically about 5GHZ, applied to the modulator. We then determined the ripple by measuring the power in the heterodyne beat note as we varied the applied frequency about the channel center frequency. Figure 6-47 illustrates how the channel response varies as a function of the signal frequency. The strength of the heterodyne tone is proportional to the square of the shaded area, which represents the product of the spot amplitudes subtended by the detector. As a first order estimate we assumed that the spots were ideal Gaussians with diameters equal to our observed fiber mode profiles. We calculated the ripple for this situation and these results are shown for comparison with the measurement results.

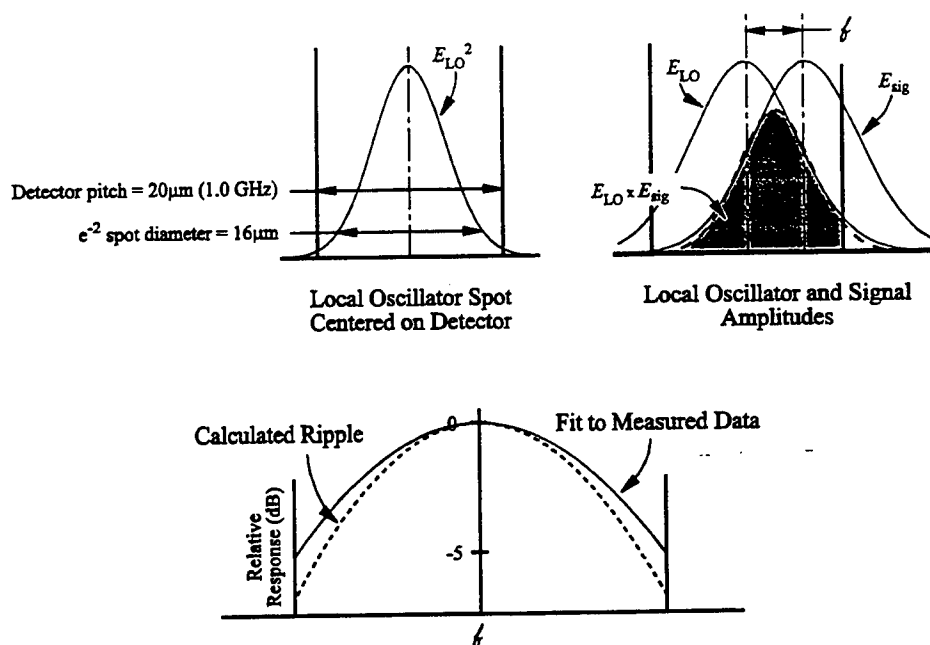


Figure 6-47. Ripple for the case of equal L.O. and signal spot sizes

Our analyses have shown that to improve ripple performance it is desirable to spread the signal spot by a factor of three to four with respect to the L.O. spot. In order not to increase unduly the insertion loss the spreading should be only along the direction parallel to the grating-induced dispersion. We constructed an anamorphic imaging system that transformed the circular mode pattern emerging from the input fiber into an elliptical pattern whose minor axis is equal to the fiber's mode diameter, and whose major axis is expanded threefold. The elliptical beam waist was positioned in the input plane of the channelizer's signal port. Figure 6-48 shows assembly consisting of a New Focus fiber optic coupling fixture, a pair of aspheric objectives, and an anamorphic prism beam expander. The prism pair expands a circular beam by a factor of three in the vertical direction as indicated by the dashed lines in the figure. The resulting focussed spot in the signal input plane would now have the desired ellipticity with its major axis oriented horizontally.

Figure 6-49 illustrates how the channel response varies as a function of the signal frequency for the unequal spot size case. As we did in the case with equal-sized L.O. and signal spots, we present the calculated response and the measurement results for comparison. For this case the ripple is about 2.2dB and we find the data to be in good general agreement with the calculated ripple.

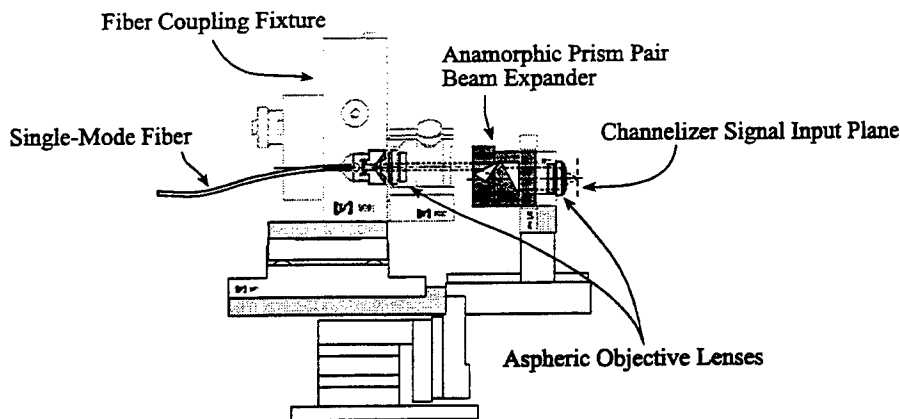


Figure 6-48. Setup for creating elliptical beam waist

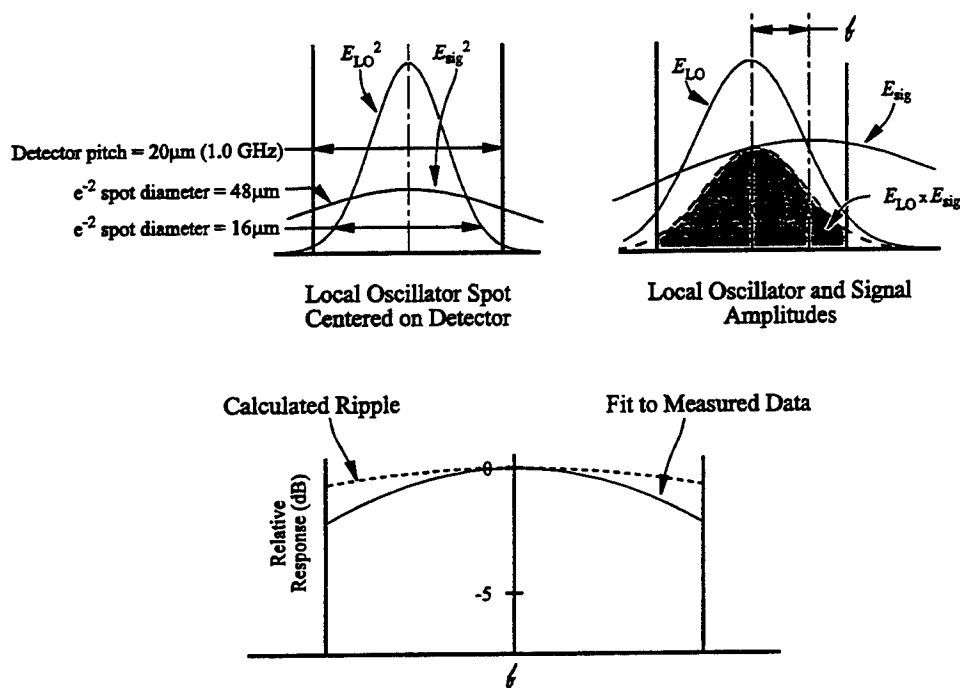


Figure 6-49. Ripple for the case of unequal L.O. and signal spot sizes

Next we installed a RF bandpass filter after the photodetector and measured the channel passband response for frequencies that extended into the neighboring channels. The filter is a 5 section coaxial filter whose center frequency is 6GHz. In Figure 6-50 we show the results of this single-channel response measurement. It can be seen that the response will drop below -50dB for signals in the second nearest channel. This means that strong signals in those channels will produce a spurious response that falls below the level necessary to satisfy the requirement for a spur-free dynamic range of greater than 50dB.

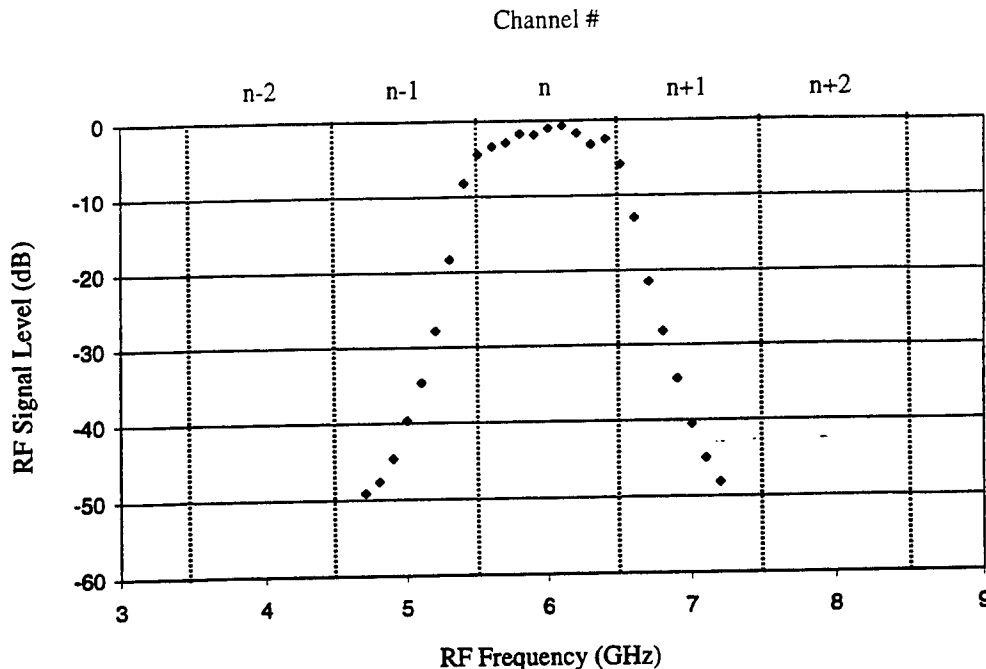


Figure 6-50. Channelizer individual channel passband response (unequal spot size case)

We also measured the crosstalk, defined as the in-band response in a given channel due to a signal at the near edge of that channel's second nearest neighbor. We should note the difference between crosstalk and the previous channel response measurement. The previous measurement gave the strength of the tone resulting from the signal beating with the local oscillator centered on the channel of interest. Thus once the beat note falls out of the channel pass band (5.5GHz to 6.5GHz in our experiment) the shape of the response primarily is determined by the electronic postdetection filter. Crosstalk, as illustrated in Figure 6-51, is a result of the signal and L.O. spots in channel $n \pm 2$ spilling over into channel n , the channel of interest. This produces a RF beat tone that is within that channel's passband and therefore appears as a spurious in-band response. The measurement consisted of centering the L.O. on our channel detector then applying a signal at the edge of the channel. We then physically translated the channel detector (the multimode fiber/slit combination) a distance equivalent to two channels in the output focal plane. We measured crosstalk for the equivalent of signals in channels $n+2$ and $n-2$. The result for channel $n-2$ was -37dB , whereas the channel $n+2$ result, which was limited by the dynamic range of the measurement apparatus, was about -53dB . This is somewhat short of the -70dB expected from the calculations that were based on the

assumption that the input fiber's mode profile was approximately Gaussian. The difference is attributable to the excessive power distributed in the wings of the fiber's actual mode profile. This apparently was a characteristic of the particular fiber we used in the system. As we have seen, data on other fibers (e.g. Fujikura single-mode fiber) showed sidelobe levels below -50dB , which would readily provide the desired crosstalk performance.

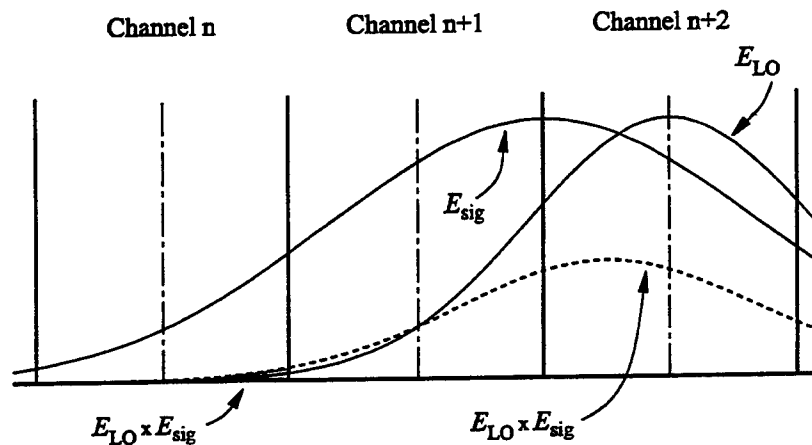


Figure 6-51. Channelizer crosstalk measurement

6.3.2.3 Spur-free dynamic range

We measured the dynamic range by applying two, equal-power RF signals to the modulator at such a level that their 3rd order intermodulation product generated a response that was equal to the system noise power. We then measured the applied power for a single-tone RF signal that produced a fundamental response that was just equal to the noise power. The ratio of these two power levels is the spur free dynamic range. The measurements were made using a spectrum analyzer set to 3KHz noise bandwidth and the results were extrapolated to a 1GHz noise bandwidth. We also calculated the dynamic range for our model of the system to compare with our experimental result. Recall from the discussion in section 3.1.2 that the dynamic range is given by [equation 3.1-29]

$$\text{SFDR} = [4(Rs^2 P_0 G_0 L_0 P_{L.O.} G_{L.O.} L_{L.O.}) / (4kTB + 2 s^2 h\nu_0 F_0 G_0 L_0 P_{L.O.} G_{L.O.} L_{L.O.} B R)]^{2/3}$$

We showed that the dynamic range is maximized if the system noise is dominated by the second term in the denominator, which results from the signal beam's amplifier ASE

beating with the L.O. We measured the dynamic for two arrangements of EDFAs that resulted in two combinations of signal and L.O. optical power levels. We note that the optical power levels in our experiment were insufficient to prevent the system from being dominated by thermal noise so we expected to obtain a dynamic range somewhat less 50dB. The results are shown in table 6-6.

Table 6-6. Channelizer spur-free dynamic range

Input optical power	Measured SFDR into 3KHz noise BW	Projected SFDR into 1GHz noise BW	Calculated SFDR into 1GHz noise BW
$G_{L.O.}P_{L.O.}L_{L.O.} = 2.8 \times 10^{-4}$ $G_O P_O L_O = 3.5 \times 10^{-2}$	79dB	42.2dB	44.7dB
$G_{L.O.}P_{L.O.}L_{L.O.} = 1.2 \times 10^{-4}$ $G_O P_O L_O = 1.7 \times 10^{-1}$	82dB	45.2dB	48.0dB

The observed performance is seen to agree very well with our calculated results. This leads us to believe that the RF performance goals are certainly within the capabilities of this technology.

7 TOP LEVEL DESIGN PLAN

During the course of this program, one of our objectives was to measure the RF performance of our channelizer test bed and relate the measured performance to that predicted by our previous modeling. When considering the RF performance of the testbed it is important to note that the testbed was designed to evaluate key receiver functions that support signal channelization such as dispersion, optical input/output coupling, and stable optical carrier/L.O. alignment. In order to accomplish this the testbed was constructed to be simply reconfigurable and provide a degree of flexibility that allows us to examine a variety of conditions that were revealed by our analyses to influence receiver performance. Our system has accomplished these goals, but consequently, we necessarily compromised certain receiver attributes, most notably that of system size. It is instructive at this time to consider how the channelizer can be reduced in size from its present 7ft³ (35"x27"x13") to something that doesn't require an optical table to support it. We have developed a compact, bulk-optic concept that is a straightforward extension of the technology used in our testbed. Figure 7-1 shows a perspective view of an optical channelizer that occupies a volume of less than 15in³. Several factors contribute to this volume reduction. First, since the dimension of the optical beam is of no consequence to the optical processing, we incorporated cylinder optics in the turning prism (see figure 7-2) to compress the beam height, which allowed us to reduce the thickness of the system to about 1in. Second, we employed a custom grating that is optimized for this application. By orienting the grating at near grazing angles for both the incident and diffracted beams the grating is operating close to its resolution limit, which means that for a given resolution the grating length is minimized. Also we would expect to achieve in excess of 90% diffraction efficiency with a custom grating, which will allow multiple passes of the optical beam on the grating. The pictured design uses eight passes, providing for an eight-fold reduction of the grating length. Finally, the diffraction takes place within glass, which allows further reduction of the grating length by a factor equal to the refractive index of the glass.

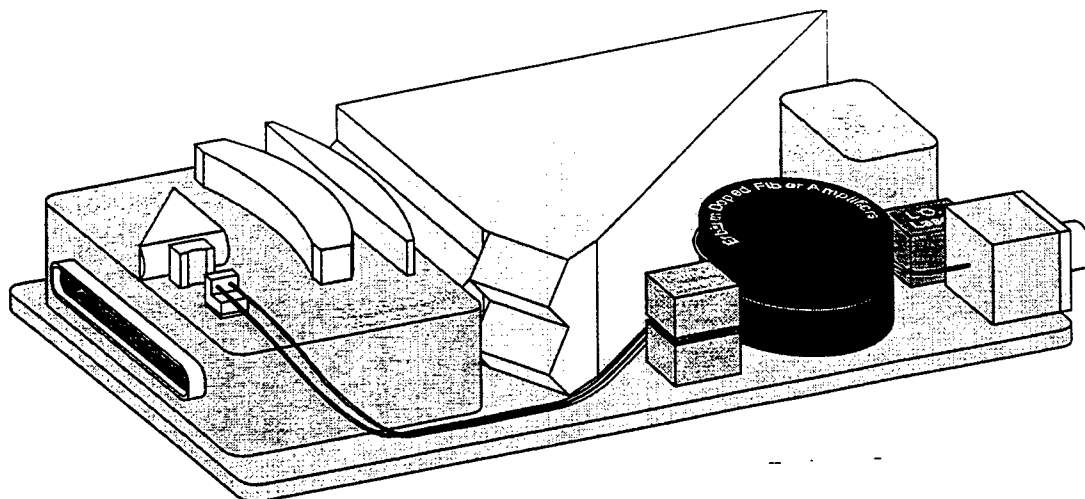


Figure 7-1. Miniaturized coherent optical channelizer

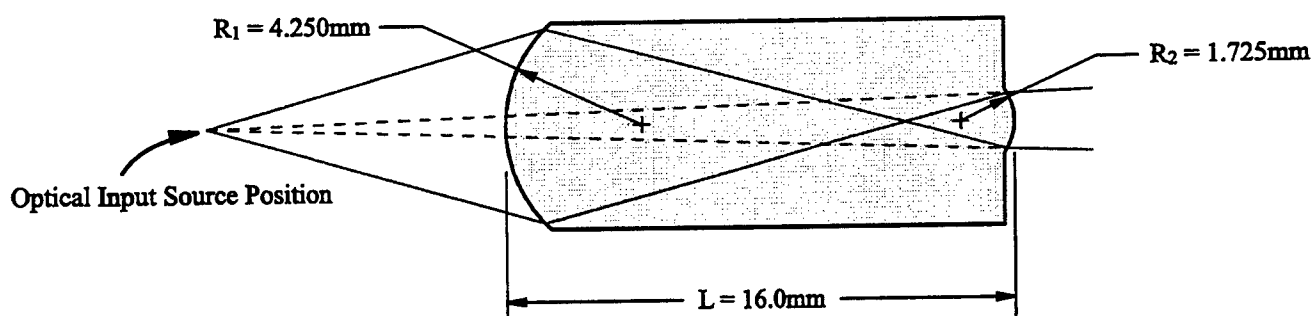


Figure 7-2. Vertical beam compression is accomplished with cylindrical surfaces on the beam turning prism (shown here with optical path unfolded)

In Table 7-1 below we present a list of major components and subassemblies that will be required to fabricate an exploratory development model patterned after the miniaturized channelizer shown in Figure 7-1.

Table 7-1. Exploratory development model parts list

Item Number	Description	Comments
1	Assembly baseplate	
2	Grating retro-mirror assembly	Custom optical component
3	Input beam-forming optics	Custom lens design w/ beam compression prism
4	Focal I/O assembly	Integrated optic circuit and mount w/ fiber-coupled signal and L.O. waveguides and waveguide fanout to detector array
5	Detector array	Integrated circuit w/ optical detectors and 1 st stage of output amplification
6	Post-detection electronics	Electronic assembly containing I.F filters and signal amplifiers if required
7	Local oscillator frequency comb generator	
7a	Mode-locked laser	External-cavity, semiconductor, hybrid mode-locked laser; or n'th harmonic fiber ring laser; or external-cavity, doped-glass micro-chip laser.
7b	Mode-locked laser drive electronics	Electronics module containing low-noise reference oscillator and laser control electronics
8	L.O. power amplifier, EDFA	High output power optical amplifier
9	Signal beam amplifier, EDFA	Low-noise, high clamped-gain, high output power optical amplifier
10	EDFA pump lasers	Semiconductor lasers and drive electronics

8 CONCLUSIONS

The Coherent Optical Receiver Engineering (CORE) program has produced a sound technical foundation for future coherent optical receivers and set the stage for the development of a prototype channelized optical receiver. Through an assessment of useful mission applications we determined the types of signal processing functions required of coherent receivers. We assessed the demands placed on a receiver system by the emerging wideband signal environments and established functional requirements as goals for our receiver development. It became clear early on that an optical channelizer was the best candidate architecture to satisfy the mission requirements.

Our analyses of receiver performance capability investigated two approaches: a Fabry-Perot filter-based approach and a free-space diffraction grating approach. We found that the crosstalk-ripple performance for the Fabry-Perot approach was so poor that this approach was ruled out. We found that for the grating approach desirable channel response characteristics could be obtained by judicious selection of the sizes of the input beams with respect to the detector pitch. Assuming that sufficient optical amplification is available to overcome system losses, the optimum dynamic range is determined entirely by the output power of the laser that is modulated with the RF signal and the noise figure of the optical amplifier used in the signal beam path. It is reasonable to expect a multi-octave, spur-free dynamic range of greater than $118\text{dB/Hz}^{2/3}$ ($>58\text{dB}$ into a 1GHz noise bandwidth). In order to achieve this performance second order nonlinearities due to the modulator must be suppressed, which dictates the use of a null-biased, highly chirp-free, Mach-Zehnder interferometric modulator. As in all analog applications, link gain and noise figure for the channelizer are strongly dependent on an efficient modulator, i.e. low V_{π} .

This work demonstrated a very low level of phase noise on the heterodyne beat of optically injection locked semiconductor lasers. To our knowledge, this is by far the lowest reported level of phase noise from injection locked semiconductor lasers. Since the noise floor of -125 dBc/Hz seen in this work appears to be due to an excess noise mechanism unrelated to injection locking, further improvements may be possible, which suggests the consideration of injection locking for the most demanding applications.

Injection locking by itself cannot constitute a complete carrier tracking solution, unless unrealistic requirements are placed on the absolute frequency stability of each laser to ensure the relative drift of the two lasers is an insignificant fraction of the injection locking range. Therefore it is necessary to supplement injection locking with a drift control mechanism. Published methods include an optical PLL, and a Pound-Drever-Hall servo loop to lock the master to the slave cavity resonance. In principle, the main advantage of injection locking, namely its large noise suppression bandwidth, should be preserved in hybrid schemes of this type, since the drift control mechanism need not have a large bandwidth.

We have demonstrated that CW injection locking of a mode-locked external cavity semiconductor laser can provide a local oscillator source for an ultra-wide band coherent optical channelizer. Nearly transform limited pulses were obtained over a tuning range of 24 nm. Pulses widths obtained were less than 2.5 ps, this corresponds to a signal bandwidth which can process signals with bandwidths greater than 100 GHz. Phase coherence between the incoming carrier signal and the local oscillator is achieved by optical injection locking. The coherence between the carrier laser and the optical frequency comb is dependent on how well the longitudinal modes of the mode-locked laser are phase locked. Optical injection locking of mode-locked semiconductor lasers opens up many new applications in optical communication systems. This technique is not limited to the use of semiconductor lasers, and is expected to be observable in other laser systems. Another alternative for a local oscillator laser source would be the new micro-chip lasers utilizing a diode pumped Er:Glass gain medium. The use of a compact gain medium allows relatively short cavities for fundamental operation at a frequency of 1 GHz. By using an actively mode-locked fiber laser, higher power per mode can be accomplished. Using coupled cavities and intra-cavity filters can increase the suppression of the troublesome side modes.

We constructed and demonstrated a coherent optical processor that can instantaneously channelize 100GHz of RF bandwidth with 1 GHz resolution and simultaneously translate the center frequency of all the channels to a common intermediate frequency band. The CORE channelizer preserves the signals' complex spectra and we have shown that this processor is capable of providing state-of-the-art RF performance.

Our demonstrated dynamic range of 45dB into a 1GHz bandwidth is superior to the performance of existing electronic and acousto-optic approaches to signal channelization. The measured channel response uniformity was excellent and crosstalk suppression can be improved to desired levels by better controlling the input optical beam profiles.

9 REFERENCES

- [1] M. Abramowitz and I. Stegun, Eds, *Handbook of Mathematical Functions*, New York: Dover Publications, 1964.
- [2] A. Yariv, *Introduction to Optical Electronics*, New York: Holt, Rinehart and Winston, 1976.
- [3] J. Senior, *Optical Fiber Communications: Principles and Practice*, 2nd edition, Prentice Hall, 1992.
- [4] E. Desurvire, *Erbium Doped Fiber Amplifiers: Principles and Applications*, Wiley, 1994.
- [5] A. Papoulis, *Probability, Random Variables and Stochastic Processes*, McGraw Hill, 2nd ed., 1984.
- [6] D. Middleton, *Introduction to Statistical Communication Theory*,
- [7] C.-C. Chen, and M. Z. Win, "Frequency noise measurement of diode-pumped Nd:YAG ring lasers," PTL 2(11), 772, 1990.
- [8] K. Kikuchi, "Effect of 1/f-type FM noise on semiconductor laser linewidth residual in high power limit," JQE 25(4), 684, 1989.
- [9] R. Centeno Neelen, D. M. Boersma, M. P. van Exter, G. Nienhuis and J.P. Woerdman, "Spectral filtering within the Schawlow-Townes linewidth of a semiconductor laser," PRL 69(4), 593, 1992.
- [10] U. Gliese, T.N. Nielsen, M. Bruun, E.L. Christensen, K.E. Stubkjær, S. Lindgren and B. Broberg, "A wideband heterodyne optical phase locked loop for generation of 3-18 GHz microwave carriers," IEEE Photonics Technology Lett., 4(8), pp936-938, 1992.
- [11] F.M. Gardner, *Phaselock Techniques*, 2nd ed. Wiley, 1979.
- [12] U. Gliese, E.L. Christensen, and K.E. Stubkjaer, "Laser linewidth requirements and improvements for coherent optical beam forming networks in satellites" JLT 9(6) 779 1991.
- [13] A.E. Siegman, *Lasers*, University Science Books, 1986.

- [14] F. Mogensen, H. Olesen, and G. Jacobsen, "Locking Conditions and Stability Properties for a Semiconductor Laser with External Light Injection," JQE 21(7) 784 1985.
- [15] R. Lang, "Injection Locking Properties of a Semiconductor Laser," JQE 18(6) 976 1982.
- [16] K. Vahala and A. Yariv, "Semiclassical Theory of Noise in Semiconductor Lasers -- Part II," JQE 19(6) 1102 1983.
- [17] L.E. Richter, H.I. Mandelberg, M.S. Kruger, and P.A. McGrath, "Linewidth determination from self-heterodyne measurements with subcoherence delay times", *IEEE Journal of Quantum Electronics*, vol. 22, pp. 2070-2074, 1986.
- [18] J.M. Liu, H.F. Chen, X.J. Meng, and T.B. Simpson, "Modulation bandwidth, noise, and stability of a semiconductor laser subject to strong injection locking", *IEEE Photonics Technology Letters*, vol. 9, no. 10, pp. 1325-1327, October 1997.
- [19] M.P. van Exeter, S.J.M. Kuppens, and J.P. Woerdman, "Excess phase noise in self-heterodyne detection", *IEEE Journal of Quantum Electronics*, vol. 28, no. 3, March 1992.
- [20] Hewlett Packard Application Note "Better phase noise measurement with the HP 8048 AR
- [21] Personal communications with Dr. Michael G. Wickham of TRW Inc.
- [22] Z. Fan, P. Heim, and M. Dagenais, "Highly coherent RF signal generation by heterodyne optical phase locking of external cavity lasers", *IEEE Photonics Technology Letters*, vol. 10, no. 5, pp. 719-721, May 1998.
- [23] R.P. Braun, G Grosskopf, D. Rohde, and F. Schmidt, "Low phase noise millimeter-wave generation at 64 GHz and data transmission using optical sideband injection locking", *IEEE Photonics Technology Letters*, vol. 10, no. 5, pp. 728-731, May 1998.
- [24] T.B. Simpson and J.M. Liu, "Enhanced modulation bandwidth in injection-locked semiconductor lasers", *IEEE Photonics Technology Letters*, vol. 9, no. 10, pp. 1322-1325, October 1997.
- [25] X.J. Meng, T. Chau, D. Tong, and M.C. Wu., "Suppression of second harmonic distortion in DFB laser with optical injection locking", LEOS 1998 11th Annual

- IEEE / Lasers and Electro-Optics Society 1998 Annual Meeting, paper number 056.
- [26] T. Saitho, M. Kourogi, and M. Ohtsu, "A waveguide-type optical-frequency comb generator", *IEEE Photonics Technology Letters*, vol. 7, no.2, pp. 197-200, February 1995.
 - [27] K.P. Ho, and J.M. Kahn, "Optical frequency comb generator using phase modulation in an amplified circulating loop", *IEEE Photonics Technology Letters*, vol. 5, no. 6, pp. 721-5, June 1993.
 - [28] Pritel Inc., Product brochure for active mode-locked fiber laser.
 - [29] Lasers, A.E. Siegman. University Science Books, Mill Valley, CA, 1986, pp. 1050-1128.
 - [30] H. Haus, "Theory of mode-locking in an external resonator", *J. Appl. Phys.*, vol. 51, pp. 4042-4049, 1980.
 - [31] J. Au Yeung, "Theory of active mode-locking of a semiconductor laser in an external cavity", *IEEE Journal of Quantum Electronics*, vol. 17, no. 3, pp. 398-403, March 1981.
 - [32] P.T. Ho, L.A. Glasser, E.P. Ippen, and H.A. Haus, "Picosecond pulse generation with a CW GaAlAs laser diode", *Appl. Phys. Letters*, vol. 33, pp. 241-242, 1978.
 - [33] R. Salvatore, T. Schrans, and A. Yariv, "Wavelength tunable source of subpicosecond pulses from a CW passively mode-locked two-section multiple quantum-well laser", *IEEE Photonics Technology Letters*, vol. 5, no.7, pp. 756-758, July 1993.
 - [34] M.C. Wu, and Y.K. Chen, "Monolithic colliding-pulse mode-locked quantum-well lasers", *IEEE Journal of Quantum Electronics*, vol. 28, no. 10, pp. 2176-2185, October 1992.
 - [35] D.J. Derickson, et al., "Short pulse generation using multisegment mode-locked semiconductor lasers", *IEEE Journal of Quantum Electronics*, vol. 28, no. 4, March 1992.
 - [36] H.A. Haus and H.L. Dyckman, "Timing of laser pulses produced by combined passive and active mode-locking", *Int. J. Electron.*, vol. 44, pp. 225-238, 1978.

- [37] J.P. van der Ziel, "Mode-locking of semiconductor lasers", *Semiconductors and Semimetals*, vol. 22, Part B, W.T. Tsang, Ed., Academic Press, Orlando, Florida, 1985, Ch. 1.
- [38] M. Schell, A. G. Weber, E. Scholl, and D. Bimberg, "Fundamental limits of sub-picosecond pulse generation by active mode-locking of semiconductor lasers: the spectral width and the facet reflectivities", *IEEE Journal of Quantum Electronics*, vol. 25, pp. 1661-1668, 1991.
- [39] P.T. Ho, "Phase and amplitude fluctuations in a mode-locked laser", *IEEE Journal of Quantum Electronics*, vol. 21, pp. 1806-1815, 1985.
- [40] L.R. Brovelli, and U. Keller, "Design and operation of antiresonant Fabry-Perot saturable absorbers for mode-locked solid-state lasers", *J. Opt. Soc. Am. B*, vol. 12, no. 2, pp. 311-322, February 1995.
- [41] U. Keller, et al., "Semiconductor saturable absorbers mirrors (SESAM's) for femtosecond to nanosecond pulse generation in solid-state lasers", *IEEE Journal of Selected Topics in Quantum Electronics*, vol. 2, no. 3, pp. 435-453, September 1996.
- [42] D. Kopf, et al., "High-average-power diode-pumped femtosecond Cr:LiSAF lasers", *Applied Physics B, Lasers and Optics*,
- [43] S. Tsuda, W.H. Knox, S.T. Cundiff, W.Y. Jan, and J.E. Cunningham, "Mode-locking ultrafast solid-state lasers with saturable Bragg reflectors", *IEEE Journal of Selected Topics in Quantum Electronics*, vol. 2, no. 3, pp. 454-464, September 1996.
- [44] E. Garmire and A. Yariv, "Laser mode-locking with saturable absorbers", *IEEE Journal of Quantum Electronics*, vol. 3, no. 6, pp. 222-377, June 1967.
- [45] O.P. McDuff and S. E. Harris, "Nonlinear theory of the internally loss-modulated laser", *IEEE Journal of Quantum Electronics*, vol. 3, no. 3, pp. 101-111, March 1967.
- [46] S.E. Harris and O.P. McDuff, "Theory of FM laser oscillation", *IEEE Journal of Quantum Electronics*, vol. 1, no. 6, pp. 245-262, June 1967.
- [47] Laser Physics, M. Sargent III, M.O. Scully, and W.E. Lamb, Addison Wesley, Reading, Mass., Ch. 3 - 12.

- [48] J.L. Shen, et. al, To be published.
- [49] D. von der Linde, "Characterization of the noise in continuously operating mode-locked lasers", *Applied Physics B* 39, pg. 201-17, 1986.
- [50] S. Sanders, T. Schrans, and A. Yariv, "Timing jitter and pulse energy fluctuations in a passively mode-locked two-section quantum-well laser coupled to an external cavity", *Applied Physics Letters* 59 (11), Sept. 9, 1991, pg 1275-1278.
- [51] D.J. Derickson, A. Mar, and J.E. Bowers, "Residual and absolute timing jitter in actively mode-locked semiconductor lasers", *Electronics Letters*, vol. 26, pp. 2026-2027, 1990.
- [52] D.J. Derickson, P.A. Morton, J.E. Bowers, and R.L. Thorton, "Comparison of timing jitter in external and monolithic cavity mode-locked lasers", *Appl. Phys. Lett.*, vol. 49, pp. 1210-1212, 1990.
- [53] Z. Ahmed, L. Zhai, A.J. Lowery, N. Onodera, and R.S. Tucker, "Locking bandwidth of actively mode-locked semiconductor lasers", *IEEE Journal of Quantum Electronics*, vol. 29, no. 6, June 1993.
- [54] R. Salvatore, S. Sanders, T. Schrans, and A. Yariv, "Supermodes of High-Repetition-Rate Passively Mode-Locked Semiconductor Lasers", *IEEE Journal of Quantum Electronics*, vol. 32, no. 6, pp. 941-952, June 1996.
- [55] Z. Ahmed, H.F. Liu, D. Novak, Y. Ogawa, M.D. Pelusi, and D.Y. Kim, "Locking characteristics of a passively mode-locked monolithic DBR laser stabilized by optical injection", *IEEE Photonics Technology Letters*, vol.8, no.1, pp. 37-39, January 1996.
- [56] M. Teshima, M. Koga, K. Sato, "Accurate Frequency Control of a Mode-Locked Laser Diode by Reference Light Injection", *Optics Letters*, vol. 22, no. 2, p. 126-8, 1997.
- [57] Y. Katagiri, A. Takada, "Supermode selection of a subterahertz-harmonic colliding-pulse mode-locked semiconductor laser using continuous-wave light injection", *IEEE Photonics Technology Letters*, vol.9, no.12,pp. 1564-6, Dec. 1997.

- [58] A. Takada, and W. Imajuku, "Linewidth narrowing and optical phase control of mode-locked semiconductor ring laser employing optical injection locking", *IEEE Photonics Technology Letters*, vol.9, no.10, pp. 1328-30, Oct. 1997.

10 APPENDICES

Presented at PSAA8 - 1998

CW Injection Locking of External Cavity Hybrid Mode-Locked Semiconductor Lasers

Thomas Jung^{†}, Ji-Lin Shen[†], Dennis T.K. Tong[†], Ming. C. Wu[†],*

Robert Lodenkamper, Larry Lembo*, Richard Davis*, and John C. Brock**

[†]UCLA, Electrical Engineering Department

*TRW, Photonics Technology Department

Injection locking is a very effective way to establish phase coherence between two free-running lasers. Most of the previous studies have focused on injection locking of two CW lasers [1]. Injection locking from a single frequency laser to a mode-locked laser is of great interest since it can synchronize the phases of the entire mode-locked optical frequency comb (OFC) to the external reference [2,3]. It opens up many new applications in ultrawide band coherent optical communications and signal processing. In this paper, we report on the successful demonstration of the CW injection locking of external cavity mode-locked semiconductor lasers. The locking range and the pulse width variations with injection power are experimentally characterized.

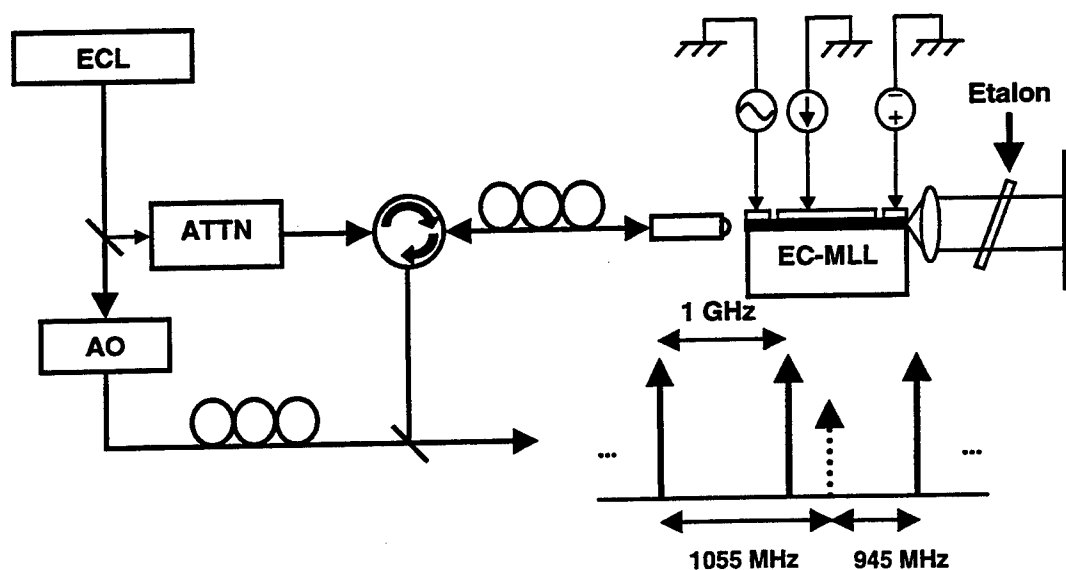


Figure 1.
Injection Locked Mode-Locked Laser Setup

The schematic diagram of our experimental setup is shown in Figure 1. A single-frequency tunable laser (master laser) is attenuated and injected into an external cavity mode-locked semiconductor laser (EC-MLL) through an optical circulator. The EC-MLL consists of a three-section monolithic laser coupled to a 15-cm-long external cavity. The EC-MLL is hybrid mode-locked at 1 GHz. In the absence of optical injection, near transform-limited optical pulses with duration of 1.9 ps and spectral width of 1.9 nm are obtained. To monitor the injection locking, part of the master laser output is split and frequency-shifted by 55 MHz using an acousto-optic modulator. It is then heterodyned with the output of the injected EC-MLL. Injection-locking is confirmed when a clean heterodyned signal at approximately 945 MHz and 1055 MHz is observed.

The parameter range of interest is when the slave laser is injection-locked to the master laser while it remains mode-locked. The heterodyned signal and the optical pulse width are monitored simultaneously as the injection power and the frequency detuning of the master laser are varied. Figure 2 shows the injection locking range and the optical pulse width of the EC-MLL versus the optical injection power. The injection locking range of the EC-MLL is shown to increase with the injected optical power (Fig. 2), similar to the injection locking of two CW lasers. When the injection power is greater than -27 dBm, the locking range exceeds the mode spacing of the EC-MLL (1 GHz). Beyond this injection level, one longitudinal mode of the mode-locked spectrum always falls within the locking range of the master laser and the EC-MLL stays injection-locked.

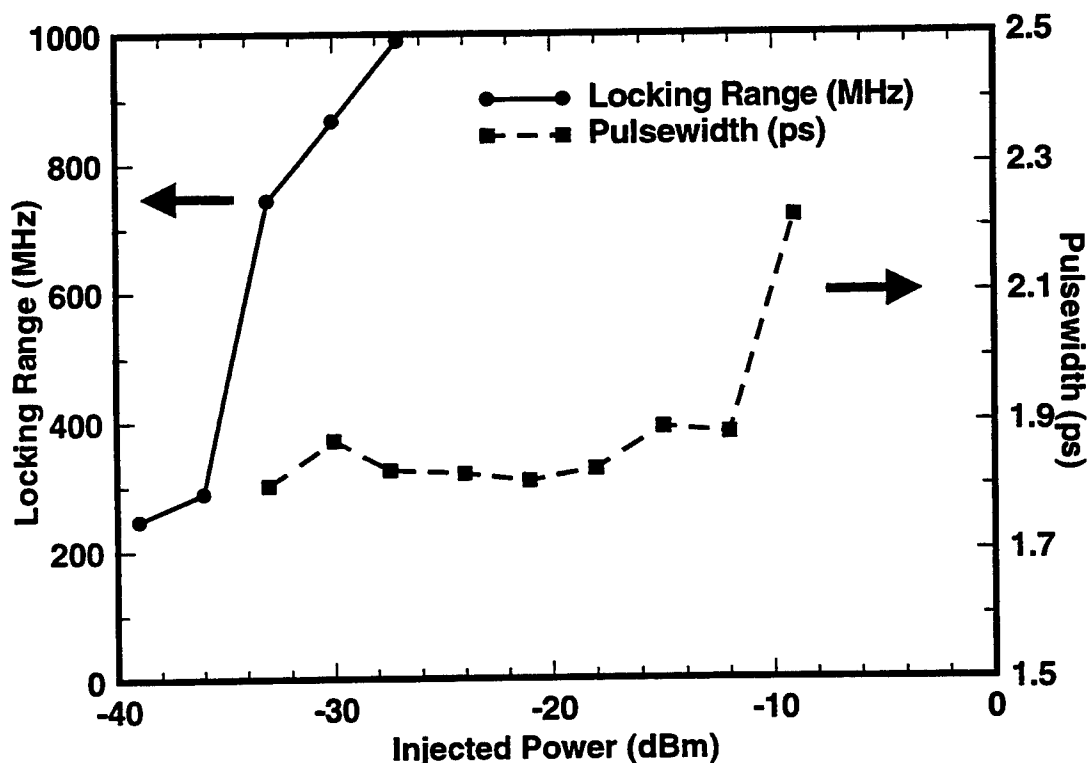


Figure 2.
Locking Range vs. Injected Power
Pulsewidth vs. Injected Power

The EC-MLL remains well mode-locked at low injection levels (< -10 dBm). The pulse width is almost independent of the injection power. Figure 3 shows the autocorrelation trace and the optical spectrum of the EC-MLL at an injected level of -13 dBm. The pulsewidth and the optical spectrum are essentially the same as those without injection. However, significant broadening in pulsewidth and autocorrelation substructure is observed when the injection level is comparable to the average output power of the EC-MLL (> -8 dBm). This is due the optical DC biasing of the integrated saturable absorber by the injected light, which causes the pulse-shaping process to be less effective.

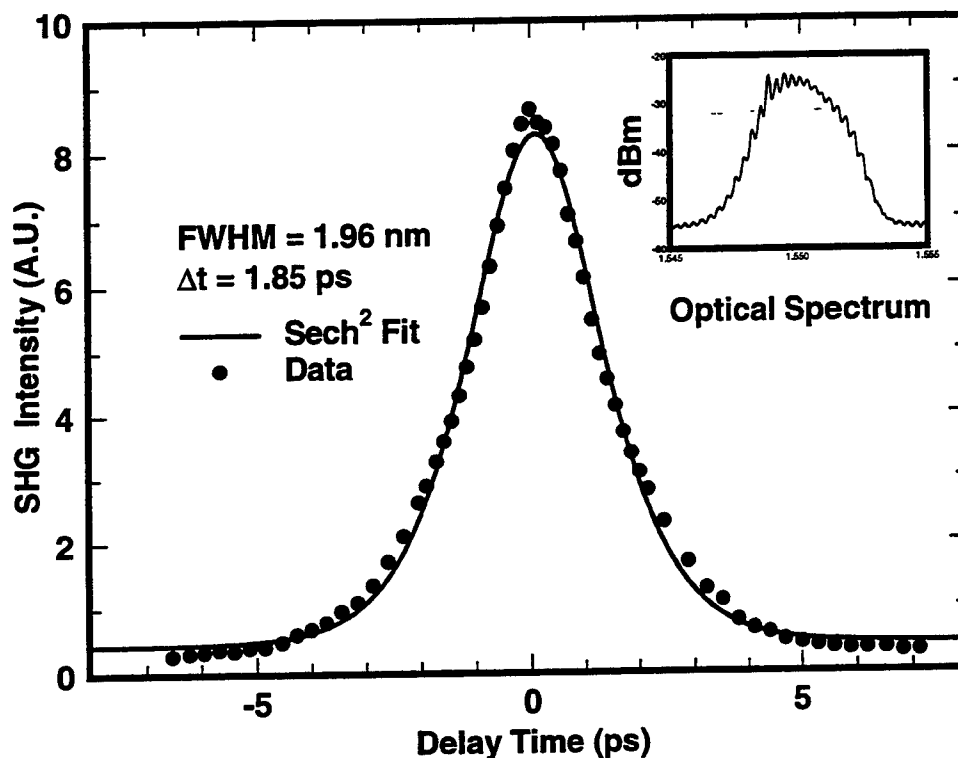


Figure 3.
Autocorrelation Trace with -13 dBm Injection

In summary, the CW injection locking of mode-locked semiconductor lasers has been experimentally demonstrated. Frequency locking has been achieved between the single-frequency source and the optical frequency comb of the mode-locked laser.

REFERENCES:

- [1] F. Mogensen, H. Olesen, G. Jacobsen, "Locking Conditions and Stability Properties for a Semiconductor Laser with External Light Injection", *IEEE Journal of Quantum Electronics*, vol. 21, no. 7, p. 784-93, 1985.
- [2] L.G. Joneckis, P. T. Ho, and G. Burdge, "CW Injection Seeding of a Mode-Locked Semiconductor Laser", *IEEE Journal of Quantum Electronics*, vol. 27, no.7, pp. 1854-1858, 1991.
- [3] M. Teshima, M. Koga, K. Sato, "Accurate Frequency Control of a Mode-Locked Laser Diode by Reference Light Injection", *Optics Letters*, vol. 22, no. 2, p. 126-8, 1997.

Presented at CLEO 1998

Phase Coherence and Frequency Control of a Hybrid Mode-Locked Semiconductor Laser by CW Optical Injection Locking

Thomas Jung^{†}, Ji-Lin Shen[†], Dennis T.K. Tong[†], Ming C. Wu[†],*

Robert Lodenkamper, Larry Lembo*, Michael Wickham*, Richard Davis*,*

John C. Brock, and Tawee Tanbun-Ek[‡].*

[†]UCLA, Electrical Engineering Department

*TRW, Photonics Technology Department

[‡]Bell Laboratories, Lucent Technologies

Mode-locked lasers have many versatile signal processing applications. However, frequency control and phase coherence of the mode-locked laser optical frequency comb is often needed to make these applications possible, as in channelizer applications. We extend the principle of optical injection locking of CW lasers to optical injection locking of mode-locked semiconductor lasers [1-3] to establish phase coherence and frequency control. This method allows us to phase lock an entire comb of frequencies to a single frequency source. Compared to pulsed injection locking of mode-locked semiconductor lasers [4], CW injection locking to mode-locked semiconductor lasers offers added simplicity but does not synchronize the timing of the pulses of the mode-locked laser.

An external cavity hybrid mode-locked laser (EC-MLL) is constructed as shown in Figure 1. A monolithic hybrid mode-locked semiconductor laser is anti-reflection

coated on one facet and coupled to an external cavity. The external cavity length is 15 cm which corresponds to a repetition rate of 1 GHz. An etalon with a 5 nm FWHM is placed in the external cavity to prevent mode-locking in clusters [2] and for tunability. The EC-MLL can be tuned over 20 nm from 1540 to 1560 nm; pulsewidths less than 2.5 ps were achieved over the entire tuning range and were approximately 1.6 times the transform limit. An external cavity laser (ECL) is used as the master laser, its output is attenuated then injected into the mode-locked slave laser via an optical circulator. Part of the master laser is frequency shifted by 55 MHz using an acousto-optic frequency shifter for heterodyne detection. Injection locking of the EC-MLL is verified when tones at 945 MHz and 1055 MHz appear. These tones are due to the heterodyne of the adjacent modes of the EC-MLL with the frequency shifted master laser (Figure 1), and can be observed up to an instrument limited 19 GHz (Figure 2).

The locking range is measured by monitoring the offset frequency of the master laser at which the tones disappear (Figure 3). Similar to injection locking of two CW lasers, the locking range is shown to increase with injected powers. Injected power levels well below the average power of the hybrid mode-locked laser show little effect on the pulsewidth (Figure 3). At injection powers comparable to the average power of the EC-MLL (-9 dBm), the pulsewidth broadens significantly and the autocorrelation trace shows a significant increase in substructure. The pulse broadening effect is due to the additional optical DC bias on the saturable absorber which reduces the pulse sharpening effect.

In conclusion we have demonstrated phase coherence between a CW single wavelength master laser and a multi-wavelength mode-locked slave laser by optical injection locking.

ACKNOWLEDGEMENT

This project is supported in part by TRW Inc. and Rome Laboratory.

REFERENCES:

- [1] F. Mogensen, H. Olesen, G. Jacobsen, "Locking Conditions and Stability Properties for a Semiconductor Laser with External Light Injection", *IEEE Journal of Quantum Electronics*, vol. 21, no. 7, p. 784-93, 1985.
- [2] L.G. Joneckis, P. T. Ho, and G. Burdge, "CW Injection Seeding of a Mode-Locked Semiconductor Laser", *IEEE Journal of Quantum Electronics*, vol. 27, no.7, pp. 1854-1858, 1991.
- [3] M. Teshima, M. Koga, K. Sato, "Accurate Frequency Control of a Mode-Locked Laser Diode by Reference Light Injection", *Optics Letters*, vol. 22, no. 2, p. 126-8, 1997.
- [4] M. Margalit, M. Orenstein, and H.A. Haus, "Injection Locking of Passively Mode-Locked Laser", *IEEE Journal of Quantum Electronics*, vol. 32, no. 1, p. 155-160, 1996.

FIGURE CAPTIONS:

- Figure 1. Injection Locking Mode-Locked Laser Setup
- Figure 2. Heterodyne tone centered at 1 GHz, 10 GHz, 15 GHz, and 19 GHz
- Figure 3. Locking Range and Pulsewidth vs. Injected Power

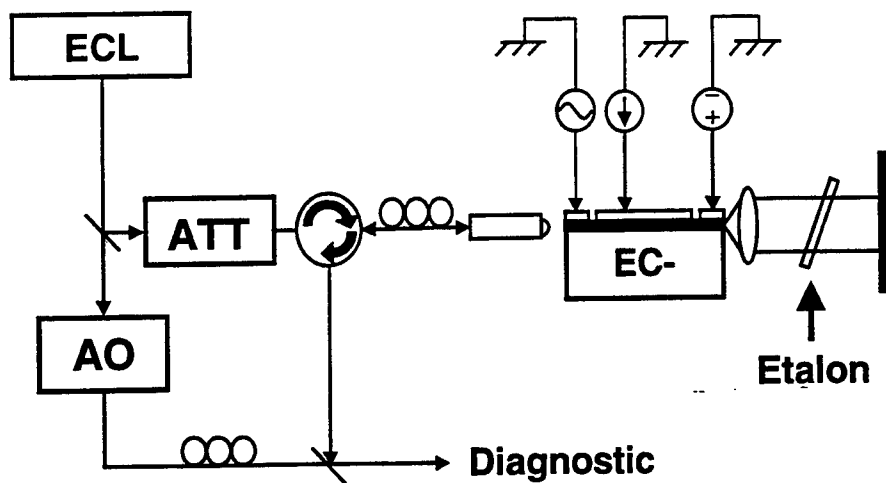


Figure 1

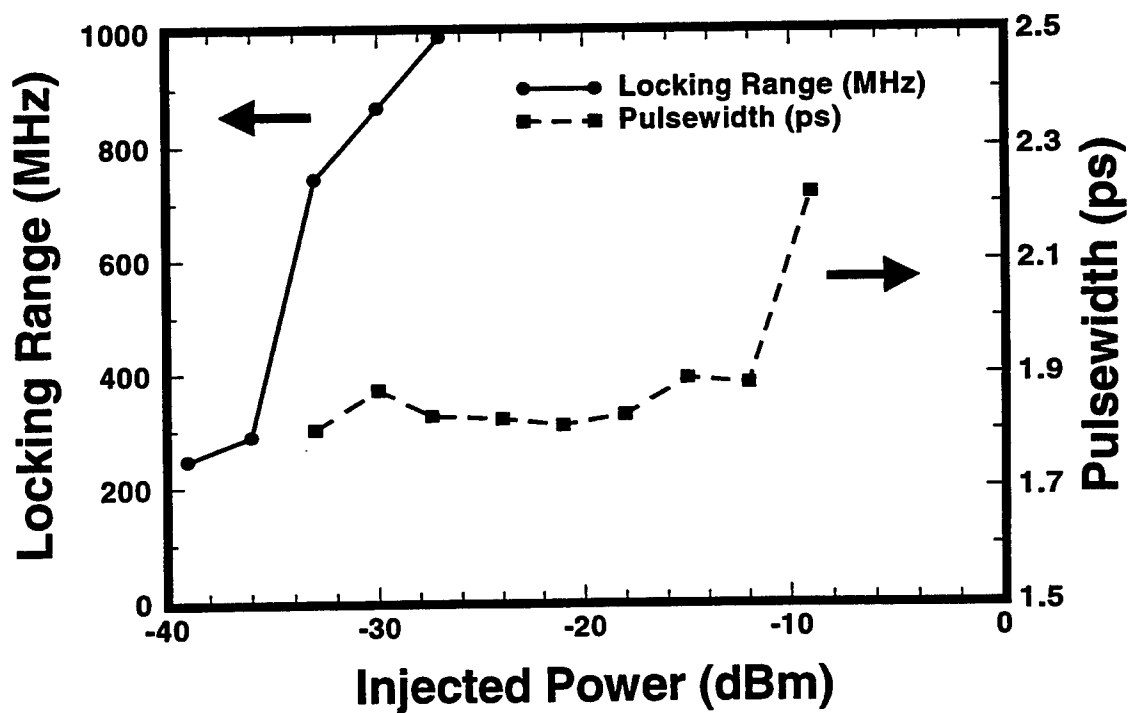


Figure 2

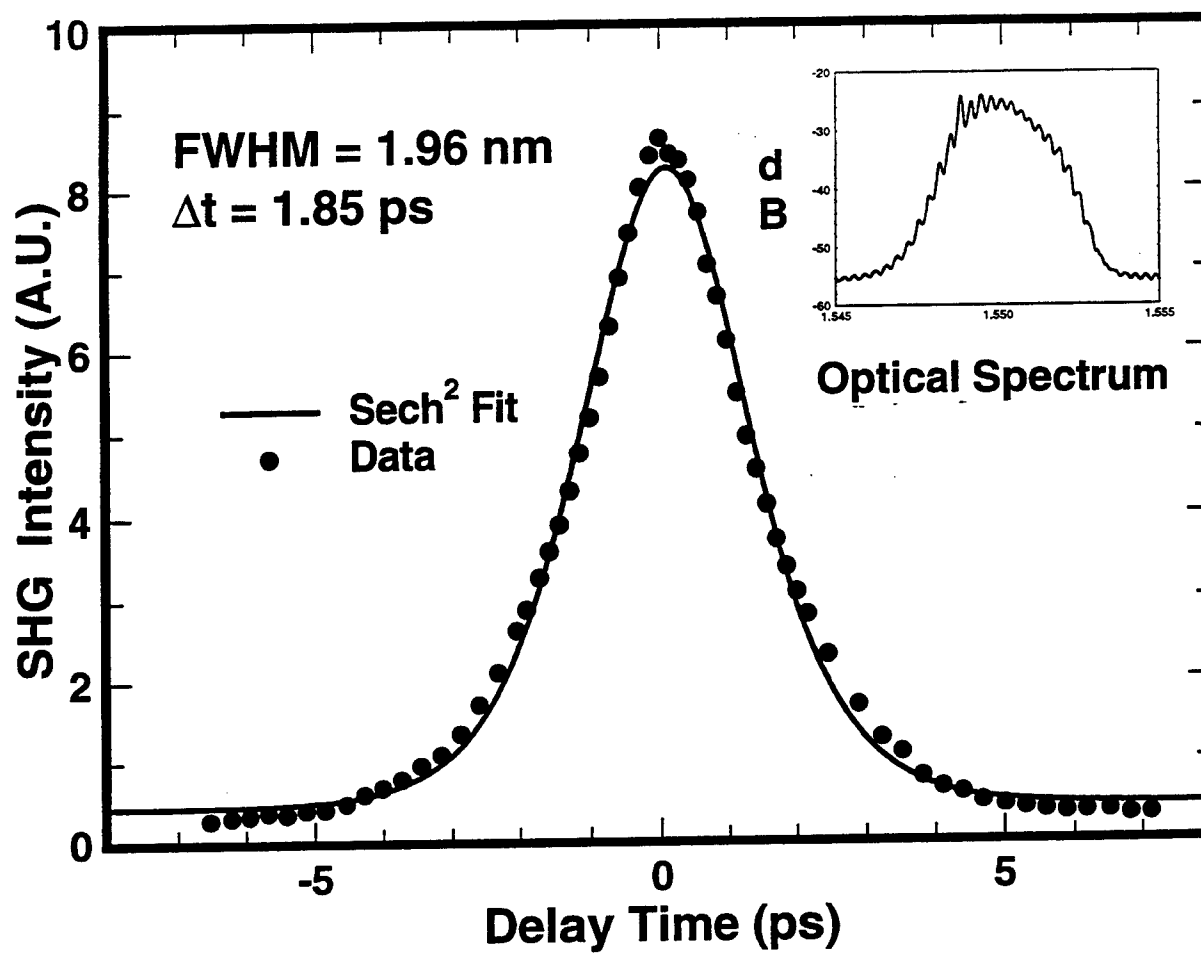


Figure 3

Presented at OFC 1998

CW Injection Locking of an External Cavity Hybrid Mode-Locked Semiconductor Laser

Thomas Jung, Ji-Lin Shen, Dennis T.K. Tong, Robert Lodenkamper*, Larry Lembo*,
Richard Davis*, Ming C. Wu, and John C. Brock**

UCLA, Electrical Engineering Department

*TRW, Photonics Technology Department

Injection locking is a very effective way to establish phase coherence between two free-running lasers. Injection locking of two CW lasers is well understood and characterized. We extend this principle of injection locking to that of mode-locked semiconductor lasers. We investigate the effects of injection on pulsewidth and the optical spectrum. We also estimate the range where phase coherence is established between the CW master and mode-locked slave laser.

The schematic diagram of our experimental setup is shown in Fig. 1. The slave laser we employ here is an external cavity hybridly mode-locked semiconductor laser (EC-MLL), which consists of a three section monolithic laser AR coated on one side and coupled to an external cavity of 15 cm. The EC-MLL is hybridly mode-locked at 1 GHz. An intracavity etalon with 5 nm FWHM bandwidth is used to prevent mode-locking in clusters. The master laser (ML) used is an external cavity tunable semiconductor laser. The output from the ML is split with a 3 dB coupler. One arm is attenuated and injected into the EC-MLL via an optical circulator. The other arm is frequency shifted by +55 MHz using an acousto-optic frequency shifter and recombined with the output of the

injection-locked EC-MLL at a high speed photodetector. Polarization controllers are employed to maintain proper polarization during injection-locking and heterodyning.

Figure 2 shows the autocorrelation traces and the optical spectra of the mode-locked pulses with and without injection locking. In fig. 2(a), the EC-MLL is subjected to no injected light. The output pulse is 1.64 times the transform-limited with a pulsewidth of 2.47 ps and a FWHM optical bandwidth of 1.68 nm. The attenuated output of the ML is then injected into the EC-MLL. The wavelength of the ML is tuned to align with one mode from the mode-locked spectrum of the EC-MLL. The injection ratio is -13 dB. Under injection locking, the output pulses from the EC-MLL shows no significant change (fig. 2(b)), compared to the pulse in fig. 2(a). The output pulse is 1.61 times the transform-limited with a pulsewidth of 2.49 ps and an optical bandwidth of 1.63 nm.

To demonstrate phase coherence between the ML and EC-MLL under injection-locking, the heterodyned signal between the output of the injection-locked EC-MLL and the frequency shifted (55 MHz) ML is measured at the output of the photodetector. In principle, since all the modes within the mode-locked spectrum are phase locked together, the mode-locked laser will produce harmonics of the mode-locked frequency. Under injection locking, phase coherence is established between the ML and the EC-MLL. Heterodyne of the frequency-shifted output of the ML and the EC-MLL results in two additional beat tones spaced 55 MHz on both sides of each mode-locked frequency harmonics. The sharp beat note serves as a evidence of injection-locking between the ML and the EC-MLL. In our measurement, these extra beat notes are observed for the fundamental mode-locked frequency at 1 GHz (fig. 3(a)), up to the 18th harmonic (fig. 3(b)) before the noise floor of the measurement system dominates.

In summary, we have experimentally demonstrated CW injection locking of a mode-locking semiconductor laser. Detailed description of the experiment will be presented.

REFERENCES:

- [1] R.A. Salvatore, T. Schrans, and A. Yariv, "Wavelength Tunable Source of Subpicosecond Pulses from CW Passively Mode-Locked Two-Section Multiple-Quantum-Well Laser", *IEEE Photonics Technology Letters*, vol. 5, no. 7, pp. 756-758, 1993.
- [2] L.G. Joneckis, P.T. Ho, and G. Burdge, "CW Injection Seeding of a Mode-Locked Semiconductor Laser", *IEEE Journal of Quantum Electronics*, vol. 27, no.7, pp. 1854-1858, 1991.
- [3] Y.K. Chen, and M.C. Wu, "Monolithic Colliding-Pulse Mode-Locked Quantum-Well Lasers", *IEEE Journal of Quantum Electronics*, vol. 28. No. 10, pp. 2176-2185, 1992.

Evaluation of optical channelizers in terms of RF performance

Robert Lodenkamper, Richard L. Davis, Larry J. Lembo, Michael G. Wickham, John C. Brock

TRW Photonics Technology Department, One Space Park, Redondo Beach CA 90278

ABSTRACT

The demonstration of RF photonic links with bandwidths of 100 GHz or more is expected in the near future, due to rapid and continuing progress in modulator and detector technology. Since it is very difficult to electronically process such a large bandwidth after photodetection, photonic approaches that reduce the burden on the electronics are increasingly relevant. One such approach is an optical channelizer, where an RF modulated optical carrier is optically dispersed onto a detector array. Each element of the array only sees a portion of the original wideband RF spectrum.

We analyze the RF performance of optical channelizers in terms of crosstalk and uniformity of response. Both direct detection and heterodyne channelizers will be considered. Analysis of this kind is necessary for our application, since the usual parameters of a dispersive optical system, such as resolution, resolving power or filter linewidth do not provide enough information to determine the RF performance. The analysis has shown that a Fabry-Perot filter based channelizer cannot provide adequate RF performance, while a grating-based channelizer can. For channelization to 1 GHz channels with a -70 dB crosstalk specification, a total grating length of roughly 80 cm is required, so a multiple bounce geometry is necessary to obtain a reasonably compact system.

Keywords: optical channelization, crosstalk, wideband signal processing

1. INTRODUCTION

The basic channelizer front-end architecture we will consider is an array of identical RF bandpass filters with equally spaced center frequencies, each of which sees the entire input RF signal. The difference between the center frequencies of two adjacent filters is, by definition, the channel spacing. Figure 1 is a schematic sketch of the frequency response of several adjacent channel filters.

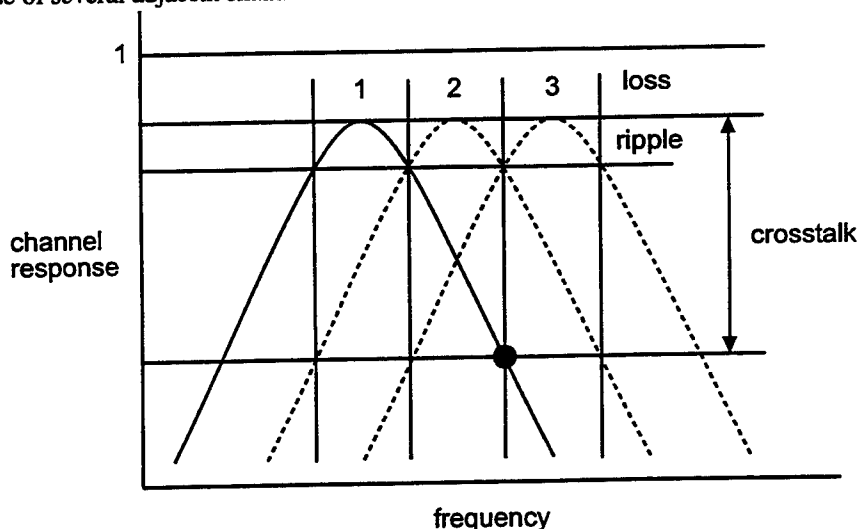


Figure 1: Schematic frequency response of several adjacent channel filters. The effect of nonideal channel filters is described by three parameters: loss, ripple and crosstalk, as shown.

Figure 1 also gives a picture for the three parameters (loss, ripple, and crosstalk) we employ to quantify the effect of nonideal channel filtering. Ripple is the ratio of center response to edge response for each channel, and is a reasonable measure of the nonuniformity of response within a channel, provided the maximum and minimum channel responses are at the center and edge of the channel as sketched. This condition will hold for all channelizers

considered in this work. Loss is the ratio of "no-channelization" response to channel center response. In simple cases, such as channelization with conventional RF filters, the loss is given by the insertion loss of the filter. Crosstalk is not as straightforward to specify as ripple and loss. The definition we employ here is that crosstalk is the ratio of "far edge of adjacent channel" response to channel center response. For example, consider channel 1 in Figure 1 (solid line). A signal at the far edge of channel 2 is "at the far edge of an adjacent channel" relative to channel 1, and the response of channel 1 to a signal of this frequency is shown by the heavy dot. As shown on Figure 1, crosstalk is the ratio of this response to the response at channel center. This definition of crosstalk is motivated in part by the difficulty of obtaining low ripple and low worst case adjacent channel crosstalk simultaneously, since the channel response must be continuous. It is possible, in principle, to obtain low ripple and low worst case 2nd nearest neighbor crosstalk simultaneously, and this worst case is precisely what is calculated in the definition of crosstalk we employ. We will consistently give numerical values of loss, ripple and crosstalk in dB, since they are all defined as ratios. In addition, the definitions have been arranged so that reducing the numerical value of any of these parameters is a performance improvement.

2. FABRY-PEROT FILTER CHANNELIZER

The first optical channelizer approach we consider is probably the most conceptually straightforward approach, and consists of a number of optical Fabry-Perot (FP) filters whose center frequencies are spaced by the desired channel spacing. The optical power transmittance of a Fabry-Perot filter is given by

$$T_{FP}(f) = \frac{1}{1 + \frac{4FSR^2}{\pi^2 \Delta f^2} \sin^2\left(\frac{\pi f}{FSR}\right)}, \quad (1)$$

where f is the optical frequency [Hz], Δf is the full-width half-maximum linewidth [Hz] of the transmission peaks, and FSR is the free spectral range [Hz], which is the frequency separation between adjacent transmission maxima. We assume that these filters are arranged in an idealized chain, where the signal that does not pass through filter 1 to detector 1 is reflected toward the rest of the chain, and so on for each successive filter-detector pair, so that each filter (approximately) sees the entire relevant signal. This system performs a channelization function, since if an optical carrier that has been modulated with a wideband RF signal is input into the filter chain, each detector will see a portion of the modulation sideband of the optical carrier whose bandwidth is essentially that of the FP filter, which can be much less than the total RF bandwidth of the modulating signal. Here we are assuming the filters are tuned to the appropriate offset frequencies relative to the optical carrier frequency for channelization of either the upper or lower optical sideband to occur.

An optical channelizer of the kind described above could perform as an activity detector to identify the channels where sources are broadcasting, but any functionality that requires electronic post-detection processing of the channelizer outputs is effectively ruled out by the square-law nonlinearity of the detector. In order for an optical channelizer to be compatible with most forms of electronic post-detection processing, the optical detection must be coherent so that the detector really mixes down the optical signal to an RF "intermediate frequency" in a linear manner. Throughout this work, we will typically assume this intermediate frequency is nonzero (i.e. a heterodyne system as opposed to a homodyne system). In the particular case of the FP channelizer above, it is possible in principle to make a heterodyne channelizer by setting the nominal intermediate frequency (IF) equal to the free spectral range of the FP filters. Accordingly, if an appropriate (i.e. frequency offset from the band to be channelized by the IF) optical local oscillator (LO) comb is superposed with the modulated optical carrier at the input to the filter chain, each detector will mix its portion of the modulated optical spectrum down to an IF band centered on the FSR of the optical filter. Here we assume the total channelization bandwidth is less than the FSR of the FP filters, so that neither the modulated input nor the corresponding LO comb span more than one transmission peak of any given FP filter.

For our purposes, it is convenient to express all frequencies as multiples of the channel spacing, so that the channel spacing is 1 by definition. Thus in Eq. 1, Δf is to be understood as the ratio of linewidth to channel spacing, and FSR is the ratio of the free spectral range to the channel spacing. The loss for either a direct detection or heterodyne FP channelizer under our assumptions is zero, since Eq. 1 does not include transmission loss. We then have the following expressions for ripple and crosstalk of a direct detection FP channelizer (calculated into channel 0 centered at $f = n \text{ FSR}$, n integer):

$$r_D = \left[\frac{rT_{FP}(0)P_s}{rT_{FP}(0.5)P_s} \right]^2 = [T_{FP}(0.5)]^{-2},$$

$$x_D = \left[\frac{rT_{FP}(1.5)P_s}{rT_{FP}(0)P_s} \right]^2 = [T_{FP}(1.5)]^2$$

where r_D is the ripple, x_D is the crosstalk, r is the detector responsivity [A/W] and P_s is the incident optical power. Note the detector responsivity and incident optical power do not affect r_D or x_D , since these quantities divide out of the defining ratios as shown, and the periodicity of T_{FP} is employed to simplify the results. Similarly, for a heterodyne FP channelizer, we have

$$r_H = \left[\frac{(rT_{FP}(FSR+0)P_i)(rT_{FP}(0)P_s)}{(rT_{FP}(FSR+0)P_i)(rT_{FP}(0.5)P_s)} \right] = [T_{FP}(0.5)]^{-1}$$

$$x_H = \left[\frac{(rT_{FP}(FSR+1)P_i)(rT_{FP}(1.5)P_s)}{(rT_{FP}(FSR+0)P_i)(rT_{FP}(0)P_s)} \right] = T_{FP}(1.5)T_{FP}(1)$$

To obtain the result for x_H , it is necessary to assume that an IF bandpass filter is placed after the detector to reject signals that fall out of the proper IF band (i.e. $f_i - 0.5 \leq f \leq f_i + 0.5$). This is why the "crosstalk" term $T_{FP}(1.5)T_{FP}(FSR+0)$, which has larger magnitude than x_H , is neglected.

The crosstalk and ripple for a FP optical channelizer depend on the two parameters in Eq. 1, namely the linewidth and the free spectral range, so the ripple-crosstalk trade is, in principle, a family of curves (e.g. ripple vs. crosstalk with linewidth as a parameter, for various free spectral ranges). However, the dependence of these curves on the free spectral range is very weak for large FSR, and a definite limit is approached as the FSR is allowed to go to infinity. In this limit, the ripple crosstalk trade is more favorable than it is for any finite FSR, although the difference is very small if the FSR is greater than roughly 10 channel spacings. Therefore, we can plot the ripple-crosstalk trade with linewidth as a parameter for infinite FSR as a (slightly) optimistic approximation to the real situation where the FSR must be finite, and this plot is given in Figure 2.

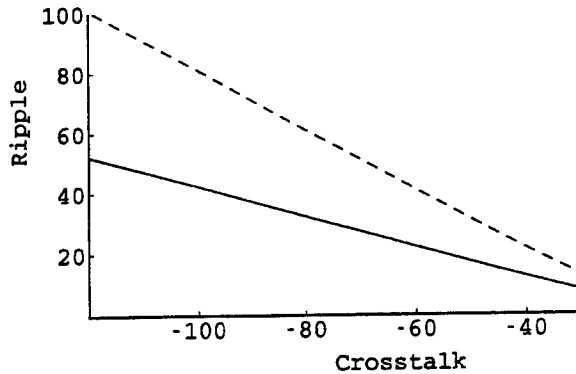


Figure 2: Ripple-crosstalk trade for direct detection (dotted line) and heterodyne (solid line) Fabry-Perot optical channelizer

From Figure 2, we immediately see that the ripple is extremely large for either type (heterodyne or direct detection) of FP optical channelizer. For example, a typical crosstalk specification is -70 dB, and for this level of crosstalk the ripple is 51 dB for a direct detection FP channelizer and 27 dB for a heterodyne FP channelizer. From the results shown in Figure 2, we conclude that Fabry-Perot filters are not a viable optical channelization approach, since even our optimistic model predicts very poor performance.

3. FREE SPACE DIFFRACTION GRATING CHANNELIZER

In the previous section, we saw that an optical Fabry-Perot filter based channelizer cannot provide any reasonable level of channelization performance because the FP filter lineshape (Eq. 1) does not attenuate out-of-band optical signals sufficiently well. Therefore, another channelization approach is necessary, and the approach we will concentrate on is the use of a free space dispersive optical system combined with a detector array in order to perform the channelization. More specifically, we assume that a monochromatic optical input to the system gives a Gaussian spot in the output focal plane, where the detector array is located. Due to the system dispersion, the position of the output spot depends on its frequency, and we assume this relation between position and frequency is linear over the relevant frequency range (i.e. the total bandwidth to be channelized). Since the dispersive element we use in our implementation of this approach is a free space diffraction grating (DG), we refer to this approach as the DG approach for brevity. Either direct detection or heterodyne channelization can be implemented with the DG approach, since all that is required to implement heterodyne channelization is the introduction of a suitable optical LO comb offset in frequency by the desired IF. For example, if a diffraction grating spectrograph is used, the desired frequency offset is obtained by spatially separating the signal and LO inputs appropriately.

Figure 3 gives schematic sketches of the spot pattern in the output focal plane of a heterodyne DG channelizer for two cases of interest. Three elements of the detector array (numbered 1, 2, and 3) are shown, along with the corresponding LO spots (light lines centered on array elements), and a "signal" spot (heavy line). Part a shows the configuration for calculating ripple for channel 2, since the signal is at the edge of channel 2. The relevant response at this signal frequency is the integral of the product of the signal spot with the LO₂ spot over detector 2. Part b shows the configuration for calculating crosstalk into channel 2, since the signal spot is centered on the far edge of channel 3. The relevant response is the integral of the product of the signal spot with the LO₃ spot over detector 2. As we did for the FP channelizer, we assume an IF filter is present after the detector to eliminate the out-of-band signal \times LO₂ into detector 2 contribution from the part b configuration.

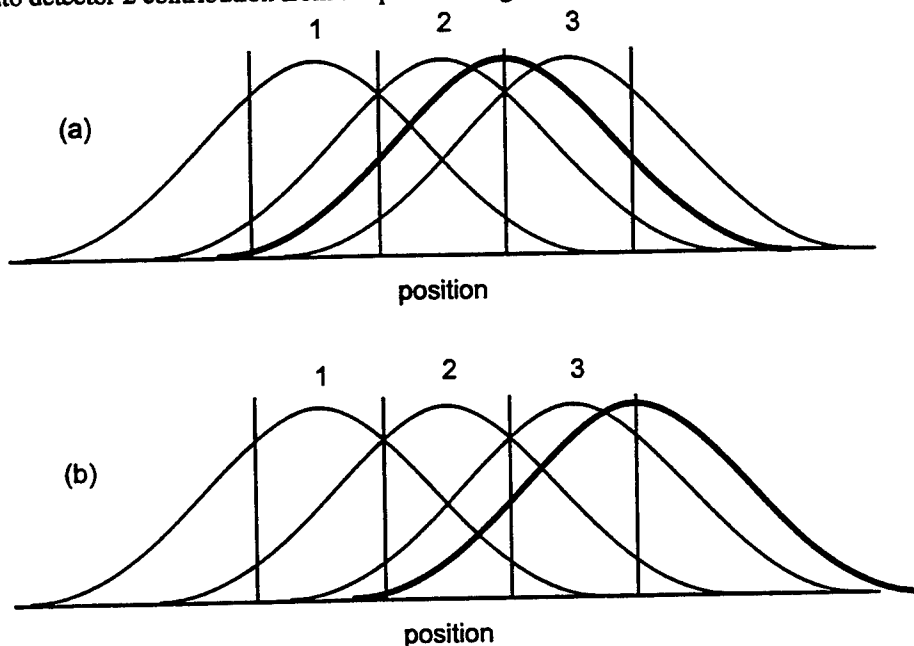


Figure 3: Schematic diagrams of output focal plane for a heterodyne DG channelizer. The spot due to the (monochromatic) optical input is shown with a heavy line, the LO comb spots are shown with lighter lines, and the vertical lines indicate the boundaries of the detector array elements. There is a frequency shift between the signal and LO spots, such that if a signal spot coincides with an LO spot, the resulting photocurrent oscillates at the IF frequency.

For a DG channelizer, we can express crosstalk, ripple and loss in the following manner. Let

$$g(x) = \left(\frac{2}{\pi w^2} \right)^{1/4} \exp \frac{-x^2}{w^2} \quad (4)$$

be the field profile for the Gaussian spots we assume in the output focal plane. The field profile $g(x)$ is normalized so that the integral of $g^2(x)$ over all x is unity. Here both the position x and the Gaussian radius w are understood to

be measured in units of the detector array element spacing, which corresponds to the channel spacing by our assumptions. This scaling of position is convenient, and is similar to the frequency scaling we employed for the FP analysis. By assuming an ideal detector array (i.e. no electrical crosstalk, zero gap between detector array elements, spatial uniformity of array element responsivity), we obtain the following simple expressions for the loss, ripple and crosstalk of a direct detection DG channelizer:

$$l_D = \left[\int_{-1/2}^{1/2} g^2(x) dx \right]^{-2}, \quad r_D = \left[\frac{\int_{-1/2}^{1/2} g^2(x) dx}{\int_{-1/2}^{1/2} g^2(x-0.5) dx} \right]^2, \quad x_D = \left[\frac{\int_{-1/2}^{1/2} g^2(x-1.5) dx}{\int_{-1/2}^{1/2} g^2(x) dx} \right]^2, \quad (5)$$

where l_D , r_D and x_D are now the loss, ripple and crosstalk respectively of a direct detection DG channelizer. The parallel with Eqs. 2 is evident. For a heterodyne DG channelizer, the results are almost as simple:

$$l_H = \left[\int_{-1/2}^{1/2} g^2(x) dx \right]^{-2}, \quad r_H = \left[\frac{\int_{-1/2}^{1/2} g^2(x) dx}{\int_{-1/2}^{1/2} g(x-0.5)g(x) dx} \right]^2, \quad x_H = \left[\frac{\int_{-1/2}^{1/2} g(x-1.5)g(x-1) dx}{\int_{-1/2}^{1/2} g^2(x) dx} \right]^2. \quad (6)$$

All of the integrals in Eqs. 5 and 6 can be explicitly evaluated in terms of the error function, which was done in the calculations. Since $g(x)$ only depends on the single parameter w (ratio of physical Gaussian radius to detector element spacing), we immediately obtain the ripple and loss vs. crosstalk trades shown in Figure 4.

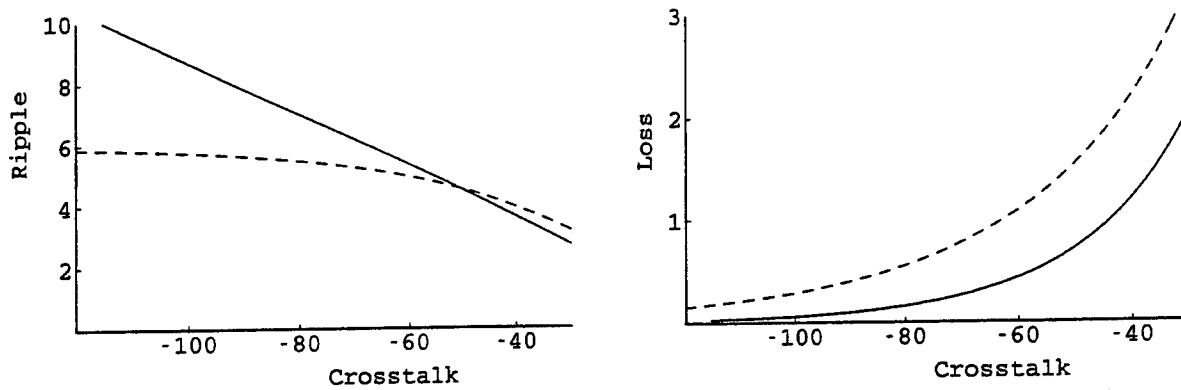


Figure 4: Ripple (a) and loss (b) trades vs. crosstalk for direct detection (dotted line) and heterodyne (solid line) free space diffraction grating optical channelizer.

The ripple-crosstalk trade (Fig. 4a) for an optical DG channelizer is much more favorable than the same trade for an optical FP channelizer, since it is possible, in principle, to obtain low crosstalk and an acceptable level of ripple simultaneously. The ripple-crosstalk trade for a heterodyne channelizer is significantly different than for a direct detection channelizer, and it is not difficult to see why. For the direct detection case, the ripple is due to the division of optical power between adjacent detectors, so in the limit of small spot size where the loss goes to zero, the ripple must approach 6.02 dB as seen in Figure 4a. For a heterodyne channelizer, the overlap between a signal spot at the edge of the detector and an LO spot centered on the detector decreases without limit as the spot size decreases, as seen in Figure 4a. Figure 4b shows the channelization loss entailed by designs providing various levels of crosstalk, and Figure 5 gives the w required to obtain various levels of crosstalk.

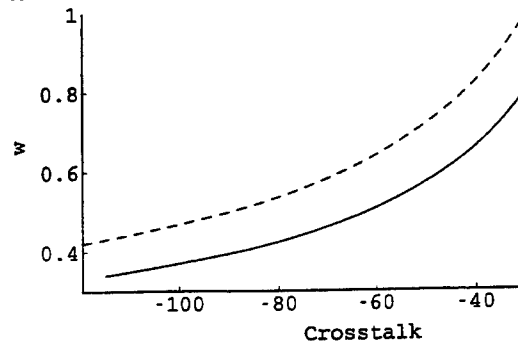


Figure 5: w parameter (Gaussian radius/array element spacing) for direct detection (dotted line) and heterodyne (solid line) DG optical channelizers

In Figure 5, we see that a smaller spot size is required for the heterodyne channelizer than for a direct detection channelizer to obtain a specified level of crosstalk, as can also be inferred from Eqs. 5 and 6. This difference in spot size leads to the lower loss seen in Figure 4b for the heterodyne case vs. the direct detection case.

4. ADDITIONAL ISSUES FOR FREE SPACE DIFFRACTION GRATING CHANNELIZER

In the previous section, we saw that a DG channelizer can, in principle, provide low crosstalk and reasonably low ripple simultaneously. The basic reason that good performance can be obtained is the exponential behavior assumed in Eq. 4. Since the idealized analysis led to a favorable conclusion, we refine the analysis to provide more support for this conclusion. Three topics will be considered in this section. The first is the effect of a finite grating length, the second is the effect of gaps between detector array elements and the third is the potential for reducing ripple by allowing the signal and LO spots at the detector array to be of different sizes. In the following three subsections, only the heterodyne case will be considered, since that is the case we are in the process of implementing.

To make the following considerations more concrete, we discuss most of these effects as they pertain to the specific example of a heterodyne channelizer designed to have a crosstalk of -70 dB. For this example, the required w is 0.46, and the resulting ripple and loss are 6.17 dB and 0.26 dB respectively. Recall that $w = 0.46$ means that the Gaussian spot radius is 0.46 times the array element spacing. To obtain maximum insight, and to simplify the presentation, these three topics will be considered individually, even though a detailed design would need to consider their combined effect.

4.1 Finite grating aperture

The effect of the finite grating aperture on the channelizer performance needs to be included in the analysis since otherwise there is, in principle, no way to determine the physical size of the diffraction grating required to achieve a specified level of channelization performance. We assume the field distribution of the signal and LO is exactly Gaussian at the diffraction grating, and is centered on the grating. We also assume the field distribution is imaged onto the output focal plane without aberration by the camera lens of the spectrograph. Under these assumptions, the finite grating aperture symmetrically truncates the field distributions imaged by the camera lens, and so the resulting output field distribution is the Fourier transform of a truncated Gaussian. Specifically, we have

$$h(x) = \left(\frac{2}{\pi w^2} \right)^{1/4} \operatorname{Re} \left\{ \operatorname{erf} \left(\frac{b}{2} + i \frac{x}{w} \right) \right\} \exp \frac{-x^2}{w^2}, \quad (7)$$

for the field distribution at the output focal plane, where b is the ratio of grating length to the Gaussian spot radius *at the grating*, and $\operatorname{erf}(z)$ is the error function. In Figure 6, we plot $h^2(x)$ (solid line) and $g^2(x)$ (dotted line) for $w = 0.46$ (our nominal example) and $b = 3$, which means the grating length is three times the Gaussian spot radius at the grating. Even though $b = 3$ is quite a large aperture by most standards (e.g. the power loss due to $b = 3$ truncation is only 0.27%), we see that this level of truncation greatly increases the intensity at points one to two channel spacings away from the spot center.

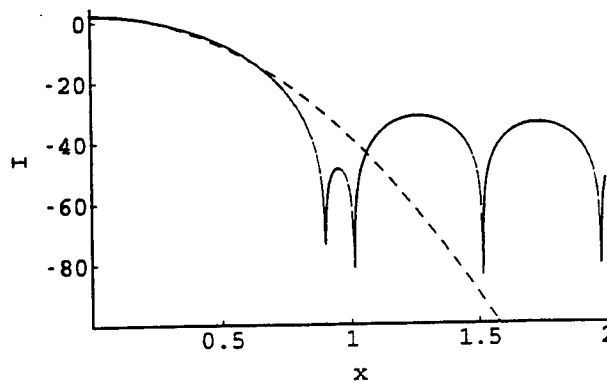


Figure 6: Output intensity ($I = h^2$) distribution due to finite grating length ($b = 3$) for $w = 0.46$. Dotted line is intensity distribution from an infinitely long grating, for comparison. The units of position are channel spacings, so this plot shows the intensity distribution for a spot centered on detector 0 where the detector edges are at 0.5, 1.5, 2.5 etc.

It is clear the behavior shown in Figure 6 can significantly increase channelizer crosstalk, if the aperture is too small. We can directly calculate the crosstalk in the presence of a finite aperture from Eqs. 6 where $g(x)$ is replaced with $h(x)$ from Eq. 7. For this case, the integrations must be performed numerically. Figure 7 shows the result of such a calculation for the nominal -70 dB crosstalk design ($w = 0.46$), and we see the crosstalk increases by over 9 dB for $b = 3.3$ which corresponds to a truncation loss of less than 0.1 %. The aperture has to increase to the range $b > 5.5$ before the aperture has no visible effect on the crosstalk level. Fortunately, in the range $4.3 < b < 5.5$, the crosstalk is actually slightly less than the -70 dB design value, so if we require $b > 4.3$, the aperture will not significantly increase the crosstalk. It is possible to adopt a different design strategy, where the spot size is chosen so that the nominal crosstalk is -73 dB (or some other convenient value less than -70 dB), and the finite grating length crosstalk is required to be < -70 dB. This approach would require a smaller grating, typically, but the price paid would be an increase in ripple due to the smaller spot size.

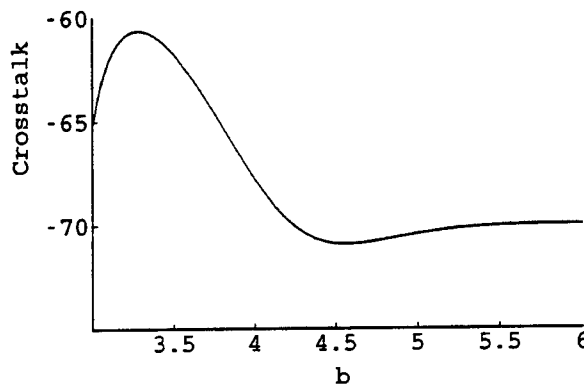


Figure 7: Crosstalk vs. grating aperture for -70 dB crosstalk example. b is the ratio of grating length to Gaussian spot radius at the grating.

Up until now, we have not considered the effect of the overlap of the LO spots, as shown schematically in Figure 3. The reason for this delay is that a discussion of LO overlap that does not incorporate the finite grating aperture is misleading. In principle, every LO spot makes some contribution to the total optical field seen by each detector. After detection, the photocurrent due to these LO overlaps has "spurs" at all integer multiples of the channel spacing. Recall we are assuming an IF bandpass filter follows the detector. If the IF filter rolls off between the center and edge of the nominal IF band, it will contribute to ripple. We require the IF filter to make no contribution to the ripple. Thus we require the IF filter transmission characteristic to be flat over the range $f_1 - 0.5 < f < f_1 + 0.5$, where f_1 is the intermediate frequency and the unit of frequency is taken to be the channel spacing, as before.

Under these assumptions, the IF filter will typically pass only one of the LO overlap spurs, so our analysis can focus on individual spurs. Since $f_1 > 1.5$ is required to achieve proper spectral separation of the heterodyne and direct detection photocurrents, $f = 2, f = 3$, etc., are the relevant LO overlap spurs with the lowest frequencies. If we choose to pass the $f = 2$ spur, we have $1.5 < f_1 < 2.5$, and if we choose to pass the $f = 3$ spur, we have $2.5 < f_1 < 3.5$, etc. Thus a calculation of the $f = 2$ and $f = 3$ spurs will provide a basis for choosing the range in which the intermediate frequency must fall: either $1.5 < f_1 < 2.5$, or $2.5 < f_1 < 3.5$ or $3.5 < f_1$. We assume that operation at the lowest possible f_1 reduces the burden on the post-detection electronics as much as possible, so we focus on the lowest two intermediate frequency ranges.

The calculation of the $f=2$ and $f=3$ spurs is not completely straightforward, since each spur is the sum of a large number of terms. In the finite grating case, it seems necessary to empirically include enough terms so that the results no longer change significantly when another term is added. Each $LO_i \times LO_j$ term makes a contribution to the total photocurrent at $f = i-j$ whose phase depends on the relative phase between LO_i and LO_j . We calculate a worst case estimate for the total spur power by adding up the magnitude of each contribution and then squaring, since it is unrealistic to design for a specific set of LO relative phases. More specifically, we calculate

$$s_2 = \left[\int_{-1/2}^{1/2} h(x-1)h(x+1)dx + 2 \sum_{j=1}^N \left| \int_{-1/2}^{1/2} h(x-1+j)h(x+1+j)dx \right| \right]^2 \quad (8)$$

$$s_3 = \left[2 \sum_{j=0}^N \left| \int_{-1/2}^{1/2} h(x-1+j)h(x+2+j)dx \right| \right]^2$$

where s_2 and s_3 are the worst case $f=2$ and $f=3$ spur powers respectively, and N is the number of terms to be considered. Eqs. 8 exploit the symmetry of the problem ($LO_{+x} \times LO_{-y}$ equivalent to $LO_{-x} \times LO_{+y}$) to avoid duplicate calculation of integrals. In Figure 8, numerical results for s_2 and s_3 as a function of b (grating aperture) are given for our -70 dB crosstalk example, and it was found that $N=5$ seemed to give enough terms. From Figure 8, we see that s_2 essentially reaches its limiting value of -82 dB for $b > 5.7$, while s_3 does not reach its limiting value over the plotted range of apertures. This difference is due to the very low limiting value of s_3 as aperture increases, namely -185 dB (!), which is reached for $b > 9$. The unrealistically large apertures required to bring s_2 and (especially) s_3 to their limiting values is the reason an analysis of LO overlap that neglects the finite grating aperture is misleading.

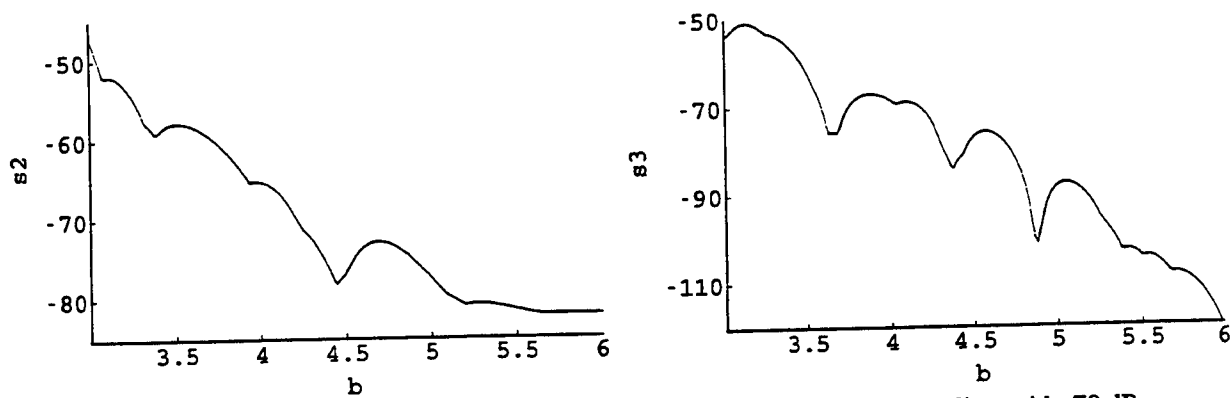


Figure 8: s_2 (part a) and s_3 (part b) vs. b (the grating aperture) for a heterodyne DG channelizer with -70 dB of crosstalk.

The requirements to be placed on s_2 and/or s_3 depend on the implementation and application of the channelizer, so only a simple example will be given here. Suppose our requirement on the LO spur is that its power be less than the additive noise power into some bandwidth B , and that the only significant additive noise terms are LO shot noise and thermal noise. This can be expressed quantitatively by

$$2r^2 P_1^2 s < (4kT/R_L + 2qrP_1/\sqrt{I_H})B, \quad (9)$$

where s is the relevant LO overlap term (Eqs. 8 give s_2 and s_3), q is the electron charge, R_L is the load resistance seen by the detector, k is Boltzmann's constant, P_1 is the LO power (per LO spot) at the detector array, r is the detector responsivity [A/W], and I_H is the heterodyne channelization loss given by Eq. 6 with $h(x)$ substituted for $g(x)$. Typically the effect of I_H is negligible, as it is for our -70 dB crosstalk example. For the following typical numbers: $r = 0.7$ A/W, $B = 40$ MHz, $T = 300$ K, $R_L = 50 \Omega$, $I_H = 1$, and P_1 in the range $10 \mu\text{W}$ to 1 mW, we obtain a requirement on s ranging from $s < -38$ dB ($P_1 = 10 \mu\text{W}$) to $s < -76$ dB ($P_1 = 1$ mW). The requirement on s gets more demanding as P_1 increases, since the spur power increases with increasing power more rapidly than the noise, as seen in Eq. 9. Note that B is assumed to be significantly less than our nominal channel spacing of 1 GHz, which is appropriate for significant post-detection electronic processing, such as further channelization. As B decreases, the requirement on s also becomes more stringent, since it becomes easier for the electronics to "see" the LO overlap spur. In this particular example, the combination of these requirements with Figure 8 provides information on what aperture and/or IF range is required to satisfy the LO overlap requirement. More specifically, we see that if P_1 is at the low end of its range, the LO overlap effect is negligible if $b > 3$, which is already ensured by the crosstalk-driven requirement that $b > 4.3$. If P_1 is at the high end of its range, we need $b > 5$ to bring s_2 within specification, and $b > 4.7$ to bring s_3 within specification, and either of these aperture requirements is more stringent than the crosstalk-driven requirement.

To summarize, we considered two effects which depend critically on the grating size --- crosstalk and LO overlap. For our -70 dB crosstalk example, $b > 4.3$ is required to avoid increased crosstalk. There is an additional

requirement on the aperture for our example based on the LO overlap calculation (Figure 8) that depends on several additional parameters as seen in Eq. 9. In practice, of course, it is necessary to choose an aperture which satisfies both the crosstalk and LO overlap requirements.

4.2 Gaps between detector array elements

Thus far we have assumed the detector array performs in a very idealized manner — specifically that there is no electrical crosstalk between array elements, every array element has a spatially uniform response with the same responsivity, and that there is no gap between array elements (i.e. the fill factor is unity). These are all assumptions that will not be obtained in practice, so it is important to relax them as much as possible in the analysis. It should be noted that the “detector array” need not be an array of detectors in close physical proximity. In fact, it may well be that a configuration of that type leads to insuperable electrical crosstalk problems. An alternative approach that will reduce electrical crosstalk is to place an array of waveguides so that the spectrograph images signal and LO spots onto an array of waveguide end faces. These waveguide end faces thus define the channels, since they will only admit light that is incident on the waveguide cores, roughly speaking. The waveguides then fan out to detectors which can be spatially separated to whatever degree is necessary to reduce electrical crosstalk to acceptable levels. An issue of major concern for this optical waveguide array approach is that the effective fill factor is likely to be much less than the fill factor of a detector array, since the waveguide cores must be far enough apart that waveguide-waveguide coupling is negligible. Therefore, our analysis of nonideal detector array behavior will focus on the effect of decreasing the fill factor, motivated primarily by the low fill factor expected of an optical waveguide array approach, and secondarily by the difficulty of adequately modeling electrical crosstalk or nonuniform element response in terms of a suitably small number of parameters.

Recall that Eqs. 6 for the loss, ripple and crosstalk of a heterodyne channelizer are based on the assumption that the relevant detector covers the range $-0.5 < x < 0.5$, where the unit of distance is the array element spacing. We can allow for a nonunity fill factor simply by assuming the active region of the detector now covers the range $-0.5\eta < x < 0.5\eta$, where η is the fill factor. The required equations follow from the corresponding modification to the limits of integration in Eqs. 6. If η is decreased while holding w fixed, the qualitative effect on loss, ripple and crosstalk is clear: the loss will increase, since more of the spot will miss the array element; the ripple will also increase, since at the relevant frequency the signal spot will be centered on a larger “hole” in the detector array; and the crosstalk will decrease, since the edge of the array element is farther from the centers of the spots that cause crosstalk.

Since crosstalk depends on only the fill factor and the spot size, we can calculate a plot showing the w parameter required to obtain crosstalk of -70 dB vs. the fill factor. Such a plot is shown in Figure 9, and we see that as the fill factor decreases, the w parameter (i.e. the spot size) increases to keep the crosstalk at the specified level of -70 dB. Our standard -70 dB crosstalk example is the $\eta = 1$ point on this plot.

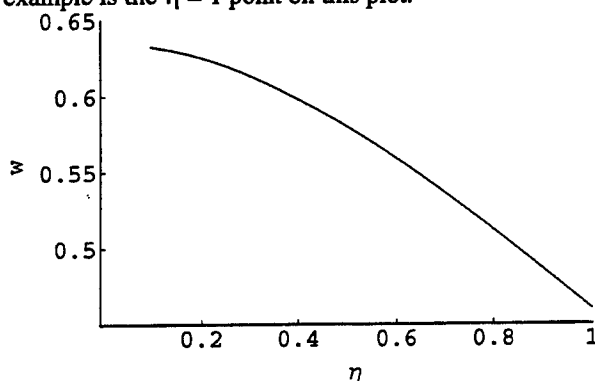


Figure 9: spot size vs fill factor for heterodyne DG channelizer with -70 dB crosstalk

Next we calculate the loss and ripple vs. η , where the crosstalk is held at -70 dB by varying w as shown in Figure 9. The resulting curves are shown in Figure 10, where part a gives the ripple and part b gives the loss. Somewhat surprisingly, the ripple actually *decreases* as the fill factor decreases, although this decrease is just a few tenths of a dB. The explanation for this result is that even though decreasing η opens up physical holes in the detector array

that act to increase ripple, decreasing η also leads to larger spot sizes to keep crosstalk at -70 dB, and larger spot sizes tend to decrease ripple. In the case shown in Figure 10a, these two effects nearly cancel.

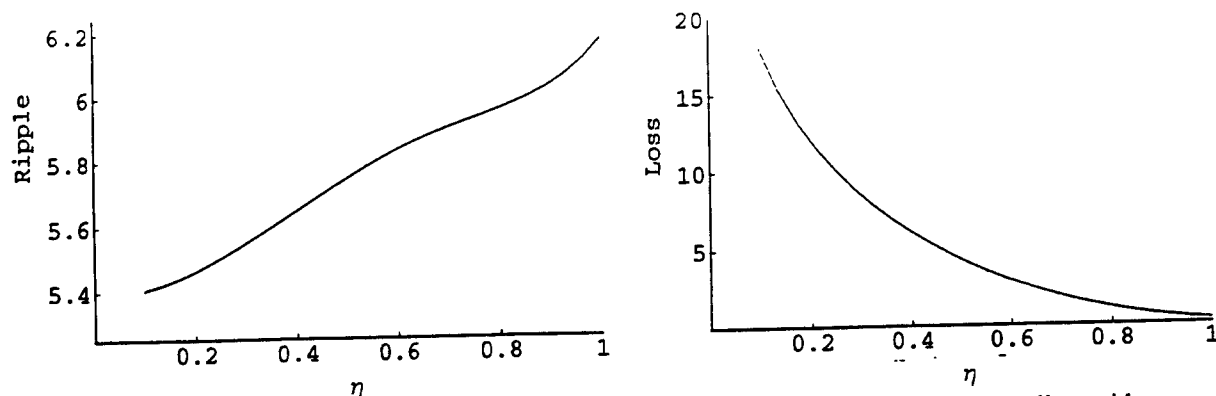


Figure 10: Ripple (part a) and loss (part b) vs. detector array fill factor for heterodyne DG channelizer with -70 dB crosstalk.

Since the effect of fill factor on ripple (for fixed crosstalk) is rather small, the primary effect of reduced fill factor is an increase of channelization loss, as seen in Figure 10b. Since ripple is a more critical issue than loss (i.e. a few extra dB of ripple is typically worse than the same amount of extra loss), the behavior of a heterodyne channelizer as the fill factor decreases is relatively benign. Even fill factors as low as 50% only lead to a few extra dB of loss.

4.3 Unequal carrier and LO spot sizes

Up to this point, we have assumed the carrier (or signal) spot and the LO spots are the same size at the detector array. There is no reason in principle why we cannot have unequal carrier and LO spots at the detector array, if some advantage can be gained by doing so. If the dispersion is performed by a grating spectrograph, all that is required to make the output spot sizes unequal is an appropriate modification of the carrier and/or LO inputs to the spectrograph. The improvement we are seeking by making the carrier and LO spot sizes different is a reduction of the ripple for a given level of crosstalk (i.e. -70 dB in our example). In Figure 11 we give the LO (part a) and carrier (part b) w parameters vs. ripple for a constant crosstalk level of -70 dB. These calculations are based on Eqs. 6 modified by letting $g_C(x)$ differ from $g_{LO}(x)$. As the ripple is reduced, we see that the LO spot gets smaller and the carrier spot gets larger. This behavior is expected, since ripple is due to a change in carrier-LO overlap as the position of the carrier spot is moved. The larger the carrier spot is, the less variation we expect in this overlap. From Figure 11, we see that significant reduction in the ripple is possible, although the required modification of the spot sizes will have a major impact on the design. For example, to reduce the ripple to 3 dB requires w_L to be roughly 0.23, which is half the value for the nominal -70 dB crosstalk design with equal carrier and LO spots. Thus the physical size of the channelizer will basically need to double (for the same channel spacing) in order to realize the reduced ripple.

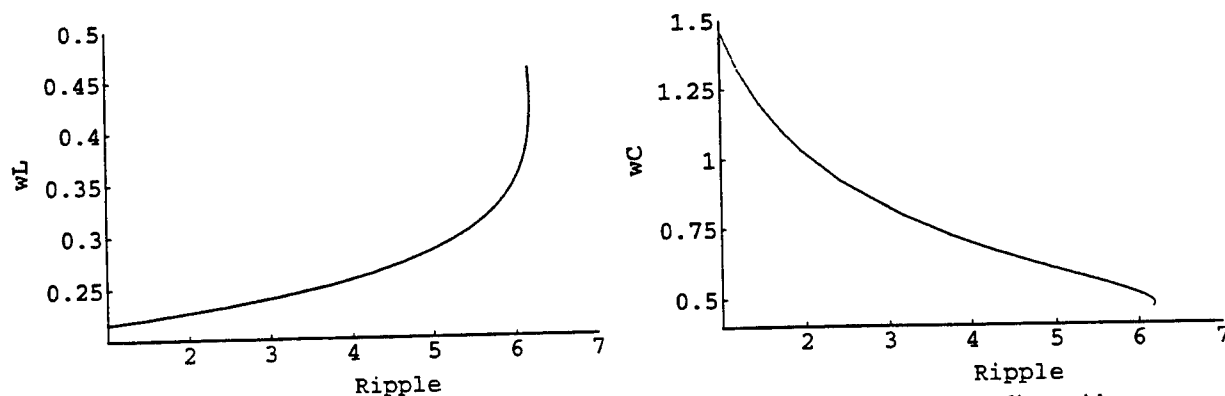


Figure 11: LO (part a) and carrier (part b) w parameters vs. ripple for a heterodyne DG channelizer with -70 dB crosstalk

There are two additional issues to consider when evaluating designs with unequal spot sizes. The first issue is the extra loss due to the larger carrier spot, as mentioned above. The second issue is a requirement that is placed on the IF filter that follows the detector. Recall that the crosstalk into detector 0 is assumed to come from the product of LO_1 with the carrier, and that the (larger) product of LO_0 with the carrier is assumed to be suppressed by the IF filter. Let $T_{IF}(f)$ be the (power) transmission function of the IF filter. Then the above suppression requirement is expressed quantitatively by

$$\frac{T_{IF}(f_I - 1.5)}{T_{IF}(f_I - 0.5)} << \left[\frac{\int_{-1/2}^{1/2} g_C(x - 1.5) g_{LO}(x - 1) dx}{\int_{-1/2}^{1/2} g_C(x - 1.5) g_{LO}(x - 0) dx} \right]^2 \equiv q, \quad (10)$$

where we have defined the RHS of the inequality to be equal to q for convenience, and $g_C(x)$ and $g_{LO}(x)$ are the carrier and LO field distributions respectively, from Eq. 4 with $w = w_C$ and $w = w_L$ respectively. Eq. 10 ensures that after the IF filter, the carrier $\times LO_0$ crosstalk term is much less than the carrier $\times LO_1$ crosstalk term we have been concerned with. For our purposes a plot of q will provide adequate information on the variation of the IF filter requirement, since we assume the IF filter suppression is required to be some fixed factor times q . Figure 12 gives plots of the loss and q parameter vs. ripple for a fixed crosstalk level of -70 dB. We see that the loss increases by roughly 1 dB for every dB the ripple decreases, which is basically a favorable trade. The effect of reducing ripple on q (i.e. the IF filter requirement) is much stronger, as see in Figure 12b, where the q parameter goes from trivial (i.e. $q = -7$ dB) to substantial (i.e. $q = -43$ dB) as the ripple is reduced from 6 dB to 3 dB.

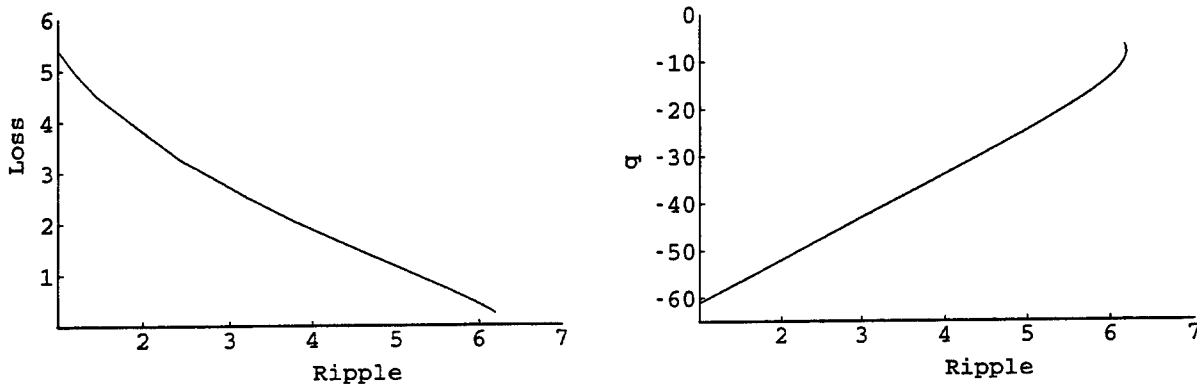


Figure 12: Loss (part a) and q (part b) vs. ripple for heterodyne DG channelizer with -70 dB crosstalk

5. RELATION OF GRATING SIZE TO CHANNEL SEPARATION

The analysis to this point has shown that a DG channelizer can have favorable channelization properties (i.e. low crosstalk and low ripple simultaneously). Our remaining task is to address the basic question of how large a grating is necessary to channelize to a given channel spacing based on our results. We assume, as above, that dispersion is provided by a single diffraction grating and that imaging of the diffraction grating to the output focal plane is performed by a thin lens of focal length f_0 . Our first relation is

$$W_g = \frac{W_i}{\cos \theta_i} = \frac{W_d}{\cos \theta_d}, \quad (11)$$

where W_g is the spot size projected onto the grating, and W_i , θ_i and W_d , θ_d are the incident and diffracted spot sizes and angles respectively. Eq. 11 is a statement of the magnification provided by the grating, due to the inequality (in general) of θ_i and θ_d . The imaging law of the thin lens is given by

$$W = \frac{f_0 \lambda}{\pi W_d}, \quad (12)$$

where W is the spot size at the output focal plane, f_0 is the lens focal length, and λ is the optical wavelength. The linear dispersion of the grating-lens system is given by

$$\frac{dx}{d\lambda} = \frac{f_0 m}{d \cos \theta_d}, \quad (13)$$

where dx is the detector array element spacing, $d\lambda$ is the channel spacing, m is the diffraction order and d is the spacing between adjacent grating grooves. And finally we have

$$\frac{m\lambda}{d} = \sin \theta_i + \sin \theta_d < 2, \quad (14)$$

which is the grating equation. By combining Eqs. 11-14, we obtain

$$\frac{m\lambda}{d} = \frac{2}{\pi} \frac{\lambda}{d\lambda} \frac{dx}{W} \frac{L}{W_g} \frac{\lambda}{2L} = \frac{2}{\pi} \frac{f}{df} \frac{1}{w} b \frac{\lambda}{2L} < 2, \quad (15)$$

where we have inserted the optical frequency f and channel spacing df [Hz], and the definitions $w = W/dx$ and $b = L/W_g$ of the spot size and aperture parameters of the preceding analysis. Rearranging this gives the following inequality on the grating length L :

$$L > \frac{c}{2\pi} \frac{b}{w} \frac{1}{df}, \quad (16)$$

where c is the speed of light. Since Eq. 16 does not depend on either the optical wavelength or the lens focal length, these two parameters can be determined by other considerations without directly affecting channelizer performance. For channelization with -70 dB crosstalk, we have $w = 0.46$ and $b = 4.3$ (assuming the LO overlap issue does not require a larger aperture), and if we assume 1 GHz channels, we have $L > 45$ cm. In practice it is not possible to come especially close to equality in Eq. 14, so a substantially larger grating length, on the order of 80 cm in this particular case, will be required. We are proceeding with a proof of concept experimental demonstration of a DG channelizer designed along these lines (i.e. -70 dB crosstalk for 1 GHz channels, nominally), and the basic idea of the implementation is to diffract from the same grating multiple times (in our case 4) in order to reduce the size requirement to a reasonable level. This approach is greatly facilitated by the fact that the instrument is a *spectrograph*, so there is no need to move the grating, or any other optical element, once initial alignment has been performed.

6. CONCLUSIONS

We have presented an analysis of two optical channelizer approaches in terms of the RF performance parameters crosstalk, ripple and channelization loss. The two approaches investigated were a Fabry-Perot (FP) filter based approach and a free space diffraction grating (DG) approach. We found that the crosstalk-ripple performance for the FP approach was so poor that the FP approach was essentially ruled out. The same calculation for the DG approach showed that low crosstalk and reasonably low ripple could be obtained simultaneously, so additional analysis was performed to consider three first order implementation issues: finite grating aperture, detector fill factor < unity, and ripple reduction by making the LO spot small and the signal spot large. These additional calculations also had reasonably favorable implications. By combining our results, chiefly the output spot size and grating aperture requirements, we obtained the estimate that a grating length on the order of 80 cm is required to channelize to 1 GHz channels with -70 dB crosstalk. The simple modification of diffracting multiple times from the same grating is sufficient to bring the size requirement down to a reasonable level for this level of channelization.

There are, of course, many other approaches for optical channelization in addition to the Fabry-Perot and diffraction grating approaches considered here. We believe the kind of analysis performed here is a useful first step in evaluating these approaches, and that the imposition of the requirement of low crosstalk and low ripple simultaneously will effectively reduce the number of approaches that merit deeper investigation.

7. ACKNOWLEDGEMENTS

This work has been supported by DARPA and Rome Labs under contract F30602-96-C-0273.

RF performance of optical injection locking

Robert Lodenkamper^a, Thomas Jung^a, Richard L. Davis^a, Larry J. Lembo^a, Ming C. Wu^b,
John C. Brock^a

^aTRW Photonics Technology Department, One Space Park, Redondo Beach CA 90278

^bDepartment of Electrical Engineering, UCLA, Los Angeles CA 90095

ABSTRACT

Coherent photonic systems promise novel functionality and/or improved performance compared to direct detection photonic systems, but have the disadvantage of being sensitive to optical phase noise. The most common approach to this problem is to force one laser to track the phase of the other with a phase locked loop (PLL), so that the phase noise of the lasers cancels out of the RF heterodyne beat note. Although the PLL approach has been implemented for semiconductor lasers, the large linewidth of these lasers and the resulting large PLL loop bandwidth severely constrain the design and limit performance. This disadvantage of the PLL approach is particularly relevant for many applications, since semiconductor lasers are preferred for system insertion.

An alternative approach for establishing coherence between two lasers is optical injection locking. Standard theory indicates that injection locking can act in the same way as a first order PLL with a bandwidth as high as several GHz, which is large enough to achieve state of the art noise levels (e.g. -130 dBc/Hz @ 1 MHz offset) with semiconductor lasers. We present phase noise measurements on the beat note of two injection locked semiconductor lasers. Our results (phase noise @ 1 MHz offset as low as -125 dBc/Hz) indicate that state of the art phase noise performance from injection locked lasers should be obtainable in practice. We found that it is necessary to length match the two paths in the experiment (master → detector and master → slave → detector) to avoid excess noise due to delay decorrelation of the master, and also that environmental noise seems dominant at offsets < 20 kHz.

Keywords: Optical injection, phase noise, optical carrier tracking

1. INTRODUCTION

Analog point-to-point communication applications can be effectively addressed by direct detection analog RF photonic links due to the high dynamic range these links provide. Since only the optical intensity is detected, the performance of these links is not degraded by optical phase noise, provided all optical components are broadband relative to the frequency jitter of the laser, which is nearly always the case in practice. However, there is a growing interest in pushing analog signal processing operations from the RF domain into the optical domain, especially as the RF carrier frequencies and/or RF bandwidths increase significantly beyond the current state of the art. Logically, there are three possibilities for how signal processing can be divided up between the optical domain and the RF domain: 1) Do all processing in the RF domain, which is essentially the current state of the art, 2) Do all processing in the optical domain, which is only possible for a limited subset of the processing functions of interest, and 3) Do some processing in the optical domain, and the rest in the RF domain, which is conceptually more complicated than the other approaches, but is also likely to be the only practical approach for moving sophisticated signal processing (partly) into the optical domain.

An example of the distinction between approaches 2 and 3 is provided by an optical channelizer. If the channelizer simply disperses a modulated optical carrier onto a detector array then all the

processing is done in the optical domain (approach 2 above), but all the system can do is give total power in each channel. If the channelizer disperses a modulated optical carrier and a suitable comb of optical LO frequencies onto a detector array, then further electronic signal processing can be performed on the outputs of any or all of the detectors. Thus a coherent optical channelizer is suitable for incorporation into a system where the signal processing task is split between the optical and RF domains (approach 3 above). This example is a clear illustration of the basic principle that coherent optical detection is required in any system where (linear) signal processing is split between the optical and RF domains, since the translation from an optical signal to an RF signal is a linear process only for coherent optical detection.

Since coherent detection is a phase sensitive process, the RF beat tone from two independently running lasers will have a phase noise spectrum equal to the sum of the phase noise spectra of the two lasers, and this phase noise will also appear as noise sidebands on every signal of interest if the carrier laser is modulated. Laser phase noise is typically large by RF standards, especially for semiconductor lasers. For example, a semiconductor laser with a linewidth of 1 MHz nominally has $L(f) = -68 \text{ dBc/Hz}$ at 1 MHz offset while a high performance requirement may be as low as $L(f) < -130 \text{ dBc/Hz}$ at 1 MHz offset, where $L(f)$ is the SSB phase noise power spectral density (PSD). Fortunately, it is not necessary to reduce the phase noise on each laser individually to such low levels --- it is only necessary to ensure that the heterodyne (or homodyne) beat has low enough noise for the application at hand. This can be done by implementing a "carrier tracking" function that forces the phase of one laser to follow that of the other laser. Since the phase of the heterodyne beat is the difference of the phases of the two lasers, the correlation of the laser phases enforced by carrier tracking leads to a reduction of the beat note phase noise.

2. OPTICAL CARRIER TRACKING

Two approaches that have been demonstrated for performing optical carrier tracking are a phase locked loop (PLL), and optical injection locking (IL). In a (heterodyne) phase lock loop, the beat signal at the photodetector is mixed with an RF reference to produce a low frequency phase signal which passes through a suitable loop filter and is then applied to a tuning input on one of the lasers. A homodyne PLL is the same system without the mixer and RF reference. In either case, when the loop is locked, it acts as a feedback control system that tends to drive the phase difference between the RF reference and the "VCO" (the combination of the two lasers and detector) to zero. Optical injection locking is the coupling of light from the "master" laser into the resonant cavity of the "slave" laser in such a way that the slave output is captured by the master and becomes phase coherent with it. The major necessary conditions for injection locking to occur are that the input light from the master be spatially mode matched to the free running slave mode, and that the frequency of the input from the master be close enough to the free running slave frequency. The frequency range over which injection locking will occur is called the locking range, and can be as much as several GHz for a monolithic semiconductor laser.

The performance of the PLL and IL approaches to carrier tracking (or that of any linear carrier tracking approach) can be quantified by a low pass, unity DC gain, phase transfer function $H(f)$ that essentially describes the strength of the phase correlation between the two lasers induced by the carrier tracking mechanism. The contribution of the laser phase noise to the photocurrent phase noise when carrier tracking is implemented is given by

$$W_{IF}(f) = |1 - H(f)|^2 (W_{L1}(f) + W_{L2}(f)), \quad (1)$$

where W_{IF} , W_{L1} , and W_{L2} are the phase noise PSD [rad^2/Hz] of the photocurrent, laser 1 and laser 2 respectively, and $H(f)$ is the carrier tracking transfer function. For a laser of FWHM linewidth $\Delta\nu$, the (one-sided) phase noise PSD is $W(f) = \Delta\nu/\pi f^2$, provided the laser's frequency noise spectrum is white, which is the usual assumption leading to a Lorentzian lineshape. In applications, the quantity of interest is often $L(f)$, the "SSB phase noise PSD" in dBc/Hz. $L(f)$ is a measure of the effect of phase noise on a

carrier, in that it gives the ratio of the noise sideband power density to the carrier power as a function of offset frequency. If the total phase variance is small, then $L(f)$ [dBc/Hz] $\approx W(f)/2$ [rad²/Hz]. If the phase variance is not small, the relation between $L(f)$ and $W(f)$ is much more complicated. In Eq. 1, the phase variance of the free running lasers is infinite (assuming white laser frequency noise), but the phase variance of the heterodyne beat is typically small, if the carrier tracking mechanism is performing properly. We will make this assumption in the remainder of the paper, so that Eq. 1 can be used to obtain estimates of $L_{\text{IF}}(f)$. As the bandwidth of $H(f)$ increases, carrier tracking performance improves, since the phase noise cancellation is effective over a wider spectrum, and the noise cancellation at low frequencies typically improves.

2.1 PLL carrier tracking

For a PLL, $H(f)$ is the usual loop transfer function which is given by

$$H(s) = \frac{2\zeta\omega_n s + \omega_n^2}{s^2 e^{s\tau} + 2\zeta\omega_n s + \omega_n^2}, \quad (2)$$

for a high gain, second order loop, where $s = j2\pi f$, ω_n is the loop natural frequency [rad/s], ζ is the loop damping factor, and τ is the loop time delay, since there is necessarily some time delay incurred in propagation around the loop. The loop time delay is a critical parameter, since it must satisfy the following inequality for a high gain, second order PLL to be stable:

$$\omega_n \tau < \frac{\tan^{-1}\left(2\zeta\sqrt{2\zeta^2 + \sqrt{4\zeta^4 + 1}}\right)}{\sqrt{2\zeta^2 + \sqrt{4\zeta^4 + 1}}}. \quad (3)$$

For the typical case $\zeta = 0.707$, this reduces¹ to $\omega_n \tau < 0.736$. Since the bandwidth scales linearly with ω_n , increasing the bandwidth to provide more noise reduction leads to a more stringent requirement on the time delay τ . Furthermore, if τ is too close to violating Eq. 3, there will be a large peak in the noise spectrum due to inadequate gain and/or phase margins which will often not be acceptable in practice.

The work reported in reference² provides a concrete example. In this work, the carrier laser had a linewidth of 2 MHz and the LO laser had a linewidth of 6 MHz. A second order loop was implemented, with $\omega_n = 7.8 \times 10^8$ rad/s and $\zeta = 0.707$, which leads to a time delay requirement of $\tau < 0.94$ ns. The time delay as implemented was only 0.4 ns, which satisfied the stability requirement, but meeting this requirement severely constrained the design, since optical and electrical path lengths had to be kept as small as possible, and loop circuitry that added too much delay could not be employed. A spectrum analyzer trace was given, and assuming the observed noise is entirely phase noise, the results were $L(f) = -117$ dBc/Hz at 1 GHz offset, $L(f)$ reaches a peak of -102 dBc/Hz between 100 MHz and 300 MHz offset, and the "low frequency" limit (on a GHz span) of $L(f)$ was -125 dBc/Hz. It seems clear from this work that the only approaches for dramatically improving PLL carrier tracking performance are to monolithically integrate the PLL to reduce the loop delay to the maximum extent possible, or to significantly reduce the phase noise of the lasers being controlled by the loop.

Our interest in injection locking for carrier tracking of lasers, especially semiconductor lasers, is motivated mainly by the difficulty of the PLL time delay issue and the absence of a similar time delay issue for injection locking. The reason injection locking has no time delay issue is that it does not depend on feedback through an external loop --- all the action is confined to the cavity of the slave laser, which is typically very small. In the next section, we obtain a simple estimate of the $H(f)$ that may be obtained from injection locking.

2.2 Injection locked carrier tracking

Laser dynamics are frequently described by a set of rate equations for the optical intensity, optical phase, and population inversion. A linearization of these rate equations about a CW operating point gives a transfer function matrix that relates the inputs (injected amplitude, injected phase, slave pump current) to the outputs (slave amplitude, slave phase, slave population inversion). In any case of practical interest, noise induced fluctuations will be small enough to justify the use of a linearized model. Although the basic ideas are always the same, the exact form and complexity of this type of analysis varies widely, depending on the approximations that are made in the development. For our purposes, it is convenient to start from a detailed recent analysis³ of semiconductor laser injection locking, and identify the additional approximations we make to obtain our estimates.

We neglect optical intensity and population inversion fluctuations. We also assume that the static phase difference between master and slave is zero, which requires the master frequency to be slightly less than that of the free running slave due to phase-amplitude coupling in semiconductor lasers⁴. With these assumptions, the system of linearized rate equations decouples, and the phase equation reduces to

$$\frac{d}{dt} \delta\phi \approx -\frac{c}{2nL} \sqrt{\frac{P_i}{P_0}} (\delta\phi_i - \delta\phi) + F_\phi(t), \quad (4)$$

where $\delta\phi$ is the slave phase, $\delta\phi_i$ is the master phase, P_i is the (mode-matched) injected power, P_0 is the free running slave power, n is the index of refraction of the slave cavity (at its free running operating point), c is the speed of light, L is the cavity length, and F_ϕ is the Langevin phase noise source for the slave laser. For a laser with Lorentzian linewidth $\Delta\nu$, we have $W_F = 4\Delta\nu$ [rad²/s²Hz] for the PSD of the Langevin source F_ϕ . Since we refer P_0 and n to the free running slave, we are also assuming a condition of low-level injection, where the injection is weak enough that it does not significantly change the operating point of the slave (i.e. output power and carrier concentration). Although the approximations needed to obtain Eq. 4 are drastic, it is important to note that it was not necessary to assume a negligible phase-amplitude coupling, so Eq. 4 is applicable to a semiconductor laser provided the stated assumptions are valid. From Eq. 4, we can show the photocurrent PSD is given by Eq. 1, as claimed above, with a transfer function given by

$$H_{IL}(f) = \frac{\Delta\omega}{s + \Delta\omega}, \text{ where} \quad (5)$$

$$\Delta\omega = \frac{c}{2nL} \sqrt{\frac{P_i}{P_0}}. \quad (6)$$

We see that Eq. 5 is a transfer function of the same form as for a first order PLL with DC loop gain (~equivalent to bandwidth) $\Delta\omega$. For typical parameters ($L = 300 \mu\text{m}$, $P_i/P_0 = 0.01$, $n = 3.5$), a bandwidth of 1.4×10^{10} rad/s is obtained, which is a bandwidth that is difficult to obtain from a stable PLL.

Given a transfer function for a carrier tracking approach, laser phase noise spectra and photocurrent phase noise requirements, it is possible to derive requirements on the bandwidth of the carrier tracking approach from Eq. 1. For example, suppose the lasers have Lorentzian lineshapes (i.e. white frequency noise) with 1 MHz linewidths, and the phase noise requirement is $L(f) < -130$ dBc/Hz at offsets ≥ 1 MHz. For a second order PLL with $\zeta = 0.707$, we obtain $\omega_n > 7.9 \times 10^9$ rad/s to meet the phase noise requirement (assuming the time delay does not significantly affect the performance), which leads to a stringent time delay requirement of $\tau \ll 90$ ps. For injection locked carrier tracking according to Eq. 5, we obtain $\Delta\omega > 1.12 \times 10^{10}$ rad/s, which is less than the bandwidth estimated above from typical laser parameters. From these estimates, it seems clear that injection locking is a promising approach for carrier tracking of semiconductor lasers, and the remainder of this paper will be devoted to phase noise measurements in support of this claim.

3. EXPERIMENTAL SETUP

Figure 1 gives a simplified schematic diagram of our injection locking experiment. All components in Figure 1 were commercially available fiber coupled components, except the slave laser which was an unpackaged distributed feedback (DFB) device which was fiber coupled via a pickup head. In Figure 1, light from the master laser (an external cavity laser with nominal linewidth of 10 kHz operating at 1.55 μm) was split by a 3 dB coupler into the two arms of the interferometer. In the upper arm, the light passed through an attenuator/isolator unit that also provided an output power readout. The next component was a circulator, which provided additional isolation for the master (ports 1 to 2). After the circulator, the light from the master passed through a polarization controller that aligned the injected polarization with the slave polarization. The output of the slave returned through the polarization controller and the circulator (ports 2 to 3), so it was separated from the injected light. The slave output from port 3 of the circulator passed through a 3 dB coupler to a detector. In the lower arm of the interferometer, the light from the master was coherently frequency shifted by an acousto-optic (AO) frequency shifter driven by an RF reference. The AO frequency shifter that was available could only generate a frequency shift of 55 MHz, which sufficed to demonstrate the concept, although a larger frequency shift is desirable. After the frequency shift, the light passed through a length of fiber intended to equalize the lengths of the two paths in the experiment (master \rightarrow slave \rightarrow detector and master \rightarrow frequency shift \rightarrow detector). The necessity for this path length balancing will be explained in the following text. The next components were a polarization controller, 3 dB coupler and detector. The purpose of the polarization controller was to align the polarizations of the two optical signals at the detector to maximize the 55 MHz beat signal. The detected signal was then amplified and input into a demodulating phase noise test set (HP 3048a) for SSB phase noise PSD (i.e. $L(f)$) measurements. A spectrum analyzer was also used, mainly to determine the presence or absence of injection locking.

There are several key features of this injection locking experiment. The first is that it was almost completely fiber coupled, and could have been used with a fiber pigtailed slave laser in an unisolated package. The second key feature is the use of an optical circulator that provided an efficient separation of the slave light from the injected master light. A third feature is the use of a demodulating phase noise test set, which provided a considerably lower measurement noise floor than can be obtained with a spectrum analyzer, and also gave about 20 dB of amplitude noise suppression. Finally, fiber coupling reduced the difficulty and uncertainty of the injection ratio measurement. The fiber to slave coupling loss applied equally to the slave output and the injected input. Thus a relatively simple coupling efficiency measurement (we obtained a slave to fiber coupling efficiency of approximately 50%) also gives the master to slave injection efficiency, which is a difficult measurement in free space.

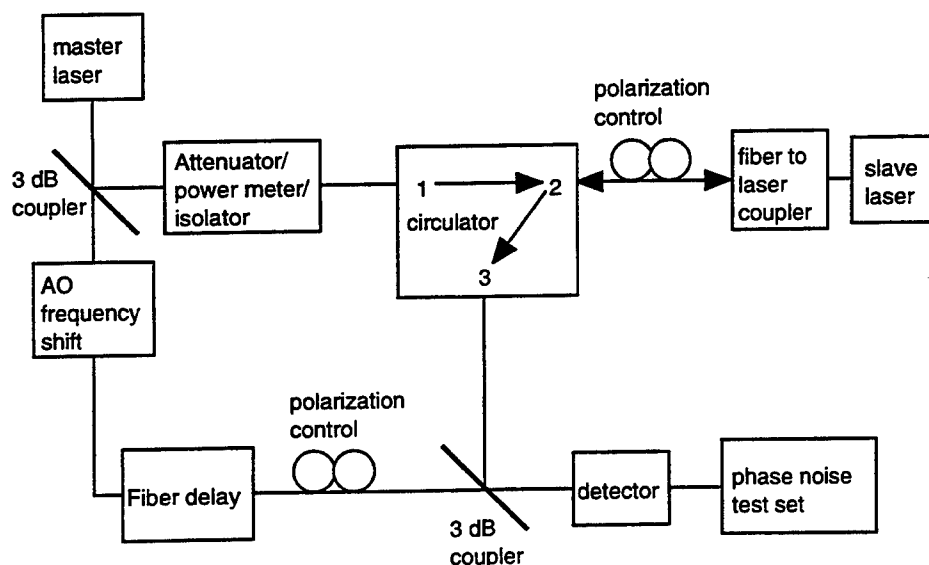


Figure 1: Schematic diagram of injection locking phase noise measurement

Before giving our results, it is necessary to consider some consequences of our measurement approach. The basic idea of the measurement is to form a heterodyne beat note between the injection locked slave laser and a frequency shifted portion of the master laser output, and measure the phase noise on this beat note with a phase noise test set, as seen in Figure 1. This is the same basic arrangement that is used for a self-heterodyne measurement⁵ of the linewidth of a single laser, so it follows that the relative time delay between the two arms of the experiment is a critical parameter. If this time delay is too large, the noise induced by decorrelation of the master will swamp the noise due to imperfect master-slave tracking that we are trying to measure. For a laser with white frequency noise and FWHM linewidth $\Delta\nu$, the self heterodyne SSB phase noise $L_{SH}(f)$ is given by⁶

$$L_{SH}(f) = \frac{\Delta\nu}{\pi} \frac{1}{f^2 + \Delta\nu^2} \left(1 - e^{-2\pi\Delta\nu\tau} \left(\cos 2\pi f\tau + \frac{\Delta\nu}{f} \sin 2\pi f\tau \right) \right), \quad (7)$$

where $\tau \geq 0$ is the magnitude of the time delay difference between the two arms of the experiment. In the limit of small τ (i.e. $\Delta\nu\tau \ll 1$ and $f\tau \ll 1$) this reduces to a white $L(f)$ given by

$$L_{SH0} \approx 2\pi\Delta\nu\tau^2. \quad (8)$$

From Eq. 8, we can obtain time delay requirements given the master laser linewidth and a self heterodyne noise floor requirement. For example, if we want self heterodyne noise to be below -140 dBc/Hz (i.e. well below the requirements of interest), and the master laser linewidth is 10 kHz, we obtain $\tau < 0.4$ ns. To obtain the same self heterodyne noise floor with a 1 MHz linewidth master laser requires $\tau < 40$ ps. Since a time delay of 0.4 ns corresponds to roughly 8 cm of fiber, it is not difficult in principle to ensure adequate path length matching in a laboratory scale experiment, especially if the master laser has a relatively narrow linewidth. It should be noted that in many applications of phase coherent lasers, such as generation and distribution of RF carriers by optical heterodyne detection, the same requirement for path length matching must be imposed on the two paths to each detector in the system.

The requirement for matched path lengths led to a number of practical difficulties. One problem was that due to the high degree of isolation in this system, it was not possible to use an optical time-domain reflectometer to measure and balance the path lengths. A second issue was that the need for balanced path lengths was not appreciated until the setup had been assembled, and completely tearing down the experiment to physically measure all lengths of fibers was not feasible. Even if this had been feasible, the accuracy of the path balancing would have been marginal at best. As a result, a trial and error procedure for path length balancing was employed. Fortunately, this could be done with only the master laser operating, since the weak reflection of the master from the slave laser facet led to a self heterodyne beat at the detector, with essentially the same relative time delay that would occur in injection locking. The noise floor (presumably due to relative time delay) on this beat note was measured, and the length of the fiber delay was varied in an attempt to minimize the noise floor according to Eq. 8.

The qualitative trend was as expected --- for fiber delays that were clearly too long or too short, the measured noise floor was higher than it was for fiber delays which were closer to the path matching condition. Quantitatively, it was not possible to reduce the noise floor to less than about -127 dBc/Hz, which suggests the presence of another source of phase noise in addition to the path length mismatch. Although it is not known what the source of this excess noise is, some potential sources have been eliminated. The two RF synthesizers (HP 8662) in the experiment (one to drive the AO frequency shifter, the other to serve as a reference in the phase noise test set) both had a noise floor of -140 dBc/Hz over the relevant range of offset frequencies. The thermal noise in the amplifier/attenuator chain between the detector and phase noise test set also appeared to be too low to account for the observed excess noise. A plausible source of the excess noise is multiple reflections from the (FC/PC) fiber connectors in the experiment, since a multiply reflected contribution to the heterodyne beat may have a very substantial path length mismatch that more than makes up for its relatively small power.

4. EXPERIMENTAL RESULTS

As mentioned above, a spectrum analyzer was connected to the detector output mainly to determine whether or not injection locking was occurring. Under injection locked conditions, the spectrum analyzer trace is a clean tone at 55 MHz. As the master laser is tuned away from the slave laser frequency, lock will eventually be lost, and on the spectrum analyzer this appears as a sudden decrease in the power of the 55 MHz tone (recall that there will always be a sharp 55 MHz tone due to reflection of the master from the slave laser end face), combined with the appearance of a broad, fluctuating peak at higher frequencies (typically > 1 GHz), due to the mixing of the master and unlocked slave. The edge of the injection locking regime exhibits hysteresis, where a detuning that will not cause loss of lock is insufficient to establish lock. Due to this behavior, we took the locking range to lie between the two frequencies at which lock is established from an unlocked condition, since in this range, if lock is lost due to some transient effect, it will always be restored. We were mainly interested in the noise performance of injection locking well within the locking range, so approximate measurements of the locking range were adequate for that purpose. The following figures show a set of phase noise measurements where the injection ratio varies as indicated, and the detuning of the master is readjusted for each spectrum such that we are at or near the center of the locking range, where one expects the lowest noise performance.

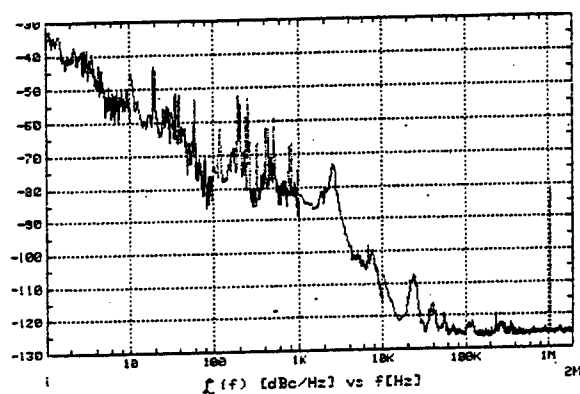


Figure 2: Injection locked phase noise PSD for -16 dB injection ratio

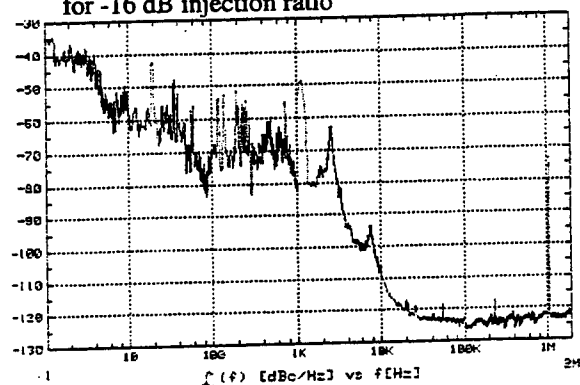


Figure 3: Injection locked phase noise PSD for -21 dB injection ratio

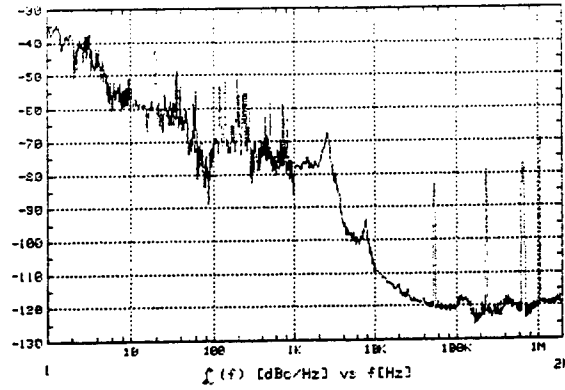


Figure 4: Injection locked phase noise PSD for -26 dB injection ratio

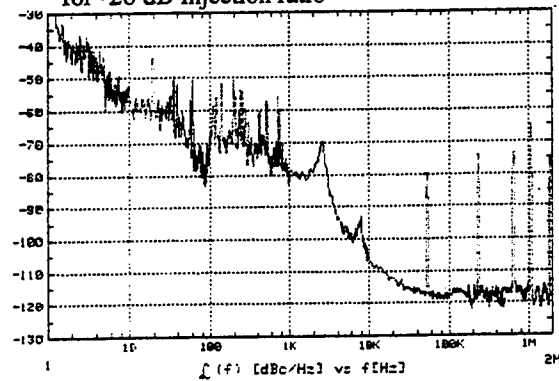


Figure 5: Injection locked phase noise PSD for -31 dB injection ratio

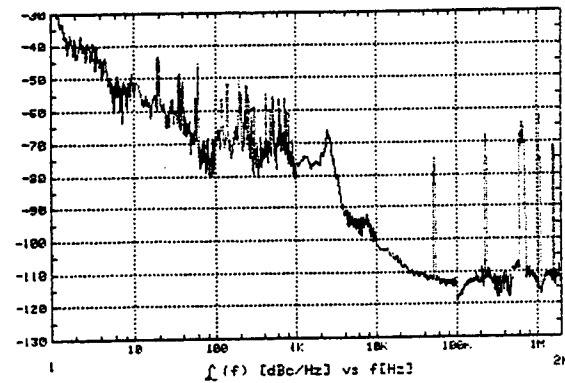


Figure 6: Injection locked phase noise PSD for -36 dB injection ratio

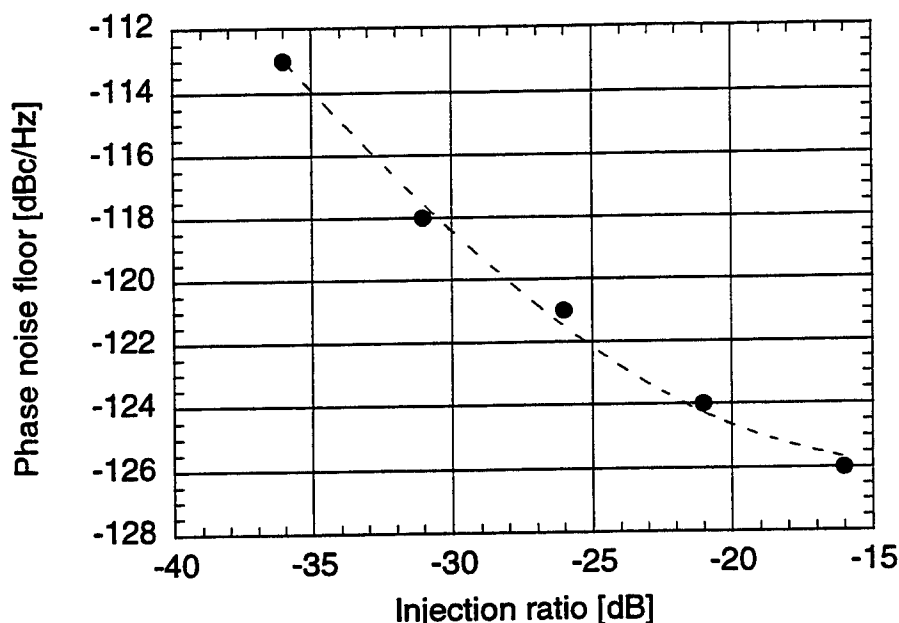
5. DISCUSSION

In Figure 7 we summarize the most significant trend observed in figures 2 through 6, namely that the noise floor at relatively high measured offset frequencies (i.e. 1 to 2 MHz) decreases as the injection ratio increases. From Eqs. 1, 5 and 6 we obtain the following estimate for the phase noise due to imperfect injection locking at low offset frequencies ($f \ll \Delta\omega$):

$$L(f) \approx \frac{2\pi\Delta\nu}{\Delta\omega^2} = \frac{8\pi\Delta\nu m^2 L^2}{c^2} \left(\frac{P_i}{P_0} \right)^{-1}, \quad (9)$$

where $\Delta\omega$ is the IL bandwidth given by Eq. 5, $\Delta\nu$ is the linewidth of the slave laser, n and L are the slave laser refractive index and length respectively, P_i/P_0 is the injection ratio, and the contribution of the master laser to the heterodyne phase noise is neglected, since the master linewidth is much less than the slave linewidth. Note that Eq. 9 is a low frequency limit compared to the IL bandwidth $\Delta\omega$, so in principle, it should apply over the entire measured range of offset frequencies. In practice, additional sources of phase noise, such as acoustic pickup, are present at offset frequencies less than roughly 100 kHz, so we only expect to see the trend predicted by Eq. 9 at relatively high measured offset frequencies (e.g. 100 kHz to 2 MHz).

The dotted line in Figure 7 is a curve fit to the measured data of the form $L = a P_0/P_i + b$, where a and b are the curve fitting parameters. The form of the a term in the curve fit follows from Eq. 9, while an excess noise term b is assumed in the curve fit to account for the data in Figure 7, as well as the observation of excess noise during the path length balancing procedure. The fitting parameters obtained are $b = -126.5$ dBc/Hz and $a = -149$ dBc/Hz. The excess noise seen in the curve fit is consistent with the roughly -127 dBc/Hz of excess noise observed when balancing the paths. If we assume plausible laser parameters in Eq. 9 (e.g. $\Delta\nu = 10$ MHz, $n = 3.5$, $L = 300$ μm), we would expect to obtain an a parameter of -145 dBc/Hz, which is quite close to the observed value. An independent measurement of the slave laser linewidth would



be a valuable check on the validity of Eq. 9.

Figure 7: Phase noise floor vs. injection ratio. The solid circles are experimental points and the dotted line is a curve fit.

As seen in figures 2 through 6, the phase noise generally increases as the offset frequency decreases, and no systematic trend in the phase noise data is seen as the injection ratio varies for offset frequencies below several kHz. We believe the measured noise in this frequency range was due primarily to acoustic pickup in the fibers instead of a degradation in the performance of injection locking at lower offset frequencies. Our reasons for this belief are that no special measures were taken to acoustically isolate the experiment, and that the self heterodyne noise spectrum of the master alone had a low frequency noise spectrum essentially identical to that shown in figures 2-6. We also modified the master self heterodyne measurement by significantly decreasing the total length of fiber in the two arms of the interferometer while maintaining an approximate path length match. By doing so, we observed a significant (10-20 dB) reduction of low frequency phase noise, due presumably to decreased acoustic sensitivity, while the high frequency (100 kHz to 2 MHz) noise floor was essentially unchanged.

6. CONCLUSIONS

In conclusion, this work has demonstrated a very low level of phase noise on the heterodyne beat of optically injection locked semiconductor lasers. To our knowledge, this is by far the lowest reported level of phase noise from injection locked semiconductor lasers. Since the noise floor of -125 dBc/Hz seen in this work appears to be due to an excess noise mechanism unrelated to injection locking, further improvements may be possible, which suggests the consideration of injection locking for the most demanding applications.

We have also seen that time delay noise, and fiber acoustic noise are issues which will usually need to be addressed in applications of phase locked lasers. Usually, time delay noise and fiber acoustic noise are not seen in measurements of PLL performance, but the reason is simply that the PLL acts to enforce phase coherence at the detector, where its performance is typically measured. Thus there is intrinsically no time delay effect in the measurement, and fiber acoustics between the lasers and detector are suppressed by the PLL. In applications, it will frequently be necessary to tap a portion of the output of each laser to make a heterodyne beat at a second detector (e.g. a detector at a remote antenna array element), and time delay noise and fiber acoustic noise along the paths to this second detector are definitely relevant issues. The results shown in figures 2 through 6 give an indication of the level of acoustic pickup that occurs along moderate lengths of connectorized fiber (~20 m or so in each arm of the interferometer) in a laboratory environment, if no attempt is made to isolate the fibers from acoustic disturbances.

Injection locking by itself cannot comprise a complete carrier tracking solution, unless unrealistic requirements are placed on the absolute frequency stability of each laser to ensure the relative drift of the two lasers is an insignificant fraction of the injection locking range. Therefore it is necessary to supplement injection locking with a drift control mechanism. Published methods include an optical PLL⁷, and a Pound-Drever-Hall servo loop to lock the master to the slave cavity resonance^{8,9}. In principle, the main advantage of injection locking, namely its large noise suppression bandwidth, should be preserved in hybrid schemes of this type, since the drift control mechanism need not have a large bandwidth. In practice, considerable care will be needed to ensure that a practical (i.e. drift stabilized) injection locking scheme really delivers the full performance promised by injection locking.

7. ACKNOWLEDGEMENTS

This work has been supported by DARPA and Rome Labs under contract F30602-96-C-0273.

8. REFERENCES

1. M. A. Grant, W. C. Michie, and M. J. Fletcher, "The performance of optical phase locked loops in the presence of nonnegligible loop propagation delay", *IEEE J. Lightwave Technology*, 5(4), pp 592-597, 1987.
2. U. Gliese, T. N. Nielsen, M. Bruun, E. L. Christensen, K. E. Stubkjær, S. Lindgren, and B. Broberg, "A wideband heterodyne optical phase locked loop for generation of 3-18 GHz microwave carriers", *IEEE Photonics Technology Lett.*, 4(8), pp 936-938, 1992.
3. J. Genest, M. Chamberland, P. Tremblay, and M. Têtu, "Microwave signals generated by optical heterodyne between injection locked semiconductor lasers", *IEEE J. Quantum Electronics*, 33(6), pp 989-998, 1997.

4. F. Mogensen, H. Olesen, and G. Jacobsen, "Locking conditions and stability properties for a semiconductor laser with external light injection", *IEEE J. Quantum Electronics*, 21(7), pp 784-793, 1985.
5. T. Okoshi, K. Kikuchi, and A. Nakayama, "Novel method for high resolution measurement of laser output spectrum", *Electronics Lett.*, 16(16), pp 630-631, 1980.
6. M. P. van Exter, S. J. M. Kuppens and J. P. Woerdman, "Excess phase noise in self-heterodyne detection", *IEEE J. Quantum Electronics*, 28(3), pp 580-584, 1992.
7. R. T. Ramos, P. Gallion, D. Erasme, A. J. Seeds, and A. Bordonalli, "Optical injection locking and phase lock loop combined systems", *Optics Letters*, 19(1), pp 4-6, 1994.
8. O. Mor and A. Arie, "Performance analysis of Drever-Hall laser frequency stabilization using a proportional + integral servo", *IEEE J. Quantum Electronics*, 33(4), pp 532-539, 1997.
9. C. D. Nabors, A. D. Farinas, T. Day, S. T. Yang, E. K. Gustafson, and R. L. Byer, "Injection locking of a 13 W cw Nd:YAG ring laser", *Optics Letters*, 14(21), pp1189-1191, 1989.

The Design and Performance of a Grating-Based, Coherent Optical, Wideband RF Signal Channelizer

R. L. Davis, R. Lodenkamper, T. J. Jung, W. Wang, M. Flannery, J. Yun,
L. J. Lembo, and J. C. Brock

TRW Space and Electronics Group
One Space Park, D1/1024
Redondo Beach, CA 90278
Tel: (310) 813-7504 FAX: (310) 812-8983
r.davis@trw.com

Abstract: A coherent optical receiver capable of channelizing up to 100GHz bandwidths into 1GHz channels is desirable for future military EW systems. We present the design and performance characteristics of a coherent optical spectrum channelizer that is the principal element in an advanced receiver.

INTRODUCTION

The basic mission of the broadband electronic support measure (ESM) system is to detect emitters throughout some frequency band of interest that are incident on the platform anywhere from within a 360° field-of-view. A principal factor driving the development of future wideband receivers is the fact that the bandwidths of emerging threats are escalating into the 100 GHz regime, and the density of threats in the higher frequencies is increasing rapidly.

We have recently completed a program whose objective was to design, fabricate, and test an engineering development model for a coherent optical receiver architecture that will enable the capability for sorting, identifying, and tracking emitter signals in the very dense, extremely wideband signal environments anticipated in the near future. Our approach is substantially different from previous embodiments of optical-based spectrum analyzers and channelizers. A wide variety of optical processor architectures have been proposed and built.¹⁻³ The most common approach is to spatially impress the unknown signal onto a light beam and Fourier transform the result with a lens, then sample the transform with an array of photodetectors in the lens's transform plane. Systems have been built that are either incoherent, producing a power spectrum of the input signal, or coherent, in which the output preserves both the amplitude and phase of the input signal. The limiting factor, in terms of bandwidth, in these systems is the spatial light modulator used to transduce the electrical signal into the optical realm. In general acousto-optic Bragg cells are used, and these are limited to RF bandwidths of at most a few GHz.⁴

We built a system wherein the RF signal is temporally impressed onto the optical carrier and the optical spectrum is analyzed directly. The advantage here is that modulators are available with bandwidths exceeding 50 GHz with near-term projections reaching 100 GHz. The difficulty presented by this approach is that the small fractional bandwidth of RF modulation relative to an optical carrier frequency makes the task of spectrally dispersing the optically carried signal difficult.

Figure 1 shows the operation of the coherent optical channelizer. In 1(a) a signal-bearing optical beam is collimated and made incident on the diffraction grating. The signal's frequency components are dispersed through a range of angles and subsequently focussed onto the detector array. The center position of a detector corresponds to a particular RF frequency and the detector's width spans the desired channelization bandwidth. In 1(b) a second beam, the L.O. beam, is derived from a mode-locked laser whose spectrum comprises an RF frequency comb with a frequency spacing equal to the channel bandwidth. This beam is made incident on the grating at some offset angle with respect to the signal beam thereby causing it's spectrum to be displaced in the detector plane. When the two beams are combined on the detectors, 1(c), each detector generates a heterodyne beat tone. In this way each photodetector translates a portion of the signal spectrum to the same IF band, so that each detector channel may use the same postdetection electronics. The IF beat frequency can be tuned by adjusting the offset in incident angles at which the signal and LO lasers illuminate the grating.

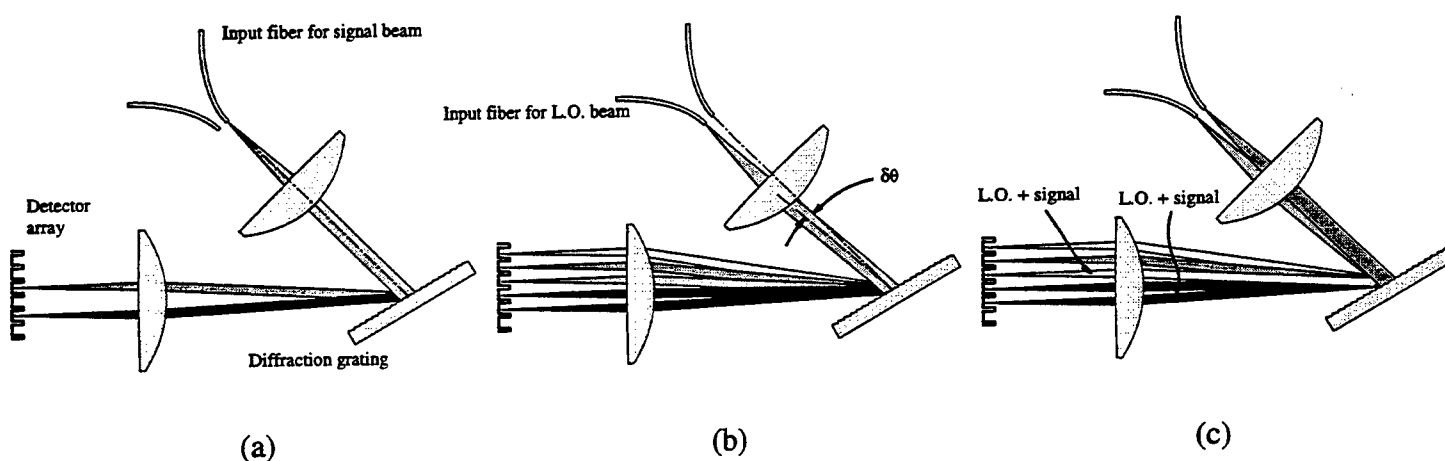


Figure 1. Grating-based coherent optical RF channelizer

Table 1 lists the set of design goals that we established at the outset of the program. These requirements primarily were derived from the RF requirements for a "typical" high-performance electronic support measure (ESM) receiver.

Table 1. Nominal channelizer RF performance requirements

Parameter	Performance Specification
Instantaneous Bandwidth	100 GHz
Channel Bandwidth	1 GHz
Spur-Free Dynamic Range	>50 dB
IF Output Frequency	~5 GHz
Crosstalk	< -70 dB
Channel Response Uniformity	< 3 dB

CHANNELIZER DESIGN

The channelizer design and optical layout is dependent on the specifications presented above. We performed analyses based on the model shown in figure 2 to determine how key channelizer performance requirements influenced various design parameters.

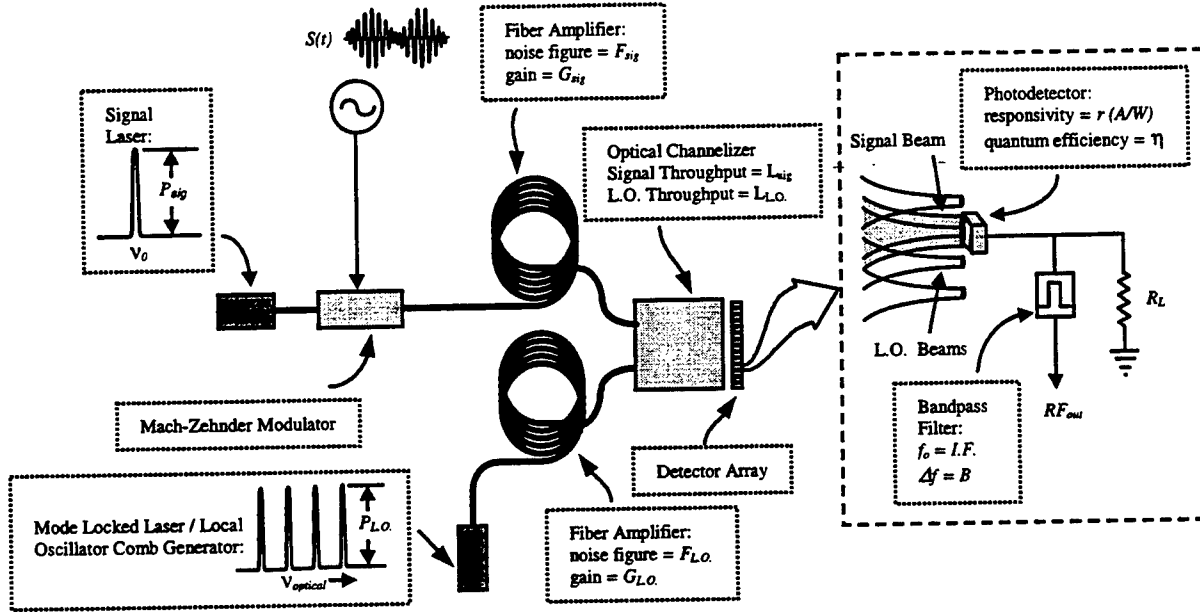


Figure 2. Model used to calculate the channelizer's RF performance characteristics

Spur Free Dynamic Range:

As shown in the figure the RF signal is impressed onto a signal carrier laser using a Mach-Zehnder (MZ) interferometric modulator. Since we are using a coherent detection scheme, the MZ is biased at its minimum transmission point to suppress second harmonics in the optical frequency spectrum. Thus the third order intermodulation products become the dominant distortion terms, which limit the upper end of the dynamic range. Detector output noise determines the minimum discernible signal. We derived the following expression for the spur-free dynamic range (SFDR). The definition of the parameters can be inferred from figure 2.

$$SFDR = 10 \log \left(\frac{4R_L r^2 P_{sig} G_{sig} L_{sig} P_{LO} G_{LO} L_{LO}}{P_N} \right)^{2/3} \text{ dB}, \quad [1]$$

where P_N is the relevant noise power. We find that the significant noise contributors are thermal noise, shot noise produced by the local oscillator, and the noise resulting from the local oscillator beating against the ASE noise from the optical amplifier placed in the signal beam path.

$$P_N = [P_{thermal}] + [P_{shot_{LO}}] + [P_{LOxASE_{sig}}]$$

$$= [4kTB] + [2qrR_LBP_{LO}G_{LO}L_{LO}] + [2r^2R_Lh\nu_0BF_{sig}G_{sig}L_{sig}P_{LO}G_{LO}L_{LO}]. \quad [2]$$

In [2] k is Boltzmann's constant, T is the temperature, h is Planck's constant, and ν_0 is the laser frequency. The most favorable situation occurs when G_{sig} is sufficiently large such that the $P_{LOxASE_{sig}}$ term dominates the detector noise. In this case dynamic range tends to a maximum value given by

$$SFDR_{max} = 10 \log \left(\frac{2P_{sig}}{h\nu_0BF_{sig}} \right)^{2/3} \text{ dB}. \quad [3]$$

For $P_{sig} = 100\text{mW}$ at a laser wavelength of $1.55\mu\text{m}$, $B = 1 \text{ GHz}$, and $F_{sig} = 2.75 \text{ (4dB)}$, we find $SFDR_{max} = 58\text{dB}$.

Channel Response:

There are three parameters that characterize an individual channel's response to signal that vary in frequency about the center frequency for that particular channel. These are the loss, ripple, and crosstalk and we define them as follows (see figure 3). Loss is the difference between the actual response to a signal at the center of the channel and the ideal response, which would occur if all of the signal optical power were to combine with all the L.O. optical power to form the response. Ripple is a measure of the response uniformity and is generally given by the variation of the channel's response as the signal frequency ranges from the center to the edge of the channel as shown in the figure.

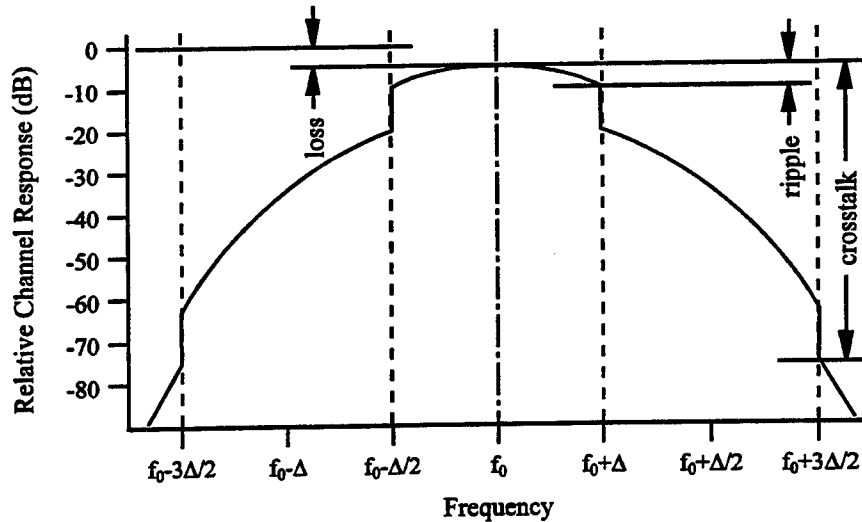


Figure 3. Channel response as signal frequency is varied about the center of the channel. We define crosstalk following the convention employed in most channelized receiver specifications. As such, crosstalk is the response of a channel to a signal that is at the near edge of the channel's next-nearest neighbor. These parameters are primarily

determined by the optical profiles of the signal beam and L.O. beam on the detector array relative to the channel width. In our initial analysis we assumed Gaussian spot profiles and allowed the $1/e^2$ spot diameters of the L.O. spot, $d_{L.O.}$, and the signal spot, d_{sig} , to vary independently. We calculated the crosstalk for all combinations of $d_{L.O.}$ and d_{sig} and in figure 4(a) we have plotted the locus of those values that yield a crosstalk of -70dB . Combinations of spot sizes that lie to the left and below the curve will yield a greater degree of crosstalk suppression, while those to the right and above will yield less. We then restricted calculations to spot sizes that lie on the -70dB curve and calculated the loss and ripple. In 4(b) we show loss and ripple as functions of L.O. spot size. These results show that acceptable levels of ripple are obtainable, but at the expense of some additional loss. For example, $d_{L.O.}=0.5\Delta$ and $d_{sig}=2.0\Delta$ provide about 2dB of ripple while causing an increase of about 3dB in loss. The impact of loss on the channelizer is to reduce the dynamic range by 2/3 of the loss (in dB), in this case about 2dB.

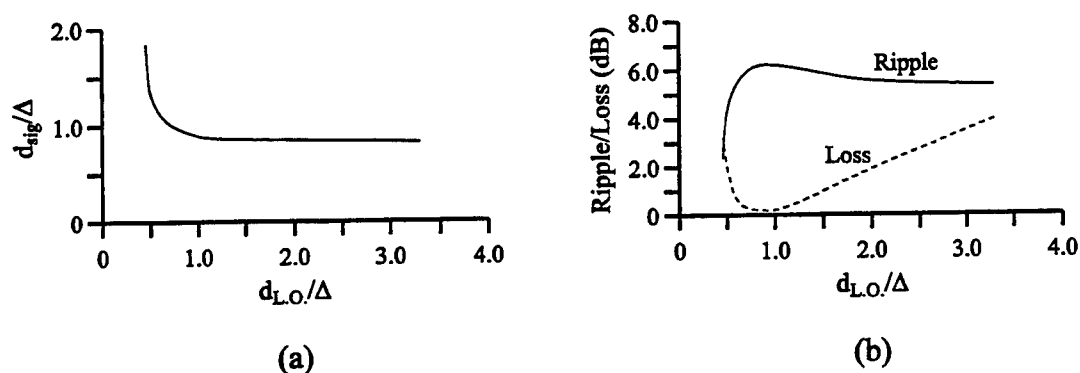


Figure 4. Channelizer spot size and ripple/loss trades for -70dB crosstalk

Channelizer Optical Layout:

The critical component in the optical system is the lens that focuses the output beams onto the detector. The actual design process of the channelizer followed the flow path shown in figure 5. Since the scope of this phase of the program was for proof-of-concept we did not undertake to design and fabricate a custom diffraction grating, therefore our system was based primarily on an "off-the-shelf" grating that could be made to provide the desired resolution. We surveyed available gratings and selected one ruled with 452 lines/mm because it provided the highest optical throughput. As indicated in the figure, we designed a multi-pass optical layout to meet the spectral resolution objective of 1GHz. The RF requirements on the beam sizes, coupled with the optical system dispersion and the mode radius of the fiber used for the L.O. input, established the collimated beam diameters, $D_{L.O.}$ and D_{sig} , in the channelizer and therefore, the optical performance requirements for the channelizer's lens. The L.O. input spot size was used as the determinant because it would be smaller than the signal beam, and thus would be obtained directly from the fiber output. The signal beam would be an expanded image of the fiber's output. These requirements were used to direct the design of the channelizer's

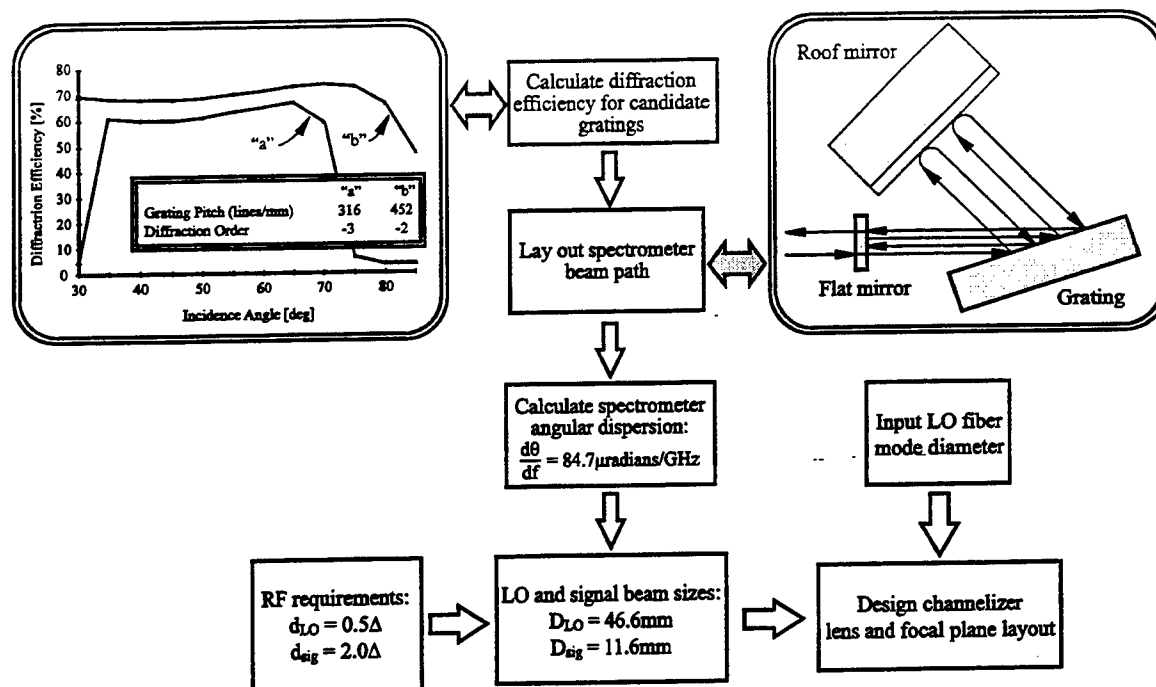


Figure 5. The channelizer design is based on a suitable off-the-shelf diffraction grating and the RF performance requirements.

lens and the layout of the input/output optics in the lens's focal plane. Our optical system used a single lens both to collimate the input signal and L.O. beams and focus the angularly dispersed beams onto the output plane. The lens requirement was for a modest numerical aperture, $\sim F:2.5$, but our application demanded nearly perfect, diffraction-limited performance over a $\pm 0.25^\circ \times 0.25^\circ$ field of view. The lens was designed and optimized using CodeV design software. The design was subjected to tolerance analysis and physical optics calculations to ensure that the necessary high level of performance was obtained over the field of regard. The design incorporated an optical beamsplitter as an integral part of the lens to provide some flexibility in the arrangement of the optical inputs and outputs. This is illustrated in figure 6, which is a scale drawing of the lens showing the beamsplitter and the basic arrangement of the optics used for our measurements. For some of our measurements the signal input was provided by an optical fiber as shown in the figure. The fiber was replaced with a free-space, anamorphic beam-expansion imaging system for those measurements requiring different L.O. and signal spot sizes. Also depending on the measurement being made, either the multi-mode output fiber was made to sample the output directly or the output was reimaged onto a slit placed directly in front of the fiber. The reimaging optics and slit dimensions were configured to simulate one channel of a complete receiver.

Figure 7 shows photographs of the RF channelizer. In 7(a) we show a view of the lens's focal plane with micropositioners for the signal and L.O. fibers. 7(b) is a picture of the grating and the mirrors used to fold the beams' paths, and provide the multiple reflections off of the grating. The dashed line traces the optical paths through the system. The beams are collimated by the lens (at the lower central part of the picture) and are diffracted by the grating. The diffracted beams are directed to the right-angle mirror where they are elevated and redirected to the grating for a second diffraction. The twice-

diffracted beams are then reflected by the circular mirror located directly above the lens, and the beams then retrace their route back along the identical path to the lens, through which they exit the system, ultimately being focused at the output of the channelizer.

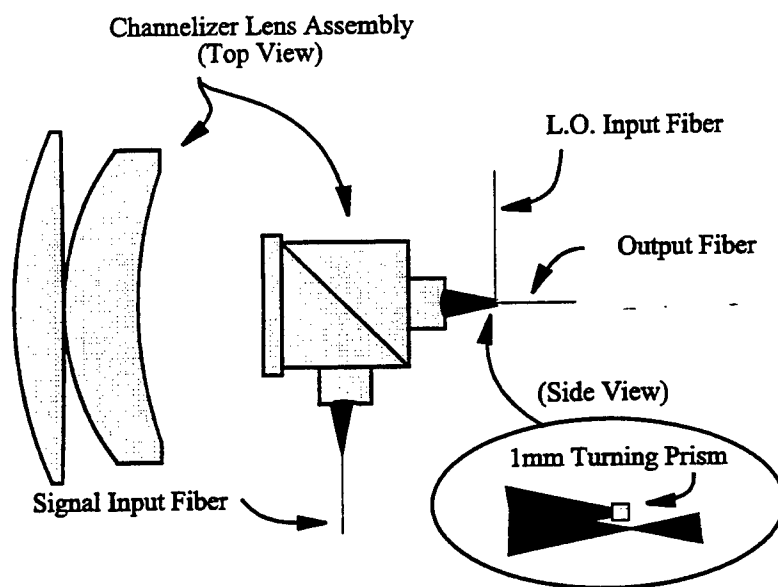
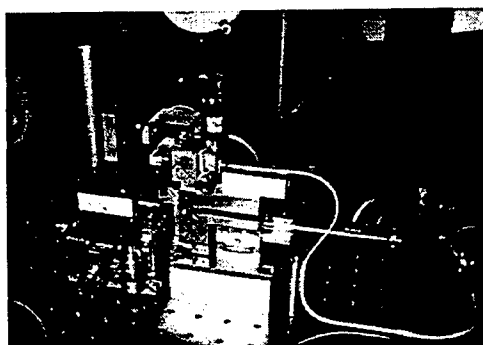
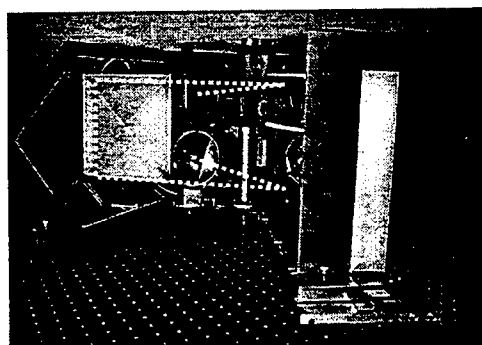


Figure 6. Channelizer lens incorporates split optical paths to relieve congestion in the input/output focal planes.



(a) Channelizer's focal plane optics



(b) Beam path in the channelizer

Figure 7. RF channelizer optical layout

CHANNELIZER PERFORMANCE

Measurements were made to characterize the performance of the channelizer and to compare the RF performance with our model-based predictions.

Optical System Characterization:

Initially we determined the optical properties of the system. We measured the mode profile of the single-mode optical fiber used for the input signal beam. These measurements revealed that the fiber's mode profile differed significantly from the ideal Gaussian mode shape that we assumed for the purpose of designing the optical system. The mode was larger in diameter than expected, and of greater significance, the sidelobe levels were substantially higher than anticipated. This had a predictable influence on the RF performance of the channelizer, most notably the crosstalk suppression was somewhat compromised.

The performance of the custom lens was evaluated using two different methods and we verified that the lens delivered the required image acuity throughout the field of regard. It was determined that, within the accuracy of our measurement techniques, the lens's performance did not deviate from the predictions of our physical optics calculations based on the lens design.

Table 2 summarizes the optical throughput for the two beam paths in the channelizer. All of the measurements were made with an optical wavelength of $1.55\mu\text{m}$. The signal and L.O. paths differ only in the manner in which they traverse the beamsplitter. The total throughput is a fiber-to-fiber measurement and includes fiber coupling losses and the beamsplitting losses for the two paths.

Table 2. Optical system throughput summary

	splitting loss	η_{grating}	miscellaneous	Total
Signal path	0.05	$0.49^4 = .058$	0.53	0.0015 (-28.1dB)
L.O. path	0.71	$0.49^4 = .058$	0.35	0.0145 (-18.4dB)

The measured grating diffraction efficiency was only 0.49, which is much less than the expected value of 0.72. This was the value that we calculated and the grating supplier subsequently measured at their facility. The reason for this degradation is still unclear.

RF Performance:

For RF performance evaluation we installed a pair of 40x diode laser objectives to reimage the output focal plane onto a $25\mu\text{m}$ wide precision air slit. A $50\mu\text{m}$ core-diameter, multi-mode fiber was positioned directly behind the slit to collect the transmitted beams. The slit defines the physical extent of the channel. Repositioning the lenses and slit/output-fiber can alter the magnification of the diode laser objective pair quite simply. This allows us to control the RF channel bandwidth as desired. The light source we used was an amplified, New-Focus external cavity laser that was split to the LO arm and the signal arm. The light in the signal arm goes through a Mach-Zehnder modulator and is then sent to the signal input port of the channelizer, whereas the light in the LO arm is sent to the LO port directly. The LO beam is spatially overlapped with one

of the signal sidebands at the output port to generate the heterodyne signal. As shown, this setup provides equal-size spots for the signal and L.O. beams.

We have shown that to improve ripple it is desirable to spread the signal spot by a factor of three to four with respect the L.O. spot. In order not to increase the insertion loss the spreading should be only along the direction parallel to the grating-induced dispersion. We constructed an anamorphic imaging system that transformed the circular mode pattern emerging from the input fiber into an elliptical pattern whose minor axis is equal to the fiber's mode diameter, and whose major axis is expanded threefold. The elliptical beam waist was positioned in the input plane of the channelizer's signal port. Figure 8 shows the results of measurements made on the in-channel response (ripple) for the two cases. We find the data to be in good general agreement with the calculated ripple.

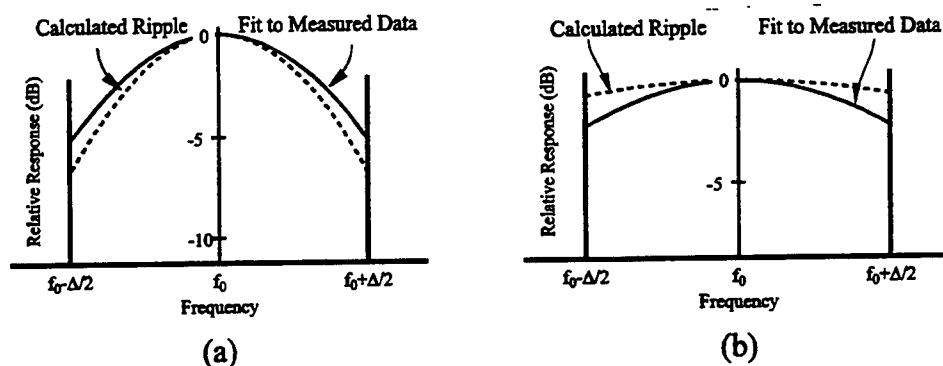


Figure 8. Measured ripple for equal-size signal and L.O. spots, (a), and for unequal-size signal and L.O. spots, (b)

We also measured the crosstalk, as defined earlier, for the channelizer. Our best result was about -53dB . This is somewhat short of the -70dB expected from the calculations that were based on the assumption that the input fiber's mode profile was approximately Gaussian. The difference is attributable to the excessive power distributed in the wings of the fiber's actual mode profile. This apparently was a characteristic of the particular fiber we used in the system. We have seen data on other fibers (e.g. Fujikura single-mode fiber) that showed sidelobe levels below -50dB , which would readily provide the desired crosstalk performance.

We measured the dynamic range by applying two, equal-power RF signals to the modulator at such a level that their 3rd order intermodulation product generated a response that was equal to the system noise power. We then measured the applied power for a single-tone RF signal that produced a fundamental response that was just equal to the noise power. The ratio of these two power levels is the spur free dynamic range. The measurements were made using a spectrum analyzer set to 3KHz noise bandwidth and the results were extrapolated to a 1GHz noise bandwidth. We also calculated the dynamic range for our model of the system to compare with our experimental result. We note that the optical power levels in our experiment were insufficient to prevent the system from being dominated by thermal noise so we expected to obtain a dynamic range of about 48dB. The results are shown in table 3.

Table 3. Channelizer two-tone, spur-free dynamic range

Input optical power (W):	Measured SFDR into 3kHz noise BW	SFDR into 1GHz noise BW	Calculated SFDR into 1GHz noise BW
$G_{LO} P_{LO} L_{LO} = 1.2 \times 10^{-4}$ $G_{sig} P_{sig} L_{sig} = 1.7 \times 10^{-1}$	82dB	45.2dB	48.0dB

The observed performance is seen to agree very well with our calculated results. This leads us to believe that the RF performance goals are certainly within the capabilities of this technology.

CONCLUSIONS

We have demonstrated that a high-resolution, grating-based optical spectrum channelizer is capable of the RF performance required by next generation EW receiver systems. We feel that a 1GHz channel bandwidth has merit since it will provide a valuable asset that is compatible with developments in electronic processors are approaching the 1GHz range.

ACKNOWLEDGMENT

This work was sponsored under DARPA/AFRL contract F30602-96-C-0273.

REFERENCES

1. M. C. King, et. al., "Real-Time Electro-Optical Signal Processors with Coherent Detection," Applied Optics, vol. 6, P. 1367, (1967).
2. A. Vanderlugt, "Interferometric Spectrum Analyzer," Applied Optics, vol. 20, p. 2770, (1981).
3. Todd Bader, Peter Kellman, and Harry Shaver, "Time Integrating Optical Processing," Final Technical Report, Air Force Office of Scientific Research contract F49260-78-C-0102, 1981.
4. I. C. Chang, "Wideband Acousto-Optic Spectrometer," proc. SPIE, vol. 1476, p.257, 1991.

Injection Locking of Mode-Locked Semiconductor Lasers for Channelizing Ultrawide Band Signals

T. Jung, *Student Member, IEEE*, J.L. Shen, D.T.K. Tong, S. Murthy,
M.C. Wu, *Member, IEEE*, T. Tanbun-Ek, W.Wang, *Member, IEEE*, R. Lodenkamper,
R. Davis, L.J. Lembo, and J.C. Brock, *Member, IEEE*

Electrical Engineering Department

University of California, Los Angeles

405 Hilgard Avenue Los Angeles, CA 90095-1594

Tel: 310-825-7338

Fax: 310-794-5513

Email: wu@ee.ucla.edu

I. Introduction

Fiber optics is known to be the medium of choice for long haul digital communication systems and for RF signal distribution due to its inherent low loss. Recent advances in RF photonic systems have demonstrated the ability to receive and transmit signals greater than 50 GHz on an optical carrier [1]. As the bandwidth of photodetectors and electro-optic modulators continue to increase up to 100 GHz, the electronics that processes these signals at the receiver end have not kept pace with the rapid growth in bandwidth. An approach to alleviate this problem is to exploit the parallel nature of optics to "slice" up the large instantaneous bandwidth into smaller channels of 1 GHz for signal processing while this information is being carried in the optical domain; this process is often referred to as channelization. Current state-of-the-art electronics can process signals below 1 GHz with very high dynamic range and low crosstalk but have a formidable task of operating at millimeter wave frequencies [2, 3]. Electronic channelizers also tend to have high insertion loss and high power consumption. In order to monitor the entire frequency range, the electronic warfare receiver must scan over the entire frequency range, which

takes a considerable amount of time and lowers the probability of intercept (POI). Other methods used to alleviate this bandwidth bottleneck include the acousto-optic (AO) channelizer, proposed since the late 1970's [4, 5]. The advantages of the AO channelizer is the fine channel resolution that can be obtained, on the order of MHz. Channel isolation greater than 50dB and a signal-to-noise ratio greater than 70dB have also been demonstrated [6]. However, this approach can only handle up to several GHz of bandwidth. In this paper, we report on a novel optical frequency comb local oscillator for a coherent broadband optical channelizer. The optical frequency comb is generated by hybrid mode-locking of an external cavity semiconductor laser. Phase coherence between the optical carrier of the signal and the optical frequency comb is established by CW optical injection locking of the mode-locked laser.

II. Concept of Coherent Optical Channelizer

A high resolution grating spectrometer is built to channelize the wide band signals into 100 channels of 1 GHz bandwidth [7]. This approach can be conceptualized in Fig. 1, where a wideband signal on an optical carrier and an optical frequency comb are combined at the input of the grating channelizer and spatially dispersed onto a detector array. Details of the coherent optical channelizer system design can be found in [7]. An optical frequency comb is used to provide a local oscillator in each channel to down convert the signal to an intermediate frequency (IF) for signal processing. To achieve efficient heterodyne detection, the incoming signal carrier and the local oscillator must be phase coherent with each other. The local oscillator must also be able to follow the frequency drift of the optical carrier of the incoming signal to minimize the phase noise in the IF signal. By exploiting the parallel nature of optics, an instantaneous bandwidth larger than 100 GHz can be achieved with a very high POI. The key technical issues of the channelizer to be discussed in this paper are: 1) optical frequency comb generation and 2) establishing phase coherence between the optical frequency comb and optical carrier by optical injection locking.

III. Frequency Comb Generation

Methods used to generate an optical frequency comb (OFC) include the resonant waveguide modulator, where the modulator is made resonant at a particular frequency to enhance the modulation depth [8]. The output will then consist of harmonics spaced at multiples of the modulation frequency. However, the sidebands generated drop off rather quickly. As a result the amplitudes of the frequency comb varies by several orders of magnitude, which is undesirable for an optical channelizer. Since the modulator is made resonant at a particular frequency, changing the frequency comb spacing is rather difficult and the required RF power is still quite large. Supercontinuum generation has also been used to generate frequency combs with a bandwidth of several THz [9, 10]. However, this nonlinear process requires very high optical powers and long lengths of fiber to enhance the nonlinearity. The phases of the individual modes are also very sensitive to power fluctuations.

An alternative method for comb generation is to use an Erbium doped fiber amplifier (EDFA) to amplify and recirculate the output of a phase modulator [11]. However, the recirculating loop forms a long ring cavity which requires the comb spacing to be an integral multiple of the mode spacing. An extension of this approach is the mode-locked fiber laser, where an electro-optic intensity modulator is used. Typical cavity lengths of a fiber laser is on the order of 20 meters or more, corresponding to a mode-spacing on the order of 10 MHz. Therefore, to generate a comb spacing of 1 GHz would require the suppression of 99 modes between the teeth of the OFC. Typical mode suppression is on the order of 40 dB optically [12], which will limit the dynamic range of the channelizer.

Another approach to generating an optical frequency comb is to use a mode-locked semiconductor laser [13, 14]. The length of an external cavity laser can be made substantially shorter than that of a fiber laser, therefore, fundamental operation can be achieved at frequencies above 1 GHz.

IV. External Cavity Mode-Locked Semiconductor Laser for Optical Comb Frequency Generation

To generate the desired frequency comb, a hybrid mode-locked external cavity semiconductor laser is constructed with a 15 cm cavity length to achieve a mode spacing

of 1 GHz. (Fig. 2(a)) A multi-quantum well etched mesa buried heterostructure (EMBH) laser is anti-reflection (AR) coated with a multi-layer dielectric coating on one facet. An aspheric lens is used to couple the output into an external cavity consisting of a plane metal mirror. Wavelength tuning is achieved using an intracavity etalon with a full width half maximum (FWHM) bandwidth of 5 nm. The EMBH laser is divided into three separate sections (Fig. 2(b)). The longest section is used as the gain and the two small sections near the facets are either reverse biased as a saturable absorber or modulated with a synthesizer. By comparing L-I curves before and after the AR coating, the reflectivity is estimated to be less than 1%.

Typical CW output power in the external cavity configuration is 1 mW centered at 1550 nm. By angle tuning the intracavity etalon the center wavelength can be tuned from 1540 nm to 1580 nm. The use of an etalon allows wavelength tuning without a significant change in cavity length as opposed to using a tilted grating end reflector. The etalon also limits the bandwidth of the mode-locked semiconductor laser to increase the power per mode, which is important for channelizer applications. A smaller bandwidth also helps prevent incomplete mode-locking, where certain groups of the spectrum are phase locked, but not phase locked together as a whole and gives rise to coherence spikes in the autocorrelation trace [15, 16].

Hybrid mode-locking of the external cavity laser is employed, where a saturable absorber and loss modulation are utilized together [17-19]. In a hybrid mode-locked laser, the saturable absorber performs the majority of the pulse-shaping process and the RF modulation is used to provide a timing reference. Passively mode-locked lasers tend to have large timing jitter due to the lack of an external reference. By introducing a small modulation section the timing jitter can be reduced significantly. Actively mode-locked semiconductor lasers typically require more than 25 dBm of modulation power and produce highly chirped pulses. Whereas in a hybrid mode-locked scheme, a relatively low RF power of 5 dBm is adequate.

V. Mode-Locked Laser Experimental Results

The output of the hybrid mode-locked external cavity laser is measured with a non-collinear autocorrelator. Fig. 3(a) shows the autocorrelation trace of the pulses with a

deconvolved pulsewidth of 2.4 ps. Neglecting the modulation depth in the optical spectrum, the bandwidth of the pulse is approximately 137 GHz centered at a nominal wavelength of 1550 nm. (Fig. 3(b)) This corresponds to a time-bandwidth product of 0.328, which is very close to the transform limit of 0.3148 for a sech^2 pulseshape [15]. By angle tuning the intracavity etalon, the center wavelength can be tuned to precisely overlap the detector array of the optical channelizer. A tuning range larger than 20 nm has been achieved while maintaining nearly transform limited pulsewidths of less than 3 ps. (Fig. 4)

An imperfect AR coating modulates the gain spectrum by the monolithic mode spacing (Fig. 3(b)), which translates to trailing pulses in the time domain [16]. The imperfect AR coating also increases the likelihood of exciting higher order supermodes which can lead to pulse break up and longer pulsewidths [16]. These trailing pulses can be eliminated by either perfecting the AR coating, employing angled waveguide structures, or an intracavity saturable absorber [20].

Typical average mode-locked power is -8 dBm, corresponding to approximately 1 μW per mode. The output power is limited by the saturation energy of the monolithic saturable absorber, typically on the order of 1 pJ. Higher average powers can be obtained by replacing the external mirror with a saturable Bragg reflector (SBR) [21, 22]. The saturable absorber can then be placed in its most effective position, as well as increasing the saturation energy resulting in higher power per mode and a narrower linewidth. Recent experiments have demonstrated an external cavity mode-locked semiconductor laser using a SBR with compressed pulsewidths as short as 570 fs [23].

VI. Injection Locking of a Mode-Locked Laser for Carrier Tracking

Optical injection locking is a viable technique to stabilize two, free running lasers without the use of high speed electronics. This technique offers a large locking bandwidth whereas electronic phase lock loops are limited by the electrical bandwidth and inherent loop delay [24-26]. The RF phase noise performance of two injection locked CW lasers can be as low as -125 dBc/Hz at 100 kHz offset [27], which is comparable to high performance synthesizers. More recently injection locking of mode-locked semiconductor lasers has spurred new interest in temporal synchronization and in

controlling the spectral qualities of mode-locked lasers. Three variations of this injection locking technique have been reported: 1) Mode-locked master laser injected into mode-locked slave laser; 2) CW master laser injected into a mode-locked slave laser; and 3) Mode-locked master injected into several CW slave lasers.

Variant 1 of this injection locking scheme offers both spectral and temporal control of the mode-locked slave laser [28], and can be viewed as a form of multi-mode injection locking. Variant 2 is very useful for phase locking the output of the mode-locked laser with a single frequency master laser. This method can be used to select a particular supermode of a harmonic mode-locked laser [29] and also be used to stabilize a passively mode-locked slave laser without direct modulation [30]. Linewidth narrowing of the optical frequency comb has also been observed using this technique [31]. Variant 3 is relatively new and offers a new method to phase lock several free running CW lasers for photonic oscillator applications [32]. In this paper we will discuss our results for the second scheme and show that this can serve as carrier tracking of the incoming signal.

Fig. 5 shows a schematic layout of the experimental setup for CW injection locking of the mode-locked slave laser. An external cavity laser is used as the master laser. The output is split with one arm directed to an acousto-optic frequency shifter, and the other arm is attenuated and injected into the mode-locked slave laser via an optical circulator. Polarization controllers are utilized in the injection arm and in the detection arm. A delay line is introduced into the heterodyne arm to minimize the excess phase noise found in heterodyne detection schemes [33].

When the master laser is injected into one of the modes of the slave laser, phase coherence is established between the master and that particular mode, similar to CW optical injection locking. Since in a mode-locked laser where all the modes are phase locked, the whole frequency comb is phase coherent with the slave laser. The modes of the slave laser can also be slightly pulled from the free running frequency. To detect this phase coherence and mode-pulling phenomena, the heterodyne detection scheme of Fig. 6 is used.

When detected with a high speed photodetector and RF spectrum analyzer, harmonics of the mode-locked laser can be seen at multiples of 1 GHz. In addition, tones spaced 55 MHz from the harmonics can be observed, as shown in Fig. 7(a)-(d). These tones are due

to the heterodyne of the frequency shifted master with the modes of the mode-locked laser.

In Fig. 7(a)-(d), sidebands at 945 MHz and 1055 MHz indicate that the modes adjacent to the injected mode are phase coherent with the master laser. The sidebands at 9.945 GHz and 10.055 GHz indicate the modes that are 10 GHz away from the injected mode are phase coherent with the master laser. These tones can be observed up to 19 GHz indicating that the two modes 19 GHz away from the injected mode are also phase coherent with the master laser. This corresponds to the supermode behavior where the optical spectrum of a mode-locked laser operates as a quasi-single mode [34-36]. For comparison, figure 7(e) shows the free running beat tone of a filtered mode 6 GHz apart from the CW master laser. The free running tone is relatively broad indicating that the lasers are incoherent. The harmonics of the mode-locked laser are also observed due to the finite finesse of the filter used.

The first parameter of interest is how the pulse characteristics change with injected optical power. When the laser is well mode-locked using the hybrid technique, the autocorrelation trace shows 100% modulation depth in the pulses. (Fig. 8(a)) Again, trailing pulses are observed due to the imperfect AR coating. Taking the autocorrelation trace over a full scan of 100 ps shows that there is also no slow varying substructure. The master laser is then tuned to the center wavelength of the mode-locked laser until injection locking is observed on the RF spectrum analyzer. Autocorrelation traces are then taken at various injected optical powers while injection locked. The pulsewidth and pulse shape show little change at low optical injection levels. At injected optical powers comparable to the external average mode-locked power, the balance between gain and saturable absorption is greatly perturbed. This gives rise to a broader pulsewidth and an increase in substructure. (Figs. 8(a)-(c)). Fig. 9 shows the pulsewidth versus the injected optical power. When the injected optical power is much larger than the average power of the mode-locked laser, the optical injection tends to force the slave laser to operate as a double pass amplifier.

VII. Physics of Injection Locking of a Mode-Locked Laser

Active mode-locking is achieved by using a modulator to couple the individual modes of the laser. The modulator modulates the cavity modes at approximately the cavity mode spacing and generates sidebands. These sidebands are coupled into the adjacent cavity modes and create phase coherence throughout the spectrum [37, 38]. (Fig. 10(a)) Similarly, when the master laser is injected into a mode of the slave laser, phase coherence is established with that particular mode. This mode is then modulated to generate sidebands which are phase coherent with the master laser. These sidebands then couple into adjacent modes throughout the spectrum to establish phase coherence between the mode-locked slave laser and master laser. The evidence of sideband generation can be observed using a high resolution scanning Fabry-Perot. Fig. 10(b) shows the injected light that is far away from a cavity mode and thus not injection locked. The sidebands generated by the modulation of the injected light are shown and have comparable power due to the inherent gain in the medium.

Similar results have been published in [30], where a double side-band suppressed carrier (DSB-SC) signal is used to stabilize a passively mode-locked distributed Bragg reflector (DBR) laser. The DSB-SC signal will inject into two modes of the mode-locked laser and establish phase coherence. Also, the frequency spacing of the DSB-SC signal will pull the slave laser mode spacing and thus alter the repetition rate. Fig. 10(b) shows similar results where the modulation section of the monolithic laser does the sideband generation.

The locking bandwidth can be determined by simultaneously tuning the wavelength of the master laser and monitoring the heterodyne tones on the RF spectrum analyzer. The locking bandwidth is defined as the tuning range such that injection locking tones can be seen up to 5 GHz. By monitoring the heterodyne tones at frequencies up to 5 GHz, the generated sidebands from the injected mode would not contribute to the heterodyne tones in Fig. 7(a)-(c) since powers of higher harmonics drop off rapidly with harmonic number. Therefore the heterodyne tones are due to the beating of the frequency comb with the frequency shifted master, not with the generated sidebands. Fig. 11 shows the total locking range at various injection levels and is shown to increase with increasing injected

optical power, similar to that of CW injection locking. The average external mode-locked power in this case was -6 dBm.

The entire frequency comb does not pull uniformly; modes far away are not affected significantly by the injected light. This is evident in the heterodyne detection RF spectrum. The tones at 19 GHz are much more sensitive to tuning of the master laser, indicating modes far away are not well locked. Due to the imperfect AR coating ($\approx 1\%$), the gain profile is modulated by the monolithic mode spacing and gives rise to multiple supermodes. Fig. 12 shows the pulling of the frequency comb. With an injection ratio of -15 dB, the modes can be pulled approximately 400 MHz, which gives a total locking range of 800 MHz. The locking range cannot be larger than the mode spacing (1 GHz) since there will be a mode within 500 MHz of the injected signal. Locking range appears to be symmetric, whereas injection locking of CW lasers results in an asymmetric locking range skewed towards negative frequency detuning [39, 40]. A larger mode spacing, which eliminates the effects of neighboring modes, is required to determine the exact symmetry of the locking range. This can be achieved with monolithic mode-locked semiconductor lasers. Similar to injection locking of CW lasers, the locking range is expected to be a function of the cavity Q and the operating point of the laser. Again, the low average power of the mode-locked laser indicates that the laser is slightly above threshold and is limited by the saturation intensity of the saturable absorber. Also shown in Fig. 12 is an increase in power of the injected mode due to optical injection; at sufficiently high optical injection levels, this single mode will dominate and the slave laser will operate as a single mode laser, similar to a double pass amplifier.

Since the laser is hybrid mode-locked, it is difficult to characterize how much pulse shaping the saturable absorber is doing compared to the modulator section. To achieve mode-locking, the reverse bias on the saturable absorber is increased until nearly 100% modulation depth of the pulses is observed in the autocorrelation trace. When this condition was obtained, a RF drive of less than +10 dBm is applied to help stabilize the pulses. Due to the large impedance mismatch between the microwave probe and the laser (measured $Z_{in} = 5 + j25$), less than 25% of the RF power is used to drive the laser. A larger spectral pulling range is expected for passively mode-locked lasers than for actively mode-locked lasers.

VIII. Discussion

We have demonstrated that CW injection locking of a hybrid mode-locked external cavity semiconductor laser can provide a local oscillator frequency comb for an ultra-wide band coherent optical channelizer. Nearly transform limited pulses were obtained over a tuning range of 24 nm. Pulsewidths less than 2.5 ps were obtained. This corresponds to a signal bandwidth which can process signals with bandwidths greater than 100 GHz. CW injection locking of a hybrid mode-locked laser is implemented to achieve phase coherence between the incoming carrier signal and the local oscillator. The coherence between the carrier laser and the optical frequency comb is dependent on how well the modes of the mode-locked laser are phase locked. Injection locking is also shown to be able to pull the optical frequency comb by as much as 400 MHz (corresponding to a total locking bandwidth of 800 MHz), which allows the local oscillator to track small frequency drifts in the carrier signal. Only at injection levels comparable to the average power of the mode-locked laser do the pulses begin to distort and break up.

Optical injection locking of mode-locked semiconductor lasers opens up many new applications in optical communication systems. This technique is not limited to the use of semiconductor lasers and is expected to be observable in other laser systems. An alternative for a local oscillator laser source would be the new micro-chip lasers utilizing a diode pumped Er:Glass gain medium. The use of a compact gain medium allows relatively short cavities for fundamental operation at a frequency of 1 GHz, and eliminates the problem of side mode suppression in harmonic mode-locking. Besides coherent channelization of broadband signals, injection locking of a mode-locked laser can also be used as a frequency reference for dense wavelength division multiplexing systems.

IX. Acknowledgement

We would like to acknowledge the help of Roosevelt Johnson of the Photonics Technology Department, TRW for his help with the lasers used. Tai Chau and Rich Chen of the Integrated Photonics Lab, UCLA for their help with the AR coating. Prof.

Mario Dagenais and Yimin Hsu of the Photonics Switching and Integrated Optoelectronics Lab, University of Maryland, for the high performance AR coatings. This work was supported by DARPA under contract F30602-96-C-0273, and administered by James Nichter of Rome Labs.

REFERENCES

- [1]. R.P. Braun, G Grosskopf, D. Rohde, and F. Schmidt, "Low phase noise millimeter-wave generation at 64 GHz and data transmission using optical sideband injection locking", *IEEE Photonics Technology Letters*, vol. 10, no. 5, pp. 728-731, May 1998
- [2]. G.W. Anderson, D.C. Webb, A.E. Spezio, and J.N. Lee, "Advanced channelization technology for RF, microwave, and millimeterwave applications", *Proceedings of the IEEE*, vol. 79, no. 3, March 1991.
- [3]. S. Gopani, R. Mouton, R. Hays, R. Almar, J. Vandendriessche, and M. Garrity, "State of the art SAW channelizer for EW receiver application", *IEEE Ultrasonics Symposium 1994*, p. 55-60.
- [4]. D.L. Hecht, "Spectrum analysis using acousto-optic devices", *Optical Engineering*, vol. 16, no. 5, pp. 461-466, Sept.-Oct. 1977.
- [5]. R.A. Coppock, R.F. Croce, "Wideband optical channelizer for simultaneous frequency and direction finding", *Proceedings of the Society of Photo-Optical Instrumentation Engineers*, vol.214 - Acousto-Optic Bulk Wave Devices, pp. 124-129.
- [6]. T.K. Yee, C.H. Chalfant, J.F. Coward, J.R. Titus, H.E. Morrow, D. Henderson, J.T. Salsman, D. Pechner, J.L. Newell, S. Strunk, and K.M. Morrisroe, "A high

dynamic range wideband heterodyne acousto-optical channelizer", *IEEE Ultrasonics Symposium 1989*, p. 491-494.

- [7]. R. L. Davis, R. Lodenkamper, T. Jung, W. Wang, M. Flannery, J. Yun, L.J. Lembo, and J.C. Brock, "The design and performance of a grating -based, coherent optical, wideband RF signal channelizer", *The Ninth Annual DARPA Symposium on Photonic Systems for Antenna Applications (PSAA-9)*, Monterey, California, Feb 17-19, 1999.
- [8]. T. Saitoh, M. Kourogi, and M. Ohtsu, "A waveguide-type optical-frequency comb generator", *IEEE Photonics Technology Letters*, vol. 7, no.2, pp. 197-200, February 1995.
- [9]. T. Morioka, K. Mori, S Kawanishi, and M. Saruwatari, "Multi-WDM -channel, Gbit/s pulse generation from a single laser source utilizing LD-pumped supercontinuum in optical fibers", *IEEE Photonics Technology Letters*, vol. 6, no. 3, pp. 365-8, March 1994.
- [10]. G. A. Sefler and K. Kitayama, "Frequency comb generation by four-wave mixing and the role of fiber dispersion", *IEEE Journal of Lightwave Technology*, vol. 16, no. 9, pp. 1596-1605, September 1998.
- [11]. K.P. Ho, and J.M. Kahn, "Optical frequency comb generator using phase modulation in an amplified circulating loop", *IEEE Photonics Technology Letters*, vol. 5, no. 6, pp. 721-5, June 1993.
- [12]. Pritel Inc., Product brochure for active mode-locked fiber laser.
- [13]. Laser Physics, M. Sargent III, M.O. Scully, and W.E. Lamb, Addison Wesley, Reading, Mass., Ch. 3 - 12.

- [14]. Lasers, A.E. Siegman. University Science Books, Mill Valley, CA, 1986, pp. 1050-1128.
- [15]. J.P. van der Ziel, "Mode-locking of semiconductor lasers", *Semiconductors and Semimetals*, vol. 22, Part B, W.T. Tsang, Ed., Academic Press, Orlando, Florida, 1985, Ch. 1.
- [16]. H. Haus, "Theory of mode-locking in an external resonator", *J. Appl. Phys.*, vol. 51, pp. 4042-4049, 1980.
- [17]. Y.K. Chen and M.C. Wu, "Monolithic colliding-pulse mode-locked quantum-well lasers", *IEEE Journal of Quantum Electronics*, vol. 28, no. 10, pp. 2176-2185, October 1992.
- [18]. D.J. Derickson, et al., "Short pulse generation using multisegment mode-locked semiconductor lasers", *IEEE Journal of Quantum Electronics*, vol. 28, no. 4, March 1992
- [19]. H.A. Haus and H.L. Dyckman, "Timing of laser pulses produced by combined passive and active mode-locking", *International Journal of Electronics*, vol. 44, pp. 225-238, 1978.
- [20]. D.J. Derickson, R.J. Helkey, A. Mar, J.R. Karin, and others, "Suppression of multiple pulse formation in external-cavity mode-locked semiconductor lasers using intrawaveguide saturable absorbers", *IEEE Photonics Technology Letters*, vol.4, no. 4, pp. 333-335, April 1992.
- [21]. S. Tsuda, W.H. Knox, S.T. Cundiff, W.Y. Jan, and J.E. Cunningham, "Mode-locking ultrafast solid-state lasers with saturable Bragg reflectors", *IEEE Journal of Selected Topics in Quantum Electronics*, vol. 2, no. 3, pp. 454-464, September 1996.

- [22]. U. Keller, et al., "Semiconductor saturable absorbers mirrors (SESAM's) for femtosecond to nanosecond pulse generation in solid-state lasers", *IEEE Journal of Selected Topics in Quantum Electronics*, vol. 2, no. 3, pp. 435-453, September 1996.
- [23]. J.L. Shen, T. Jung, D.T.K. Tong, T. Chau, S. Murthy, M.C. Wu, Y.H. Lo, C.L. Chua, and Z.H. Zhu, "Mode-locking of external cavity semiconductor lasers with saturable bragg reflectors", submitted to *Journal of the Optical Society of America B*.
- [24]. R.T. Ramos and A.J. Seeds, "Delay, linewidth, and bandwidth limitations in optical phase-locked loop design", *Electronics Letters*, vol. 26, no. 6, pp. 389-391, March 15, 1990
- [25]. R.T. Ramos, P. Gallion, D. Erasme, A.J. Seeds, and A. Bordonalli, "Optical injection locking and phase-lock loop combined systems" *Optics Letters*, vol.19, no.1, pp. 4-6, Jan. 1, 1994.
- [26]. C. Walton, A.C. Bordonalli, and A.J. Seeds, "High-performance heterodyne optical injection phase-lock loop using wide-linewidth semiconductor lasers", *IEEE Photonics Technology Letters*, vol. 10, no. 3, pp. 427-429, September 1996.
- [27]. R. Lodenkamper, T. Jung, R. Davis, L.J. Lembo, M.C. Wu, and J.C. Brock, "RF Performance of Optical Injection Locking", *Proceedings of the SPIE – The International Society for Optical Engineering*, 1998, vol. 3463, no. 29.
- [28]. M. Margalit, M. Orenstein, G. Eisenstein, and V. Mikhaelshvili, "Injection locking of an actively mode-locked semiconductor laser", *Optics Letter*, Dec. 15, 1994, vol. 19, no. 24, pp. 2125-7.
- [29]. Y. Katagiri, A. Takada, "Supermode selection of a subterahertz-harmonic colliding-pulse mode-locked semiconductor laser using continuous-wave light

- injection", *IEEE Photonics Technology Letters*, vol. 9, no. 12), pp. 1564-1566, Dec. 1997.
- [30]. Z. Ahmed, H.F. Liu, D. Novak, Y. Ogawa, M.D. Pelusi, and D.Y. Kim, "Locking characteristics of a passively mode-locked monolithic DBR laser stabilized by optical injection", *IEEE Photonics Technology Letters*, vol.8, no.1, pp. 37-39, January 1996.
- [31]. A. Takada, and W. Imajuku, "Linewidth narrowing and optical phase control of mode-locked semiconductor ring laser employing optical injection locking", *IEEE Photonics Technology Letters*, vol.9, no.10, pp. 1328-30, Oct. 1997.
- [32]. R. Logan, "Photonic Oscillator Concepts", *The Ninth Annual DARPA Symposium on Photonic Systems for Antenna Applications (PSAA-9)*, Monterey, California, Feb 17-19, 1999.
- [33]. M.P. van Exeter, S.J.M. Kuppens, and J.P. Woerdman, "Excess phase noise in self-heterodyne detection", *IEEE Journal of Quantum Electronics*, vol. 28, no. 3, March 1992.
- [34]. J. Au Yeung, "Theory of active mode-locking of a semiconductor laser in an external cavity", *IEEE Journal of Quantum Electronics*, vol. 17, no. 3, pp. 398-403, March 1981.
- [35]. R. Salvatore, S. Sanders, T. Schrans, and A. Yariv, "Supermodes of High-Repetition-Rate Passively Mode-Locked Semiconductor Lasers", *IEEE Journal of Quantum Electronics*, vol. 32, no. 6, pp. 941-952, June 1996.
- [36]. P.T. Ho, "Phase and amplitude fluctuations in a mode-locked laser", *IEEE Journal of Quantum Electronics*, vol. 21, pp. 1806-1815, 1985.

- [37]. O.P. McDuff and S. E. Harris, "Nonlinear theory of the internally loss-modulated laser", *IEEE Journal of Quantum Electronics*, vol. 3, no. 3, pp. 101-111, March 1967.
- [38]. S.E. Harris and O.P. McDuff, "Theory of FM laser oscillation", *IEEE Journal of Quantum Electronics*, vol. 1, no. 6, pp. 245-262, June 1967.
- [39]. F. Mogensen, H. Olesen, and G. Jacobsen, "Locking conditions and stability properties for a semiconductor laser with external light injection", *IEEE Journal of Quantum Electronics*, vol. QE-21, pp. 784-793, 1985.
- [40]. R. Hui, A. D'Ottavi, A. Mecozzi, P. Spano, "Injection locking in distributed feedback semiconductor lasers", *IEEE Journal of Quantum Electronics*, vol. 27, no. 6, pp. 1688-1695, June 1991.

Figure Captions:

Fig. 1. Channelization of wide-band RF signal on optical carrier.

Fig. 2(a). External cavity mode-locked laser configuration.

Fig. 2(b). EMBH multi-quantum well three section laser.

Fig. 3(a). Autocorrelation trace of external cavity hybrid mode-locked laser.

Fig. 3(b). Optical spectrum of hybrid mode-locked laser.

Fig. 4. Pulseswidth at various center wavelengths.

Fig. 5. Experimental setup for injection locking of a mode-locked semiconductor laser.

Fig. 6. Heterodyne detection of injection locked mode-locked laser.

Fig. 7. Heterodyne tones of injection locked mode-locked laser, (a) modes 1 GHz away from injected mode, (b) modes 10 GHz away, (c) modes 15 GHz away, and (d) modes 19 GHz away. Beat tone of filtered free-running mode-locked slave laser and CW master laser (e).

Fig. 8(a)-(c) Autocorrelation trace of mode-locked laser at various injected optical powers: (a) Autocorrelation trace of mode-locked laser with no optical injection. (b) Autocorrelation trace of mode-locked laser with -12.5 dBm injected optical power. (c) Autocorrelation trace of mode-locked laser with -9.5 dBm injected optical power.

Fig. 9. Pulsewidth at various optical injection levels.

Fig. 10(a) Sideband generation in a mode-locked laser.

Fig. 10(b) Generation of sidebands from injected mode; injected signal (i), generated sidebands (ii).

Fig. 11. Locking range at various injected optical powers.

Fig. 12. Pulling of mode-locked laser modes.

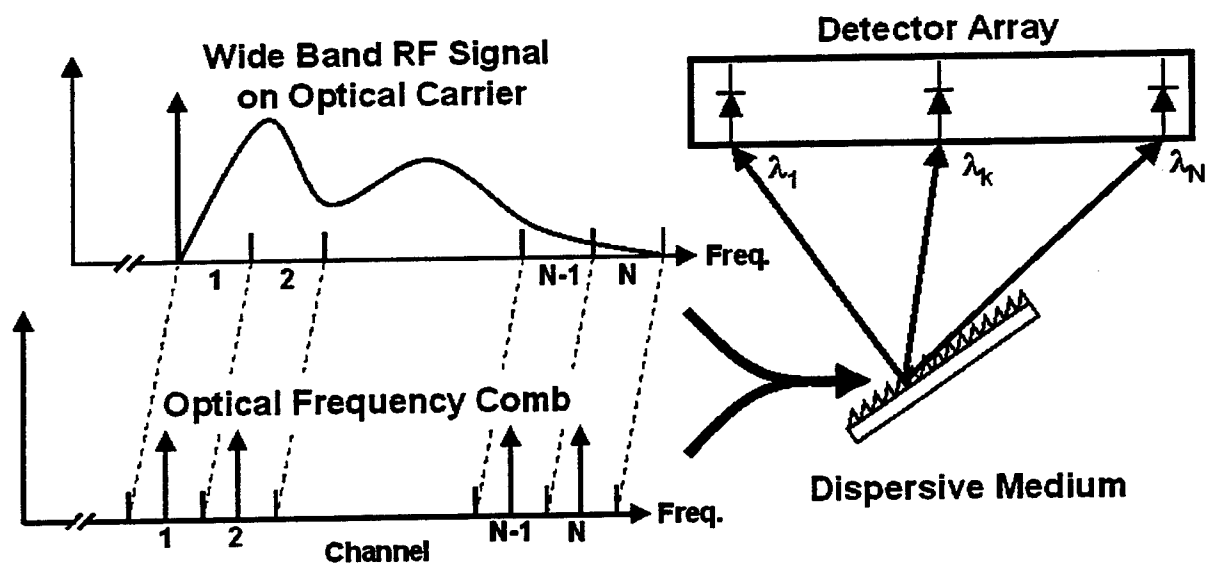


Fig. 1

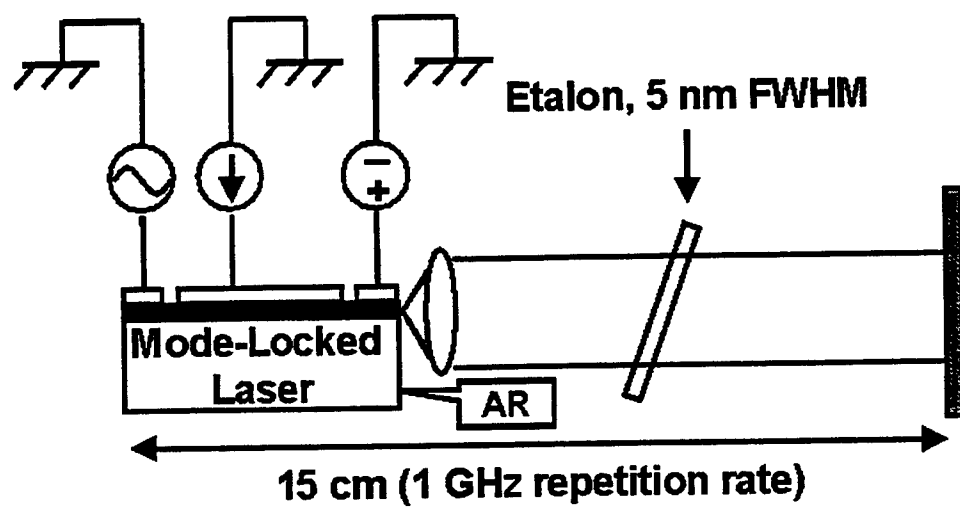


Fig. 2(a)

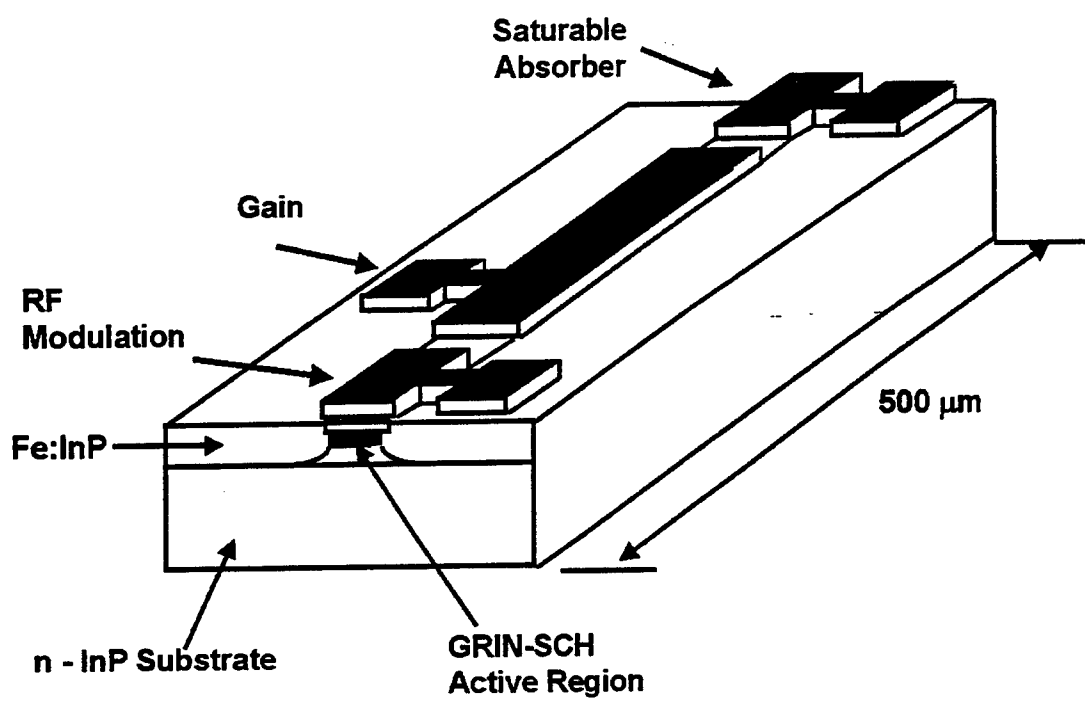


Fig. 2(b)

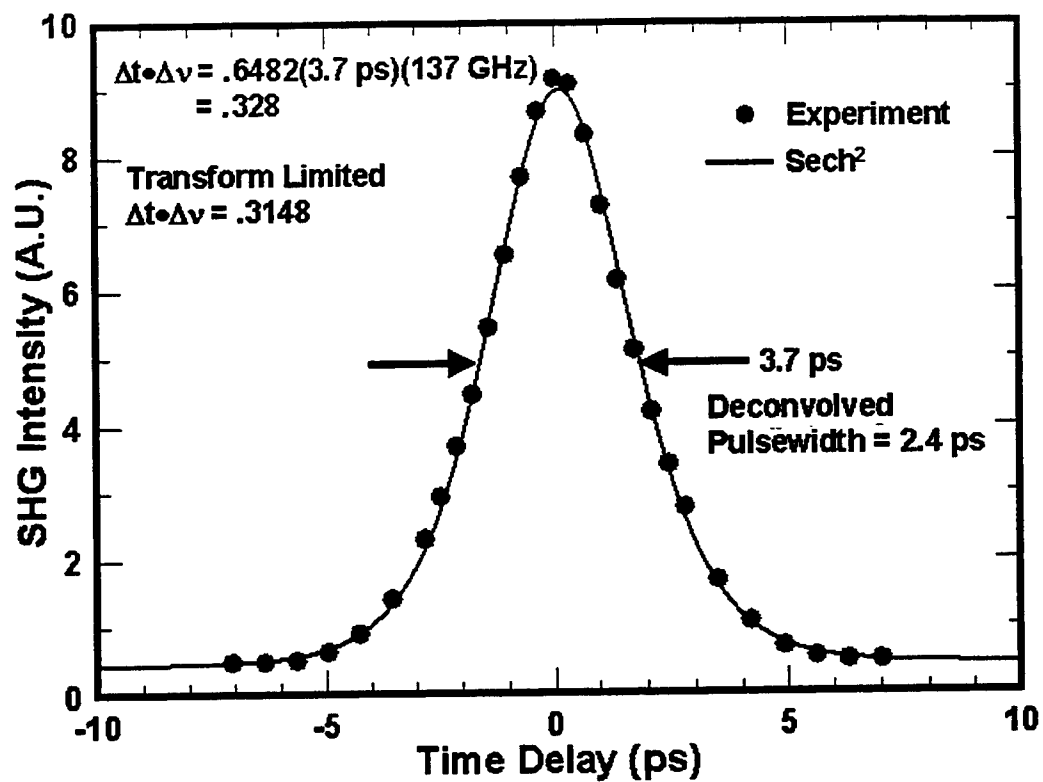


Fig. 3(a)

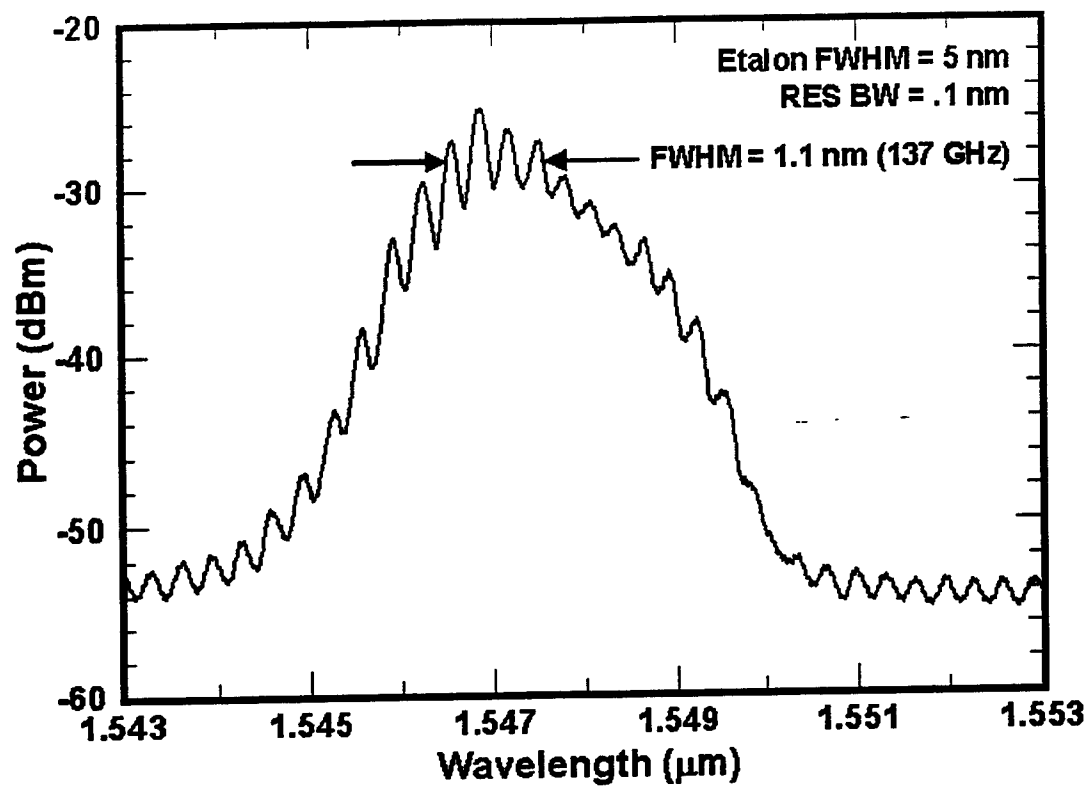


Fig. 3(b)

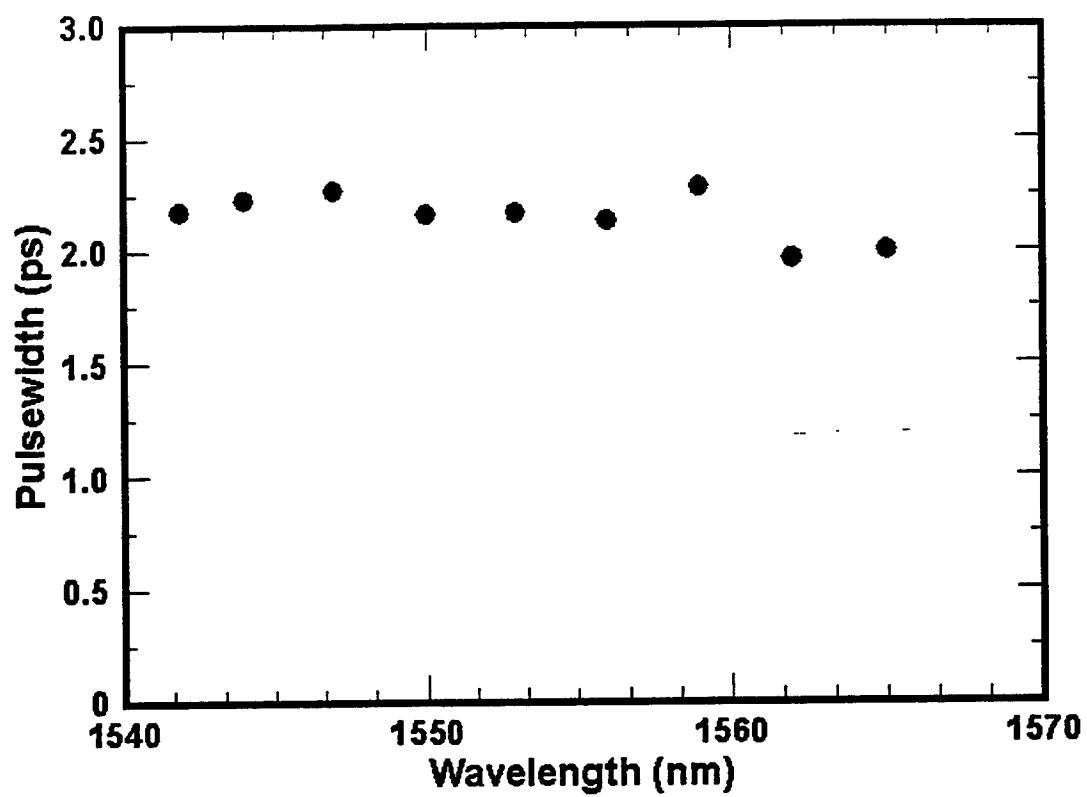


Fig. 4

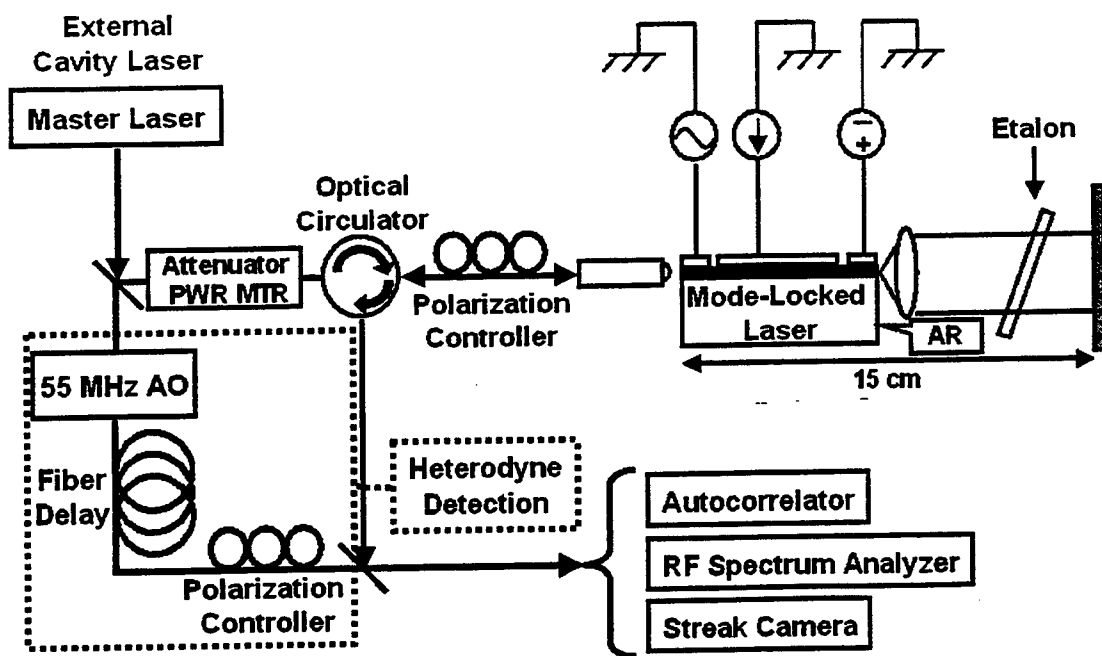


Fig. 5

Optical Frequency Comb

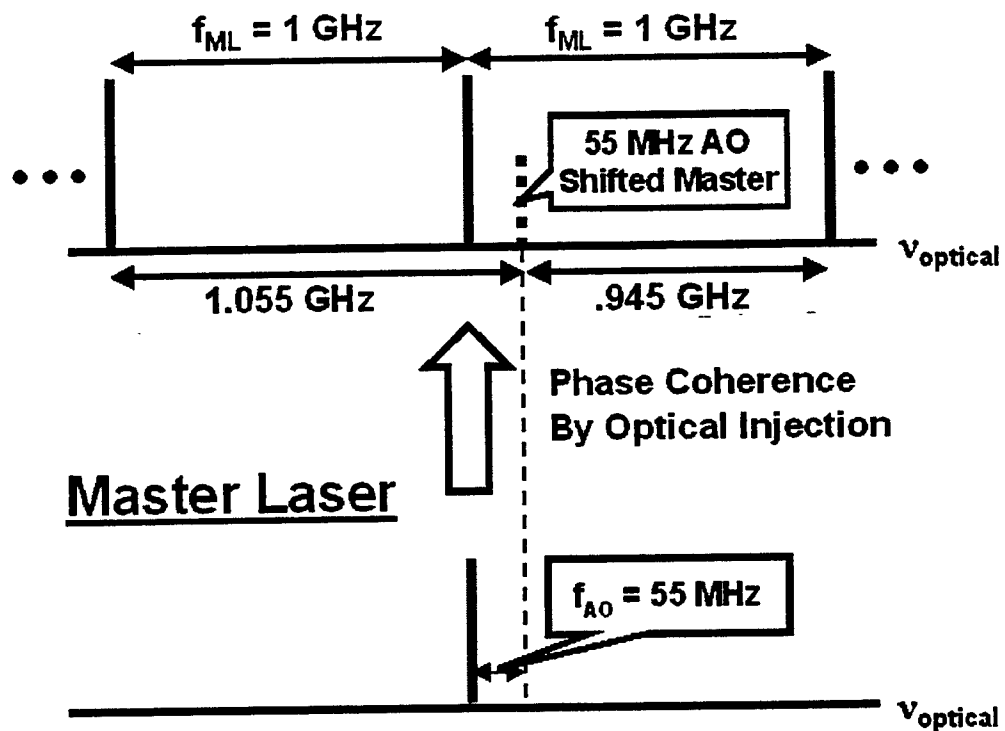


Fig. 6

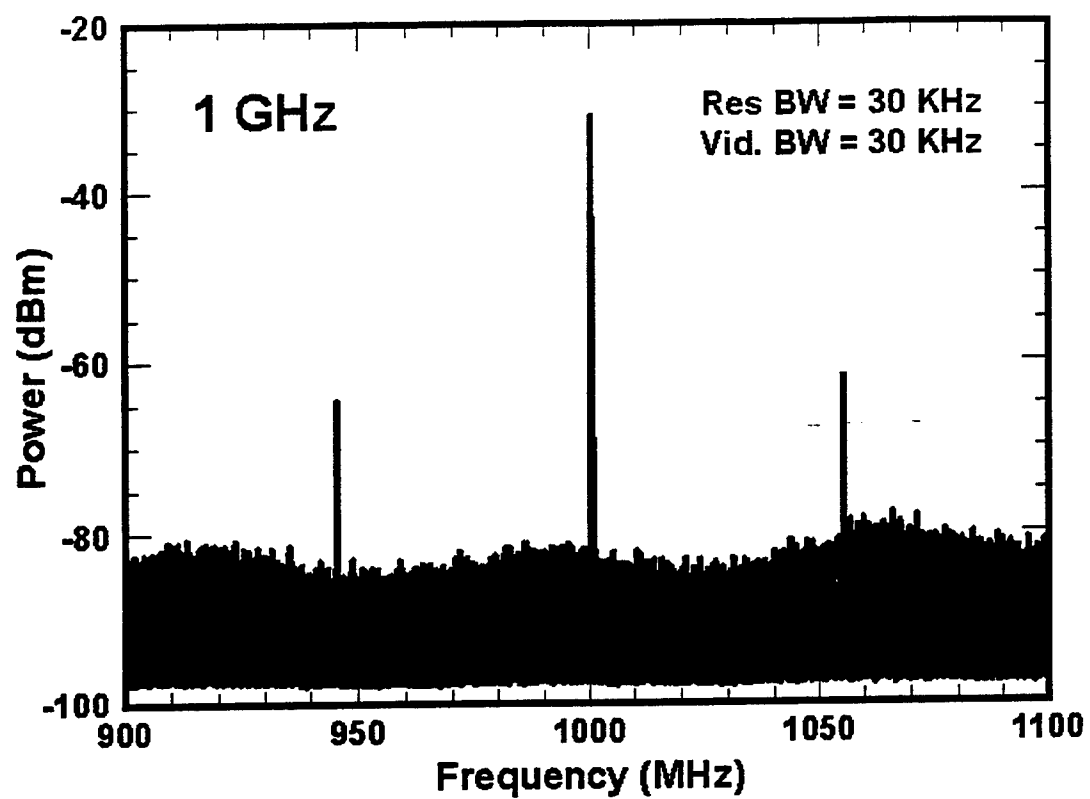


Fig. 7(a)

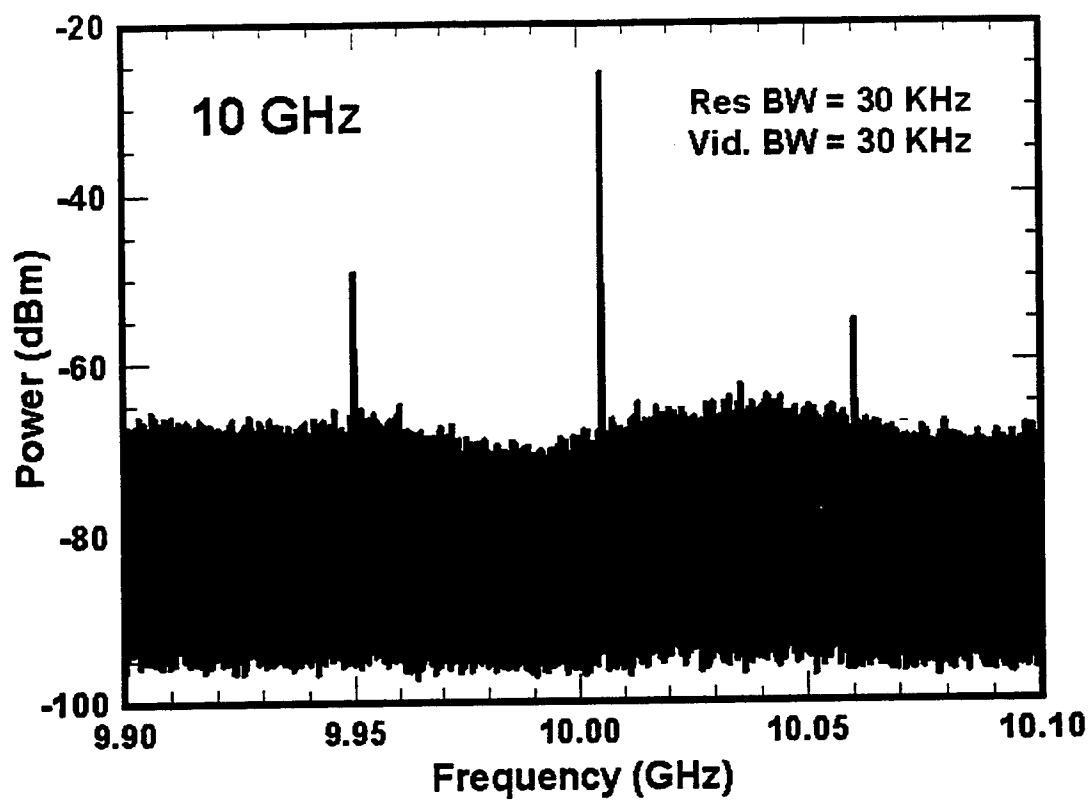


Fig. 7(b)

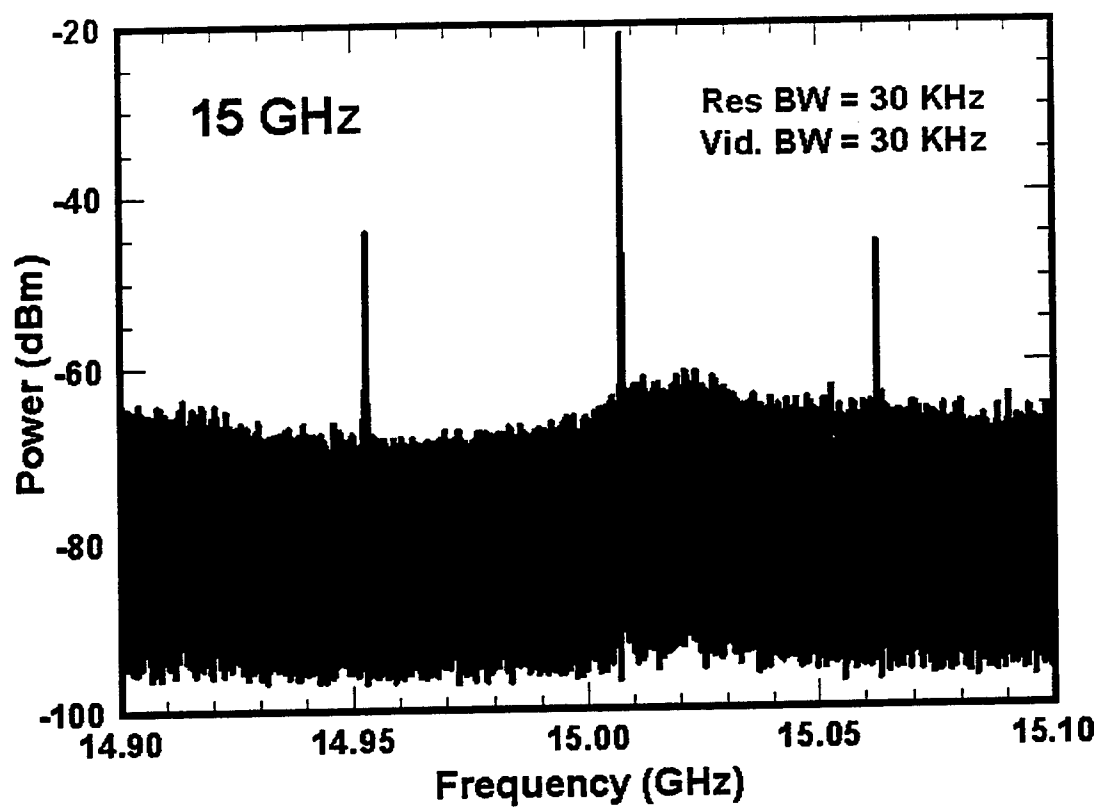


Fig. 7(c)

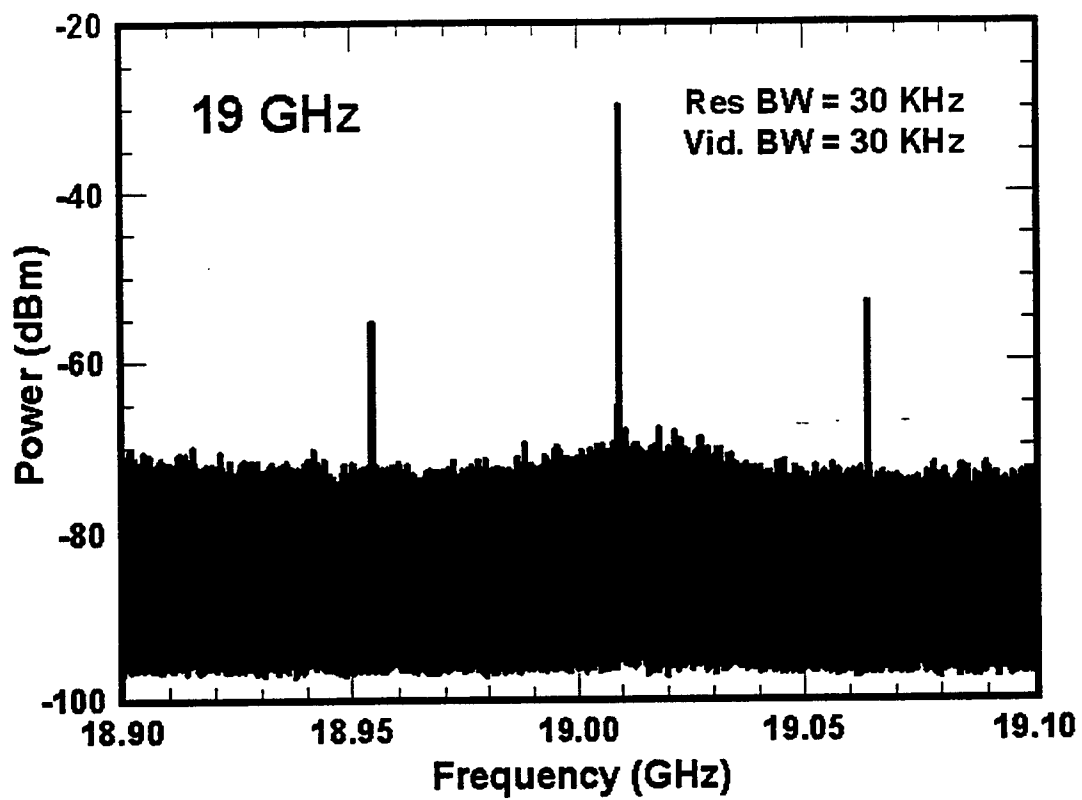


Fig. 7(d)

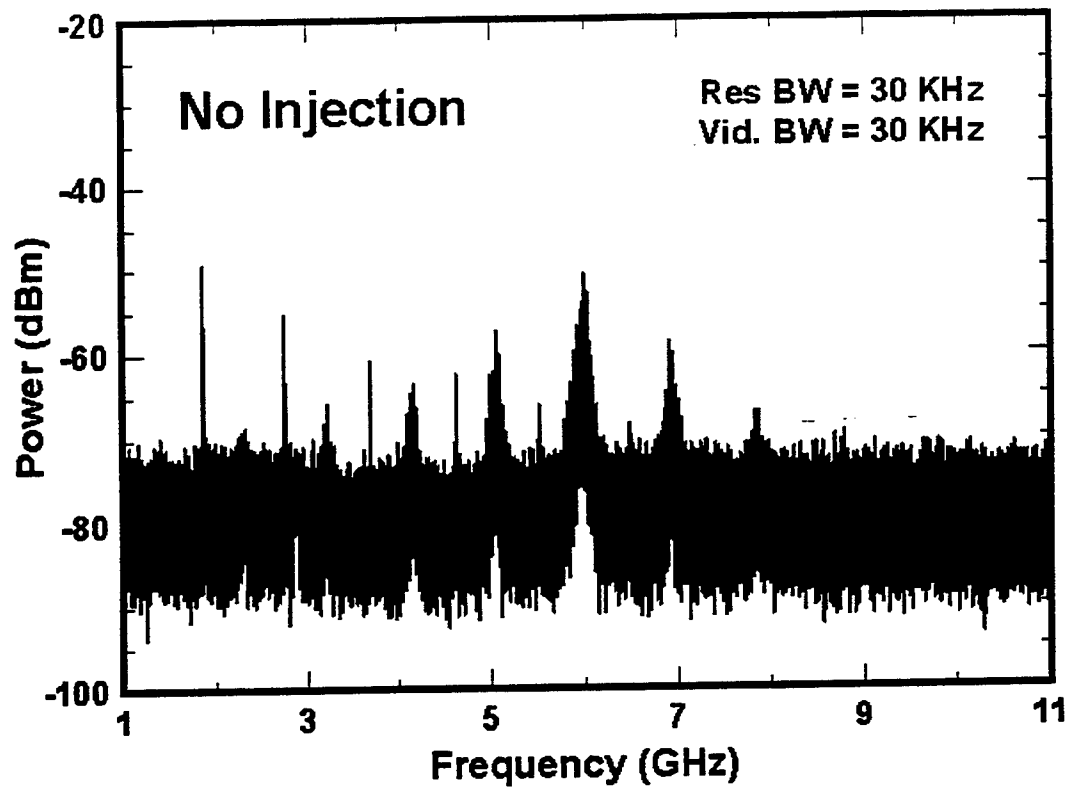


Fig. 7(e)

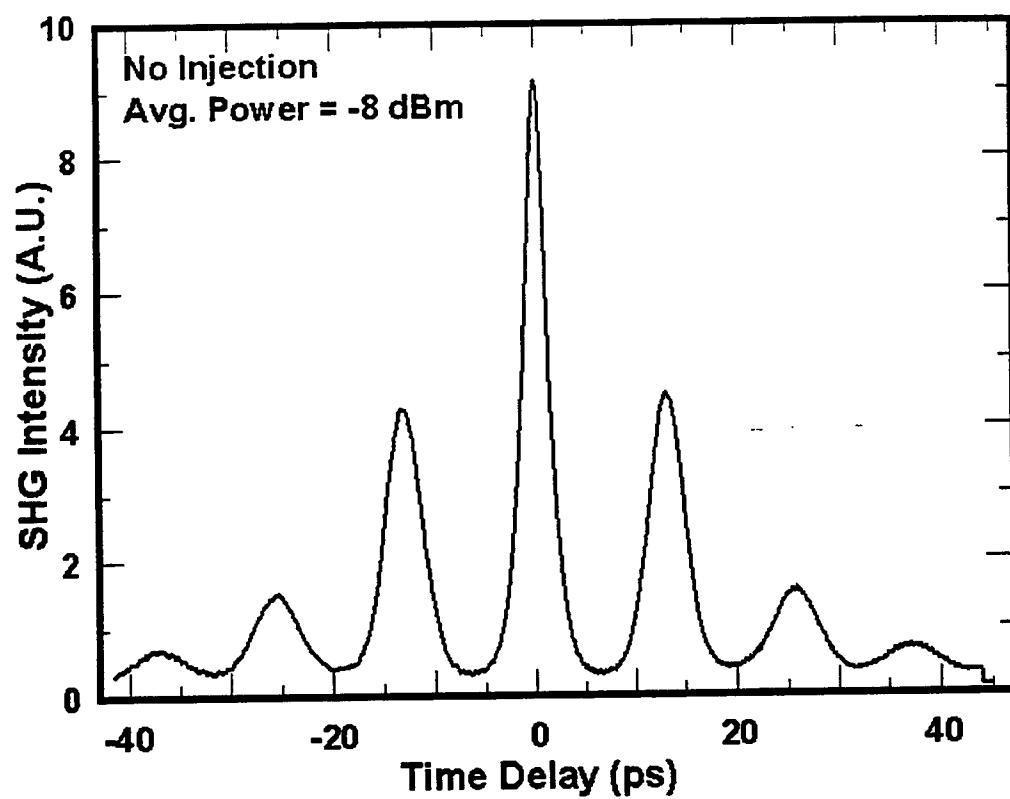


Fig. 8(a)

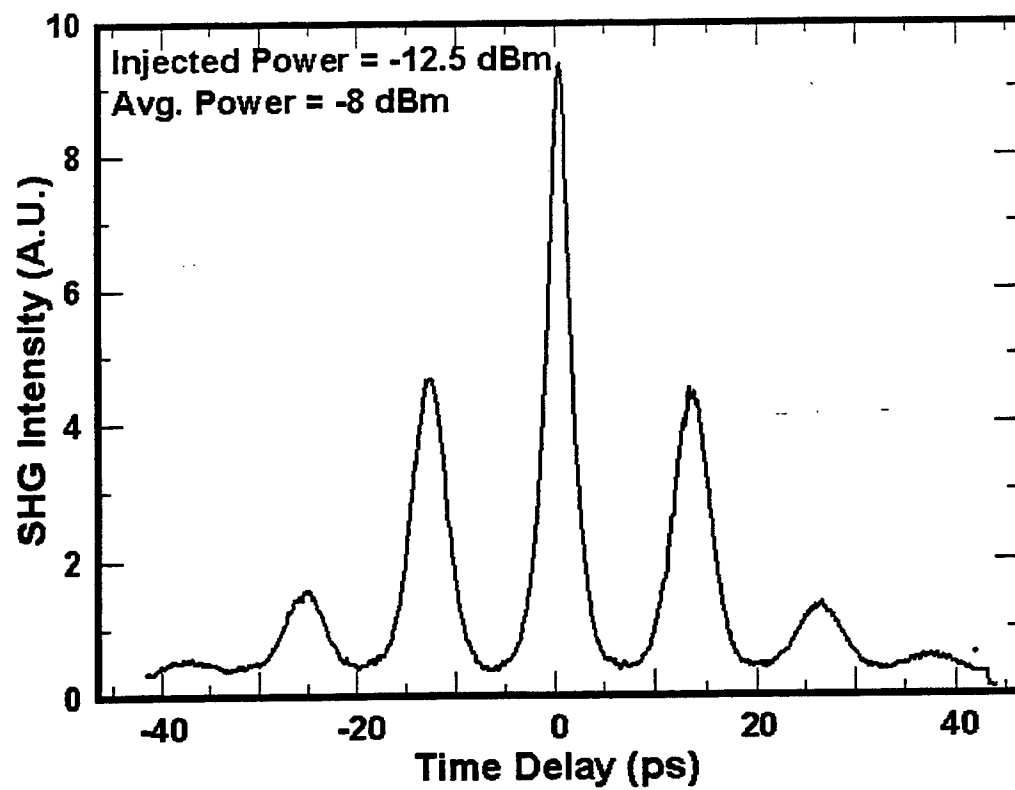


Fig. 8(b)

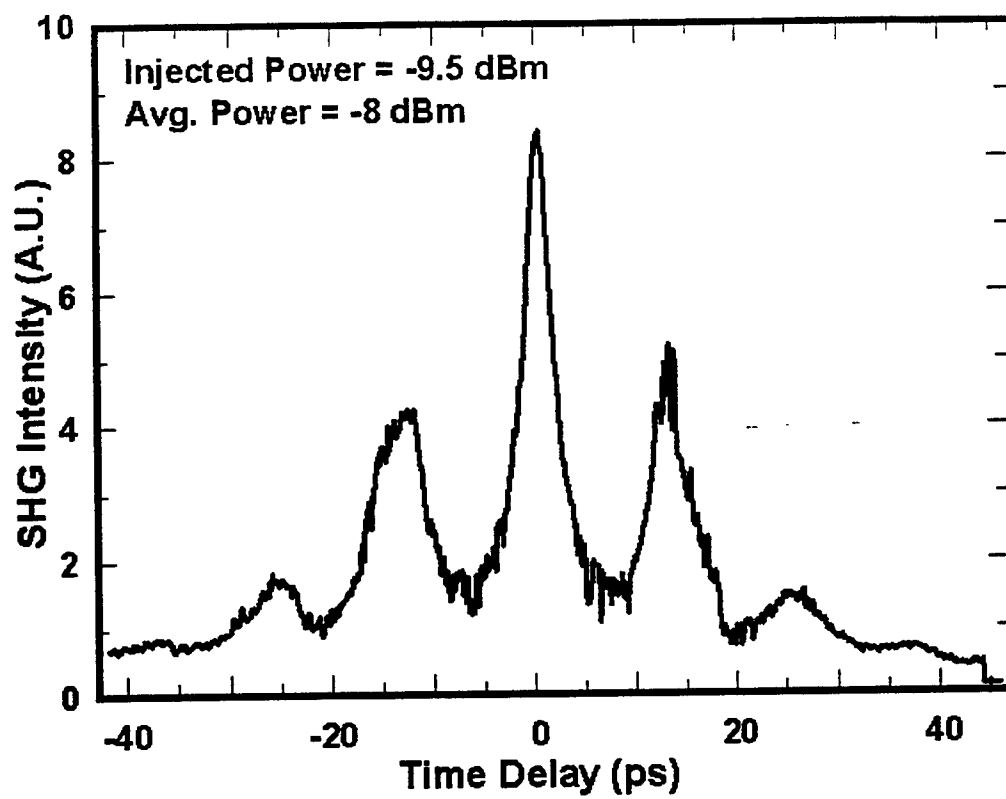


Fig. 8(c)

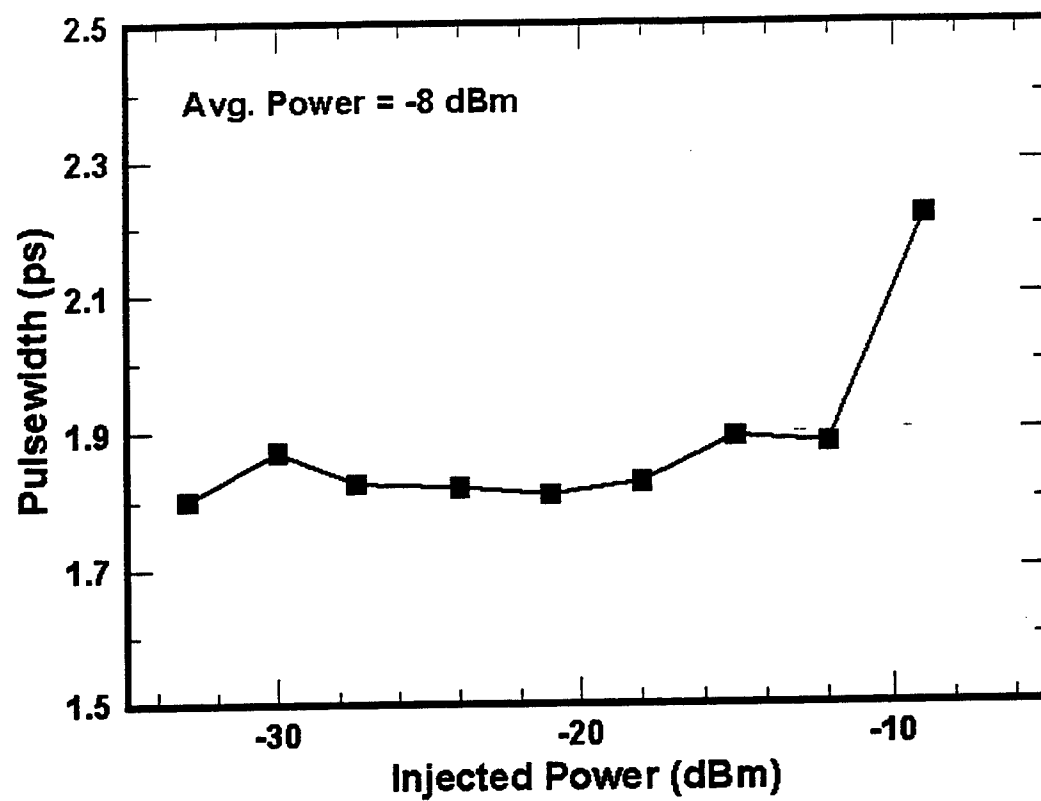


Fig. 9

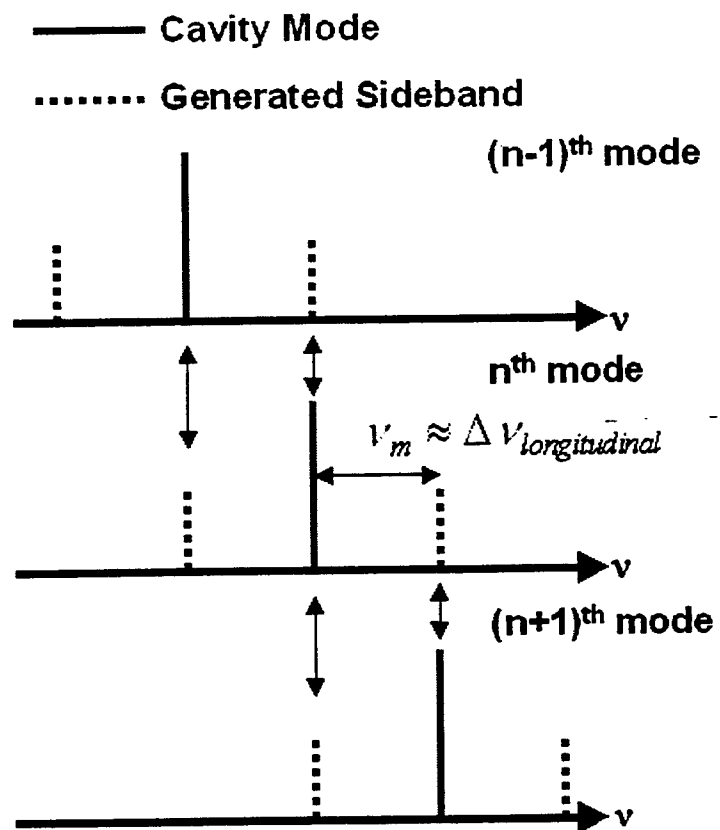


Fig. 10(a)

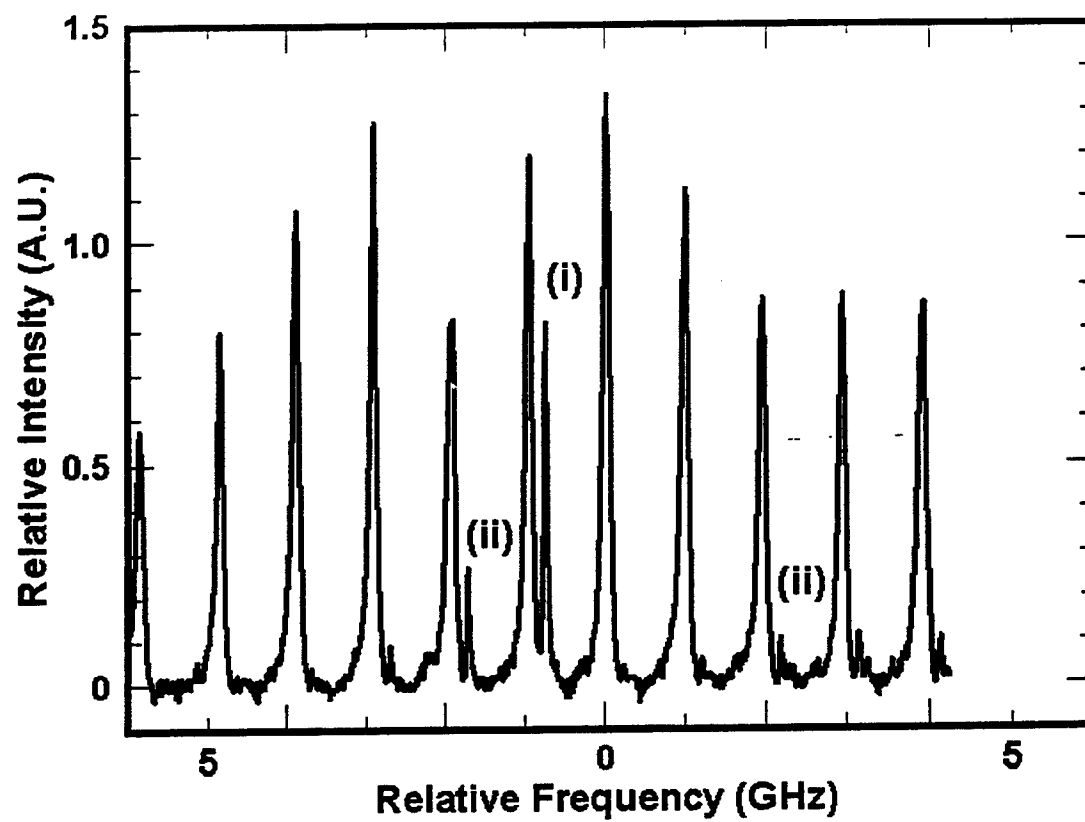


Fig. 10(b)

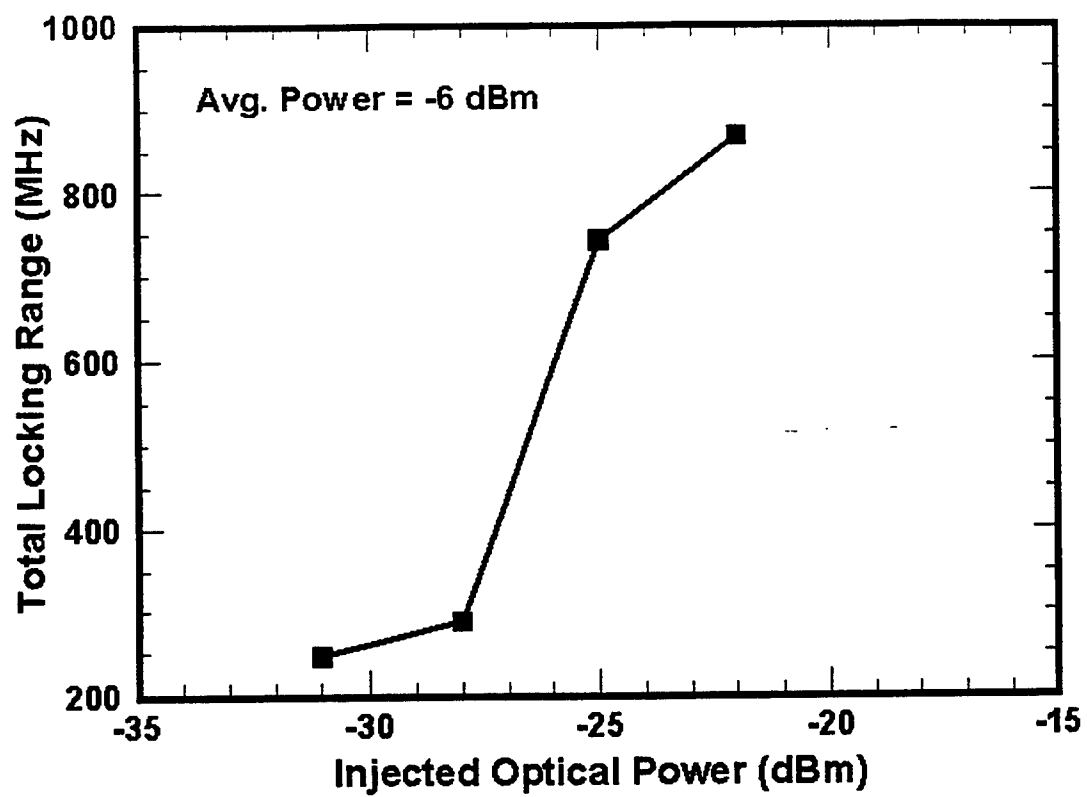


Fig. 11

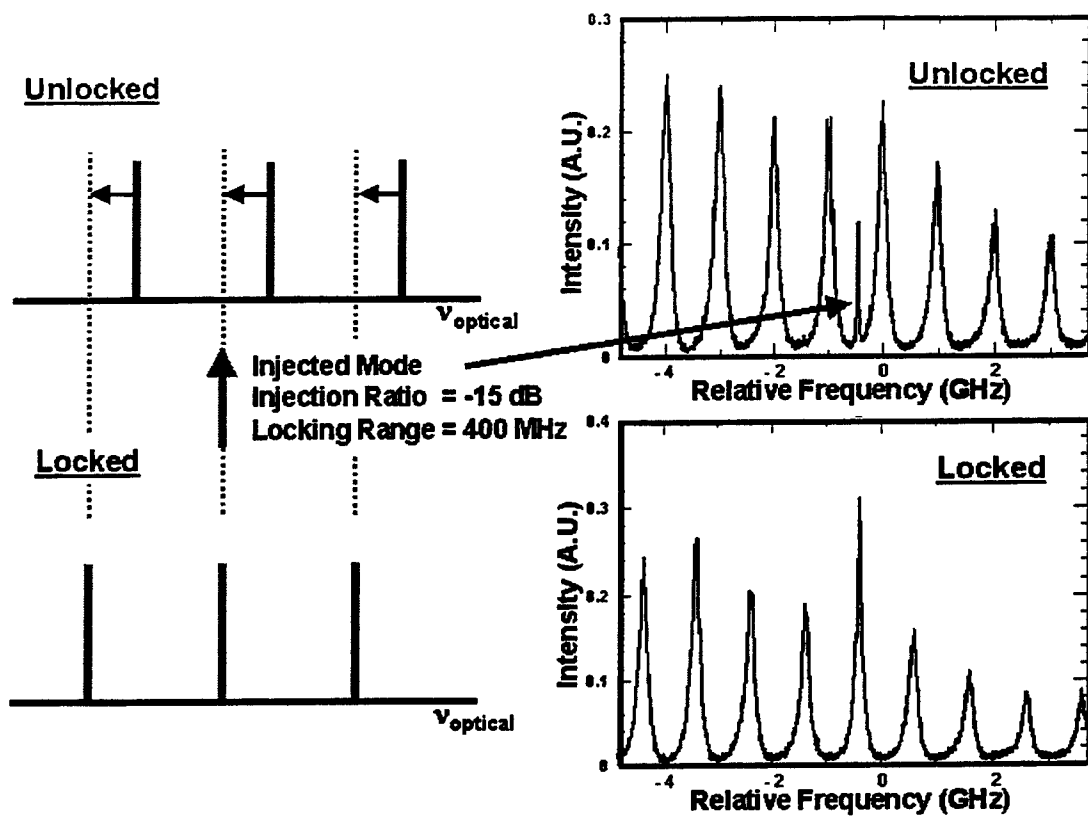


Fig. 12

DISTRIBUTION LIST

addresses	number of copies
AFRL/SNDR JAMES NICTER 25 ELECTRONIC PKY ROME NY 13441-4515	8
TRW INC SPACE AND TECHNOLOGY DIVISION ONE SPACE PARK REDONDO BEACH CA 90278	5
AFRL/IFOIL TECHNICAL LIBRARY 26 ELECTRONIC PKY ROME NY 13441-4514	1
ATTENTION: DTIC-DCC DEFENSE TECHNICAL INFO CENTER 8725 JOHN J. KINGMAN ROAD, STE 0944 FT. BELVOIR, VA 22060-6218	2
DEFENSE ADVANCED RESEARCH PROJECTS AGENCY 3701 NORTH FAIRFAX DRIVE ARLINGTON VA 22203-1714	1
ATTN: NAN PFRIMMER IIT RESEARCH INSTITUTE 201 MILL ST. ROME, NY 13440	1
AFIT ACADEMIC LIBRARY AFIT/LDR, 2950 P. STREET AREA B, BLDG 642 WRIGHT-PATTERSON AFB OH 45433-7765	1
AFRL/MLME 2977 P STREET, STE 6 WRIGHT-PATTERSON AFB OH 45433-7739	1

AFRL/HESC-TDC
2698 G STREET, BLDG 190
WRIGHT-PATTERSON AFB OH 45433-7604

1

ATTN: SMDC IM PL
US ARMY SPACE & MISSILE DEF CMD
P.O. BOX 1500
HUNTSVILLE AL 35807-3801

1

TECHNICAL LIBRARY D0274(PL-TS)
SPAWARSYSCEN
53560 HULL ST.
SAN DIEGO CA 92152-5001

1

COMMANDER, CODE 4TL000D
TECHNICAL LIBRARY, NAWC-WD
1 ADMINISTRATION CIRCLE
CHINA LAKE CA 93555-6100

1

CDR, US ARMY AVIATION & MISSILE CMD
REDSTONE SCIENTIFIC INFORMATION CTR
ATTN: AMSAM-RD-OB-R, (DOCUMENTS)
REDSTONE ARSENAL AL 35898-5000

2

REPORT LIBRARY
MS P364
LOS ALAMOS NATIONAL LABORATORY
LOS ALAMOS NM 87545

1

ATTN: D'BORAH HART
AVIATION BRANCH SVC 122.10
FDB10A, RM 931
800 INDEPENDENCE AVE, SW
WASHINGTON DC 20591

1

AFIWC/MSY
102 HALL BLVD, STE 315
SAN ANTONIO TX 78243-7016

1

ATTN: KAROLA M. YOURISON
SOFTWARE ENGINEERING INSTITUTE
4500 FIFTH AVENUE
PITTSBURGH PA 15213

1

USAF/AIR FORCE RESEARCH LABORATORY
AFRL/VSCSA(LIBRARY-BLDG 1103)
5 WRIGHT DRIVE
HANSCOM AFB MA 01731-3004

1

ATTN: EILEEN LADUKE/D460
MITRE CORPORATION
202 BURLINGTON RD
BEDFORD MA 01730

1

OUSD(P)/DTSA/DUTD
ATTN: PATRICK G. SULLIVAN, JR.
400 ARMY NAVY DRIVE
SUITE 300
ARLINGTON VA 22202

1

RICHARD PAYNE
AIR FORCE RESEARCH LAB/SNH
HANSCOM AFB, MA 01731-5000

1

JOSEPH P. LORENZO, JR.
AIR FORCE RESEARCH LAB/SNHC
HANSCOM AFB, MA 01731-5000

1

JOSEPH L. HORNER
AIR FORCE RESEARCH LAB/SNHC
HANSCOM AFB, MA 01731-5000

1

RICHARD A. SOREF
AIR FORCE RESEARCH LAB/SNHC
HANSCOM AFB, MA 01731-5000

1

ALBERT A. JAMBERDINO
AIR FORCE RESEARCH LAB/IFED
32 HANGAR RD
ROME NY 13441-4114

1

AIR FORCE RESEARCH LAB/SND
25 ELECTRONIC PKY
ROME NY 13441-4515

1

JOANNE L. ROSSI
AIP FORCE RESEARCH LAB/SNW
25 ELECTRONIC PKY
ROME NY 13441-4515

1

NY PHOTONIC DEVELOPMENT CORP
MVCC ROME CAMPUS
UPPER FLOYD AVE
ROME, NY 13440

1

ROBERT T. KEMERLEY
AIR FORCE RESEARCH LABORATORY/SND
2241 AVIONICS CIRCLE, RM C2G69
WRIGHT-PATTERSON AFB OH 45433-7322

1

ASC2A/C2N
COL BLACKMORE
130 ANDREWS ST STE 210
LANGLEY AFB VA 23665-1993

1

MILSATCOM JOINT TERMINAL ENG OFFICE
MR WILLIAM FIZELL
5111 LEESBURG PIKE STE 100
FALL CHURCH VA 22241

1

JOSEPH WILGUS
2241 AVIONICS CIRCLE STE 32
WRIGHT PATTERSON AFB OH 45433-7318

1

US ARMY COMM ELECTRONICS COMMAND
MR JAMES G WRIGHT
AMSEL-RD-ST-SY-TE
FORT MONMOUTH NJ 07703-5203

1

SPAWARSSYSCEN DAN DIEGO
CODE D895
MR STEPHEN A PAPPERT
53560 HULL ST
SAN DIEGO CA 92152-5001

1

AIR FORCE RESEARCH LABORATORY/IFGC
STEVEN YAX
525 BROOKS RD
ROME NY 13441-4505

1

TRW PHOTONICS TECHNOLOGY
RICHARD I DAVIS
M/S: 01-1024
ONE SPACE PARK
REDONDO BEACH CA 90278

1

MIT LINCOLN LABORATORY
CHARLES COX
M/S: J-149
244 WOOD ST
LEXINGTON MA 02173-9108

1

DARPA/STO
4001 N FAIRFAX DRIVE
ARLINGTON VA 22203-1714

1

SPAWARSYSCEN SAN DIEGO
STEPHEN A PAPPERT
CODE D895
53560 HULL ST
SAN DIEGO CA 92152-5001

1

WL/AASA
JOSEPH S WILGUS
2241 AVIONICS CIRCLE STE 32
WPAFB OH 45433-4171

1

US ARMY COMM ELECTRONIC COMMAND
AMSEL-RD-ST-SY-TE
JAMES G WRIGHT
FORT MONMOUTH NJ 07703-5203

1

AFRL/SNDR
NORMAN BERNSTEIN
25 ELECTRONIC PKY
ROME NY 13441-4515

1

AFRL/SNDR
RICHARD MICHALAK
25 ELECTRONIC PKY
ROME NY 13441-4515

1

AFRL/SNDR
GEORGE BROST
25 ELECTRONIC PKY
ROME NY 13441-4515

1